

AD\_\_\_\_\_

Award Number: W81XWH-13-1-0031

TITLE: Investigating the Mechanism of MenaINV-Driven Metastasis

PRINCIPAL INVESTIGATOR: Madeleine J. Oudin

CONTRACTING ORGANIZATION: Massachusetts Institute of Technology  
Cambridge, MA 02139

REPORT DATE: February 2016

TYPE OF REPORT: Final

PREPARED FOR: U.S. Army Medical Research and Materiel Command  
Fort Detrick, Maryland 21702-5012

DISTRIBUTION STATEMENT: Approved for Public Release;  
Distribution Unlimited

The views, opinions and/or findings contained in this report are those of the author(s) and should not be construed as an official Department of the Army position, policy or decision unless so designated by other documentation.

REPORT DOCUMENTATION PAGE				Form Approved OMB No. 0704-0188	
Public reporting burden for this collection of information is estimated to average 1 hour per response, including the time for reviewing instructions, searching existing data sources, gathering and maintaining the data needed, and completing and reviewing this collection of information. Send comments regarding this burden estimate or any other aspect of this collection of information, including suggestions for reducing this burden to Department of Defense, Washington Headquarters Services, Directorate for Information Operations and Reports (0704-0188), 1215 Jefferson Davis Highway, Suite 1204, Arlington, VA 22202-4302. Respondents should be aware that notwithstanding any other provision of law, no person shall be subject to any penalty for failing to comply with a collection of information if it does not display a currently valid OMB control number. <b>PLEASE DO NOT RETURN YOUR FORM TO THE ABOVE ADDRESS.</b>					
1. REPORT DATE February 2016		2. REPORT TYPE Final		3. DATES COVERED 1 Dec 2012 - 30 Nov 2015	
4. TITLE AND SUBTITLE  Investigating the Mechanism of MenaINV-Driven Metastasis				5a. CONTRACT NUMBER	
				5b. GRANT NUMBER W81XWH-13-1-0031	
				5c. PROGRAM ELEMENT NUMBER	
6. AUTHOR(S)  Madeleine J. Oudin  E-Mail: mjoudin@mit.edu				5d. PROJECT NUMBER	
				5e. TASK NUMBER	
				5f. WORK UNIT NUMBER	
7. PERFORMING ORGANIZATION NAME(S) AND ADDRESS(ES)  Massachusetts Institute of Technology 77 Massachusetts Avenue Cambridge, MA 02139				8. PERFORMING ORGANIZATION REPORT NUMBER	
9. SPONSORING / MONITORING AGENCY NAME(S) AND ADDRESS(ES) U.S. Army Medical Research and Materiel Command Fort Detrick, Maryland 21702-5012				10. SPONSOR/MONITOR'S ACRONYM(S)	
				11. SPONSOR/MONITOR'S REPORT NUMBER(S)	
12. DISTRIBUTION / AVAILABILITY STATEMENT Approved for Public Release; Distribution Unlimited					
13. SUPPLEMENTARY NOTES					
14. ABSTRACT Mena, an actin regulatory protein, is upregulated in human breast cancer and is alternatively spliced to produce protein isoforms with distinct functions during tumor progression. Here, we show that Mena <sup>INV</sup> promotes synergy between growth factors and ECM cues, by driving crosstalk downstream of the receptors for these cues, suggesting that Mena supports metastasis via chemotaxis and haptotaxis, and that both of these pathways are important for metastatic progression. Furthermore, we show that Mena isoform expression is associated with resistance to Taxol, the front line chemotherapy used to treat metastatic breast cancer, both <i>in vitro</i> and <i>in vivo</i> . The mechanism driving this resistance is still under investigation. Overall, these data identify new targetable mechanisms by which tumors cells are able to metastasize, and highlight new ways in which resistance to chemotherapy may be predicted and eventually overcome.					
15. SUBJECT TERMS metastasis, RTK signaling, integrins, MenaINV, resistance, chemotherapy, chemotaxis, haptotaxis, Taxol, survival, intravital imaging, synergy					
16. SECURITY CLASSIFICATION OF:			17. LIMITATION OF ABSTRACT	18. NUMBER OF PAGES	19a. NAME OF RESPONSIBLE PERSON
a. REPORT	b. ABSTRACT	c. THIS PAGE			USAMRMC
U	U	U	UU		19b. TELEPHONE NUMBER (include area code)

## Table of contents

	Page
Introduction.....	4
Body.....	5
Key research accomplishments.....	12
Reportable outcomes.....	13
Conclusion.....	15
References.....	16
Supporting data.....	18
Appended publications.....	29

## Introduction

Mena is a member of the Ena/VASP family proteins that regulate actin polymerization and modulate the morphology and dynamics of membrane protrusions thereby influencing cell motility<sup>12</sup>. Mena expression is upregulated in human breast cancers and plays a significant role in breast cancer metastasis<sup>3</sup>. Mena is alternatively spliced and the Mena isoform containing the “INV” exon (“Mena<sup>INV</sup>”) is upregulated significantly in invasive cells<sup>4</sup>. Mena<sup>INV</sup> increases tumor cell invasion, coordinated “streaming” motility, and tumor cell intravasation<sup>5–7</sup>. Mena<sup>INV</sup>-expressing cells exhibit potent effects on EGF-elicited tumor cell motility, promoting actin polymerization and a more rapid and extensive lamellipodial protrusion, increasing invasion and sensitizing cells to respond to 50-fold lower EGF concentrations than control cells<sup>5</sup>. Analysis of several canonical signalling components downstream of EGFR (such as Erk and Akt) revealed no obvious effect of Mena<sup>INV</sup> on their activities despite increased activation of the receptor itself (unpublished). The goal of this project is to further investigate the mechanism through which Mena<sup>INV</sup> drives invasion as well as understand the dynamics of Mena<sup>INV</sup> expression. In year 1, significant progress was made towards achieving these goals. First, we showed that Mena<sup>INV</sup> can drive invasion by regulating several RTKs, mainly EGFR, Met and IGFR through dysregulation of PTP1B. Mena<sup>INV</sup> does not affect responses to growth factors whose receptors are not regulated by PTP1B. Mena<sup>INV</sup> also drives resistance to several RTK inhibitors, mainly Erlotinib for EGFR and SU110274 for Met. Next, I showed that FN drives invasion of Mena<sup>INV</sup>-expressing cells in the absence of growth factor, an effect which is dependent on Mena<sup>INV</sup>'s interaction with  $\alpha 5 \beta 1$  as well as EGFR and Met. Finally, I generated and validated of the INV reporter *in vitro*, and optimized and characterized staining for endogenous Mena<sup>INV</sup> in mouse and human tumor sections using a newly generated isoform specific antibody. The data collected in Year 1 led to two first author publications<sup>8,9</sup>. In Year 2, I continued to investigate the role of FN as a directional cue in migration, describing Mena<sup>INV</sup>-driven haptotaxis both *in vitro* and *in vivo*. I studied the mechanistic basis for haptotaxis, which involves inside-out signaling at focal adhesions and outside-in ECM reorganization. I also developed novel ways to study haptotaxis *in vivo*<sup>10</sup>. I also further investigate how RTKs may be involved in drug resistance, demonstrating that proteolytic shedding of RTKs from the tumor cell surface is a key resistance mechanism when the MAPK signaling pathway is targeted (Miller & Oudin et al., 2015 Cancer Disc in press). Finally, in Year 3, I have continued to investigate the role of Mena isoforms in directed cell migration and drug resistance in breast cancer.

## Investigate the signaling downstream of invasion promoting factors

(Task 2)

### Mena<sup>INV</sup> at the nexus between chemotaxis and haptotaxis

Given the multitude of ECM and GF cues present in the tumor microenvironment, tumor cells must integrate multiple extracellular signals to coordinate directional invasive responses. Mena<sup>INV</sup> sensitizes cells to low GF concentrations via dysregulation of phosphatase signaling<sup>7</sup>. Using a microfluidic device *in vitro* and an implantable device *in vivo* to generate FN gradients, we have shown that Mena<sup>INV</sup> drives haptotaxis on FN gradients, via its interaction with  $\alpha 5$ , signaling at focal adhesions and ECM remodeling. Furthermore, most tumor cell motility studies focus on responses to one guidance cue at a time. How tumor cells integrate combinations of ECM and growth factor (GF) cues, known to be simultaneously present in the tumor microenvironment, is poorly understood. Understanding the mechanisms by which the ECM and GF cues coordinately drive invasion and metastatic colonization will help develop prognostic markers to predict metastatic risk and identify new therapeutic tractable targets.

### Mena and Mena<sup>INV</sup>-driven haptotaxis at concentrations requires EGFR signaling

Given the established role of Mena<sup>INV</sup> in driving growth factor sensitization<sup>8</sup> and driving haptotaxis on FN gradients and the emerging role of RTKs in response to ECM cues<sup>1</sup>, we asked whether Mena<sup>INV</sup>-driven haptotaxis on FN gradients requires EGFR signaling. Cultured breast tumor cells express low levels of Mena and undetectable levels of Mena<sup>INV</sup> relative to the amounts found within primary tumors and invasive cells collected from these tumors<sup>4,9</sup>. We generated cell lines from the p53-mutant triple negative breast cancer cell line MDA-MB-231 expression levels of Mena and Mena<sup>INV</sup> similar to those found in invasive tumor cells (approximately 10-fold overexpression, cells referred to as 231-Control, 231-Mena or 231-Mena<sup>INV</sup>). Erlotinib, an EGFR-specific kinase inhibitor, blocked Mena-driven haptotaxis at all concentrations on low FN gradients, at all concentrations of the drug tested (Fig 1A). 231-Mena<sup>INV</sup> cells required a 10-fold higher concentration of Erlotinib than 231-Mena cells to completely block haptotaxis completely (Fig 1A). We have previously shown that expression of Mena<sup>INV</sup> allows cells to haptotax at high FN concentrations. We found that Erlotinib also inhibited Mena<sup>INV</sup>-haptotaxis at high FN concentrations (Fig 1B). We then investigated whether EGFR activity on FN gradients was driven by autocrine activation of EGFR or intracellular transactivation via crosstalk. Addition of mab225, which blocks EGF-dependent activation of EGFR but not its intrinsic kinase activity<sup>12</sup>, had no effect on haptotaxis, suggesting the requirement for EGFR kinase activity revealed by sensitivity to erlotinib was not dependent on autocrine or paracrine activation of EGFR by EGF ligand (Fig 1C,D). Together, these data suggest Mena<sup>INV</sup>-driven haptotaxis on low and high FN gradients requires EGFR signaling.

### FN-driven growth factor-independent invasion requires EGFR signaling

To investigate this further in a 3D context, we examined invasion responses in 3D collagen gels where we introduced increasing amounts of FN. Briefly, cells are plated in collagen and FN solutions, the plates are spun down so cells are at the bottom, and the gels are then left to polymerize, and cells are fixed 24hrs later. Invasion up into the gel is quantified using confocal imaging and a custom-made Matlab code. We found that 231-Control and 231-Mena cells exhibited a biphasic response to FN, with FN inducing a growth-factor independent invasion response in this assay at 50  $\mu\text{g/ml}$ , with no effect at the higher 125  $\mu\text{g/ml}$  dose (Fig 2A,B). However, these high concentrations of FN did not affect invasion of 231-Mena<sup>INV</sup> cells, who were still able to migrate in the absence of growth factor at this high dose. In fact, a concentration of 250  $\mu\text{g/ml}$  FN was needed to

no longer promote invasion of 231-Mena<sup>INV</sup> cells (Fig 2C). As a control, increasing volumes of PBS were used instead of FN, and we found that addition of PBS did not drive invasion into collagen, confirming the effect of FN on this process (data not shown). We have shown that Mena<sup>INV</sup>-driven haptotaxis requires the direct interaction with the cytoplasmic tail of  $\alpha 5$  integrin, mediated by the LERER domain of the protein (REF). The pro-invasive effect of FN was dependent on Mena<sup>INV</sup>'s interaction with  $\alpha 5$ , as 231-Mena<sup>INV</sup> $\Delta$ LERER cells did not display this biphasic response to FN (Fig 2D). Inhibition of  $\alpha 5\beta 1$ , with the blocking antibody P1D6, but not of  $\alpha v\beta 3$  with Cilengitide, inhibited FN-driven invasion of 231-Mena<sup>INV</sup> cells (Fig 2E). We then asked if EGFR signaling was involved in Mena<sup>INV</sup>-driven invasion into FN, and found that Erlotinib could inhibit invasion of 231-Mena<sup>INV</sup> cells at all FN concentrations (Fig 2F). Together, these data suggest that FN-driven growth factor-independent 3D collagen invasion requires both  $\alpha 5\beta 1$  and EGFR signaling.

### **Mena<sup>INV</sup> expression promotes EGFR signaling on FN**

These results prompted us to ask if it was possible that the ligand-independent EGFR kinase function reflected  $\alpha 5\beta 1$ -mediated phosphorylation of EGFR. We quantified levels of phosphorylation of EGFR at Y1173 in haptotaxing cells. We have shown that 231-Mena<sup>INV</sup> cells show increased levels of phosphorylation at the residue when stimulated with low EGF concentrations<sup>8</sup>. Using immunofluorescence, we quantified pEGFR<sup>Y1173</sup> levels in cells plated on gradients of FN of different concentrations. On a low FN gradient, there was a positive significant correlation between FN concentration and pEGFR<sup>Y1173</sup> in 231-Mena and 231-Mena<sup>INV</sup> cells but not in MDA-MB-231 cells (Fig 3A-C). This correlation was absent when cells were treated with Erlotinib. However, at high concentration of FN, only 231-Mena<sup>INV</sup> cells showed a significant correlation between pEGFR<sup>Y1173</sup> and FN (Fig 3D-F). We then investigated whether the Mena<sup>INV</sup> expression in human breast cancer patients was associated with phosphorylation of EGFR, using the TCGA database to assess Mena and Mena<sup>INV</sup> expression levels at the RNA level, and the available Reverse Phase Protein Assay (RPPA) data, available for a subset of patients in the cohort. There was a significant correlation between Mena<sup>INV</sup>, but not Mena, levels and pY1068, but not pY1173 levels in human breast patients from TCGA with available RPPA data (Fig5G). Interestingly, in patients with high tumor FN levels, there was a significant correlation between Mena<sup>INV</sup> and pEGFR<sup>Y1173</sup> (Fig5H).

### **Mena<sup>INV</sup> promotes synergy between EGF and FN**

So far, our studies have focused on how Mena<sup>INV</sup> drives directional migration in response to growth factors and ECM cues separately. However, given that both cues are present simultaneously within the tumor microenvironment, we investigated how cells would respond to both cues present at the same. A low dose chemotactic EGF gradient (0.5 nM) in the presence of 25  $\mu$ g/ml FN did not affect the invasion of cells expressing 231-Control or 231-Mena cells. However, in 231-Mena<sup>INV</sup> cells, the same dose of EGF in the presence of 25  $\mu$ g/ml FN had a significant increase on 3D invasion, which increased compared to low dose EGF on its own without FN and to the same dose of FN on its own without EGF (Fig 4A). These data suggest that Mena<sup>INV</sup> promotes synergy between FN and EGF. We then investigated the role of the Mena- $\alpha 5$  interaction in this synergistic response. Interestingly, deletion of the LERER region in Mena or Mena<sup>INV</sup> did not affect the protrusion response to low doses on EGF in cells plated on collagen and matrigel, suggesting that acute actin polymerization in response to growth factor stimulation is intact in the absence of interaction with  $\alpha 5$  (Fig S5). However, in 3D in the presence of FN, abrogating the interaction between Mena<sup>INV</sup> and  $\alpha 5\beta 1$  in 231-Mena<sup>INV</sup> $\Delta$ LERER cells (Fig4B) or inhibition of  $\alpha 5\beta 1$  with the P1D6 blocking antibody (Fig4C) inhibited this synergistic effect. To test this effect *in vivo*, we used the *in vivo* invasion assay, which allows for chemotaxis and collection of cells within a primary tumors into needles filled with growth factors and various ECM factors<sup>13</sup>. *In vivo*, we were able to show that the combination of EGF and FN attracted

more cells from Mena<sup>INV</sup>-GFP tumors that each cue alone (Fig 4D). At the same concentrations, the combination of EGF and FN did not have a synergistic effect on invasion in the Control-GFP or Mena-GFP tumors. Overall, these data suggest that Mena<sup>INV</sup> promotes invasion by sensitizing cells to both soluble chemotactic signals and substrate-bound ECM signals.

### **Inhibition of PTP1B phenocopies Mena<sup>INV</sup> expression and drives haptotaxis**

It is now well established that Mena<sup>INV</sup> expression affects sensitivity to various growth factors known to promote invasion, such as EGF, HGF and IGF, by dysregulating the phosphatase PTP1B<sup>5,8</sup>. We have previously shown that inhibition of PTP1B (PTP1Bi) phenocopies Mena<sup>INV</sup>, leading to increased sensitivity to EGF in control cells<sup>8</sup>. Here, we find that inhibition of PTP1B can drive haptotaxis of wild-type MDA-MB-231 cells on a 2D FN gradient (Fig 5A). This pro-haptotactic effect was dependent on the presence of Mena in cells, as MDA-MB-231 cells where Mena expression was deleted (231-sgMena) were unable to haptotax in response to PTP1Bi (Fig 5B). This effect also requires the interaction between Mena and  $\alpha 5$ , as cells with an LERER deletion were also unable to haptotax in the presence of PTP1Bi (Fig 5C).

To further investigate the mechanism by which PTP1Bi was driving haptotaxis, we looked at the phosphorylation level of Paxilin, known to be localized at focal adhesions and play a role in motility. We performed immunofluorescence studies on haptotaxing cells plated on a 2D FN gradient for 3 hrs and measured the number of pPAX Y118 adhesions in cells expressing different Mena isoforms plated on a 2D FN gradient. 231-Mena<sup>INV</sup> cells that haptotax towards high FN concentrations, had a significantly increased number of pPAX -positive adhesions (Fig 5D). To test whether the effect of the PTP1B inhibitor on 2D haptotaxis is due to changes in phosphorylation of proteins at FAs, we measured the number of pPAX Y118 positive adhesions in Control cells treated with the PTP1Bi and found that, in cells pated on a FN gradient, inhibition of PTP1B increased the number of pPAX Y118-positive adhesions in Control-GFP cells (Fig 5D). Finally, we wanted to confirm that Mena<sup>INV</sup> could also promote FA signaling downstream of RTK activation, to support the idea that Mena<sup>INV</sup> acts downstream of both growth factor and FN to promote motility. We have shown that at low dose EGF (0.25nM), only cells expressing Mena<sup>INV</sup> respond with active actin polymerization and protrusion, while cells expressing Mena do not show a response<sup>8</sup>. Here, we show that after EGF stimulation, 231-Mena<sup>INV</sup> have increased phosphorylation of Pax at residue Y118 compared to cells expressing Mena (Fig 75E). In addition treatment with a PTP1B inh significantly increased pPAX Y118 in Mena cells to similar levels as those see in cells expressing Mena<sup>INV</sup> (Fig5E). Overall, these data suggest that Mena<sup>INV</sup> promotes chemotactic and haptotactic responses to EGF and FN by increases phosphorylation of FA proteins, via dysregulation of the phosphatase PTP1B.

Our previous data showed that to haptotaxis also requires ECM reorganization. We asked whether inhibition of PTP1B and therefore increased phosphorylation of Pax was enough to drive haptotaxis of wild-type cells in 3D and on high FN gradients. Our data demonstrate that PTP1B is not sufficient to drive haptotaxis at high FN (Fig5F) and in 3D (Fig5G). Together, these data show that while focal adhesion signaling is important for 2D haptotaxis, it is not sufficient to drive haptotaxis in 3D or at high FN concentrations.

### **Mena<sup>INV</sup>-driven haptotaxis, ECM reorganization and 3D invasion requires RCP-dependent recycling of $\alpha 5\beta 1$ and EGFR**

Another way that EGFR and  $\alpha 5\beta 1$  crosstalk can contribute to invasion is via their co-trafficking<sup>14</sup>. Indeed, recent work has shown that RCP-dependent recycling of  $\alpha 5\beta 1$ /EGFR is important for 3D invasion of tumor cells<sup>15</sup>. We measured levels of recycling of both  $\alpha 5\beta 1$  and EGFR in MDA-MB-231 cells expressing the different Mena isoforms. We have previously reported that 231-Mena<sup>INV</sup> cells show a 30% increase in surface  $\alpha 5$  levels, while 231-Mena and 231-Mena<sup>INV</sup> cells show similar

EGFR levels, and these levels are unaffected by deletion of the LERER regions (data not shown). We asked whether RCP-dependent recycling of  $\alpha 5\beta 1$ /EGFR may also be involved in 3D haptotaxis<sup>15</sup>. Breast cancer patients with mutant-p53, which promotes invasion in MDAMB231 cells<sup>15</sup> via increased  $\alpha 5\beta 1$ /EGFR recycling, showed significantly higher levels of Mena<sup>INV</sup> (Fig6A). Knockdown of p53 or RCP (Fig 6B-D), which has previously been shown to block 3D invasion and recycling of  $\alpha 5\beta 1$ /EGFR<sup>15</sup>, decreased Mena<sup>INV</sup>-driven haptotaxis in 3D (Fig5E,F). Furthermore, Knockdown of p53 or RCP inhibited Mena<sup>INV</sup>-driven collagen and FN reorganization in haptotaxing cells (Fig 6G,H). Altogether, these data demonstrate that Mena-driven haptotaxis involves EGFR signaling, and suggests a role for RCP-mediated co-trafficking of  $\alpha 5\beta 1$ /EGFR complexes. Mena<sup>INV</sup> cells are able to haptotax at higher concentrations due to sustained ligand-independent activation of EGFR.

## Aim 2: Investigating the role of Mena isoforms in response to chemotherapy

Triple-negative breast cancer (TNBC), defined by a lack of expression of both estrogen and progesterone receptor as well as low levels of human epidermal growth factor receptor 2 (HER2, )accounts for 15% of breast tumors<sup>16</sup>. Due to the lack of known specific therapeutic targets, conventional cytotoxic chemotherapy remains the only treatment guideline for these patients. Platinum agents, taxanes and anthracyclines are used in mono- or poly-chemotherapy as front line treatment or in adjuvant therapy to prevent metastases<sup>17</sup>. Chemotherapy targets proliferating cells present in the tumor, and induces cell death in these cells via different mechanisms. Platinum drugs, such as Cisplatin, are alkylating agents, that generate crosslinks in the DNA, blocking DNA synthesis<sup>18</sup>. Anthracyclines such as Doxorubicin induce DNA-damage by causing DNA double strand breaks, by intercalating in the DNA and inhibiting topoisomerase II leading to double strands break<sup>19</sup>. Taxanes, such as Taxol, lead to mitotic catastrophe by stabilizing microtubules and inhibiting their disassembly during metaphase<sup>20</sup>. This damages induces intracellular stress signals leading to activation of cell death pathways<sup>21</sup>.

Although patients in the TNBC subgroup show decreased survival rates compared with non-TNBC, the benefits of chemotherapy for TNBC have now been clearly demonstrated in multiple studies. The poor overall survival is due to the fact that over 50% of TNBC patients become resistant to chemotherapy<sup>22</sup>. A number of cellular processes have been identified that can drive tumor cell resistance to Cisplatin, Doxorubicin and Taxol. Cell intrinsic mechanisms of resistance include intracellular modifications such as changes in expression of the adenosine triphosphate-binding cassette (ABC) superfamily of transporters, alteration in DNA repair pathways, mutations in cellular targets, resistance to initiation of the apoptotic pathway and the development of constitutively activated pro-survival signaling pathways<sup>23</sup>. In addition, the tumor microenvironment can also initiate survival signals and protect tumor cells from chemotherapy-induced cell death<sup>24</sup>.

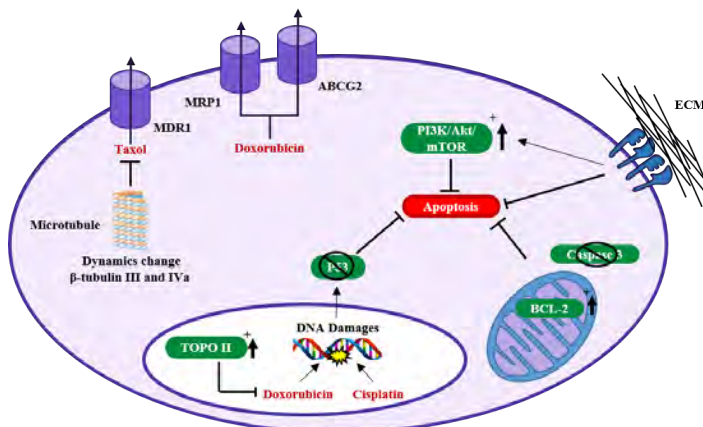


Figure 1: Mechanisms of chemoresistance in TNBC (A) ABC transporters efflux chemotherapeutics out of cancer cells (B) Modifications in the drug's cellular target (C) Impair in DNA damage sensor induced apoptosis (D) Constitutive activation of pro-survival pathway (E) Alterations in genes involved in apoptosis prevent chemotherapy-induced apoptosis (F) Activation of tumor microenvironment-driven extrinsic survival signals

Given the role of Mena isoforms in driving metastasis, we were now interested in elucidating their potential role in response to chemotherapy in TNBC.



## **Mena isoforms are associated with increased survival during Taxol treatment *in vitro***

We first studied the role of Mena isoforms in cell survival in response to chemotherapy *in vitro*. To study the role of each Mena isoform independently we used a triple-negative breast adenocarcinoma cell line (MDA-MB-231) which expresses low levels of Mena and an undetectable levels of Mena<sup>INV</sup> *in vitro*<sup>25</sup>, stably expressing GFP, GFP-tagged Mena or Mena<sup>INV</sup>. Cells overexpressing a single Mena isoform or a GFP-control were plated in 96-well plates and treated with Doxorubicin or Taxol at concentrations ranging from 0.1 nM to 100  $\mu$ M or Cisplatin at concentration ranging from 1 nM to 100 nM during 24h or 72h. We observed that the fraction of viable MDA-MB-231 GFP-Mena (Mena) or MDA-MB-231 GFP-Mena<sup>INV</sup> (Mena<sup>INV</sup>) was at least 65% higher than the fraction of viable MDA-MB-231 GFP (Control) cells, after 72h (Fig7A) or 24h (data not shown) of Taxol treatment at 100 nM, 1 $\mu$ m or 10 $\mu$ M. However, Mena or Mena<sup>INV</sup> expression did not affect response to the different concentrations of Doxorubicin or Cisplatin (Fig 7B,C). These experiments revealed that cell death in the presence of high Taxol concentrations is decreased with ectopic expression of Mena or Mena<sup>INV</sup>.

As the first experiments relied on overexpression in a single cell line, we wanted to test whether the observations held true in other breast cancer cell lines, by looking at endogenous Mena expression. We therefore measured Taxol efficacy and quantified levels of endogenous Mena protein expression across several human breast cancer types, including Luminal A (MDA-MB 175IIV and T47D), HER2 positive (MDA-MD 453) and TNBC (SUM 159, BT-20, MDA-MB 436, LM2, BT-549, MDA-MB 231) cell lines. We restricted our analysis to Mena, as Mena<sup>INV</sup> is not expressed at detectable levels in any of these breast cancer cell lines in culture. Taxol efficacy was assayed by determining the fraction of viable cells in response to different concentrations of Taxol (Fig 7D). Levels of endogenous Mena protein expression in the 9 human breast cancer cell lines was measured by Western Blot analysis (Fig 7E). There was a highly significant anti-correlation between Taxol efficacy and endogenous Mena expression levels (Fig 7F). Together, these data suggest that Mena isoforms may be involved in resistance to Taxol.

## **Mena isoform expression is associated with increased tumor growth *in vivo***

We then wanted to investigate whether these pheonyptes would hold true *in vivo*. Xenograft tumors were generated by injecting MDA-MB-231 cells expressing GFP (Control), GFP-Mena (Mena) or GFP-Mena<sup>INV</sup> (Mena<sup>INV</sup>) into the mammary fat pad of NOD-SCID mice. Mice were treated with three doses of Taxol or two of Doxorubicin, once the primary tumor had reached 1 cm in diameter. Tumor size was measured before and after treatment. Treatment with the both drugs significantly decreased growth of Control tumors compared to mice treated with vehicle (Fig 8A,D). However, the growth of Mena or Mena<sup>INV</sup> tumors was unaffected by the drug treatment(Fig 8A,D). This *in vivo* experiment confirmed results obtained in the *in vitro* screen and support the potential role of Mena and Mena<sup>INV</sup> in resistance to Taxol. Whereas the *in vitro* screen did not reveal any role of Mena or Mena<sup>INV</sup> in cell response to Doxorubicin, tumors expressing these isoforms showed decreased response to Doxorubicin *in vivo*.

We investigated whether this increased tumor size was due to increased levels of proliferation of decreased levels of cell death. We stained tumor sections from these tumors with the proliferation marker Ki67, as well as the apoptotic marker Cleaved Caspase 3. We find that Taxol treatment did not affect proliferation in Mena or Mena<sup>INV</sup>-expressing tumors (Fig 8B,E), but did increase cell death (Fig 8C,F). These data suggest that tumors expressing Mena or Mena<sup>INV</sup> are still able to proliferate during Taxol treatment.

## **Taxol treatment selects for high Mena expression *in vitro* and *in vivo***

Previous results have shown that a high level of Mena or Mena<sup>INV</sup> expression is associated with a low response to Taxol. However, we hypothesized that Taxol treatment might also affect the level of Mena expression. We analyzed Mena expression by Western Blot in MDA-MB 231 GFP cells exposed to 100nM of Taxol or vehicle. After 24h, there was no significant increase expression of Mena in lysate from Taxol-treated cells compared to vehicle (Fig 9A,B). 72h after Taxol treatment, the expression level of Mena was 70% higher than in vehicle-treated cells. We performed a similar expression of GFP-tagged Mena expressing cell lines. FACS analysis reveals that treatment with Taxol selects for high GFP-expressing cells for Mena and Mena<sup>INV</sup> cells (Fig 9C). Finally, immunohistochemical analysis of tissue sections from Control tumors confirmed an increase in expression of not only Mena, but also Mena<sup>INV</sup> in tumors from the Taxol-treated mice compared to vehicle. Two hypotheses could explain this increase: cells expressing a high level of Mena or Mena<sup>INV</sup> are selected for by the treatment with Taxol, or surviving cells overexpress Mena in response to Taxol (Fig 9D,E).

### **Taxol treatment decreases cell velocity *in vitro*, but does not affect Mena<sup>INV</sup>-driven tumor cell motility and dissemination in mice.**

Mena and Mena<sup>INV</sup> have been shown to be involved in tumor cell motility<sup>26,27</sup>. Mena, and more strikingly Mena<sup>INV</sup> expression, increases the number of cells moving in a tumor as visualized by intravital imaging and promotes metastasis formation<sup>5</sup>. Therefore, we were interested in studying effect of Taxol on tumor cell motility and dissemination. Control, Mena and Mena<sup>INV</sup> cells treated with low concentrations of Taxol or vehicle were plated on glass-bottom dishes coated with Collagen or Collagen and FN and tracked overnight. Taxol treatment decreased velocity of the three cell lines (Fig.6B) without affect cell spreading (data not shown). The effect of Taxol on cell motility *in vivo* was assessed using multiphoton intravital imaging. Treatment with Taxol significantly reduced the number of cells moving in Control tumors. On the contrary, motility of Mena<sup>INV</sup> tumor cells was not affected by the treatment (Fig 6B). To investigate the consequences of Taxol treatment on tumor cell dissemination, we counted the number of metastases in the lung and the number of colonies in cultured bone marrow from mice bearing Control, Mena or Mena<sup>INV</sup> tumor for 12 weeks. The number metastases in the lung or colonies in the bone marrow from Mena<sup>INV</sup> tumors was not affected by treatment with Taxol. Even though low concentration of Taxol decreased Mena<sup>INV</sup>-driven cell motility *in vitro*, motility and dissemination of this cell line was unaffected in mice treated with Taxol.

### **Investigation into the mechanisms driving Mena- and Mena<sup>INV</sup>-induced resistance to Taxol**

We were next interested in understanding the mechanism by which Mena and Mena<sup>INV</sup> drive resistance to Taxol. Taxol efflux through the MDR1 pump is one of the main and most well described mechanisms of Taxol resistance. We used a third-generation MDR1 inhibitor, HM30181, to investigate the role of this pump in our model<sup>28</sup>. HM30181 did not affect the proliferation of Control and Mena<sup>INV</sup> cells (data not shown). Co-treatment with HM30181 and 100nM of Taxol negligibly affected the fraction of viable Control cells and did not increase Taxol efficacy in Mena<sup>INV</sup> cells (Fig 11A). These data suggest that drug efflux does not play an important role in Mena<sup>INV</sup>-driven resistance to Taxol. Recent studies have highlighted the role of focal adhesions and FAK signaling in resistance to Taxol<sup>29</sup>. Mena interacts with  $\alpha 5$  via its LERER domain and localizes at the focal adhesions. Deletion of the LERER region abolishes the interaction between Mena and  $\alpha 5$ , resulting in a decrease in Mena and  $\alpha 5$  localization at focal adhesion and in the level of FAK phosphorylation<sup>26</sup>. Cells with deletions of LERER in Mena and Mena<sup>INV</sup> were treated with 100nM of Taxol (Fig 11B) and were found to behave the same as cells expressing a full length version of Mena and Mena<sup>INV</sup>. These data suggest that the interaction between Mena and  $\alpha 5$ , does not drive resistance to Taxol. Finally, one of the key steps in Taxol-induced cell death is cell arrest in G2/M. We performed cell cycle

analysis on Control, Mena and Mena<sup>INV</sup> cells treated with 10nM or 100nM of Taxol for 16h (Fig11C). Similar percentage of Control, Mena and Mena<sup>INV</sup> cells blocked in G2/M phase were found for the different treatments. Moreover, the amount of cells blocked in G2/M phase seemed dose-dependent. Therefore, Mena or Mena<sup>INV</sup> expression does not impair Taxol-induced arrest in G2/M.

## Key research accomplishments

- FN-driven haptotaxis requires crosstalk between RTKs and integrins and recycling of RTKs and integrins (Task 2)
- Inhibition of PTP1B can drive haptotaxis of breast tumor cells, but only on low FN gradients, not on high FN gradients or in 3D (Task 2)
- Mena isoform expression is associated with resistance to Taxol, but not Doxorubicin or Cisplatin *in vitro*
- Mena isoform expression is associated with resistance to Taxol and Doxorubicin *in vivo*, via increased cell proliferation
- Treatment with Taxol does not decrease Mena<sup>INV</sup>-driven migration or metastasis, but does inhibit haptotaxis, *in vitro* and *in vivo*
- Taxol treatment selects for cells expressing high levels of Mena, *in vitro* and *in vivo*
- Mena isoform driven resistance to Taxol is not due to increased efflux through MDR1, signaling at focal adhesions via  $\alpha 5$ , or increased G2/M arrest.

## Reportable outcomes

### 1. Manuscripts

#### Accepted :

**Oudin MJ**, Shannon K. Hughes, Nazanin Rohani, Mira N. Moufarrej, Joan Jones, John Condeelis, Douglas Lauffenburger, Frank B. Gertler (2015) Characterization of MenaINV expression during tumor progression, Clin Exp Metastasis, in press

Li CM, Gocheva V, **Oudin MJ**, Bhutkar A, Wang SY, Ng SR, Whittaker C, Bronson R, Snyder E, Gertler FB, Jacks T. (2015) Foxa2 and Cdx2 synergize with Nkx2-1 to limit metastasis of lung adenocarcinoma, *Genes & Dev*, Sep 1;29(17):1850-62

Shannon K. Hughes\*, **Oudin MJ\***, Jenny Tadros, Mira N. Moufarrej, Jason Neil, Amanda Del Rosario, Brian Joughin, Laila Ritsma, Jeff Wyckoff, Alisha Lussiez, John Condeelis, Jacco van Rheenen, Forest White, Douglas Lauffenburger, Frank B. Gertler (2015) Regulation of receptor tyrosine kinase signaling by the actin binding protein Mena, *Molecular Biology of the Cell*, Sep 2. pii: mbc.E15-06-0442, Epub

**Oudin MJ**, Oliver Jonas, Tatiana Kosciuk, Andrew Riching, Liliane C. Broye, Jeff Wyckoff, Shannon K. Hughes, John M. Lamar, Sreeja Asokan, Robert Langer, Michael J Cima, Kari B. Wasinski, Douglas A. Lauffenburger, Patrica Keely, James E. Bear, Frank B. Gertler (2016) Haptotaxis and direct remodeling of the ECM by tumor cells is important for metastasis, Cancer Discovery, in press

Miller MA\*, **Oudin MJ\***, Sullivan RJ, Frederick DT, Meyer AS, Tadros J, Griffith LG, Flaherty K, Gertler FB, Lauffenburger DA (2016) Reduced proteolytic shedding of receptor tyrosine kinases is a post-translational mechanism of kinase inhibitor resistance, Cancer Discovery, in press

#### In preparation:

Madeleine J. Oudin, Miles A. Miller, Joelle Klazen, Tatsiana Kosciuk, Alisha Lussiez, Shannon K. Hughes, James E. Bear, Douglas A. Lauffenburger<sup>1</sup>, Frank B. Gertler (2016) Mena at the nexus of chemotaxis and haptotaxis, *Molecular Biology of the Cell*, in preparation

### 2. Presentations

Selected speaker, AACR Tumor Metastasis Workshop	Dec 2015
Invited Speaker, University of Manchester, Wellcome Centre for Matrix Research	Nov 2015
Invited speaker, Ludwig Institute for Metastasis Research Annual Retreat	May 2015
Selected speaker, GRS 'FN, Integrins and Related Molecules'	May 2015
Selected speaker, GRS 'Directed Cell Migration'	Jan 2015

### 3. Conferences and workshops

November 2015      **AACR Tumor Metastasis Workshop**  
Austin, TX, USA

June 2015	<b>Ludwig Institute for Metastasis Research Annual Retreat</b> MIT, Cambridge, MA
May 2015	<b>Gordon Research Seminar and Conference “Fibronectin &amp; Integrins”</b> <i>Barga, Italy</i>
April 2015	<b>AACR Annual meeting</b> Philadelphia, USA
January 2015	<b>Gordon Research Seminar and Conference “Directed Cell Migration”</b> Galveston, TX, USA

#### 4. Awards

January 2016	<b>MIT Infinite Kilometer Award</b> Recipients of these awards are exceptional contributors to their research programs as well as deeply committed to their local or global MIT community.
November 2015	<b>AACR Scholar-in-Training Award</b> Competitive award to attend AACR Tumor Metastasis conference
May 2015	<b>1<sup>st</sup> prize</b> for poster presentation GRC ‘FN, Integrins and Related Molecules’

#### 5. Service

- Active volunteer for scientific community outreach events (Cambridge Science Festival, career panels, student shadowing) at the Koch Institute since 2013
- Reviewer for the Journal of Experimental and Clinical Cancer Research
- Member of organizing committee for the 2015 ‘Path of Professorship’ Workshop organized at MIT by the Graduate School of Education
- Member of the Committee for Community Life of the Koch Institute and 3<sup>rd</sup> floor meeting co-organizer

## Conclusions

The third year of my fellowship was a fruitful one, with most of my projects undertaken throughout this fellowship coming to completion, resulting in 4 first author publications accepted between September 2015 and January 2016. Two of these publications focused on identifying novel mechanisms of Mena<sup>INV</sup>-driven metastasis, mainly chemotaxis and haptotaxis, while another focused on the characterization of a novel isoform specific antibody for Mena<sup>INV</sup> used to describe the localization and expression of this isoform in breast cancer tumors. The fourth publication focused on proteolytic shedding as a novel mechanism of drug resistance in breast cancer.

In my third year, I also started working on two novel aspects of Mena<sup>INV</sup>-driven metastasis: the relationship between chemotaxis and haptotaxis and the role of Mena isoforms in chemoresistance. Given that I have published two stories separately investigating how Mena<sup>INV</sup> increases sensitivity to soluble chemotactic cues as well as substrate-bound haptotactic, it was only logical for me to investigate how these two cues together affected migration. I found that Mena<sup>INV</sup> promotes synergy between EGF and FN, regulating crosstalk between these two signaling pathways to promote hyper-invasive phenotypes. This story brings up many questions I hope to follow up in my own lab, with regards to how multiple cues simultaneously present within the tumor microenvironment can drive local invasion.

After working on resistance to targeted therapies, I became more broadly interested in mechanisms of resistance, particularly with regards to chemotherapy, which is the only treatment for metastatic triple negative breast cancer. My data gathered so far show that Mena isoforms play a role in resistance to Taxol, both *in vitro* and *in vivo*. I am currently investigating the mechanism by which this happens, and hope to submit a manuscript on this later this year.

Finally, I have continued to grow as a scientist. In addition to attending scientific conferences and career development workshops, I was able to develop my mentoring skills, managing a team of three (two masters students and a technician) and experiencing what it would be like to run my own lab. Overall, this fellowship has provided me with amazing opportunities- to develop and mature as a cancer researcher, broaden my horizons and initiate novel collaborations with engineers and clinicians, attend conferences, share my research and network with members of community, as well as gain the confidence I needed to move on in my academic career. I have now applied for a K99/R00 Transition to Independence grant from the NCI.

## References

1. Gertler, F. B., Niebuhr, K., Reinhard, M., Wehland, J. & Soriano, P. Mena, a relative of VASP and Drosophila Enabled, is implicated in the control of microfilament dynamics. *Cell* **87**, 227–239 (1996).
2. Bear, J. E. & Gertler, F. B. Ena/VASP: towards resolving a pointed controversy at the barbed end. *J. Cell Sci.* **122**, 1947–1953 (2009).
3. Gertler, F. & Condeelis, J. Metastasis: tumor cells becoming MENAcing. *Trends Cell Biol.* **21**, 81–90 (2011).
4. Goswami, S. *et al.* Identification of invasion specific splice variants of the cytoskeletal protein Mena present in mammary tumor cells during invasion in vivo. *Clin. Exp. Metastasis* **26**, 153–159 (2009).
5. Philippar, U. *et al.* A Mena Invasion Isoform Potentiates EGF-Induced Carcinoma Cell Invasion and Metastasis. *Dev. Cell* **15**, 813–828 (2008).
6. Roussos, E. T. *et al.* Mena invasive (MenaINV) promotes multicellular streaming motility and transendothelial migration in a mouse model of breast cancer. *J. Cell Sci.* **124**, 2120–2131 (2011).
7. Roussos, E. T. *et al.* Mena invasive (Mena(INV)) and Mena11a isoforms play distinct roles in breast cancer cell cohesion and association with TMEM. *Clin. Exp. Metastasis* **28**, 515–27 (2011).
8. Hughes, S. K. *et al.* PTP1B-dependent regulation of receptor tyrosine kinase signaling by the actin-binding protein Mena. *Mol. Biol. Cell* (2015). doi:10.1091/mbc.E15-06-0442
9. Oudin, M. J. *et al.* Characterization of the expression of the pro-metastatic Mena(INV) isoform during breast tumor progression. *Clin. Exp. Metastasis* (2015). doi:10.1007/s10585-015-9775-5
10. Oudin, M. J. *et al.* Tumor cell-driven extracellular matrix remodeling enables haptotaxis during metastatic progression. *Cancer Discov.* (2016). doi:10.1158/2159-8290.CD-15-1183
11. Zhu, J. & Clark, R. a F. Fibronectin at select sites binds multiple growth factors and enhances their activity: expansion of the collaborative ECM-GF paradigm. *J. Invest. Dermatol.* **134**, 895–901 (2014).
12. Meyer, A. S., Miller, M. a, Gertler, F. B. & Lauffenburger, D. a. The receptor AXL diversifies EGFR signaling and limits the response to EGFR-targeted inhibitors in triple-negative breast cancer cells. *Sci. Signal.* **6**, ra66 (2013).
13. Wyckoff, J. B., Segall, J. E. & Condeelis, J. S. The collection of the motile population of cells from a living tumor. *Cancer Res.* **60**, 5401–5404 (2000).
14. Muller, P. A. J., Vousden, K. H. & Norman, J. C. p53 and its mutants in tumor cell migration and invasion. *J. Cell Biol.* **192**, 209–218 (2011).
15. Muller, P. A. J. *et al.* Mutant p53 Drives Invasion by Promoting Integrin Recycling. *Cell* **139**, 1327–1341 (2009).
16. Perou, C. M. *et al.* Molecular portraits of human breast tumours. *Nature* **406**, 747–752 (2000).
17. Isakoff, S. J. Triple Negative Breast Cancer: Role of Specific Chemotherapy Agents. *cancer J.* **16**, 53–61 (2010).
18. Siddik, Z. H. Cisplatin: mode of cytotoxic action and molecular basis of resistance. *Oncogene* **22**, 7265–7279 (2003).
19. Hofmann, G. a & Mattern, M. R. Topoisomerase II in multiple drug resistance. *Cytotechnology* **12**, 137–154 (1993).



20. Jordan, M. a. Mechanism of action of antitumor drugs that interact with microtubules and tubulin. *Curr. Med. Chem. Anticancer. Agents* **2**, 1–17 (2002).
21. Kaufmann, S. H. & Earnshaw, W. C. Induction of apoptosis by cancer chemotherapy. *Exp. Cell Res.* **256**, 42–49 (2000).
22. Gluz, O. *et al.* Triple-negative breast cancer—current status and future directions. *Ann. Oncol.* **20**, 1913–1927 (2009).
23. Longley, D. B. & Johnston, P. G. Molecular mechanisms of drug resistance. *J. Pathol.* **205**, 275–292 (2005).
24. Mark B. Meads, R. A. G. and W. S. D. Environment-mediated drug resistance: a major contributor to minimal residual disease. *Nat. Reveiw* **9**, 655–674 (2009).
25. Oudin, M. J. INV staining.
26. Gupton, S. L. *et al.* Mena binds  $\alpha 5$  integrin directly and modulates  $\alpha 5 \beta 1$  function. **198**, 657–676 (2012).
27. Oudin, M. J. *et al.* MenaINV-mediated bi-directional signaling through  $\alpha 5 \beta 1$  integrin supports tumor cell haptotaxis and ECM remodeling during metastasis. *prep* (2015).
28. Laughney, A. M. *et al.* Single-cell pharmacokinetic imaging reveals a therapeutic strategy to overcome drug resistance to the microtubule inhibitor eribulin. **6**, (2014).
29. Mcgrail, D. J., Khambhati, N. N., Qi, M. X., Patel, K. S. & Ravikumar, N. Alterations in Ovarian Cancer Cell Adhesion Drive Taxol Resistance by Increasing Microtubule Dynamics in a FAK-dependent Manner. *Sci. Rep.* **5**, 9529 (2015).

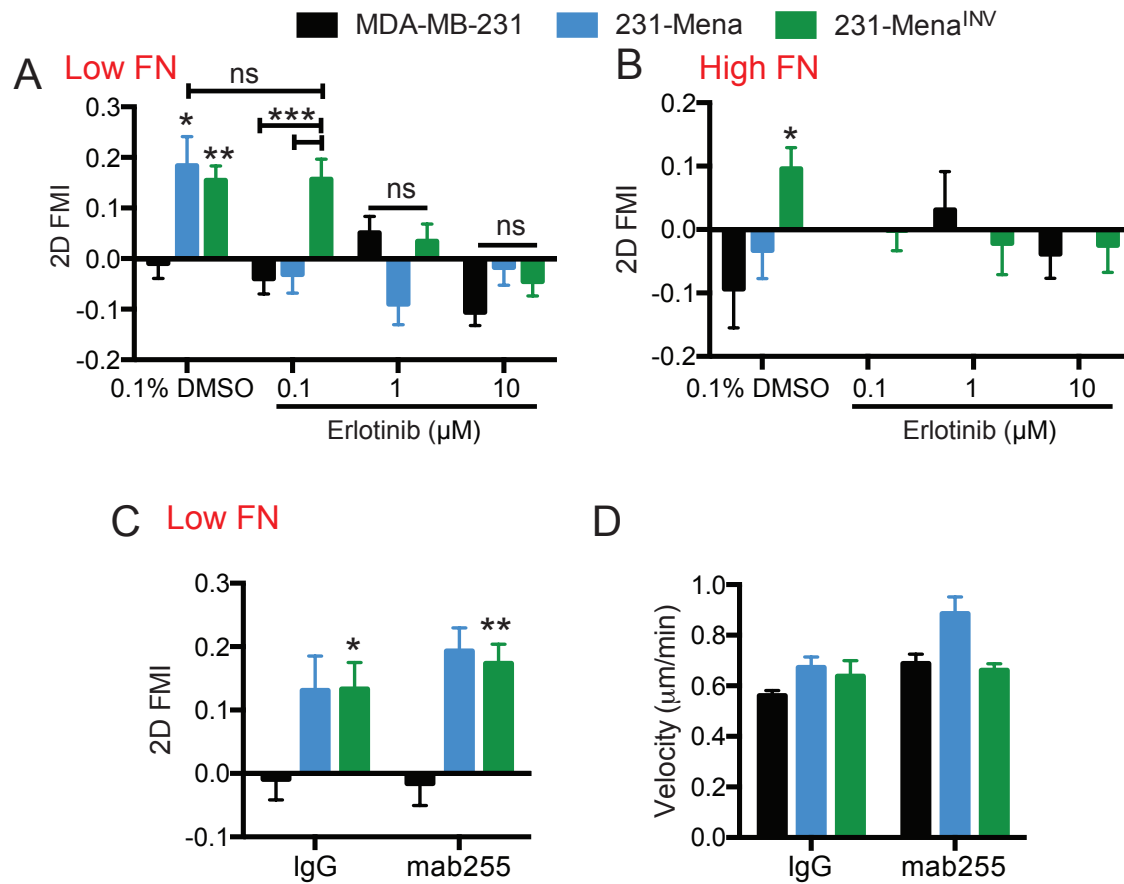


**Figure 1: Mena/Mena<sup>INV</sup>-driven FN haptotaxis requires crosstalk between EGFR.** A) Inhibition of EGFR with different concentrations of Erlotinib decreased Mena- and Mena<sup>INV</sup>-driven haptotaxis on a 2D 125μg/ml low FN gradient. B) Inhibition of EGFR with different concentrations of Erlotinib decreased Mena<sup>INV</sup>-driven haptotaxis on a 2D 500 μg/ml FN gradient. C) Velocity (μm/min) of 231, 231-Mena and 231-Mena<sup>INV</sup> cells when treated with increasing concentrations of Erlotinib on a high FN gradient. D) FMI of MDAMB231 and 231-Mena<sup>INV</sup> cells migrating on 2D low with an IgG control of mAB225. Data pooled from at least 50 cells pooled from 3 different experiments. Results show mean ± SEM, significance by one way ANOVA, \*p<0.05, \*\*p<0.01, \*\*\*p<0.005. See FigS1.

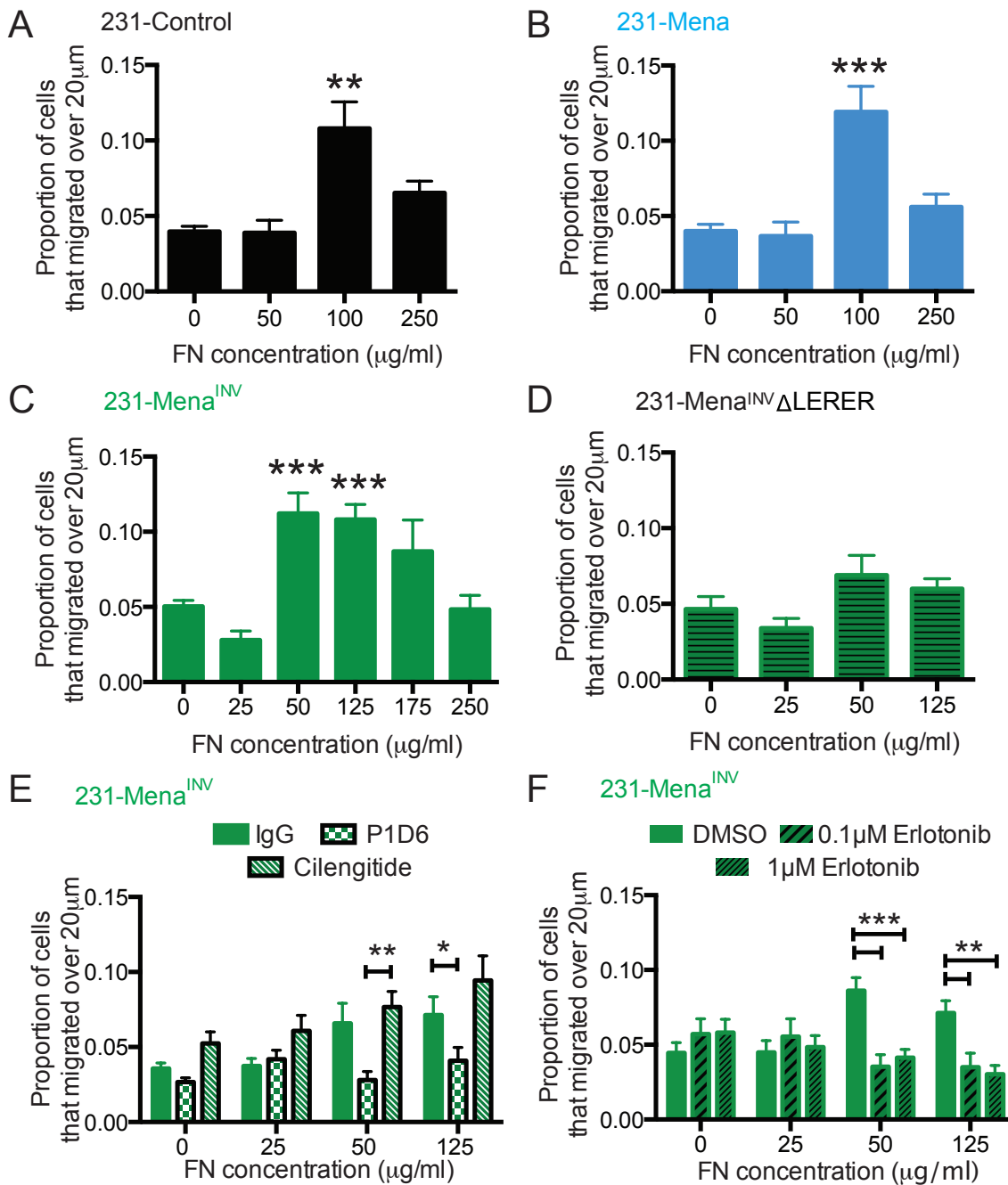


**Figure 2: The interaction between Mena<sup>INV</sup> and α5 is important for FN-driven growth-factor independent invasion.** *In vitro* chemotaxis assay in a 3D collagen gel with increasing concentrations of FN (0, 25, 50, 125, 175, 250 μg/ml) 231-Control (A), 231-Mena (B) and 231-Mena<sup>INV</sup> (C) treated with serum-free media for 24h. The proportion of cells migrating 20 μm above baseline was quantified. (D) 231-Mena<sup>INV</sup>ΔLERER cells did not respond to the increasing FN concentration in the gels. (E) Inhibition of α5 with P1D6, but not αv with Cilengitide, inhibited the Mena<sup>INV</sup>-driven pro invasive effect in response to increasing FN concentrations. (F) Treatment with Erlotinib (0.1 or 1 μM) decreased the ligand independent effect of FN on 3D invasion in 231-Mena<sup>INV</sup> cells. Results show mean ± SEM, results pooled from at least 5 different experiments, significance determined by one way ANOVA, \* p<0.05, \*\* p<0.01, \*\*\* 0.005.

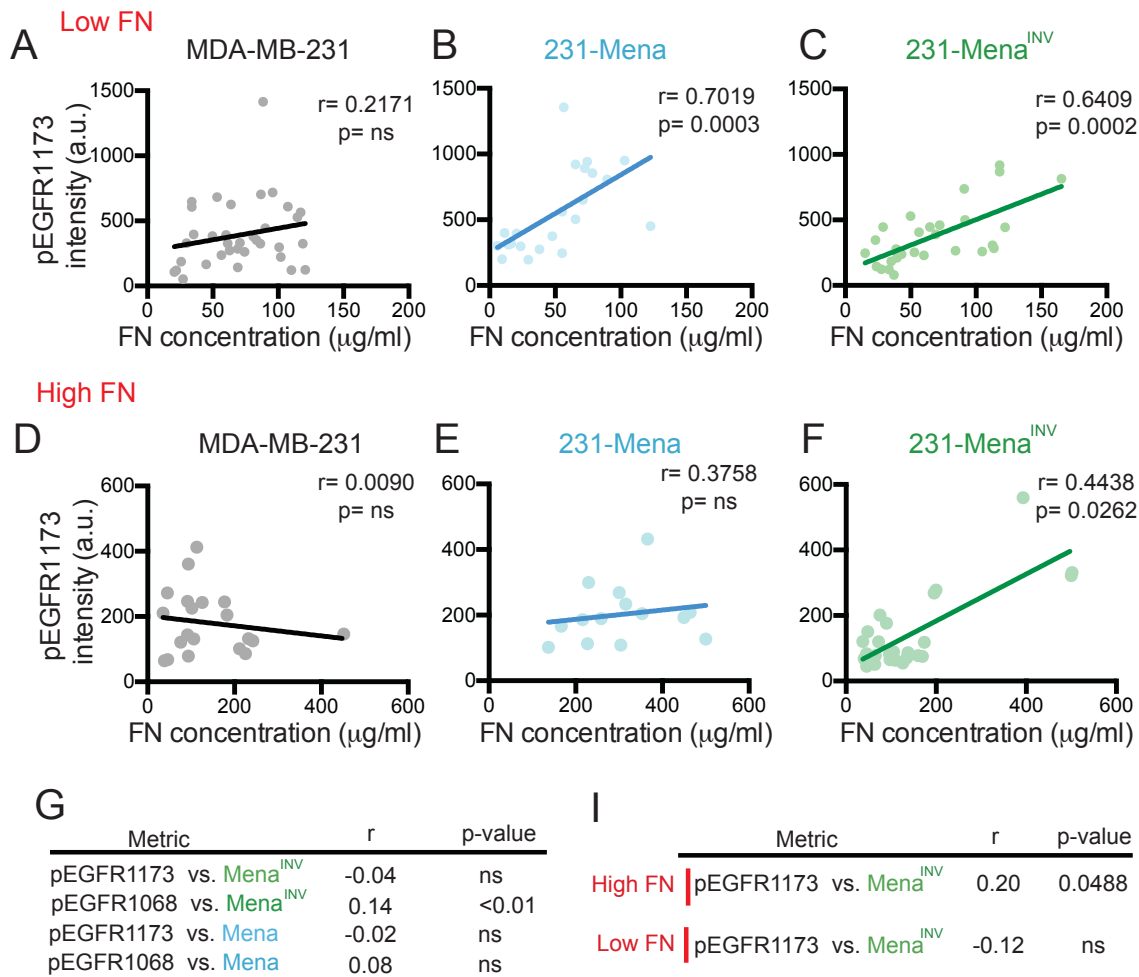


### Figure 3: Mena<sup>INV</sup> drives EGFR signaling on FN

Correlation between pEGFR1173 in whole cell relative to cell area and FN concentration under the cell in cells plated on a low 125µg/ml for MDA-MB-231 cells (A), 231-Mena (B) and 231-Mena<sup>INV</sup> cells (C). Correlation between pEGFR1173 in whole cell relative to cell area and FN concentration under the cell in cells plated on a low 125µg/ml for MDA-MB-231 cells (D), 231-Mena (E) and 231-Mena<sup>INV</sup> cells (F). Data from at least 15 cells per cell line pooled from 3 different experiments. G) Table showing correlations (R by Spearman and p-value) between Mena or Mena<sup>INV</sup> and pEGFR1173 or pEGFR1068 from the RPPA data in the TCGA breast cancer cohort. H) Table showing correlations (R by Spearman and p-value) between Mena or Mena<sup>INV</sup> and pEGFR1173 or pEGFR1068 from the RPPA data in the TCGA breast cancer cohort in patients with high or low FN.

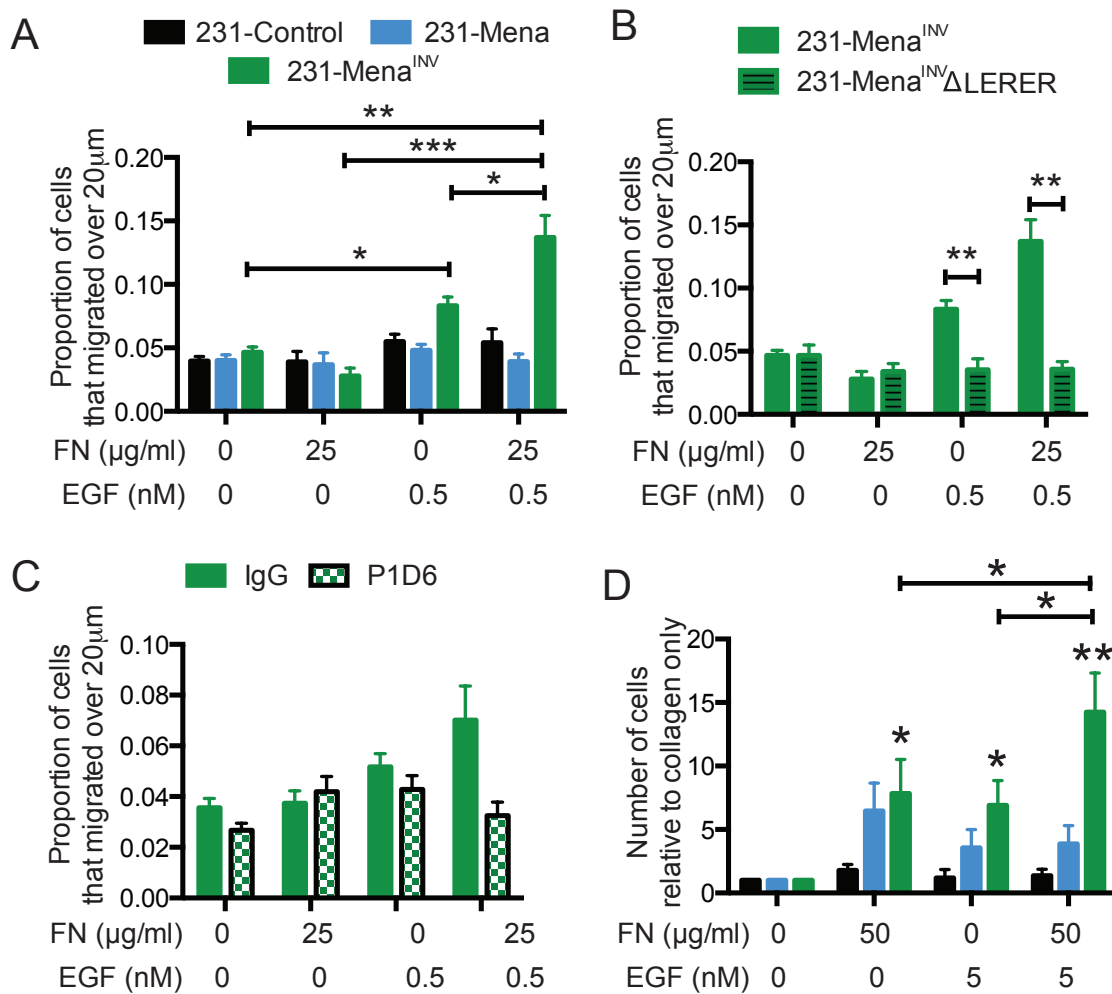


**Figure 4: Mena<sup>INV</sup> promotes synergy between FN and EGF**

(A) *In vitro* chemotaxis assay in a 3D collagen gel with either EGF (0.5nM), FN (25 μg/ml) or both, for 231-Control, 231-Mena and 231-Mena<sup>INV</sup> cells. The proportion of cells migrating 20 μm above baseline was quantified. Deletion of LERER (B) or inhibition of α5 (C) abrogated the synergy between EGF and FN. D) *In vivo* invasion assay in tumors generated in NOD/SCID mice with MDA-MB-231 cells expressing Control-GFP, Mena or Mena<sup>INV</sup>. Needles contain 1mg/ml collagen and increasing amounts of FN or EGF (n=4 mice per condition). Results show mean ± SEM, significance determined by one way ANOVA, \* p<0.05, \*\* p<0.01, \*\*\* 0.005.

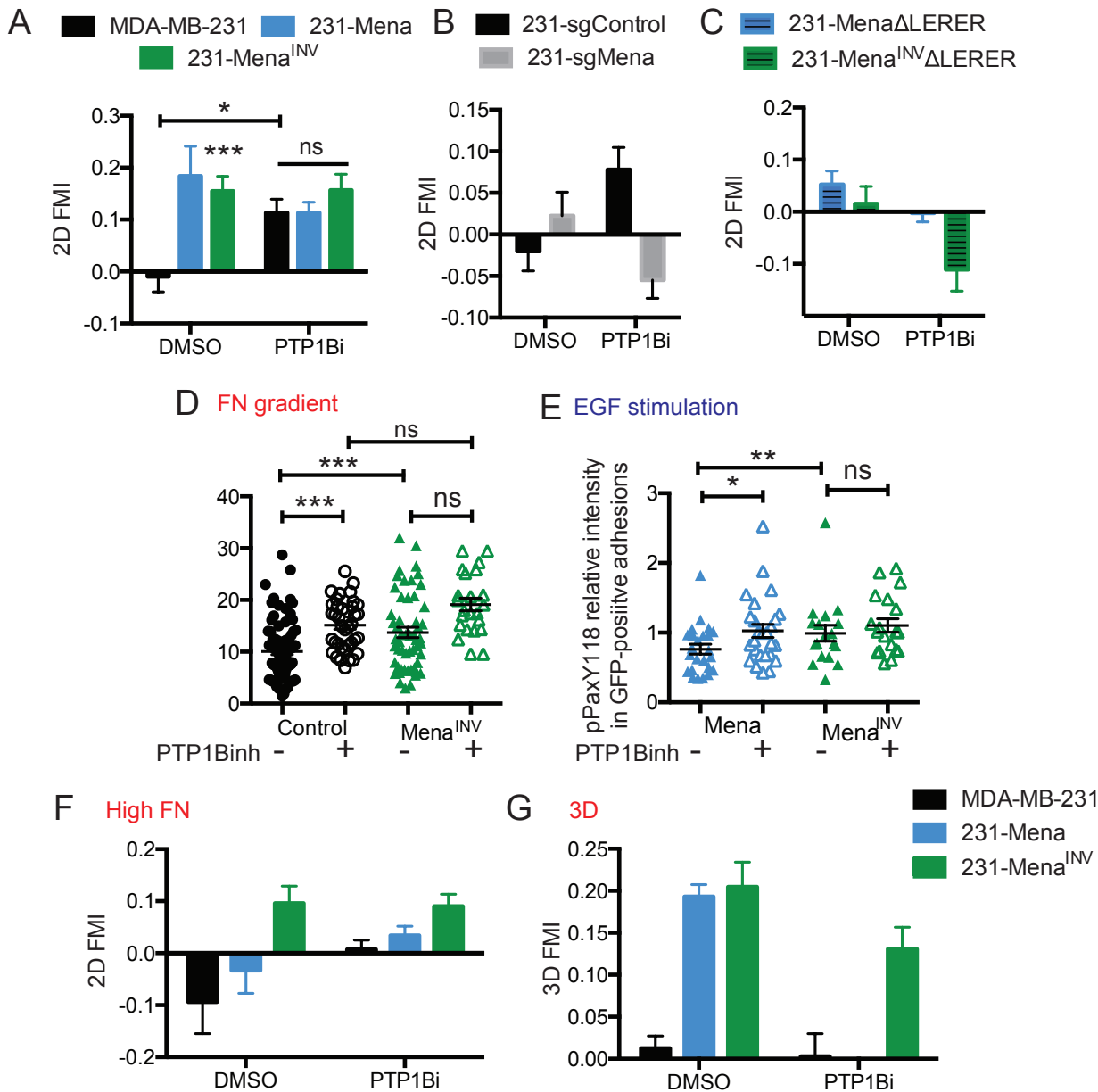


**Figure 5: Inhibition of PTP1B phenocopies Mena<sup>INV</sup>**

FMI for MDA-MB-231, 231-Mena and 231-Mena<sup>INV</sup> cells (B), MDA-MB-231 cells with sgControl or sgMena (B) or 231-Mena $\Delta$ LERER and 231-Mena<sup>INV</sup> $\Delta$ LERER cells (C) plated on a 2D low FN gradient in the presence of PT1Bi (10 $\mu$ M). D) 231-Mena<sup>INV</sup> cells plated on a 2D FN gradient showed an increase in number of Paxilin pY118- positive adhesions relative to MDA-MB-231 cells. Inhibition of PTP1B significantly increased the number of Paxilin pY118- positive adhesions in MDA-MB-231 cells. (E) Stimulation with EGF (0.25nM for 1min) increased phosphorylation of Paxilin at Y118 in Mena-positive adhesions in MDA-MB-231 cells expressing Mena<sup>INV</sup> but not Mena. F) FMI for MDA-MB-231, 231-Mena and 231-Mena<sup>INV</sup> cells plated on a 2D high FN gradient in the presence of PT1Bi (10 $\mu$ M). (G) FMI for MDA-MB-231, 231-Mena and 231-Mena<sup>INV</sup> cells plated in a 3D low FN gradient in the presence of PT1Bi (10 $\mu$ M). Results show mean  $\pm$  SEM, significance determined by one way ANOVA, \*  $p < 0.05$ , \*\*  $p < 0.01$ , \*\*\*  $p < 0.005$ .

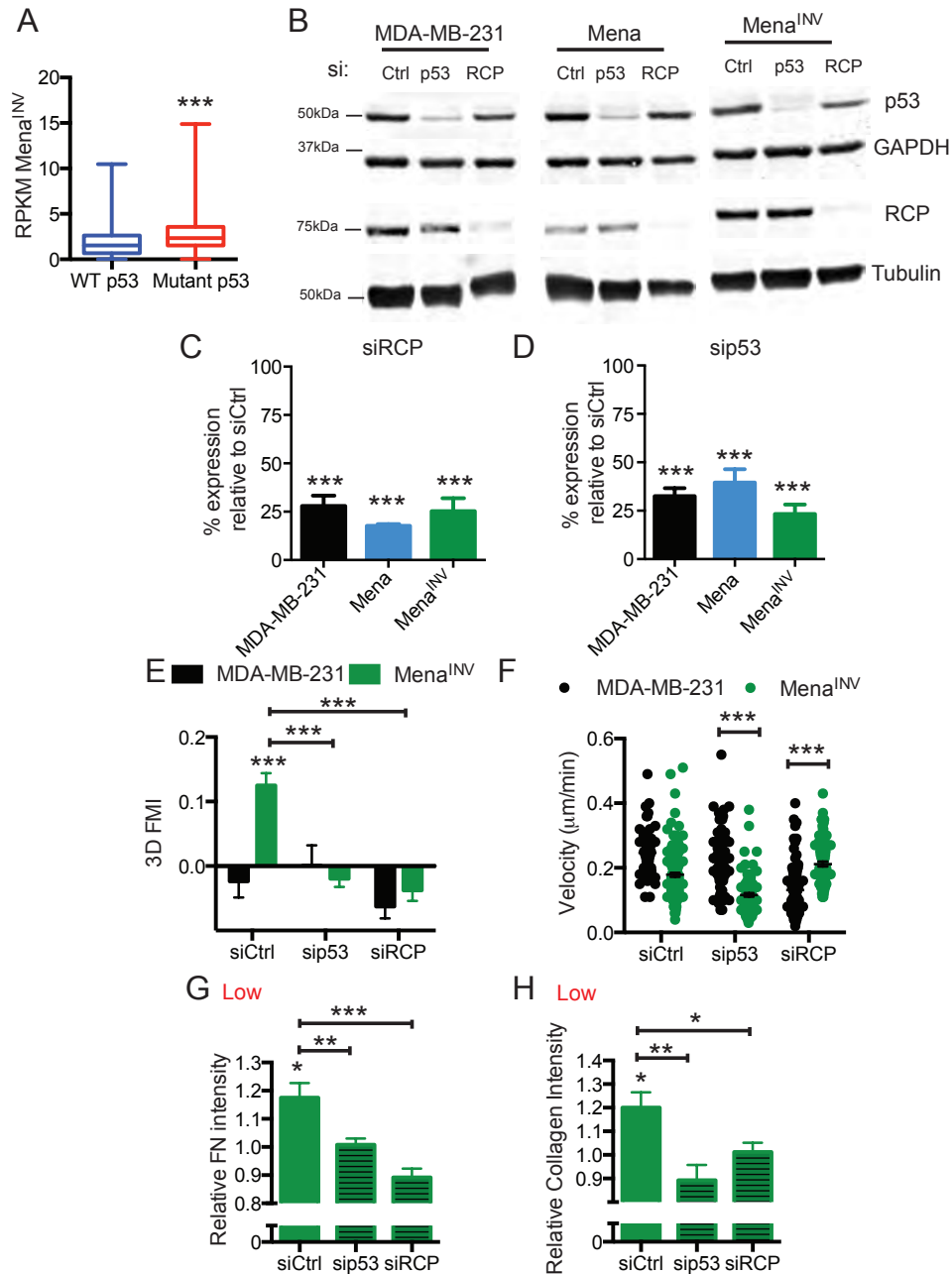


**Figure 6: RCP-driven recycling of EGFR and  $\alpha 5 \beta 1$  is important for haptotaxis and ECM reorganization.** A) RPKM values for Mena<sup>INV</sup> in TCGA breast cancer patients high WT or mutant p53. B) Western Blot showing knockdown levels of p53 and RCP in each cell line. Quantification of WBs showing in B for siRCP (C) and siP53 (D). Knockdown of p53 and RCP inhibits Mena<sup>INV</sup>-driven 3D haptotaxis, while also affecting velocity (E,F). Knockdown of p53 and RCP inhibited FN (G) and collagen (H) reorganization. Results show mean  $\pm$  SEM, significance by one way ANOVA, \* $p < 0.05$ , \*\* $p < 0.01$ , \*\*\* $p < 0.005$ . See FigS6.

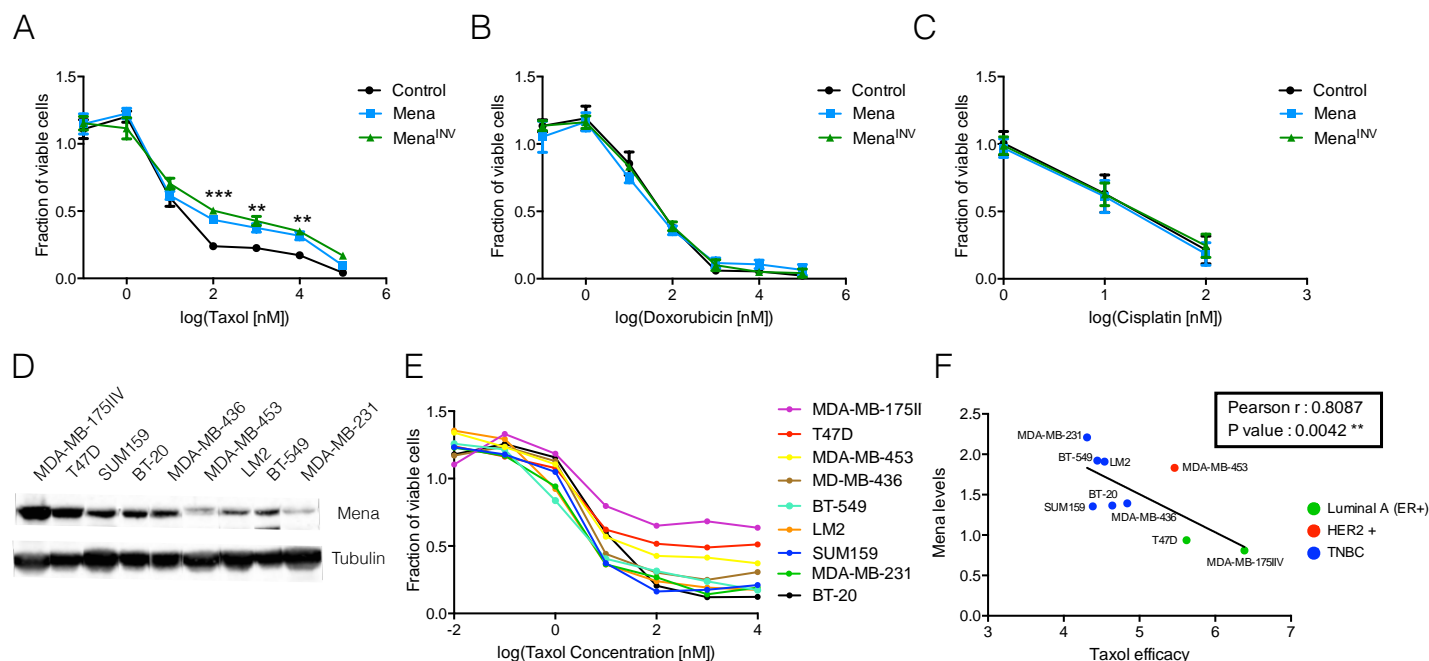


**Figure 7: Expression of Mena isoforms is associated with Taxol resistance** Cell viability was assessed in MDA-MB 231 cells expressing GFP, GFP-Mena or GFP-Mena<sup>INV</sup> in 96-well plates. Graphs show fraction of viable cells after 72h of treatment with Taxol (A) Doxorubicin (B) or Cisplatin (C) determined using Prestoblue assay. The cell viability is expressed as a fraction relative to untreated cells. The IC<sub>50</sub> values were calculated from dose–response plots using non-linear (sigmoidal) regression analysis. Data presented as mean± SEM for three independent experiments, each performed in duplicate. Statistics determined by unpaired t-test with Welch's correction, where \*\*\*  $p < 0.001$ , \*\*  $p < 0.01$ , \*  $p < 0.05$ . (D) Representative western blot of lysate prepared from the panel of breast cancer cell lines, probed with anti-Mena and anti-Tubulin antibodies. (E) Cell viability was assessed in MDA-MB 175II and T47D (Luminal A), MDA-MB 453 (HER2+), MDA-MB 436, BT-549, LM2, SUM159, MDA-MB 231 and BT-20 (TNBC). Graphs show dose response curve, data presented as mean for three independent experiments, each performed in duplicate. (F) Linear regression of Mena protein expression obtained by Western Blot and Taxol efficacy, here defined as the inverse of its area activity calculated from the dose-response curves. Each data point represents the mean of triplicate experiments for the Mena protein expression and the mean for three independent experiments, each performed in duplicate for the Taxol efficacy.



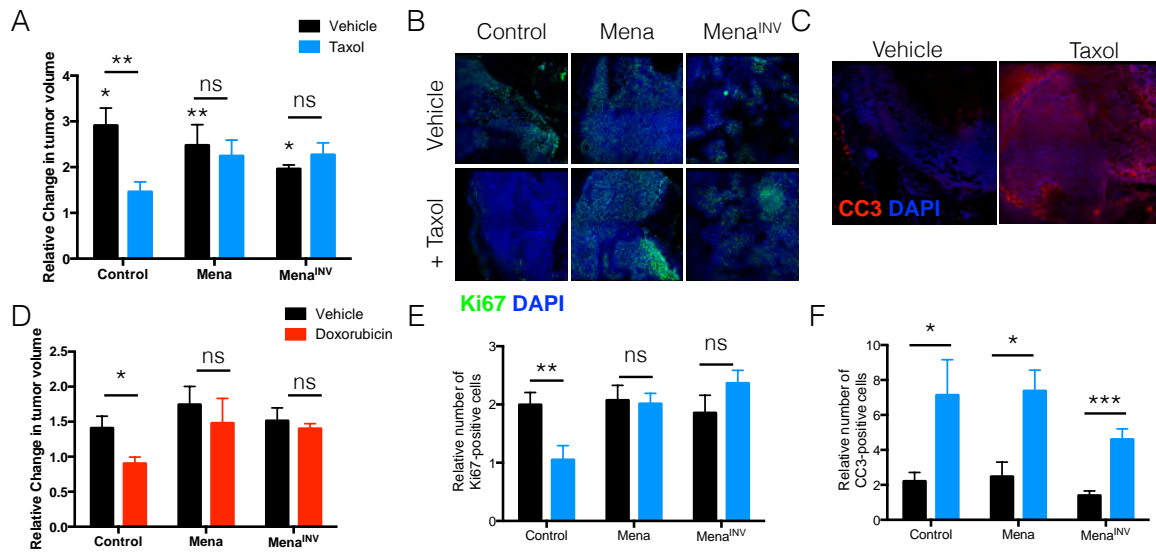


**Figure 8: *In vivo*, Mena or Mena<sup>INV</sup> expression weakened Taxol and Doxorubicin action on tumor growth.** (A) Tumors were generated by injection of 231-GFP, 231-Mena or 231-Mena<sup>INV</sup> cells in the mammary fat pad of NOD SCID mice. When they reached 1 cm in diameter, mice were treated with Taxol three times or Doxorubicin twice every 5 days. Tumor volume was measured before and after treatment. Relative change in tumor volume after treatment with Taxol (B) or Doxorubicin (C) of tumors expressing the different GFP-tagged Mena isoforms. Growth of tumors expressing Mena or Mena<sup>INV</sup> is not affected by the treatment with chemotherapies. Data presented as mean  $\pm$  SEM for at least 9 mice in each group. Statistics determined by unpaired t-test, where \*\*\*  $p < 0.001$ , \*\*  $p < 0.01$ , \*  $p < 0.05$ .

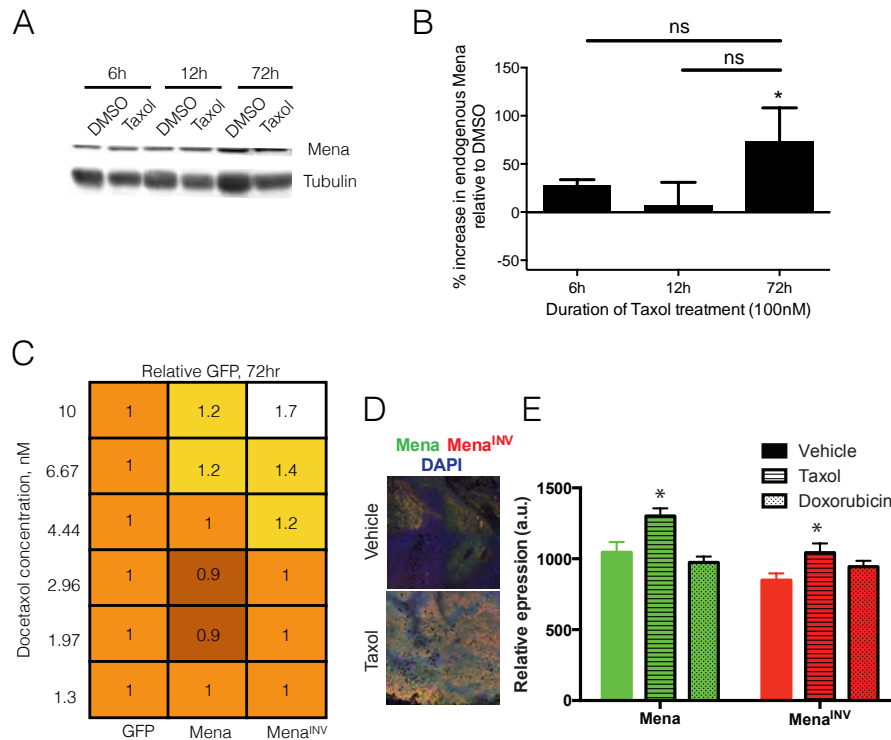


**Figure 9: Taxol treatment selects for high Mena expression *in vitro* and *in vivo***

(A) Representative western blot of whole cell lysates prepared from 231-GFP cells treated with 100nM of Taxol or DMSO as vehicle for 6, 24 or 72 hours and probed with anti-Mena and anti-Tubulin antibodies. (B) Percentage increase in Mena protein expression after Taxol treatment, here defined as the difference between Mena protein expression in cells treated with Taxol and in cells treated with DMSO relative to Mena protein expression in cells treated with DMSO. (\*Mena protein expression is significantly higher in cells treated with Taxol than DMSO treated cells, \* $p < 0.05$  by paired t test). Data presented as mean  $\pm$  SEM for two independent experiments, each western blot performed in duplicate. (C) FACS analysis of GFP expression levels of GFP, GFP-Mena or GFP-Mena<sup>INV</sup> expressing MDA-MB-231 cells and treated with Taxol. (D) Representative images of FFPE section from 231-GFP tumor grown in mice treated with Taxol or with vehicle and stained for Mena (green), Mena<sup>INV</sup> (red) and DAPI (blue). Scale bar = 200 $\mu$ m. (E) Mean of Mena fluorescence signal intensity. Data presented as mean  $\pm$  SEM for 10 fields of view per tumor, from 3 different mice. Statistics determined by unpaired t-test, where \*  $p < 0.05$ .

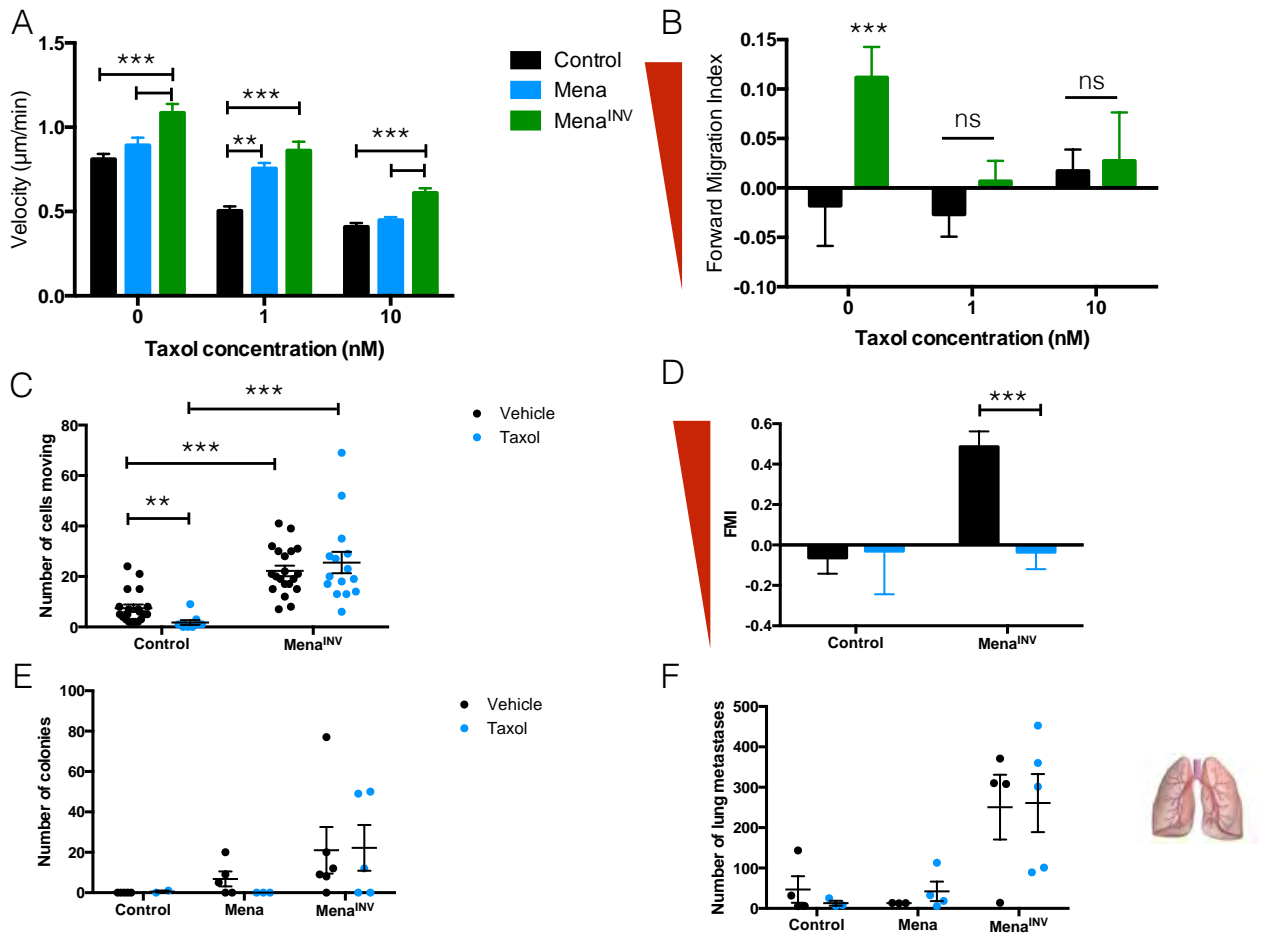


**Figure 10: Taxol treatment decreases cell velocity *in vitro* but do not affect Mena<sup>INV</sup>-driven tumor cell motility and dissemination in mice.** (A) Velocity of Control, Mena and Mena<sup>INV</sup> cells plated on glass bottom dishes coated with Collagen (0.1 mg/ml) and FN (50 μg/ml), and treated with different concentrations of Taxol. Data presented as mean± SEM for at least 50 cells tracked in two independent experiments. (B) FMI of Control and Mena<sup>INV</sup> cells on a low concentration 2D FN gradient, and treated with increasing concentrations of Taxol. (C) Quantification of motile cells by multiphoton intravital imaging in tumors expressing Mena<sup>INV</sup> or Control Tumors grown in mice treated with Taxol or vehicle. Data presented as mean± SEM. (D) *In vivo* haptotaxis assay with implanted devices relasing fluoresecently-labeled FN. Taxol treatment inhibited *in vivo* haptotaxis as measured by the FMI. (E) Number of metastases in lung of mice bearing control tumors or expressing Mena or Mena<sup>INV</sup> 12 weeks after injection. (F) Number of disseminated tumor cells corresponding to the number of colonies in cultured bone marrow collected from mice bearing control tumor or expressing Mena or Mena<sup>INV</sup> 12 weeks after injection. Data presented as mean± SEM for 3 mice per group. Statistics determined by unpaired t-test, where \*\*\* p<0.001, \*\* p<0.01, \* p<0.05.

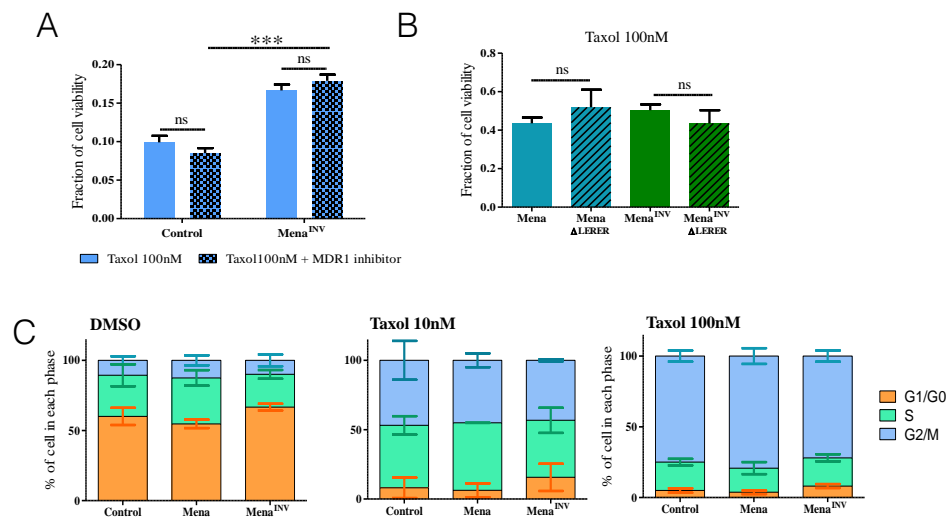


**Figure 11: Potential mechanisms for Mena isoform-driven resistance to Taxol** (A) Fraction of viable cells of Control or Mena<sup>INV</sup> cells treated during 72h by Taxol with or without MDR1 inhibitor (HM30181). Data presented as mean± SEM for three independent experiments, each performed in duplicate. (B) Fraction of viable cells after 72h of treatment with 100nM of Taxol of 231 cells expressing Mena, Mena<sup>INV</sup>, MenaΔLERER or Mena<sup>INV</sup>ΔLERER. Data presented as mean± SEM for two independent experiments, each performed in duplicate (C) Cell cycle analysis of Control, Mena and Mena<sup>INV</sup> cells treated with 10nM or 100nM of Taxol during 16 hours. Data presented as mean± SEM of two independent experiments. Statistics determined by unpaired t-test, where \*\*\* p<0.001.

# Foxa2 and Cdx2 cooperate with Nkx2-1 to inhibit lung adenocarcinoma metastasis

Carman Man-Chung Li,<sup>1</sup> Vasilena Gocheva,<sup>1</sup> Madeleine J. Oudin,<sup>1</sup> Arjun Bhutkar,<sup>1</sup> Shi Yun Wang,<sup>1</sup> Saya R. Date,<sup>1</sup> Sheng Rong Ng,<sup>1</sup> Charles A. Whittaker,<sup>1</sup> Roderick T. Bronson,<sup>2</sup> Eric L. Snyder,<sup>3,4</sup> Frank B. Gertler,<sup>1</sup> and Tyler Jacks<sup>1,5</sup>

<sup>1</sup>David H. Koch Institute for Integrative Cancer Research, Department of Biology, Massachusetts Institute of Technology, Cambridge, Massachusetts 02139, USA; <sup>2</sup>Department of Pathology, Tufts University School of Medicine and Veterinary Medicine, North Grafton, Massachusetts 01536, USA; <sup>3</sup>Department of Pathology, <sup>4</sup>Department of Anatomy, School of Medicine, University of California at San Francisco, San Francisco, California 94143, USA; <sup>5</sup>Howard Hughes Medical Institute, Massachusetts Institute of Technology, Cambridge, Massachusetts 02139, USA

Despite the fact that the majority of lung cancer deaths are due to metastasis, the molecular mechanisms driving metastatic progression are poorly understood. Here, we present evidence that loss of Foxa2 and Cdx2 synergizes with loss of Nkx2-1 to fully activate the metastatic program. These three lineage-specific transcription factors are consistently down-regulated in metastatic cells compared with nonmetastatic cells. Knockdown of these three factors acts synergistically and is sufficient to promote the metastatic potential of nonmetastatic cells to that of naturally arising metastatic cells *in vivo*. Furthermore, silencing of these three transcription factors is sufficient to account for a significant fraction of the gene expression differences between the nonmetastatic and metastatic states in lung adenocarcinoma, including up-regulated expression of the invadopodia component Tks5<sub>long</sub>, the embryonal proto-oncogene Hmga2, and the epithelial-to-mesenchymal mediator Snail. Finally, analyses of tumors from a genetically engineered mouse model and patients show that low expression of Nkx2-1, Foxa2, and Cdx2 strongly correlates with more advanced tumors and worse survival. Our findings reveal that a large part of the complex transcriptional network in metastasis can be controlled by a small number of regulatory nodes that function redundantly, and loss of multiple nodes is required to fully activate the metastatic program.

[**Keywords:** lung adenocarcinoma; metastasis; Nkx2-1; Foxa2; Cdx2; genetically engineered mouse model of cancer]

Supplemental material is available for this article.

Received June 14, 2015; revised version accepted August 13, 2015.

During tumor progression, cancer cells undergo global gene expression alterations through which they acquire the traits that allow them to successfully advance through the multiple steps of the metastatic cascade. These steps include the ability to invade and migrate through surrounding tissues, intravasate into blood vessels, survive in circulation, extravasate at secondary sites, and colonize distant organs (Steeg 2006). A comprehensive understanding of the upstream regulators that orchestrate this metastasis program is lacking.

To understand more fully the molecular mechanisms of tumor progression and metastasis in a well-defined genetic context, our laboratory developed a genetically engineered mouse model of lung adenocarcinoma, a major subtype of lung cancer that is a leading cause of cancer death worldwide. Conditional activation of oncogenic *Kras* and inactivation of *p53* in *Kras*<sup>LSL-G12D/+</sup>; *p53*<sup>fl/fl</sup> (KP) mice by viral delivery of Cre recombinase to lung epithelial cells initiates the development of lung adenocarci-

nomas that closely resemble the pathophysiological features of the human disease, including the capability to metastasize to distant organs (Jackson et al. 2001, 2005). Previously, we found that progression to metastasis in this model was closely associated with decreased expression of the lung lineage transcription factor Nkx2-1, and knockdown of Nkx2-1 in nonmetastatic tumor cells was sufficient to increase their tumor-seeding ability in transplantation experiments (Winslow et al. 2011). Nonetheless, two major lines of evidence indicate that loss of Nkx2-1 alone may not be sufficient for full progression to metastasis. First, knockdown of Nkx2-1 in nonmetastatic lung adenocarcinoma cells does not recapitulate all of the gene expression changes that occur during the transition from a nonmetastatic to a metastatic state (Winslow et al. 2011). Moreover, *Nkx2-1* deletion in KP lung adenocarcinomas was not sufficient to induce the

Corresponding author: [tjacks@mit.edu](mailto:tjacks@mit.edu)

Article is online at <http://www.genesdev.org/cgi/doi/10.1101/gad.267393>. 115.

© 2015 Li et al. This article is distributed exclusively by Cold Spring Harbor Laboratory Press for the first six months after the full-issue publication date (see <http://genesdev.cshlp.org/site/misc/terms.xhtml>). After six months, it is available under a Creative Commons License (Attribution-NonCommercial 4.0 International), as described at <http://creativecommons.org/licenses/by-nc/4.0/>.

metastasis program but instead unmasked a latent gastric differentiation state of the tumor cells (Snyder et al. 2013). These observations indicate that, in addition to Nkx2-1, additional regulatory factors likely exist that govern the program necessary for full acquisition of metastatic potential.

To investigate additional regulators of metastasis, we elected to examine the transcription factors that control the expression of the metastasis mediator Tks5<sub>long</sub>. A critical component of the proteolytic cellular protrusions, invadopodia, Tks5<sub>long</sub> promotes metastasis in a wide variety of cancer types, including lung adenocarcinoma, and its expression is consistently up-regulated in metastatic cells compared with nonmetastatic cells in the KP model (Murphy and Courtneidge 2011; Li et al. 2013). We showed previously that Tks5<sub>long</sub> is critical for promoting invadopodia formation and metastatic progression in transplant and autochthonous mouse models. Moreover, Tks5<sub>long</sub> expression correlates with a more advanced disease stage and poor survival of lung adenocarcinoma patients. Importantly, Tks5<sub>long</sub> is distinct from an invadopodia-inhibiting isoform, Tks5<sub>short</sub>, by the presence of the membrane-binding Phox homology domain and the use of an independent promoter for transcription (Li et al. 2013). A previous study has demonstrated that the protein level of Tks5<sub>long</sub> can be regulated by Src (Cejudo-Martin et al. 2014). However, the transcriptional regulation of Tks5<sub>long</sub> is not well understood.

Here, we explored the transcriptional regulation of Tks5<sub>long</sub> to uncover key regulators of metastasis in lung adenocarcinoma. We identified three transcriptional repressors of Tks5<sub>long</sub>—Nkx2-1, Foxa2, and Cdx2—and subsequently showed that they function collectively as important regulators of a metastasis program in lung adenocarcinoma. While Nkx2-1 and Foxa2 are known for lineage specification and maintenance of the lungs (among other organs), Cdx2 expression is limited to the intestines in normal adult tissues, and its role in lung adenocarcinoma has not been previously explored. Here, we provide evidence that these three transcription factors function cooperatively as critical regulators in suppressing lung adenocarcinoma metastasis.

## Results

### *Nkx2-1, Foxa2, and Cdx2 synergistically suppress the expression of Tks5<sub>long</sub> in nonmetastatic lung adenocarcinoma cells*

To identify novel mediators of the metastatic program in lung adenocarcinoma, we focused on the transcriptional regulation of Tks5<sub>long</sub>. Tks5<sub>long</sub> has a mechanistically characterized function in promoting metastasis across a wide variety of cancer types, as it mediates the formation of invadopodia, which are proteolytic membrane protrusions that facilitate cellular invasion (Paz et al. 2014). In lung adenocarcinoma, Tks5<sub>long</sub> is critical for promoting metastasis, and increased Tks5<sub>long</sub> expression correlates with poor patient outcomes (Li et al. 2013). Furthermore, Tks5<sub>long</sub> is dramatically and consistently up-regulated in

our collection of metastatic lung adenocarcinoma cells compared with the nonmetastatic cells derived from the KP model (Li et al. 2013), suggesting that its expression is under tight regulation. Importantly, H3K4me3 chromatin immunoprecipitation (ChIP) sequencing (ChIP-seq) analysis showed that Tks5<sub>long</sub> is transcribed from its own promoter independently of the other Tks5 isoform, Tks5<sub>short</sub> (data not shown), suggesting that its increased expression is likely a result of transcriptional regulation and not alternative splicing. Given these data, we hypothesized that the transcriptional regulatory mechanism for Tks5<sub>long</sub> functions as a key switch in regulating a broader metastasis program, which includes many more metastasis-related genes.

To identify potential transcriptional regulators of Tks5<sub>long</sub>, we used an existing gene expression profile of a panel of cell lines derived from nonmetastatic and metastatic primary lung adenocarcinomas as well as metastases in the KP model (termed T<sub>nonMet</sub>, T<sub>Met</sub>, and Met cells, respectively) (Winslow et al. 2011). From this data set, we generated a list of transcription factors that (1) were differentially expressed between the collection of T<sub>nonMet</sub> and T<sub>Met</sub>/Met cells and (2) had predicted binding sites in the Tks5<sub>long</sub> locus based on genomic sequence analysis.

This approach neglects potential nontranscriptional regulatory mechanisms of Tks5<sub>long</sub> expression, but we wanted to start by first focusing strictly on transcription. Among the transcription factors that are differentially expressed between T<sub>nonMet</sub> and T<sub>Met</sub>/Met cells, we identified three that meet these criteria: Nkx2-1, Foxa2, and Cdx2. Microarray gene expression profiling and quantitative RT-PCR (qRT-PCR) validation confirmed that Nkx2-1, Foxa2, and Cdx2 are highly expressed in T<sub>nonMet</sub> cells but are partially or completely lost in T<sub>Met</sub>/Met cells (Fig. 1A; Supplemental Fig. S1A,B). The expression pattern of each transcription factor is inversely proportional to Tks5<sub>long</sub>, suggesting that these three factors may suppress Tks5<sub>long</sub> expression (Fig. 1A).

In order to determine whether Nkx2-1, Foxa2, and Cdx2 inhibit Tks5<sub>long</sub> expression, we knocked down the three transcription factors in T<sub>nonMet</sub> cells using shRNAs (referred to here as T<sub>nonMet</sub>-shNFC cells) either singly or in combination and examined the effect on Tks5<sub>long</sub> expression compared with control knockdown using shRNAs against firefly and renilla luciferases. Interestingly, while single or double knockdown of these transcription factors in T<sub>nonMet</sub> cells only moderately affected Tks5<sub>long</sub> expression, triple knockdown of all three transcription factors in T<sub>nonMet</sub>-shNFC cells led to a dramatic increase in Tks5<sub>long</sub> mRNA and protein levels such that the levels were comparable with that of T<sub>Met</sub> cells with the highest Tks5<sub>long</sub> expression (Fig. 1B,C). The effect of the triple knockdown on Tks5<sub>long</sub> expression was synergistic, as the expression levels of Tks5<sub>long</sub> far exceeded that predicted by the additive effects of single knockdown. Importantly, the effect of Nkx2-1, Foxa2, and Cdx2 knockdown was specific to Tks5<sub>long</sub> and did not affect expression of the other Tks5 isoform, Tks5<sub>short</sub> (Fig. 1B,C). We validated these results in an independent T<sub>nonMet</sub> cell line using different shRNAs (Supplemental Fig. S1C). These data suggest



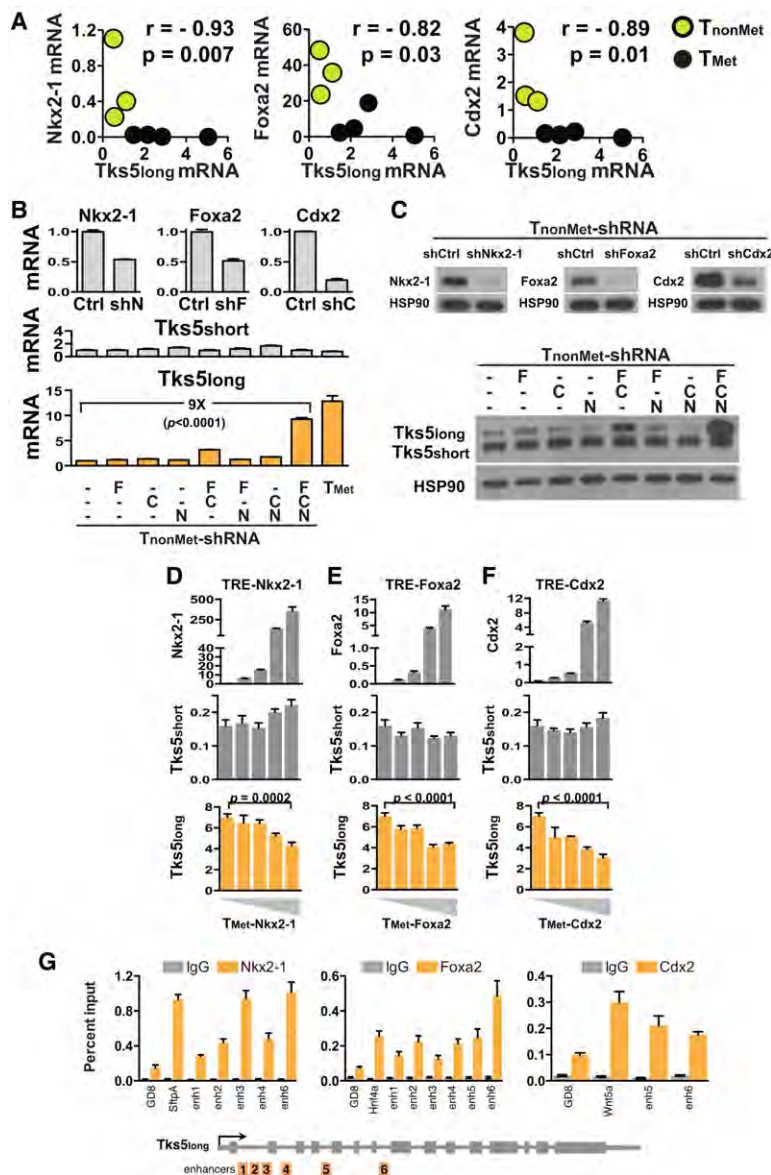


**Figure 1.** Nkx2-1, Foxa2, and Cdx2 synergistically suppress the expression of *Tks5long* in nonmetastatic lung adenocarcinoma cells. (A) mRNA levels of Nkx2-1, Foxa2, and Cdx2 in TnonMet (368T1, 394T4, and 802T4) and TMet (373T1, 393T3, 393T5, and 482T1) lung adenocarcinoma cell lines anti-correlate with *Tks5long* expression as measured by qRT-PCR. (r) Spearman's correlation coefficient; (p) P-value. (B, C) Knockdown of Nkx2-1, Foxa2, and Cdx2 in TnonMet cells (394T4) derepresses *Tks5long* expression but not *Tks5short*, as measured by qRT-PCR (B) and immunoblotting (C). Lines (—) indicate control hairpins against firefly or renilla luciferase. Data are represented as mean  $\pm$  SD. The P-value was calculated by Student's *t*-test. (D–F) Overexpression of Nkx2-1, Foxa2, and Cdx2 in TMet cells (393T5) represses *Tks5long* expression but not *Tks5short*, as measured by qRT-PCR. Data are represented as mean  $\pm$  SD. The P-values were calculated by Student's *t*-test. (G) ChIP-qPCR analysis of the enrichment of Nkx2-1, Foxa2, and Cdx2 binding at the *Tks5long* genomic locus. Data are represented as mean  $\pm$  SEM of at least three independent experiments. *Sfta*, *Hnf4a*, and *Wnt5a* served as positive controls for Nkx2-1, Foxa2, and Cdx2 binding, respectively. (GD8) Negative control mapping to a gene desert region on murine chromosome 8. For each enhancer versus GD8,  $P < 0.05$  by Student's *t*-test.

that Nkx2-1, Foxa2, and Cdx2 may suppress *Tks5long* expression in a synergistic manner.

To examine whether these transcription factors are sufficient to suppress *Tks5long* expression in metastatic cells, we overexpressed each transcription factor in a doxycycline-inducible manner in TMet cells. Increasing the levels of each transcription factor inhibited *Tks5long* expression in a dosage-dependent manner without affecting *Tks5short* mRNA levels (Fig. 1D–F). Furthermore, this suppressive effect on *Tks5long* expression was additive, as combined overexpression of Nkx2-1 and Foxa2 (or of Nkx2-1 and Cdx2) reduced the mRNA levels of *Tks5long* more significantly than one transcription factor alone (Supplemental Fig. S1D).

To determine whether these transcription factors suppress *Tks5long* expression by directly binding to its genetic locus, we performed ChIP-qPCR analysis on potential enhancer regions in the *Tks5long* locus. We observed binding

of Nkx2-1, Foxa2, and Cdx2 to multiple enhancers in the *Tks5long* locus (Fig. 1G), consistent with a direct role in down-regulating gene expression at the genetic locus.

#### *Nkx2-1, Foxa2, and Cdx2 cooperate to inhibit metastasis in vivo*

To test whether Nkx2-1, Foxa2, and Cdx2 suppress metastasis, we transplanted TnonMet-shNFC cells subcutaneously into nude mice and examined their ability to metastasize from the subcutaneous tumor to the lungs over a period of 6 wk. This assay tests a full range of metastatic properties, as it requires that tumor cells invade and intravasate into circulation at the primary site and then extravasate and colonize a distant organ at the metastatic site. Notably, while TnonMet cells with Nkx2-1 knockdown (TnonMet-shN cells) formed more lung nodules than control TnonMet cells, TnonMet-shNFC cells were

strikingly more metastatic (Fig. 2A,B). The increase in metastatic potential in  $T_{\text{nonMet-shNFC}}$  cells was more than the additive effect induced by single or double knockdown. Importantly, the knockdown of these transcription factors did not significantly affect the size of the primary tumors in the subcutaneous site (Supplemental Fig. S2). These data suggest that loss of Nkx2-1, Foxa2, and Cdx2 functions cooperatively to promote metastasis in lung adenocarcinoma.

The increased number of lung metastases seen with  $T_{\text{nonMet-shNFC}}$  cells could be explained by changes in their ability to complete different steps along the metastatic cascade. We first examined how knockdown of Foxa2, Cdx2, and Nkx2-1 affected cell morphology and motility in vivo. We observed that  $T_{\text{nonMet-shNFC}}$  subcutaneous tumors adopted a mesenchymal morphology similar to that of  $T_{\text{Met}}$  tumors, in contrast to the predominantly epithelial morphology in tumors formed by  $T_{\text{nonMet}}$  cells and the epithelial/slight mesenchymal

morphology in  $T_{\text{nonMet-shN}}$  tumors (Fig. 3A,B). This change to mesenchymal morphology for  $T_{\text{nonMet-shNFC}}$  cells occurred only in vivo but not in vitro (Supplemental Fig. S3A), suggesting that it is at least in part induced by non-cell-autonomous factors present in the tumor microenvironment. Consistent with this change to a mesenchymal morphology, qRT-PCR analysis of  $T_{\text{nonMet-shNFC}}$  tumors showed loss of the epithelial marker Krt19 and a small increase in expression of mesenchymal markers Twist, Snail, Zeb1, and N-cadherin compared with  $T_{\text{nonMet}}$  tumors but no change in Slug, Vimentin, and E-cadherin (Supplemental Fig. S3B; data not shown). These data suggest a partial epithelial-to-mesenchymal transition (EMT), an important step in the metastatic process (Sato et al. 2012; Tsai and Yang 2013), of  $T_{\text{nonMet-shNFC}}$  cells in vivo.

Because mesenchymal morphology is associated with increased motility (Thiery et al. 2009; Tsai and Yang 2013), we performed intravital imaging to monitor migration of GFP-positive cancer cells within subcutaneous tumors.  $T_{\text{nonMet-shNFC}}$  tumors contained significantly more migratory cells than  $T_{\text{nonMet}}$  and  $T_{\text{nonMet-shN}}$  cells (Fig. 3C; Supplemental Movies S1–S6). Furthermore, when we measured the chemotactic ability of the tumor cells by performing in vivo fine-needle collection assay using 10% fetal bovine serum (FBS) as a chemoattractant (Wyckoff et al. 2000), we collected a higher number of GFP-positive cancer cells from  $T_{\text{nonMet-shNFC}}$  subcutaneous tumors than from  $T_{\text{nonMet}}$  and  $T_{\text{nonMet-shN}}$  tumors (Fig. 3D). Taken together, these data suggest that  $T_{\text{nonMet-shNFC}}$  cells are more motile in vivo than  $T_{\text{nonMet}}$  and  $T_{\text{nonMet-shN}}$  cells.

To test whether the enhanced metastatic ability of  $T_{\text{nonMet-shNFC}}$  cells can also be explained by differences in the colonization of secondary sites during the metastatic cascade, we injected tumor cells intravenously into immunocompromised mice to test their ability to establish tumor nodules upon arriving at the lung capillaries. We observed that  $T_{\text{nonMet-shNFC}}$  cells and  $T_{\text{nonMet-shN}}$  cells had equally high colonization capacities compared with  $T_{\text{nonMet}}$  control (Fig. 3E,F), suggesting that while knockdown of Nkx2-1 enhances metastatic colonization, additional inhibition of Foxa2 and Cdx2 does not further contribute to this property.

Taken together, our data support a model in which Nkx2-1, Foxa2, and Cdx2 inhibit metastasis by acting on different steps of the metastatic cascade. While Nkx2-1 inhibits the extravasation/colonization step towards the end of the metastatic cascade, Nkx2-1, Foxa2, and Cdx2 together inhibit migration and invasion in the early steps of metastasis (Fig. 3G). The gain of metastatic ability in  $T_{\text{nonMet-shNFC}}$  cells compared with  $T_{\text{nonMet-shN}}$  cells is correlated with an increase in invasion and migration in the primary tumor.

#### *Nkx2-1, Foxa2, and Cdx2 collectively repress a program of metastasis genes*

Given the increased metastatic ability of  $T_{\text{nonMet-shNFC}}$  cells compared with  $T_{\text{nonMet}}$  and  $T_{\text{nonMet-shN}}$  cells, we

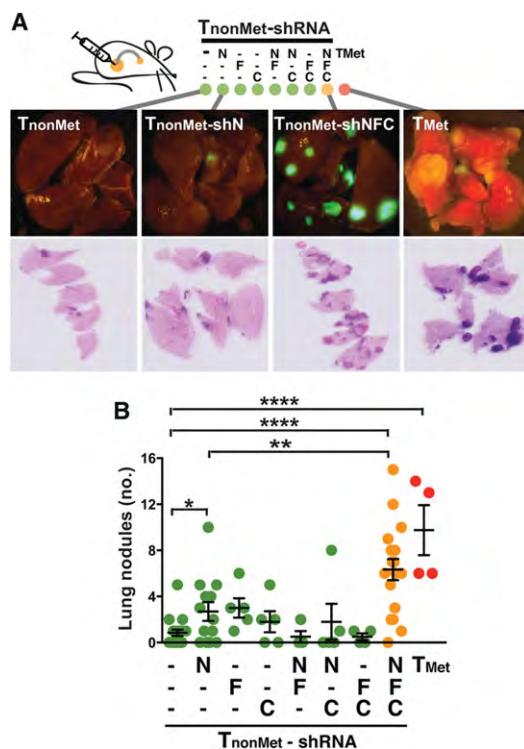


**Figure 2.** Foxa2 and Cdx2 synergize with Nkx2-1 in inhibiting metastasis in vivo. (A) Triple knockdown of Nkx2-1, Foxa2, and Cdx2 in a subcutaneous transplantation assay increases the metastatic potential of  $T_{\text{nonMet}}$  cells (394T4)—in comparison with control  $T_{\text{nonMet}}$  cells and  $T_{\text{nonMet}}$  cells with single/double knockdown—to a level similar to that of  $T_{\text{Met}}$  cells (373T1). Representative images of lung metastases are shown. Lines (—) indicate control hairpins against firefly or renilla luciferase. (B) Quantification of metastasis frequencies as determined by numbers of tumor nodules visible on the lung surface. Each circle represents an individual mouse. Data are represented as mean  $\pm$  SEM. The  $P$ -values were calculated by Student's  $t$ -test. (\*)  $P < 0.05$ ; (\*\*)  $P < 0.01$ ; (\*\*\*\*)  $P < 0.0001$ .



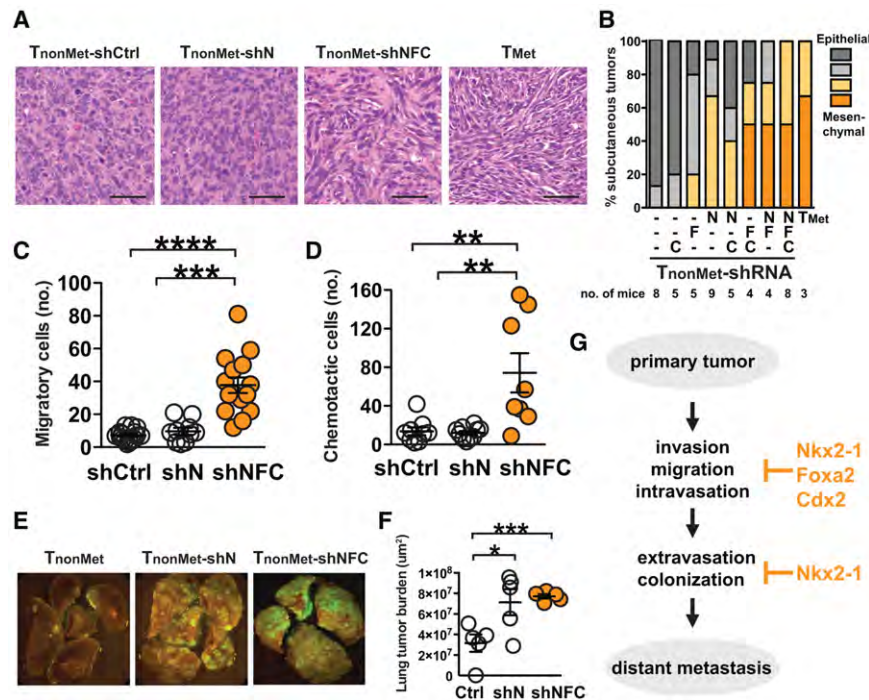


**Figure 3.** Foxa2 and Cdx2 synergize with Nkx2-1 in inhibiting migration in vivo. (A,B) Triple knockdown of Nkx2-1, Foxa2, and Cdx2 in T<sub>nonMet</sub> (394T4) subcutaneous tumors induces a mesenchymal morphology similar to T<sub>Met</sub> (373T1) tumors, in contrast to the epithelial T<sub>nonMet</sub>-shCtrl tumors. (A) Representative H&E staining of subcutaneous tumors. Bar, 50  $\mu$ m. (B) Quantification of epithelial and mesenchymal morphology by a pathologist (RT Bronson). Lines (—) indicate control hairpins against firefly or renilla luciferase. (C,D) Knockdown of Nkx2-1, Foxa2, and Cdx2 in T<sub>nonMet</sub> (394T4) subcutaneous tumors enhances migration in vivo compared with T<sub>nonMet</sub>-shCtrl and T<sub>nonMet</sub>-shN tumors, as measured by intravital imaging (C) and fine-needle collection assay (D). Data are represented as mean  $\pm$  SEM. The *P*-values were calculated by Student's *t*-test. (\*\*) *P* < 0.01; (\*\*\*) *P* < 0.001; (\*\*\*\*) *P* < 0.0001. (E,F) T<sub>nonMet</sub>-shNFC and T<sub>nonMet</sub>-shN (394T4) cells show similar colonization ability in the lungs after intravenous transplantation. (E) Representative images of lungs with tumor nodules. (F) Quantification of lung tumor burden. Each circle

represents an individual mouse. Data are represented as mean  $\pm$  SEM. The *P*-values were calculated by Student's *t*-test. (\*) *P* < 0.05; (\*\*\*) *P* < 0.001. (G) Model for distinct roles of Nkx2-1, Foxa2, and Cdx2 in inhibiting metastatic progression.

next investigated whether a network of metastasis-related genes might be differentially regulated upon knockdown of Nkx2-1, Foxa2, and Cdx2. Transcription factors generally regulate a broad network of target genes, often genes with similar functions. Therefore, we hypothesized that, in addition to suppressing the expression of Tks5<sub>long</sub> (a critical mediator of metastasis), Nkx2-1, Foxa2, and Cdx2 may also regulate the expression of other metastasis-related genes. Thus, we performed RNA sequencing (RNA-seq) on T<sub>nonMet</sub>, T<sub>nonMet</sub>-shN, T<sub>nonMet</sub>-shNFC, and T<sub>Met</sub> cells and used an unsupervised blind source separation strategy using independent component analysis (ICA) (see the Supplemental Material; data not shown). to elucidate statistically independent gene expression signatures that characterize the transcriptomes of these cells. This high-resolution approach allowed us to identify two statistically significant and biologically relevant signatures that are separate from a "clonal signature" that embodies the background identity of T<sub>Met</sub> versus T<sub>nonMet</sub>-derived cells (Fig. 4A): (1) a signature differentiating Nkx2-1-high samples (T<sub>nonMet</sub>) from all Nkx2-1-low samples (T<sub>nonMet</sub>-shN, T<sub>nonMet</sub>-shNFC, and T<sub>Met</sub> cells), which we termed an "shN signature," and (2) a signature clustering T<sub>nonMet</sub>-shNFC/T<sub>Met</sub> cells away from T<sub>nonMet</sub>/T<sub>nonMet</sub>-shN cells, which we designated as the "shNFC signature."

Our analysis provides several lines of evidence that T<sub>nonMet</sub>-shNFC cells significantly recapitulated the major metastasis-related gene expression patterns associated with T<sub>Met</sub> cells. First, hierarchical clustering based on the top and bottom second percentile of genes identi-

fied in the shNFC signature showed clustering of T<sub>nonMet</sub>-shNFC cells with T<sub>Met</sub> cells, and this cluster segregated away from T<sub>nonMet</sub> and T<sub>nonMet</sub>-shN cells (Fig. 4B,C), indicating that the identified gene expression pattern robustly supports the signature. Highly similar clustering patterns were also obtained in analysis of the top and bottom first percentile and fifth percentile of genes in the shNFC signature (data not shown). Second, clustering based on global gene expression profiles after depletion of the background clonal signature showed that T<sub>nonMet</sub>-shNFC cells were substantially more closely related to T<sub>Met</sub> cells than T<sub>nonMet</sub>-shN and T<sub>nonMet</sub> cells (Supplemental Fig. S4A). Finally, the shNFC signature was highly enriched for the "Tmet/Met" gene set and depleted for the "TnonMet" gene set (Winslow et al. 2011) when analyzed using gene set enrichment analysis (GSEA) (Fig. 4D; Subramanian et al. 2005). In contrast, the shN signature did not show a similar enrichment or depletion pattern of T<sub>Met</sub>/Met or T<sub>nonMet</sub> gene sets (Fig. 4D).

Of the 388 genes identified by the shNFC signature, 169 genes were up-regulated (among which is Tks5<sub>long</sub>), and 219 genes were down-regulated in the T<sub>nonMet</sub>-shNFC/T<sub>Met</sub> cells compared with the T<sub>nonMet</sub>/T<sub>nonMet</sub>-shN cells (Fig. 4C). Interestingly, GSEA analyses using publicly available gene sets in the Molecular Signatures Database (Subramanian et al. 2005) revealed that the shNFC signature is significantly enriched for gene sets that represent poor patient prognosis, metastasis/EMT, and TGF $\beta$  targets (Fig. 4E). Furthermore, the shNFC signature is significantly depleted for gene sets related to gastrointestinal/

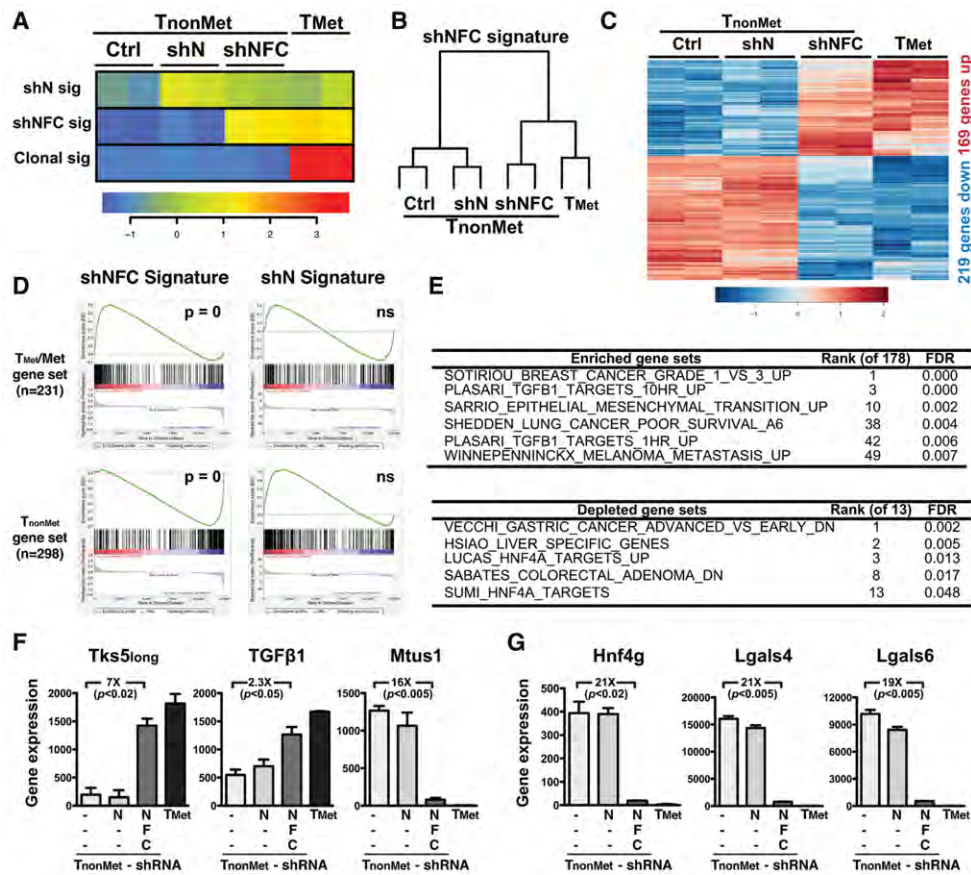


**Figure 4.** Nkx2-1, Foxa2, and Cdx2 together repress a program of metastasis genes. (A) RNA-seq gene expression analysis of 394T4  $T_{nonMet}$ ,  $T_{nonMet}$ -shN,  $T_{nonMet}$ -shNFC, and 373T1  $T_{Met}$  cells reveals two statistically significant and biologically relevant signatures: an shN signature and an shNFC signature, both separate from a clonal signature that embodies the background identity of  $T_{Met}$ - versus  $T_{nonMet}$ -derived cells. (B) Dendrogram showing sample relationships via clustering based on the top and bottom second percentile of genes in the shNFC signature. (C) Differentially expressed genes that drive the shNFC signature distinguishing  $T_{nonMet}$ -shNFC/ $T_{Met}$  cells from  $T_{nonMet}$ / $T_{nonMet}$ -shN cells. (D) GSEA (gene set enrichment analysis) reveals that the shNFC signature is highly enriched for  $T_{Met}$ /Met genes and depleted for  $T_{nonMet}$  genes, whereas the shN signature does not show similar enrichment. (ns) Not significant. (E) GSEA using the Molecular Signatures Database (MSigDB) curated gene set collection shows that the shNFC signature is enriched for gene sets associated with metastasis and poor prognosis and depleted for gene sets associated with Hnf4a-related gastrointestinal/hepatic differentiation. (F) Examples of prometastatic (*Tks5<sub>long</sub>* and *TGFβ1*) and anti-metastatic (*Mtus1*) genes that were identified in the shNFC signature by RNA-seq. Data are represented as mean  $\pm$  SEM. The *P*-values were calculated by Student's *t*-test. (G) Examples of gastrointestinal differentiation genes (*Hnf4g*, *Lgals4*, and *Lgals6*) that were identified in the shNFC signature by RNA-seq. Data are represented as mean  $\pm$  SEM. The *P*-values were calculated by Student's *t*-test.

liver-related genes, reflecting the gene expression changes induced upon knockdown of Foxa2 and Cdx2 (Fig. 4E). Many of the gene expression changes identified in the shNFC signature that were relevant for metastasis or gastrointestinal differentiation were validated by qRT-PCR and immunoblotting (Fig. 4F,G; Supplemental Fig. S4B; data not shown).

To directly answer the question of what fraction of the gene expression differences between our collection of  $T_{nonMet}$  and  $T_{Met}$ /Met cells was recapitulated by combined knockdown of Nkx2-1, Foxa2, and Cdx2 in  $T_{nonMet}$  394T4 cells, we performed targeted pairwise differential analysis. We found that a large fraction (32%) of the genes that were differentially expressed between  $T_{nonMet}$  and  $T_{Met}$ /Met cells also showed significant gene expression alterations by twofold or more in comparing 394T4  $T_{nonMet}$

versus  $T_{nonMet}$ -shNFC cells ( $P = 2.22 \times 10^{-16}$ , hypergeometric test), suggesting that reduced expression of the three transcription factors can explain about one-third of the gene expression changes in metastatic progression. In contrast, only 9% of the genes that were differentially expressed between  $T_{nonMet}$  and  $T_{Met}$ /Met cells were found to be altered when comparing 394T4  $T_{nonMet}$  versus  $T_{nonMet}$ -shN cells ( $P = 2.22 \times 10^{-16}$ , hypergeometric test).

Taken together, these data argue that the  $T_{nonMet}$ -shNFC gene expression program driven by loss of Nkx2-1, Foxa2, and Cdx2 significantly recapitulated the characteristics of  $T_{Met}$  cells. These findings are consistent with data from our in vivo metastasis assays that  $T_{nonMet}$ -shNFC cells are more metastatic than  $T_{nonMet}$ -shN cells and further support that Foxa2 and Cdx2 cooperate with Nkx2-1 to regulate a network of metastasis-related genes.



*The inhibitory effect of Nkx2-1, Foxa2, and Cdx2 on metastasis depends on the activation of Tks5<sub>long</sub>, Hmga2, and Snail expression*

Given the large number of genes activated in the shNFC signature, we then examined whether some of these genes might be functionally required for promoting the metastatic capacity of T<sub>nonMet</sub>-shNFC cells. In addition to Tks5<sub>long</sub>, we elected to examine the embryonal proto-oncogene Hmga2 and the EMT transcription factor Snail, as these metastasis-promoting genes are also significantly up-regulated in T<sub>Met</sub>/Met cells compared with T<sub>nonMet</sub> cells in microarray-based gene expression analysis (Supplemental Fig. S5A; Winslow et al. 2011). T<sub>nonMet</sub>-shNFC cells exhibited a significant increase in Hmga2 and Snail expression at the levels of both mRNA and protein, exceeding the levels in T<sub>nonMet</sub> and T<sub>nonMet</sub> single/double-knockdown cells (Fig. 5A,B). The activation effect was synergistic, as the expression levels of Hmga2 and Snail were much higher than predicted by the additive effects of single knockdown. To test whether increased expression of Tks5<sub>long</sub>, Hmga2, and Snail are required for increased metastatic ability of T<sub>nonMet</sub>-shNFC cells, we knocked down these three genes by shRNAs or CRISPR/Cas sgRNAs (Fig. 5C). Decreased expression of Tks5<sub>long</sub>, Hmga2, or Snail individually impaired the metastatic ability of T<sub>nonMet</sub>-shNFC cells without affecting the size of the primary subcutaneous tumors (Fig. 5D,E; Supplemental Fig. S5E). Importantly, Hmga2 and Snail knockdown did not affect the expression of Tks5<sub>long</sub> or of each other (Supplemental Fig. S5C,D), suggesting that they each contributed individually to increasing metastatic potential. These data support our hypothesis that Nkx2-1, Foxa2, and Cdx2 may function as key regulators for a net-

work of metastasis-related genes that include Tks5<sub>long</sub>, Hmga2, and Snail.

*The endogenous expression pattern of Nkx2-1, Foxa2, and Cdx2 correlates with tumor progression in vivo*

To further characterize the suppressive roles of Nkx2-1, Foxa2, and Cdx2 during tumor progression, we examined their endogenous expression in the KP model of lung adenocarcinoma. This animal model provides a well-defined genetic context and a stereotypic temporal pattern of histologic progression, which facilitate the identification of patterns of gene expression alterations that accompany tumor progression. We analyzed 195 tumor regions from mice ranging from 17 to 33 wk post-initiation and scored them as low grade (grades 1–3) or high grade (grade 4, poorly differentiated) based on nucleocytoplasmic morphology, tumor architecture, and the presence of stromal invasion. Consistent with previous findings (Winslow et al. 2011), expression of Nkx2-1 and Hmga2 anti-correlated with each other in these tumors (Fig. 6A), and Nkx2-1<sup>low</sup> and Hmga2<sup>high</sup> tumors were mostly high grade (Fig. 6D,E).

The pattern of Foxa2 expression was highly similar to that of Nkx2-1 and was anti-correlated with Hmga2 (Fig. 6B,C). The inverse correlation of Foxa2 expression to tumor grade was more striking than Nkx2-1: Foxa2<sup>high</sup> expression was invariably associated with low-grade tumors (117 of 117; 100%), while Foxa2<sup>low</sup> tumors were consistently high grade (21 of 21; 100%) (Fig. 6F). These data suggest that Foxa2, similar to Nkx2-1, marks an early state of tumor progression, and loss of Foxa2 expression is a stringent diagnostic marker of high-grade tumors.

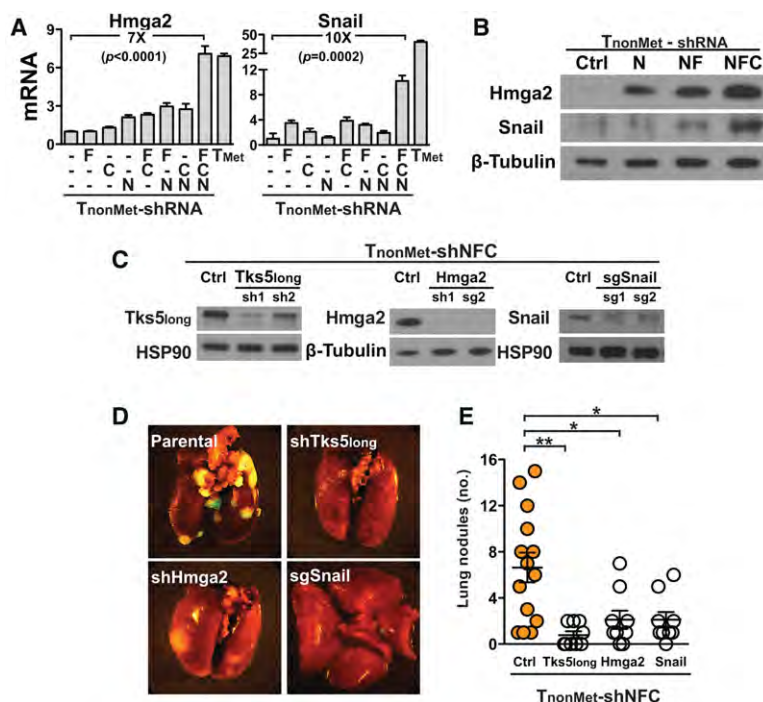


**Figure 5.** The inhibitory effect of Nkx2-1, Foxa2, and Cdx2 on metastasis depends on the activation of Tks5<sub>long</sub>, Hmga2, and Snail expression. (A,B) Combined knockdown of Nkx2-1, Foxa2, and Cdx2 in T<sub>nonMet</sub> cells (394T4) derepresses the expression of Hmga2 and Snail, as analyzed by qRT-PCR (A) and immunoblotting (B). Lines (—) indicate control hairpins against firefly or renilla luciferase. Data are represented as mean ± SD. The *P*-values were calculated by Student's *t*-test. (C–E) Knockdown of Tks5<sub>long</sub>, Hmga2, or Snail dampens the metastatic ability of 394T4 T<sub>nonMet</sub>-shNFC cells after subcutaneous transplantation. (C) Validation of knockdown by immunoblotting. (D) Representative images of lungs with tumor nodules. (E) Quantification of lung tumor nodules. Each circle represents an individual mouse. Control includes T<sub>nonMet</sub>-shNFC cells (*n* = 10 mice) and T<sub>nonMet</sub>-shNFC-sgRosa cells (*n* = 4 mice); Tks5<sub>long</sub> knockdown was generated by hairpins shTks5<sub>long</sub>#1 (*n* = 5 mice) and shTks5<sub>long</sub>#2 (*n* = 4 mice), Hmga2 knockdown was generated by hairpin shHmga2#1 (*n* = 5 mice) and sgRNA sgHmga2#2 (*n* = 4 mice), and Snail knockdown was generated by sgRNAs sgSnail#1 (*n* = 5 mice) and sgSnail#2 (*n* = 4 mice). Data are represented as mean ± SEM. The *P*-values were calculated by Student's *t*-test. (\*) *P* < 0.05; (\*\*) *P* < 0.01.

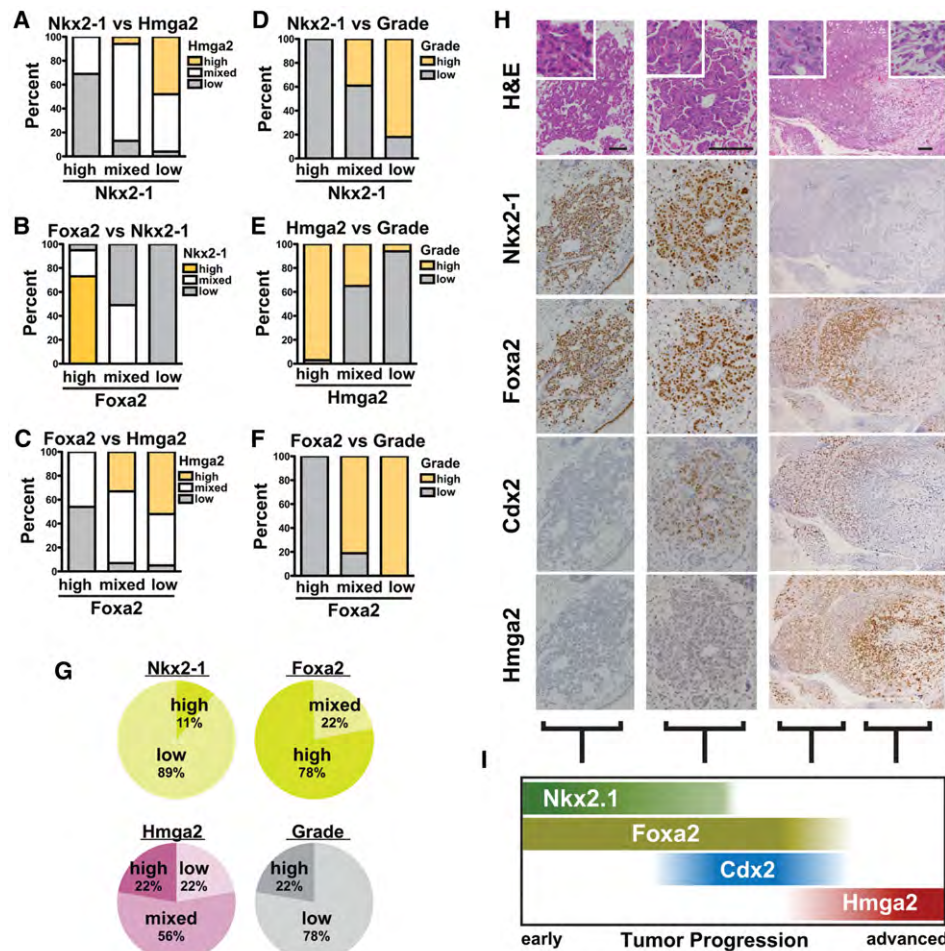


**Figure 6.** The endogenous expression pattern of Nkx2-1, Foxa2, Cdx2, and Hmga2 correlates with tumor progression in an autochthonous model of lung adenocarcinoma. (A–C) Pairwise correlation of Nkx2-1, Foxa2, and Hmga2 expression in KP lung adenocarcinomas. (D–F) Correlation of Nkx2-1, Foxa2, and Hmga2 expression in KP lung adenocarcinomas with tumor grades. Tumor regions were scored as low grade (grades 1–3) or high grade (grade 4, poorly differentiated) based on nucleocytoplasmic morphology, tumor architecture, and the presence of stromal invasion. (G) High expression of Cdx2 in KP lung adenocarcinomas is frequently associated with low expression of Nkx2-1, high expression of Foxa2, low-medium expression of Hmga2, and low-grade histology. (H) Representative H&E and immunohistochemical stainings of KP lung adenocarcinomas. Bar, 150  $\mu$ m. The insets show the nucleocytoplasmic morphology of the tumor cells. (I) Model summarizing expression changes of Nkx2-1, Foxa2, Cdx2, and Hmga2 in lung adenocarcinomas.

Interestingly, loss of Foxa2 expression in high-grade tumors often lagged behind loss of Nkx2-1 (see examples in Fig. 6H, third column; Supplemental Fig. S6A). These observations indicate that loss of Foxa2 expression in tumor progression does not occur concurrently with loss of Nkx2-1 but happens after Nkx2-1 expression is lost (Fig. 6I).

Cdx2 staining was detected in a significant fraction of these lung adenocarcinomas (35 of 195; ~20%), albeit at a lower frequency than the staining of Nkx2-1 (139 of 195; ~70%) and Foxa2 (174 of 195; ~90%). This lower frequency of Cdx2 staining suggests that Cdx2 expression may represent a transient state during tumor progression that is only detectible when a large number of tumors are analyzed. Importantly, the Cdx2<sup>high</sup> tumors showed a consistent pattern that argues that Cdx2 marks an intermediate state of tumor progression that is temporally

situated after loss of Nkx2-1 but before loss of Foxa2 and full activation of Hmga2 (Fig. 6G). First, the vast majority of Cdx2<sup>high</sup> tumor areas were Nkx2-1<sup>low</sup> (eight of nine, 89%), indicating a strong anti-correlation between Cdx2 and Nkx2-1 expression. Second, tumor sections with high Cdx2 levels were typically Foxa2<sup>high</sup> (seven of nine, 87%). In fact, all of the Nkx2-1<sup>low</sup> Foxa2<sup>high</sup> tumor regions were invariably Cdx2<sup>high</sup> (six of six, 100%), and we did not observe any Nkx2-1<sup>low</sup>, Foxa2<sup>low</sup>, and Cdx2<sup>high</sup> regions. Finally, the majority of Cdx2<sup>high</sup> tumor regions were Hmga2<sup>mixed</sup> (five of nine, 56%), whereas only a small fraction was Hmga2<sup>high</sup> (two of nine; 22%) or Hmga2<sup>low</sup> (two of nine; 22%). Even though some of these Cdx2<sup>high</sup> regions were found adjacent to Hmga2<sup>high</sup>, high-grade, and poorly differentiated areas, Cdx2<sup>high</sup> regions themselves were invariably well/moderately differentiated and never part of the poorly differentiated regions (Fig. 6H, third column;



Supplemental Fig. S6A). Collectively, these data strongly suggest that Cdx2 marks an intermediate state of tumor progression (Fig. 6I).

An alternative model that could explain these observations is that Cdx2-expressing tumors represent a “dead end” differentiation state that will never progress to advanced metastatic tumors. However, multiple lines of evidence argue against this model. First, within a single tumor, well/moderately differentiated tumor regions with strong Cdx2 expression and weak Hmga2 expression were frequently associated with adjacent poorly differentiated regions that exhibit a reciprocal expression pattern of low Cdx2 staining and intense Hmga2 staining (Fig. 6H, third column; Supplemental Fig. S6A). Second, cell line-based experiments showed that knockdown of Nkx2-1 in T<sub>nonMet</sub> cells derepressed Cdx2 mRNA and protein levels, while knockdown of Foxa2 in T<sub>nonMet</sub>-shN cells reduced Cdx2 levels (Supplemental Fig. S6B,C), suggesting that Cdx2 expression in these tumor cells is plastic and can be regulated by changes in expression of Nkx2-1 and Foxa2. Furthermore, ChIP-qPCR analysis detected binding of Nkx2-1 and Foxa2 to an enhancer downstream from the genomic locus of *Cdx2* (Supplemental Fig. S6D). Based on these findings, we propose a model for the regulation of Cdx2 expression in lung adenocarcinoma in which transcription of Cdx2 is inhibited by binding of Nkx2-1 to a nearby enhancer region. Upon loss of Nkx2-1, expression of Cdx2 is derepressed in a manner dependent on Foxa2 binding to the same enhancer (Supplemental Fig. S6E).

Taken together, these observations suggest that lung adenocarcinoma progress from early tumors that express Nkx2-1 and Foxa2 (Fig. 6I). Over time, Nkx2-1 is silenced, leading to activation of Cdx2 and partial activation of metastasis-promoting genes such as Hmga2 in at least a subset of tumors. Finally, suppression of Foxa2 leads to reduced Cdx2 expression, and the combined loss of Nkx2-1,

Foxa2, and Cdx2 leads to complete derepression of Hmga2 and other metastasis-promoting genes, resulting in full acquisition of metastatic potential.

### *Nkx2-1, Foxa2, and Cdx2 gene expression signatures predict clinical outcomes of lung adenocarcinoma patients*

We next asked whether our observations could provide prognostic information relevant to human lung adenocarcinomas. To this end, we analyzed RNA-seq expression data for 488 lung adenocarcinoma primary tumors from patients with stage I–IV disease from The Cancer Genome Atlas (TCGA, <http://cancergenome.nih.gov>). Unsupervised signature analysis (see the Supplemental Material) of the expression patterns of NKX2-1, FOXA2, CDX2, and HMGA2 in these tumors revealed three gene expression signatures (Fig. 7A,B). Interestingly, these signatures closely correlated with the expression patterns of Nkx2-1, Foxa2, Cdx2, and Hmga2 in the KP mouse model of lung adenocarcinoma. The first signature is driven by high expression of NKX2-1 and FOXA2 as well as low expression of HMGA2, similar to the early tumors in mice. The second signature is characterized by high expression of CDX2, similar to tumors in the intermediate state. Finally, the third signature is characterized by high expression of HMGA2, similar to advanced tumors in our mouse model. While the gene expression patterns in these signatures are consistent with our observations in the KP model, we note that there is a small increase of FOXA2 levels in the third signature compared with the second signature. This difference from our KP model is not surprising given the larger heterogeneity and complexity that exist in human lung adenocarcinomas compared with the genetically engineered model.

Importantly, these signatures also strongly correlated with clinical outcomes (Fig. 7C,D). The NKX2-1/

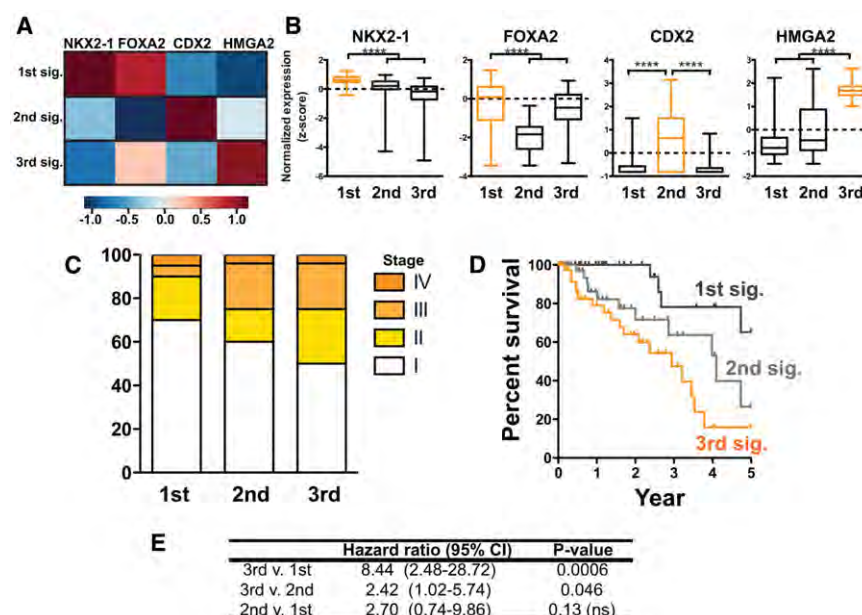


**Figure 7.** NKX2-1, FOXA2, CDX2, and HMGA2 gene expression signatures predict clinical outcomes of lung adenocarcinoma patients. (A) Heat map showing the expression patterns of NKX2-1, FOXA2, CDX2, and HMGA2 in signatures identified in TCGA human primary lung adenocarcinoma ( $n = 488$ ) using ICA. (B) Box and whisker plots of standardized expression levels of NKX2-1, FOXA2, CDX2, and HMGA2 in each signature. The horizontal dashed line reflects the mean expression level across all tumors. The  $P$ -values were calculated by Student's  $t$ -test. (\*\*\*\*)  $P < 0.0001$ . (C–E) Analysis of the top 10th percentile of the 488 lung adenocarcinoma patients in each signature identified by ICA shows that the three signatures correlate with disease stage (C) and overall survival ( $P = 0.0006$  by log-rank test) (D). (E) Multivariate Cox proportional hazard regression analysis of overall survival after adjustments for gender, age, and stage.

FOXA2-driven signature and the CDX2-driven signature were associated with favorable and intermediate disease stage and patient survival, respectively. In contrast, the HMGA2-driven signature was associated with the worst stage and survival. Furthermore, the prognostic values of these four gene pattern-derived signatures were more powerful than analysis using a single gene alone (data not shown). Finally, a multivariate Cox proportional hazard regression analysis showed that these signatures of gene expression pattern were significant prognostic factors independent of gender, age, and disease stage (Fig. 7E; Supplemental Fig. S7A). These results provide further support to our proposed model that early-stage tumors are marked by NKX2-1 and FOXA2 expression, while intermediate tumors acquire expression of CDX2, and most advanced tumors acquire expression of HMGA2. Interestingly, these signatures are prognostic for survival outcome even for patients with early-stage disease (i.e., stages I and II), suggesting that the signatures could be informative for identifying high-risk patients with micro-metastatic disease who may benefit from adjuvant treatment after surgical tumor resection (Supplemental Fig. S7B). Taken together, these data argue that our proposed model for lung adenocarcinoma progression is highly relevant for human cancer. Our findings provide important information for the prognosis of lung adenocarcinoma patients and may inform the future development of therapeutic strategies for this highly metastatic disease.

## Discussion

In this study, we present evidence from the autochthonous KP model of lung adenocarcinoma, derivative cell lines, and human patients that together demonstrate that Nkx2-1, Foxa2, and Cdx2 function collectively to suppress metastatic progression of lung adenocarcinoma. We found that loss of Nkx2-1, Foxa2, and Cdx2 profoundly enhanced metastasis in a subcutaneous transplantation model compared with loss of a single factor alone. In particular, these three factors regulated metastasis by acting on multiple steps of the metastatic cascade: Loss of Nkx2-1 alone promoted colonization at distant sites, whereas combined loss of Nkx2-1, Foxa2, and Cdx2 cooperated to promote tumor cell migration. The observed increase in metastatic ability upon loss of Nkx2-1, Foxa2, and Cdx2 can be explained by activation of a network of transcriptional targets that account for a large and significant fraction of the gene expression alterations between  $T_{\text{nonMet}}$  and  $T_{\text{Met/Met}}$  cells. These target genes include the invadopodia component *Tks5<sub>long</sub>*, the embryonal proto-oncogene *Hmga2*, and the EMT mediator *Snail*, all of which functionally contribute to metastasis. Furthermore, analysis of autochthonous lung tumors in the KP model revealed a strong correlation between loss of expression of these three factors and tumor progression to an advanced, poorly differentiated, and metastatic state. Finally, in human lung adenocarcinoma, the expression patterns of NKX2-1, FOXA2, CDX2, and HMGA2 predicted tumor differentiation states that significantly correlat-

ed with disease stage and survival outcome. Thus, our results are highly relevant for the human disease and provide prognostic information for lung adenocarcinoma patients.

Combining these data, we propose a model for lung adenocarcinoma progression (Fig. 6I). This model starts with high Nkx2-1 and Foxa2 expression that restrains tumors in a well-differentiated, nonmetastatic state. Subsequent loss of Nkx2-1 expression, presumably as a result of extracellular stimulatory signals or intracellular stochastic alterations in gene expression, leads to activation of Cdx2, shifting the cells to an aberrant, albeit still differentiated, state. Finally, suppression of Foxa2 leads to loss of Cdx2, and these alterations synergize with silencing of Nkx2-1 to induce a dedifferentiated stem-like state in the tumor cells, leading to activation of a metastasis program.

Our findings provide two important conclusions. First, Nkx2-1, Foxa2, and Cdx2 can function as key regulatory nodes in transcriptional regulation of the metastasis program. Our data strongly suggest that a relatively small number of factors could be responsible for the vast amount of gene expression alterations in metastasis. It is very likely that only a subset of the gene expression changes induced by loss of Nkx2-1, Foxa2, and Cdx2 is a direct target of these three factors, while other targets may be indirectly controlled via secondary transcription factors downstream from Nkx2-1, Foxa2, and Cdx2. The fact that suppression of Nkx2-1, Foxa2, and Cdx2 is sufficient to derepress this network of metastasis-related genes also suggests that the transcriptional activators for a subset of these target genes may be expressed in tumors and therefore available to act upon loss of these three transcriptional suppressors. As such, while there are multiple pathways regulating the metastasis program, Nkx2-1, Foxa2, and Cdx2 function as three central regulatory nodes in governing transcriptional programs that together restrain tumor metastasis.

Second, the roles of Nkx2-1, Foxa2, and Cdx2 in regulating metastasis underscore the intricate links between dysregulated differentiation and metastasis progression. Striking overlaps exist between genes involved in development and cancer (Kho et al. 2004; Liu et al. 2006; Ben-Porath et al. 2008; Kopantzev et al. 2008). All three transcription factors in this study are well-established developmental regulators. Nkx2-1 and Foxa2 are important developmental regulators of the lungs as well as other endoderm-derived organs (Kimura et al. 1996; Zhou et al. 1997; Minoo et al. 1999; Wan et al. 2005). Nkx2-1 is a homeodomain-containing transcription factor essential for differentiation of the lungs during early embryogenesis (Kimura et al. 1996). In the lungs, Nkx2-1 is expressed in all epithelial cells in early pulmonary development but becomes progressively restricted to alveolar type II and Club cells in adults (Minoo et al. 1999), where Nkx2-1 activates expression of pulmonary-specific genes, including *SftpA*, *SftpB*, *SftpC*, and *CCSP* (Minoo et al. 1999). Foxa2 is a forkhead transcription factor that is expressed in the endoderm and cooperates with its paralog, Foxa1, in mediating organogenesis of the lungs as well as the stomach, intestine, liver, pancreas, and other organs (Kaestner

2010). Foxa2 is important for alveolarization of the lungs during development (Wan et al. 2004). Adult lungs express Foxa2 in the bronchiolar epithelium and alveolar type II cells (Besnard et al. 2004). Interestingly, while Foxa2 expression and function overlap largely with Foxa1, we did not see differential expression of Foxa1 between  $T_{\text{nonMet}}$  and  $T_{\text{Met}}$ /Met cells (Supplemental Fig. S8). In contrast to Nkx2-1 and Foxa2, the expression of Cdx2 is not appreciably expressed in normal embryonic or adult lungs. Instead, as a member of the Caudal-type homeobox protein, Cdx2 is required for intestine morphogenesis during embryonic development and is expressed in the small and large intestines in adults (Beck and Stringer 2010). Cdx2 also functions in an earlier stage in development for trophoblast formation and axial patterning (Beck and Stringer 2010). While detection of Cdx2 expression in the KP lung adenocarcinoma is perhaps surprising, it is unlikely to be an artifact of the mouse model, as other studies on human lung adenocarcinomas have reported expression of Cdx2 in a subset of patients, although the role of Cdx2 in this context was not previously understood (Yatabe et al. 2004; Grimminger et al. 2009).

Our findings reflect the redundant nature of the cellular differentiation program in impeding tumor progression. The lungs and the intestines are developmentally related, as they are both derived from the developing gut tube. We showed that, during progression of lung adenocarcinoma, partial loss of the lung differentiation program by silencing of Nkx2-1 can lead to aberrant activation of an alternative differentiation program of the intestine that is driven by Cdx2 in at least a subset of these tumors. The activation of the latent intestinal program may serve as a redundant mechanism in the cells to restrain tumor dedifferentiation and metastatic progression. Subsequent loss of both the pulmonary and intestinal differentiation programs upon silencing of Nkx2-1, Foxa2, and Cdx2 expression is required for full progression to a cellular state of more primitive differentiation and higher metastatic potential. This hypothesis about redundancy is further corroborated by the results from a previous study in our laboratory, which showed that deletion of Nkx2-1 alone in the KP model of lung adenocarcinoma was not sufficient to promote metastasis (Snyder et al. 2013). In fact, loss of Nkx2-1 expression early at tumor initiation led to activation of a gastric differentiation program driven by Hnf4 $\alpha$ , Foxa1, and Foxa2 in these cancer cells. In this study, loss of Nkx2-1 at a later stage of tumor progression, as opposed to at tumor initiation, activated the expression of Cdx2 instead of Hnf4 $\alpha$ . This difference may reflect the different cellular states of early and late tumors and the existence of multiple possible alternative differentiation states in the progression of the same tumor type. Interestingly, the aberrant activation of Cdx2 has also been identified to induce intestinal differentiation in other tumor types, including gastric cancer, esophageal cancer, nasal adenocarcinoma, pancreatic cancer, and ovarian cancer, and in some cases has been shown to associate with favorable prognosis (Mizoshita et al. 2003; Yuasa 2003; Guo et al. 2004; Matsumoto et al. 2004). These studies, together with our findings, strongly suggest that the activation

of a Cdx2-driven alternative differentiation program in tumors may be a common phenomenon in the evolution of cancer development and may serve as a mechanism to restrain malignant progression.

Our study has shown that the developmental transcription factors Foxa2 and Cdx2 function cooperatively with Nkx2-1 as important regulators in inhibiting metastasis of lung adenocarcinoma. These data provide strong evidence for the important roles of active and latent developmental regulators in restraining the programs of tumor dedifferentiation and metastatic progression. Our findings also demonstrate that while the pathways in the metastasis program are diverse and complex, they can be controlled by a small number of transcription factors that together govern a network of downstream targets to regulate metastasis.

## Materials and methods

### *Autochthonous K-ras<sup>G12D/WT</sup>; p53<sup>-/-</sup> lung tumors and derivative cell lines*

Lung tumors were initiated via intratracheal delivery of Lenti-Cre or Adeno-Cre in *K-ras<sup>LSL-G12D/WT</sup>; p53<sup>flox/flox</sup>* mice as described previously (DuPage et al. 2009). The Massachusetts Institute of Technology Institutional Animal Care and Use Committee approved all animal studies and procedures.

$T_{\text{nonMet}}$ ,  $T_{\text{Met}}$ , and Met cell lines were generated previously using Lenti-Cre-initiated primary tumors and metastases harvested at 6–14 mo post-infection (Winslow et al. 2011). All cell lines were cultured in complete medium (DMEM with 10% FBS, 50 U/mL penicillin, 50 mg/mL streptomycin). Five  $T_{\text{nonMet}}$  cell lines (368T1, 393T1, 394T4, 802T4, and 2557T1), six  $T_{\text{Met}}$  cell lines (373T1, 373T2, 389T2, 393T3, 393T5, and 482T1) and five Met cell lines (373N1, 393N1, 393M1, 482N1, and 482M1) were used for subsequent gene expression analysis and/or functional experiments in this study.

### *Transplantation assays for metastasis*

For subcutaneous transplantation,  $5 \times 10^4$  cells resuspended in 100  $\mu$ L of PBS were injected under the skin on the hind flank of nude mice. Mice were analyzed 6.5 wk after injection. For intravenous transplantation,  $5 \times 10^4$  cells resuspended in 100  $\mu$ L of PBS were injected into the lateral tail vein. Animals were analyzed 2.5 wk after injection.

### *Intravital imaging*

Multiphoton imaging of GFP-labeled tumors was performed as described previously (Wyckoff et al. 2011). Briefly, subcutaneous tumors at 5–6 wk after injection were exposed by skin flap surgery performed on anesthetized animals. Tumors were imaged with an Olympus FV1000 multiphoton microscope using a 25 $\times$ , 1.05 NA water immersion objective with correction lens. Thirty-minute time-lapse movies were analyzed for numbers of migratory GFP-positive tumor cells using ImageJ. Three mice were used per condition, with four to seven fields imaged per mouse.

### *In vivo fine-needle collection assay*

The in vivo invasion assay was performed as previously described (Wyckoff et al. 2000). In brief, four to six catheterized



microneedles held in place by micromanipulators were inserted into the primary tumor of an anesthetized mouse. Needles contained a mixture of 10% Matrigel and 0.01 mM EDTA with L-15 medium  $\pm$  10% FBS. After 4 h, the contents of the needle were extruded, and the total number of tumor cells that migrated into each needle was quantified using DAPI. Three mice were used per condition.

## Acknowledgments

We thank Phillip Sharp, David Barbie, Mandar Muzumdar, and Talya Dayton for critical reading of the manuscript. We also thank Hideo Watanabe for assistance with ChIP-PCR, and Monte Winslow, David Feldser, Nadya Dimitrova, Nikhil Joshi, Wen Xue, Thales Papagiannakopoulos, Francisco Sanchez-Rivera, Tuomas Tammela, Kim Mercer, Kim Dorans, and the entire Jacks laboratory for helpful discussions and experimental assistance. We acknowledge the Swanson Biotechnology Center—and especially Jeff Wyckoff, Eliza Vasile, Denise Crowley, Kathleen Cormier, Michael Brown, and Michele Griffin—for technical support. This work was partially supported by the Cancer Center Support Grant (CCSG) P30-CA14051 from the National Cancer Institute, grants from the Howard Hughes Medical Institute and the National Institutes of Health (5-U01-CA84306) to T.J., Department of Defense Breast Cancer Research Program grant W81XWH-12-1-0031 to M.J.O, and funds from the Ludwig Center at Massachusetts Institute of Technology to F.B.G. T.J. is a Howard Hughes Investigator and a Daniel K. Ludwig Scholar.

## References

- Beck F, Stringer EJ. 2010. The role of Cdx genes in the gut and in axial development. *Biochem Soc Trans* **38**: 353–357.
- Ben-Porath I, Thomson MW, Carey VJ, Ge R, Bell GW, Regev A, Weinberg RA. 2008. An embryonic stem cell-like gene expression signature in poorly differentiated aggressive human tumors. *Nat Genet* **40**: 499–507.
- Besnard V, Wert SE, Hull WM, Whitsett JA. 2004. Immunohistochemical localization of Foxa1 and Foxa2 in mouse embryos and adult tissues. *Gene Expr Patterns* **5**: 193–208.
- Cejudo-Martin P, Yuen A, Vlahovich N, Lock P, Courtneidge SA, Diaz B. 2014. Genetic disruption of the Sh3pxd2a gene reveals an essential role in mouse development and the existence of a novel isoform of Tks5. *PLoS One* **9**: e107674.
- DuPage M, Dooley AL, Jacks T. 2009. Conditional mouse lung cancer models using adenoviral or lentiviral delivery of Cre recombinase. *Nat Protoc* **4**: 1064–1072.
- Grimminger P, Ling FC, Neiss S, Vallböhmer D, Lurje G, Schneider PM, Hölscher AH, Metzger R, Brabender J. 2009. The role of the homeobox genes BFT and CDX2 in the pathogenesis of non-small cell lung cancer. *Anticancer Res* **29**: 1281–1286.
- Guo RJ, Suh ER, Lynch JP. 2004. The role of Cdx proteins in intestinal development and cancer. *Cancer Biol Ther* **3**: 593–601.
- Jackson E, Willis N, Mercer K, Bronson R, Crowley D, Montoya R, Jacks T, Tuveson D. 2001. Analysis of lung tumor initiation and progression using conditional expression of oncogenic K-ras. *Gene Dev* **15**: 3243–3248.
- Jackson E, Olive K, Tuveson D, Bronson R, Crowley D, Brown M, Jacks T. 2005. The differential effects of mutant p53 alleles on advanced murine lung cancer. *Cancer Res* **65**: 10280–10288.
- Kaestner KH. 2010. The FoxA factors in organogenesis and differentiation. *Curr Opin Genet Dev* **20**: 527–532.
- Kho AT, Zhao Q, Cai Z, Butte AJ, Kim JYH, Pomeroy SL, Rowitch DH, Kohane IS. 2004. Conserved mechanisms across development and tumorigenesis revealed by a mouse development perspective of human cancers. *Gene Dev* **18**: 629–640.
- Kimura S, Hara Y, Pineau T, Fernandez-Salguero P, Fox CH, Ward JM, Gonzalez FJ. 1996. The T/ebp null mouse: thyroid-specific enhancer-binding protein is essential for the organogenesis of the thyroid, lung, ventral forebrain, and pituitary. *Gene Dev* **10**: 60–69.
- Kopantzev EP, Monastyrskaya GS, Vinogradova TV, Zinovyeva MV, Kostina MB, Filyukova OB, Tonevitsky AG, Sukhikh GT, Sverdlov ED. 2008. Differences in gene expression levels between early and later stages of human lung development are opposite to those between normal lung tissue and non-small lung cell carcinoma. *Lung Cancer* **62**: 23–34.
- Li CM-C, Chen G, Dayton TL, Kim-Kiselak C, Hoersch S, Whittaker CA, Bronson RT, Beer DG, Winslow MM, Jacks T. 2013. Differential Tks5 isoform expression contributes to metastatic invasion of lung adenocarcinoma. *Gene Dev* **27**: 1557–1567.
- Liu H, Kho AT, Kohane IS, Sun Y. 2006. Predicting survival within the lung cancer histopathological hierarchy using a multi-scale genomic model of development. *PLoS Med* **3**: e232.
- Matsumoto K, Mizoshita T, Tsukamoto T, Ogasawara N, Hirata A, Shimizu Y, Haneda M, Yamao K, Tatematsu M. 2004. Cdx2 expression in pancreatic tumors: relationship with prognosis of invasive ductal carcinomas. *Oncol Rep* **12**: 1239–1243.
- Minoo P, Su G, Drum H, Bringas P, Kimura S. 1999. Defects in tracheoesophageal and lung morphogenesis in Nkx2.1<sup>-/-</sup> mouse embryos. *Dev Biol* **209**: 60–71.
- Mizoshita T, Tsukamoto T, Nakanishi H, Inada K-I, Ogasawara N, Joh T, Itoh M, Yamamura Y, Tatematsu M. 2003. Expression of Cdx2 and the phenotype of advanced gastric cancers: relationship with prognosis. *J Cancer Res Clin* **129**: 727–734.
- Murphy DA, Courtneidge SA. 2011. The ‘ins’ and ‘outs’ of podosomes and invadopodia: characteristics, formation and function. *Nat Rev Mol Cell Biol* **12**: 413–426.
- Paz H, Pathak N, Yang J. 2014. Invading one step at a time: the role of invadopodia in tumor metastasis. *Oncogene* **33**: 4193–4202.
- Sato M, Shames DS, Hasegawa Y. 2012. Emerging evidence of epithelial-to-mesenchymal transition in lung carcinogenesis. *Respirology* **17**: 1048–1059.
- Snyder EL, Watanabe H, Magendantz M, Hoersch S, Chen TA, Wang DG, Crowley D, Whittaker CA, Meyerson M, Kimura S, et al. 2013. Nkx2-1 represses a latent gastric differentiation program in lung adenocarcinoma. *Mol Cell* **50**: 185–199.
- Steeg PS. 2006. Tumor metastasis: mechanistic insights and clinical challenges. *Nat Med* **12**: 895–904.
- Subramanian A, Tamayo P, Mootha VK, Mukherjee S, Ebert BL, Gillette MA, Paulovich A, Pomeroy SL, Golub TR, Lander ES, et al. 2005. Gene set enrichment analysis: a knowledge-based approach for interpreting genome-wide expression profiles. *Proc Natl Acad Sci* **102**: 15545–15550.
- Thiery JP, Acloque H, Huang RYJ, Nieto MA. 2009. Epithelial-mesenchymal transitions in development and disease. *Cell* **139**: 871–890.
- Tsai JH, Yang J. 2013. Epithelial-mesenchymal plasticity in carcinoma metastasis. *Gene Dev* **27**: 2192–2206.
- Wan H, Kaestner KH, Ang S-L, Ikegami M, Finkelman FD, Stahlman MT, Fulkerson PC, Rothenberg ME, Whitsett JA. 2004.



Li et al.

- Foxa2 regulates alveolarization and goblet cell hyperplasia. *Development* **131**: 953–964.
- Wan H, Dingle S, Xu Y, Besnard V, Kaestner KH, Ang S-L, Wert S, Stahlman MT, Whitsett JA. 2005. Compensatory roles of Foxa1 and Foxa2 during lung morphogenesis. *J Biol Chem* **280**: 13809–13816.
- Winslow MM, Dayton TL, Verhaak RGW, Kim-Kiselak C, Snyder EL, Feldser DM, Hubbard DD, Dupage MJ, Whittaker CA, Hoersch S, et al. 2011. Suppression of lung adenocarcinoma progression by Nkx2-1. *Nature* **473**: 101–104.
- Wyckoff JB, Segall JE, Condeelis JS. 2000. The collection of the motile population of cells from a living tumor. *Cancer Res* **60**: 5401–5404.
- Wyckoff J, Gligorijevic B, Entenberg D, Segall J, Condeelis J. 2011. High-resolution multiphoton imaging of tumors in vivo. *Cold Spring Harb Protoc* **2011**: 1167–1184.
- Yatabe Y, Koga T, Mitsudomi T, Takahashi T. 2004. CK20 expression, CDX2 expression, K-ras mutation, and goblet cell morphology in a subset of lung adenocarcinomas. *J Pathol* **203**: 645–652.
- Yuasa Y. 2003. Control of gut differentiation and intestinal-type gastric carcinogenesis. *Nat Rev Cancer* **3**: 592–600.
- Zhou L, Dey CR, Wert SE, Yan C, Costa RH, Whitsett JA. 1997. Hepatocyte nuclear factor-3 $\beta$  limits cellular diversity in the developing respiratory epithelium and alters lung morphogenesis in vivo. *Dev Dyn* **210**: 305–314.



## Foxa2 and Cdx2 cooperate with Nkx2-1 to inhibit lung adenocarcinoma metastasis

Carman Man-Chung Li, Vasilena Gocheva, Madeleine J. Oudin, et al.

*Genes Dev.* 2015 29: 1850-1862

Access the most recent version at doi:[10.1101/gad.267393.115](https://doi.org/10.1101/gad.267393.115)

---

### Supplemental Material

<http://genesdev.cshlp.org/content/suppl/2015/09/04/29.17.1850.DC1.html>

### References

This article cites 34 articles, 12 of which can be accessed free at:  
<http://genesdev.cshlp.org/content/29/17/1850.full.html#ref-list-1>

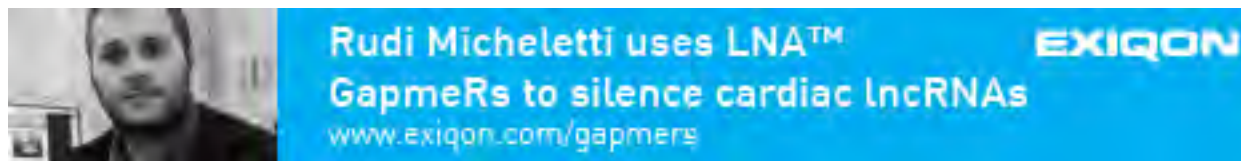
### Creative Commons License

This article is distributed exclusively by Cold Spring Harbor Laboratory Press for the first six months after the full-issue publication date (see <http://genesdev.cshlp.org/site/misc/terms.xhtml>). After six months, it is available under a Creative Commons License (Attribution-NonCommercial 4.0 International), as described at <http://creativecommons.org/licenses/by-nc/4.0/>.

### Email Alerting Service

Receive free email alerts when new articles cite this article - sign up in the box at the top right corner of the article or [click here](#).

---



---

To subscribe to *Genes & Development* go to:  
<http://genesdev.cshlp.org/subscriptions>

---

# PTP1B-dependent regulation of receptor tyrosine kinase signaling by the actin-binding protein Mena

Shannon K. Hughes<sup>a,b,\*</sup>, Madeleine J. Oudin<sup>a,\*</sup>, Jenny Tadros<sup>a</sup>, Jason Neil<sup>a</sup>, Amanda Del Rosario<sup>a</sup>, Brian A. Joughin<sup>a,b</sup>, Laila Ritsma<sup>c</sup>, Jeff Wyckoff<sup>d</sup>, Eliza Vasile<sup>a</sup>, Robert Eddy<sup>d</sup>, Ulrike Philipp<sup>a,†</sup>, Alisha Lussiez<sup>a</sup>, John S. Condeelis<sup>d</sup>, Jacco van Rhee<sup>c</sup>, Forest White<sup>a,b</sup>, Douglas A. Lauffenburger<sup>a,b</sup>, and Frank B. Gertler<sup>a,e</sup>

<sup>a</sup>Koch Institute for Integrative Cancer Research, <sup>b</sup>Department of Biological Engineering, and <sup>e</sup>Department of Biology, Massachusetts Institute of Technology, Cambridge, MA 02139; <sup>c</sup>Cancer Genomics Netherlands–Hubrecht Institute–KNAW and University Medical Centre Utrecht, 3584 CX Utrecht, Netherlands; <sup>d</sup>Department of Anatomy and Structural Biology, Albert Einstein College of Medicine, New York, NY 10461

**ABSTRACT** During breast cancer progression, alternative mRNA splicing produces functionally distinct isoforms of Mena, an actin regulator with roles in cell migration and metastasis. Aggressive tumor cell subpopulations express Mena<sup>INV</sup>, which promotes tumor cell invasion by potentiating EGF responses. However, the mechanism by which this occurs is unknown. Here we report that Mena associates constitutively with the tyrosine phosphatase PTP1B and mediates a novel negative feedback mechanism that attenuates receptor tyrosine kinase signaling. On EGF stimulation, complexes containing Mena and PTP1B are recruited to the EGFR, causing receptor dephosphorylation and leading to decreased motility responses. Mena also interacts with the 5' inositol phosphatase SHIP2, which is important for the recruitment of the Mena-PTP1B complex to the EGFR. When Mena<sup>INV</sup> is expressed, PTP1B recruitment to the EGFR is impaired, providing a mechanism for growth factor sensitization to EGF, as well as HGF and IGF, and increased resistance to EGFR and Met inhibitors in signaling and motility assays. In sum, we demonstrate that Mena plays an important role in regulating growth factor-induced signaling. Disruption of this attenuation by Mena<sup>INV</sup> sensitizes tumor cells to low-growth factor concentrations, thereby increasing the migration and invasion responses that contribute to aggressive, malignant cell phenotypes.

## Monitoring Editor

Alpha Yap  
University of Queensland

Received: Jun 29, 2015

Revised: Aug 21, 2015

Accepted: Aug 25, 2015

This article was published online ahead of print in MBoC in Press (<http://www.molbiolcell.org/cgi/doi/10.1091/mbc.E15-06-0442>) on September 2, 2015.

Address correspondence to: Douglas A. Lauffenburger ([lauffen@mit.edu](mailto:lauffen@mit.edu)); Frank B. Gertler ([fgertler@mit.edu](mailto:fgertler@mit.edu)).

\*These authors contributed equally to this work.

<sup>†</sup>Present address: Janssen Research and Development Oncology, 2340 Beerse, Belgium.

S.K.H. and M.J.O. designed and performed experiments, performed data analysis, and prepared the manuscript. F.B.G. guided overall experimental design and prepared the manuscript. J.T. performed *in vitro* binding assays, J.N. performed mass spectrometry, L.R. performed PIP2 and actin-cofilin FRET assays, J.C. and J.v.R. interpreted FRET experiments, J.B.W. and J.C. contributed the *in vivo* invasion assay, U.P. and J.T. performed Mena-SHIP2 coIP, and A.L. supported PLA assays. A.D.R. and B.A.J. analyzed mass spectrometry data. J.C., J.v.R., F.W., and D.A.L. guided experimental design and commented on the manuscript.

Conflict of interest: J.J., J.C., and F.G. are compensated members of the scientific advisory board of MetaStat (Boston, MA). No funding was provided by MetaStat for this work.

Abbreviations used: CME, clathrin-mediated endocytosis; ECM, extracellular matrix; EGF, epidermal growth factor; EGFR, epidermal growth factor receptor; EVH, Ena/Vasp homology; GFP, green fluorescent proteins; GST, glutathione-S-transferase; HGF, hepatocyte growth factor; IGF, insulin growth factor; IGFR, insulin growth factor receptor; Immuno-EM, immuno-electron microscopy; IP, immuno-precipitation; LC-MS/MS, liquid chromatography tandem mass spectrometry; Lpd, lamellipodin; PLA, proximity ligation assay; PLCγ, phospholipase C gamma; RTK, receptor tyrosine kinase; TKI, tyrosine kinase inhibitor; TMEM, tumor microenvironment of metastasis.

© 2015 Hughes, Oudin, et al. This article is distributed by The American Society for Cell Biology under license from the author(s). Two months after publication it is available to the public under an Attribution–Noncommercial–Share Alike 3.0 Unported Creative Commons License (<http://creativecommons.org/licenses/by-nc-sa/3.0>).

"ASCB®," "The American Society for Cell Biology®," and "Molecular Biology of the Cell®" are registered trademarks of The American Society for Cell Biology.

## INTRODUCTION

Tumor initiation, growth, and malignant progression are governed by interactions between cancer cells and their microenvironment (Hanahan and Weinberg, 2011). Aggressive, invasive cancer cells exit the primary tumor in response to growth factors, extracellular matrix (ECM) proteins, and other signals that cause them to invade surrounding tissue. After extravasation, invasive cells migrate to and enter blood or lymphatic vessels and are transported to sites of metastasis (Joyce and Pollard, 2009). Invading cells encounter numerous signals that trigger multiple intracellular pathways, whose activity is integrated to evoke appropriate, spatiotemporally coordinated responses. Tumor cell migration within this complex microenvironment requires continuous, coordinated cytoskeletal remodeling, which matches corresponding dynamic changes in cell–matrix and cell–cell adhesion (Bear and Haugh, 2014). Although distinct tumor cell migration modalities have been described (Petrie and Yamada, 2012), motility is typically initiated by rapid actin polymerization-driven membrane protrusion in response to acute activation of epidermal growth factor receptor (EGFR) and other receptor tyrosine kinases (RTKs; Nürnberg et al., 2011; Roussos et al., 2011b). Many aspects of RTK-regulated actin remodeling have been established (Bear and Haugh, 2014), but little is known about whether, or how, actin networks provide feedback to RTKs.

The Mena protein acts via multiple processes that are important for tumor cell invasion and metastasis: actin polymerization, adhesion, and EGF-elicited motility responses (Gertler and Condeelis, 2011). Mena and the related vasodilator-stimulated phosphoprotein (VASP) and EVL proteins are members of the Ena/VASP family, which increase F-actin elongation rates and delay the termination of filament growth by capping proteins (Bear and Gertler, 2009; Hansen and Mullins, 2010; Breitsprecher et al., 2011). Ena/VASP proteins localize primarily to lamellipodia and filopodia and sites of cell–matrix and cell–cell adhesion (Pula and Krause, 2008). They contain two highly conserved regions—an N-terminal Ena/VASP homology (EVH) 1 domain and a C-terminal EVH2 domain—as well as a central polyproline-rich core. The EVH1 domain mediates protein–protein interactions and typically binds to molecules via a conserved proline-rich motif (Ball et al., 2002). The EVH2 domain harbors actin-binding motifs and a coiled-coil that mediates formation of stable Ena/VASP tetramers (Pula and Krause, 2008). Mena also contains an LERER repeat region not found in other Ena/VASP proteins, and multiple functionally distinct Mena isoforms are produced from alternatively spliced Mena mRNAs (Gertler and Condeelis, 2011).

Mena is up-regulated in breast cancers and other solid tumor types (Gertler and Condeelis, 2011). The aggressive mortality, morbidity, and metastatic burden associated with the polyoma middle T antigen–mouse mammary tumor virus transgenic mouse breast cancer model is almost fully eliminated by genetic ablation of Mena; Mena deficiency does not affect tumor formation or growth but does slow progression and decreases tumor cell invasion, intravasation, and metastasis (Roussos et al., 2010). Highly migratory and invasive tumor cell subpopulations produce Mena mRNAs that contain a 57-nucleotide, alternately included exon (designated INV) to produce Mena<sup>INV</sup> (Gertler and Condeelis, 2011). Further, Mena<sup>INV</sup> mRNA levels in biopsies correlate with the density of Tumor Microenvironment of Metastasis (Roussos et al., 2011c; Pignatelli et al., 2014), a prognostic indicator of metastatic risk that consists of a Mena-expressing carcinoma cell, an endothelial cell, and a macrophage that are all in contact (Robinson et al., 2009; Rohan et al., 2014). Mena<sup>INV</sup> has effects on tumor cell behavior that are potent but differ from those of Mena in magnitude, type, or both (Gertler and Condeelis, 2011). Ectopic Mena<sup>INV</sup> sensitizes carcinoma cells to

EGF and allows them to extend lamellipodia, chemotax, or invade in response to significantly lower concentrations of EGF than required for similar responses by control cells (Philippart et al., 2008; Roussos et al., 2011a). Ectopic Mena<sup>INV</sup> also increases invasion, intravasation, and lung metastasis from xenograft mammary tumors. The mechanisms underlying Mena<sup>INV</sup>-driven increases in metastatic potential and tumor cell sensitivity to EGF are unknown.

Here we show that Mena participates in a mechanism that attenuates RTK signaling by interacting with the tyrosine phosphatase PTP1B and the 5' inositol phosphatase SHIP2. Expression of Mena<sup>INV</sup> disrupts this regulation and results in a prometastatic phenotype characterized by increased RTK/activation signaling from low ligand stimulation and decreased sensitivity to targeted RTK inhibitors. Overall our findings explain why Mena<sup>INV</sup>-expressing tumor cells display enhanced sensitivity to several growth factors both in vitro and in vivo.

## RESULTS

### Mena<sup>INV</sup> increases sensitivity to ligands for specific RTKs and confers resistance to targeted kinase inhibitors

Although Mena<sup>INV</sup> is expressed robustly in aggressive tumor cell populations harvested from rodent mammary carcinomas, and in biopsies of human breast cancer patients, we have been unable to identify immortalized breast cancer cell lines that express more than trace amounts of the Mena<sup>INV</sup> mRNA or protein. Thus, to facilitate analysis of the mechanism of Mena<sup>INV</sup>-dependent growth factor sensitization, we used human cell lines that ectopically express green fluorescent protein (GFP)–Mena, GFP–Mena<sup>INV</sup>, or GFP alone. Mena was found to be upregulated ~10-fold at the RNA level in invasive tumor cells collected from primary xenograft tumors, and therefore we engineered our cells to express levels roughly comparable to those seen in invasive cells from primary tumors (Wang et al., 2004; Supplemental Figure S1). As expected, Mena<sup>INV</sup>-expressing cells invaded further into three-dimensional (3D) collagen gels (Figure 1A). When looking at lamellipodial protrusion, an assay that has been described as accurately predicting 3D invasion responses (Meyer et al., 2012), we found that Mena<sup>INV</sup>-expressing cells exhibited increased lamellipodial protrusion in response to fourfold-lower EGF concentrations than required to elicit similar responses by GFP control cells (Figure 1B). Supplemental Figure S2 shows representative images of cells treated with EGF in this assay. Our engineered human cell lines thus faithfully replicate our previously published results demonstrating that ectopic expression of Mena<sup>INV</sup> in rat MTLn3 mammary adenocarcinoma cells enhanced protrusion responses elicited by stimulation with low EGF concentrations (Philippart et al., 2008).

In addition to EGF, other growth factors can drive tumor invasion and metastasis. We thus asked whether Mena<sup>INV</sup> also increased sensitivity to three other breast cancer-relevant growth factors—insulin-like growth factor (IGF), hepatic growth factor (HGF), and neuregulin 1 (NRG1; Friedl and Alexander, 2011)—using the lamellipodial protrusion assay. Similar to the sensitization seen with EGF, ectopic GFP–Mena<sup>INV</sup> enabled MDA-MB231 cells to extend lamellipodia when stimulated with significantly lower IGF and HGF concentrations (20- and 5-fold, respectively) than required for similar responses by control cells (Figure 1, C and D). GFP–Mena-expressing cells exhibited approximately twofold increase in response to IGF and HGF (as well as EGF); however, these effects were modest compared with those induced by GFP–Mena<sup>INV</sup> (Figure 1, A–D). Thus Mena<sup>INV</sup> expression evokes enhanced tumor cell responses, which are mediated by at least three RTKs relevant to breast cancer progression: EGFR, IGFR, and Met (receptors for EGF, IGF, and HGF,



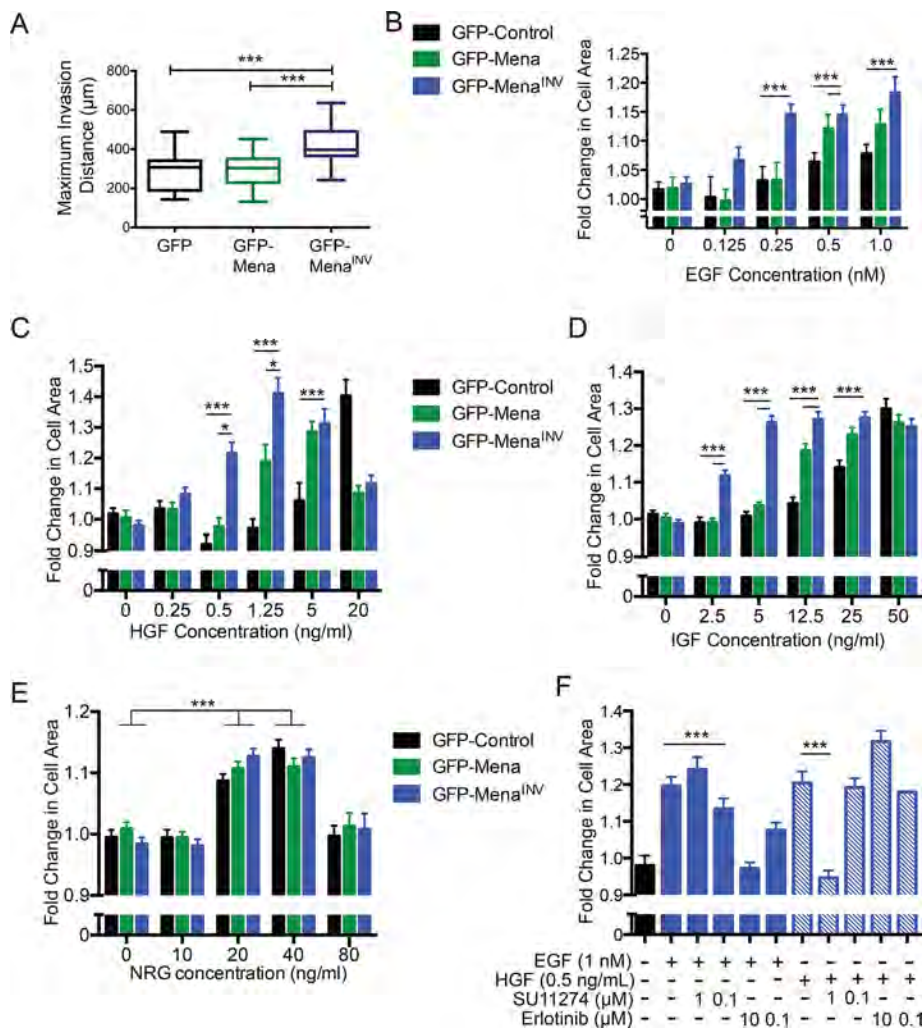


**FIGURE 1:** Mena<sup>INV</sup> expression confers sensitivity to select growth factors. (A) Invasion distance into 2 mg/ml collagen gel in full serum medium, using high-throughput 3D collagen invasion Iuvo platform (Bellbrook Labs) of MDA-MB231 cells expressing different Mena isoforms. \*\*\* $p < 0.001$  by nonparametric Kruskal–Wallis test and Dunn’s multiple-comparison test. (B) Dose-response of lamellipodial protrusion in MDA-MB231 cells, reflected by fold change in cell area 8 min after addition of EGF. Results shown as mean  $\pm$  SEM. Asterisks indicate significant difference by nonparametric Kruskal–Wallis test and Dunn’s multiple-comparison test, with comparisons indicated by lines above; 35–158 cells/condition. (C–E) Dose-response of lamellipodial protrusion in MDA-MB231 cells, reflected by fold change in cell area 8 min after addition of IGF (C), HGF (D), or NRG (E). Results shown as mean  $\pm$  SEM. Asterisks indicate significant difference by nonparametric Kruskal–Wallis test and Dunn’s multiple-comparison test, with comparisons indicated by lines above; 35–158 cells/condition. (F) Lamellipodial protrusion dose-response 8 min after costimulation with 1 nM EGF or 0.5 ng/ml HGF and SU11274 or erlotinib, respectively. Significance measured by nonparametric Kruskal–Wallis test and Dunn’s multiple-comparison test; \* $p < 0.05$ , \*\*\* $p < 0.001$  as indicated. See also Supplemental Figures S1 and S2.

respectively; Alexander and Friedl, 2012). Note, however, that the response to NRG1, a ligand for HER3 and HER4, was unaffected by ectopic GFP-Mena or GFP-Mena<sup>INV</sup> (Figure 1E), indicating that the potentiating effects of Mena<sup>INV</sup> on RTK ligand sensitivity specifically affect only a subset of RTK signaling pathways. Because activation of Met by HGF decreases the efficacy of EGFR TKIs (Suda et al., 2010; Gusenbauer et al., 2013), we asked whether the Mena<sup>INV</sup>-mediated sensitivity to EGF and HGF involved cross-talk between the two receptors. Inhibition of EGFR using the EGFR tyrosine kinase inhibitor (TKI) erlotinib or of Met using the Met-TKI inhibitor

SU11274 in Mena<sup>INV</sup>-expressing cells had no effect on lamellipodial protrusion in response to HGF or EGF, respectively, indicating that the increased sensitivity to EGF and HGF observed in GFP-Mena<sup>INV</sup>-expressing cells was receptor specific (Figure 1F).

To analyze the effects of Mena<sup>INV</sup> on targeted RTK inhibitors, we performed dose-response experiments using the EGFR TKI erlotinib and the Met-TKI SU11274. Cells expressing GFP-Mena<sup>INV</sup> were resistant to at least 10-fold-greater inhibitor than required to block lamellipodial protrusion in GFP control cells (Figure 2, A and B). Collectively these data indicate that Mena<sup>INV</sup> confers increases in ligand sensitivity for responses by EGFR, Met, and IGF, as well as in resistance to EGFR- and Met- targeted TKIs.

### Mena<sup>INV</sup> dysregulates tyrosine kinase signaling

To address whether cell behaviors influenced by the Mena<sup>INV</sup>-induced increase in EGF sensitivity and resistance to erlotinib arise from increased actin polymerization (a process that is directly modulated by Mena), by a specific effect on EGFR pathway function, or both, we used anti-pY1173 antibodies to measure EGFR phosphorylation levels. We observed increased phosphorylation in cells expressing Mena<sup>INV</sup> compared with those expressing equivalent levels of ectopic Mena or GFP (Figure 3, A and B). Similarly, expression of Mena<sup>INV</sup> in a second triple-negative breast cancer cell line, BT-549, also significantly increased EGFR phosphorylation at Y1173 (Supplemental Figure S3). Despite the significant differences in magnitude, the relative kinetics of EGFR phosphorylation were similar across the cell lines stimulated with 0.25 nM EGF (Figure 3C) and mirrored the kinetics of membrane protrusion in MDA-MB-231 cells expressing Mena<sup>INV</sup>. Measurement of EGFR abundance and internalization indicated that the Mena<sup>INV</sup>-driven increase in EGFR phosphorylation was not attributable to increased total EGFR protein level or altered receptor internalization (Figure 3, D and E). Whereas Mena<sup>INV</sup>

expression induced a small (<10%) increase in surface levels of EGFR (Figure 3F), this minor increase is unlikely to account for the observed Mena<sup>INV</sup>-dependent enhanced response to EGF, given that an ~10-fold increase in total EGFR level is required to increase lamellipodial protrusion detectably at the EGF concentrations tested (Bailey et al., 2000). Furthermore, no apparent changes in EGFR clustering or spacing were evident in immuno-electron microscopy analyses (unpublished data). Overall these data indicate that the increased sensitivity to EGF conferred by Mena<sup>INV</sup> expression is unlikely to arise through changes in EGFR abundance or distribution.

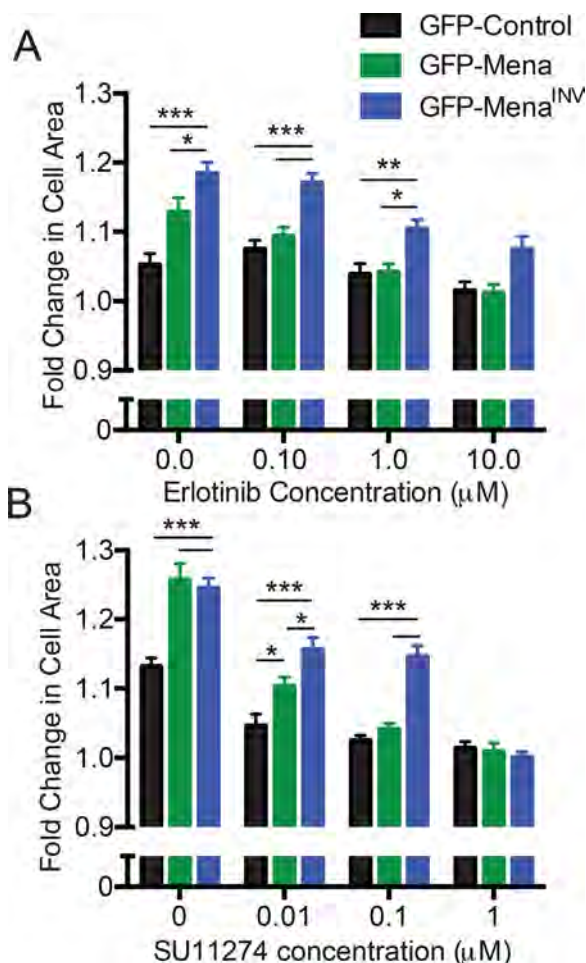


**FIGURE 2:** Mena<sup>INV</sup> expression confers resistance to targeted kinase inhibitors. (A) Lamellipodial protrusion response after stimulation with 1 nM EGF and increasing erlotinib doses. Fold change in cell area calculated 8 min poststimulation. Results shown as mean  $\pm$  SEM; 16–48 cells/condition. Asterisks indicate significant difference by two-way analysis of variance (ANOVA). (B) Lamellipodial protrusion dose-response after costimulation with 0.5 ng/ml HGF and increasing SU11274. Fold change in cell area calculated 8 min poststimulation. Results shown as shown as mean  $\pm$  SEM; 39–71 cells/condition. Asterisks indicate significant difference by two-way ANOVA; \* $p < 0.05$ , \*\* $p < 0.01$ , and \*\*\* $p < 0.001$  as indicated.

We reasoned that the ligand-dependent RTK activation that leads to Mena<sup>INV</sup>-induced increases in membrane protrusion should be reflected in increased activity of downstream signaling pathways that mediate the protrusion. Analysis of several canonical signaling components downstream of EGFR (such as Erk and Akt) revealed no obvious effect of Mena<sup>INV</sup> on their activities despite increased activation of the receptor itself (Philippart *et al.*, 2008). In breast cancer cells, the actin polymerization needed for EGF-elicited protrusion is initiated by the phospholipase C  $\gamma$  (PLC $\gamma$ )–cofilin pathway (van Rheenen *et al.*, 2007); therefore we asked whether EGFR-dependent activation of PLC $\gamma$  enzymatic activity is altered by Mena<sup>INV</sup>. PLC $\gamma$  activity can be quantified in living cells by measuring the abundance of its substrate, phosphatidylinositol 4,5-bisphosphate (PI(4,5)P<sub>2</sub>), using monomeric red fluorescent protein (mRFP)–PLC $\delta$ -PH, a reporter that is localized to the plasma membrane by binding to PI(4,5)P<sub>2</sub> and is released into the cytosol upon its hydrolysis (van Rheenen *et al.*, 2007). MDA-MB231 cells were unsuitable for this assay due to sensitivity to

expression of mRFP-PLC $\delta$ -PH; thus we performed the assay in MTLn3 mammary adenocarcinoma cell lines, which we used for our initial characterization of Mena<sup>INV</sup>-dependent effects on metastasis (Philippart *et al.*, 2008). Mena<sup>INV</sup> expression increased both PI(4,5)P<sub>2</sub> hydrolysis (Figure 3G) and cofilin activity (Figure 3H) in response to significantly less EGF than required to trigger similar responses in GFP control cells. Consistent with these data, Mena<sup>INV</sup>-expressing cells required 10-fold more erlotinib than controls to decrease ligand-induced EGFR phosphorylation significantly (Figure 3I). We conclude that Mena<sup>INV</sup> potentiates EGF-elicited responses by increasing the activity of EGFR-mediated signaling pathways that are upstream of, and are required for, the initiation of actin polymerization.

### Mena may associate with the tyrosine phosphatase PTP1B

Because abundance, surface levels, or internalization of EGFR did not account for the Mena<sup>INV</sup>-dependent increases in receptor phosphorylation and downstream signaling, we investigated other mechanisms that could increase RTK phosphorylation at a low ligand concentration. Activated RTKs cycle rapidly between phosphorylation and dephosphorylation; the half-life of EGFR tyrosine phosphorylation is  $\sim$ 10–30 s (Kleiman *et al.*, 2011). Changes in the balance of this rapid cycling are believed to control receptor sensitivity to ligand by altering net kinase activity. We hypothesized that Mena<sup>INV</sup>-dependent increases in ligand sensitivity could arise via increased net receptor phosphorylation due to dysregulation of a phosphatase. The tyrosine phosphatase PTP1B (PTPN1) regulates EGFR, IGFR, and MET-mediated signaling responses (Haj *et al.*, 2003; Sangwan *et al.*, 2011), and, given that Mena<sup>INV</sup> sensitizes responses to ligands of all three RTKs (Figure 1), we asked whether Mena is involved in PTP1B regulation.

PTP1B contains the sequence LEPPPEHIPP, with similarities to the consensus EVH1-binding motif ([F/L/W/PX $\phi$ ]<sub>2</sub>); X = any residue,  $\phi$  = any hydrophobic residue; Ball *et al.*, 2002; Pula and Krause, 2008), raising the possibility that PTP1B binds to Mena through its EVH1 domain and thereby allows Mena/Mena<sup>INV</sup> to modulate RTK dephosphorylation. We used purified, recombinant glutathione S-transferase (GST)–PTP1B and His-Mini-Mena proteins to test whether PTP1B can bind Mena directly. Immobilized GST-PTP1B, but not the immobilized control GST protein, bound to soluble, purified His-Mini-Mena in vitro (Figure 4A). To determine whether endogenous Mena and PTP1B are present in protein complexes in situ, we used proximity ligation assays (PLAs). To confirm the specificity of the assay, we performed control PLAs using only one antibody or in Mena<sup>−/−</sup> cells (Supplemental Figure S4, A and B), which significantly reduced the detected PLA signal. Furthermore, transient knockdown of PTP1B expression in MDA-MB231 cells also reduced the Mena-PTP1B PLA signal, further supporting the specificity of this assay for Mena/PTP1B-containing complexes (Supplemental Figure S4, C–E). Significant PLA signal between Mena and PTP1B was observed in MDA-MB231 cells and was unchanged by EGF stimulation, indicating that Mena and PTP1B are in complex independent of EGFR signaling (Figure 4B). Quantification of Mena-PTP1B PLA signal abundance across four human breast cancer cell lines revealed that the amount of Mena-PTP1B PLA signal was correlated with PTP1B expression levels (Figure 4, C–E). The extremely low levels of Mena<sup>INV</sup> normally expressed in cultured cell lines precluded use of PLA to determine whether endogenous Mena<sup>INV</sup> is present in complexes with PTP1B. These results, however, demonstrate that PTP1B and Mena can directly bind each other in vitro and that complexes containing endogenously expressed Mena and PTP1B can be detected within breast cancer cells by PLA.



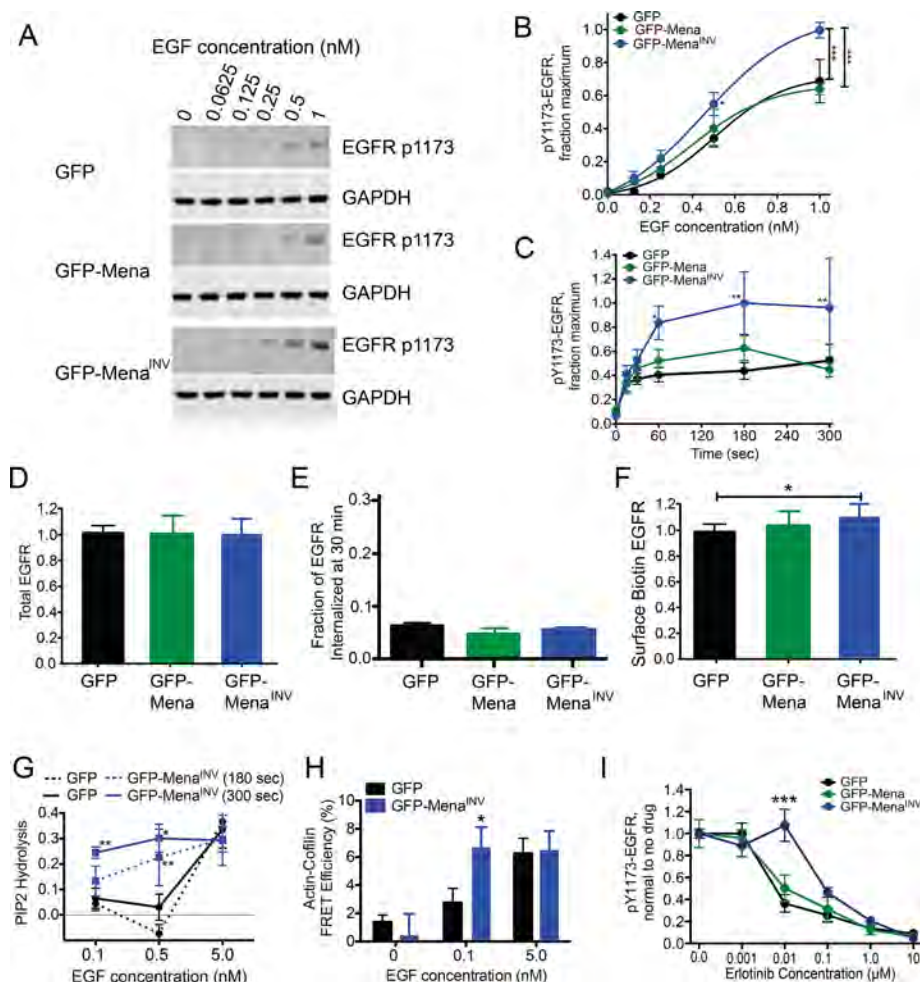


**FIGURE 3:** Mena<sup>INV</sup> expression does not affect EGFR presentation but increases signaling pathway activation at low levels of EGF. (A) Representative Western blot of MDA-MB231 cells expressing GFP, GFP-Mena, or GFP-Mena<sup>INV</sup> stimulated after bolus stimulation with EGF for 3 min. (B) Quantification of EGFR phosphorylation at Y1173 shown in A by densitometry. Results are mean  $\pm$  SD; three experiments. Asterisks indicate significant difference by ANOVA with Tukey multiple-comparison test (\* $p$  < 0.05 vs. MDA-MB231-GFP cells, \*\*\* $p$  < 0.001). (C) Time course of EGFR phosphorylation at Y1173 in response to 0.25 nM EGF. Asterisks indicate significant difference by ANOVA with Tukey multiple-comparison test (\* $p$  < 0.05 vs. MDA-MB231-GFP cells at 0.5 nM or \*\* $p$  < 0.01 vs. conditions indicated by bar). (D) Total EGFR protein normalized to GFP control measured by ELISA.  $n$  > 10 for each bar in MDA-MB231 cells. Data shown as mean  $\pm$  SD. (E) Fraction of total EGFR internalized at basal (no EGF) conditions in serum-free medium after 30 min at 37°C. Data shown as mean  $\pm$  range;  $n$  = 2. (F) Membrane level of EGFR measured by biotin labeling of surface proteins, EGFR capture ELISA, and detection of protein by HRP-labeled streptavidin in MDA-MB231 cells. Data normalized to GFP control cells in each experiment. Data shown as mean  $\pm$  SD;  $n$  > 10 for each bar. (G) Fraction of PI(4,5)P2 lost from the cell membrane at specified time after EGF stimulation, measured using PLC $\delta$ -PH domain FRET assay in MTLn3 cells. \* $p$  < 0.05 and \*\* $p$  < 0.01 vs. GFP at respective time point using ANOVA with Tukey posttest. (H) Cofilin activity, reflected by the amount of cofilin bound to actin quantified by an antibody FRET assay 300 s after EGF stimulation in MTLn3 cells. \* $p$  < 0.05 vs. GFP at respective EGF concentration using two-tailed  $t$  test. (I) EGFR phosphorylation dose-response 3 min poststimulation with 1 nM EGF and increasing erlotinib in MDA-MB231 cells. Data shown as mean  $\pm$  SEM; \*\*\* $p$  < 0.001 vs. MDA-MB231-GFP and GFP-Mena by two-way ANOVA. See Supplemental Figure S3.

### Inhibition of PTP1B phosphatase activity phenocopies Mena<sup>INV</sup> expression

We next hypothesized that Mena<sup>INV</sup> decreases negative regulation of RTK activity by PTP1B and, thus, that specific inhibition of PTP1B will mimic some or all of the effects of Mena<sup>INV</sup> on EGF responses. Treatment with a specific PTP1B inhibitor increased membrane protrusion

in response to 0.25 nM EGF by both MDA-MB231-GFP-Mena<sup>INV</sup> and GFP-expressing control cells but not in MDA-MB231-GFP-Mena<sup>INV</sup> cells (Figure 5A). Therefore PTP1B inhibition mimics Mena<sup>INV</sup>-dependent increased sensitivity to EGF but cannot induce EGF responses of greater magnitude in cells expressing Mena<sup>INV</sup>. PTP1B inhibition also increased the magnitude and kinetics of membrane protrusion in parental MTLn3 cells in response to 0.5 nM EGF, confirming that the effects of PTP1B inhibition were not cell-type dependent (Supplemental Figure S5A). Further, PTP1B inhibition did not increase membrane protrusion in cells expressing Mena<sup>INV</sup> in response to 0.125 nM EGF (Supplemental Figure S5B), a concentration below the threshold required to elicit significant membrane protrusion or EGFR activation in Mena<sup>INV</sup>-expressing cells (Figure 1B), suggesting that PTP1B inhibition alone is not sufficient to drive membrane protrusion independently of EGFR activation.

We next asked whether decreasing PTP1B activity mimics the effects of Mena<sup>INV</sup> expression on EGF-dependent tumor cell invasion in vitro or in vivo. PTP1B inhibition increased EGF-elicited invasion of MDA-MB231-GFP and -GFP-Mena-expressing cells into collagen I gels but had no significant effect on cells expressing Mena<sup>INV</sup> (Figure 5B). Expression of Mena<sup>INV</sup> in xenografted tumor cells decreases the concentration of EGF required for efficient chemotaxis/invasion by 25-fold in vivo (Roussos et al., 2011a); we thus asked whether PTP1B inhibition similarly increases the EGF sensitivity of invading cells in tumors. Consistent with the in vitro assays, a dose-response analysis using the in vivo invasion assay (Wyckoff et al., 2000) on xenografts showed that PTP1B inhibition increased the sensitivity of control cells to EGF: maximal tumor cell invasion was elicited into needles containing 5 nM EGF, a fivefold-lower concentration than normally required for such a response (Figure 5C). Furthermore, PTP1B inhibition had no effect at any of the EGF concentrations assayed on invasion in xenograft tumors arising from Mena<sup>INV</sup>-expressing cells (Figure 5C). In sum, these data indicate that PTP1B inhibition mimics the effects of Mena<sup>INV</sup> on EGF-elicited motility, chemotaxis, and invasion in vitro and in vivo but does not increase EGF responses in cells that express Mena<sup>INV</sup>.

Because the effects of Mena<sup>INV</sup> on biophysical cell responses to EGF are mimicked by PTP1B inhibition, we asked whether Mena<sup>INV</sup> similarly dysregulated EGFR signaling. Pretreatment with PTP1B inhibitor increased EGFR Y1173 phosphorylation in control cells stimulated with 0.25 nM EGF but failed to increase Y1173 phosphorylation further in Mena<sup>INV</sup>-expressing cells (Figure 5D). In addition,

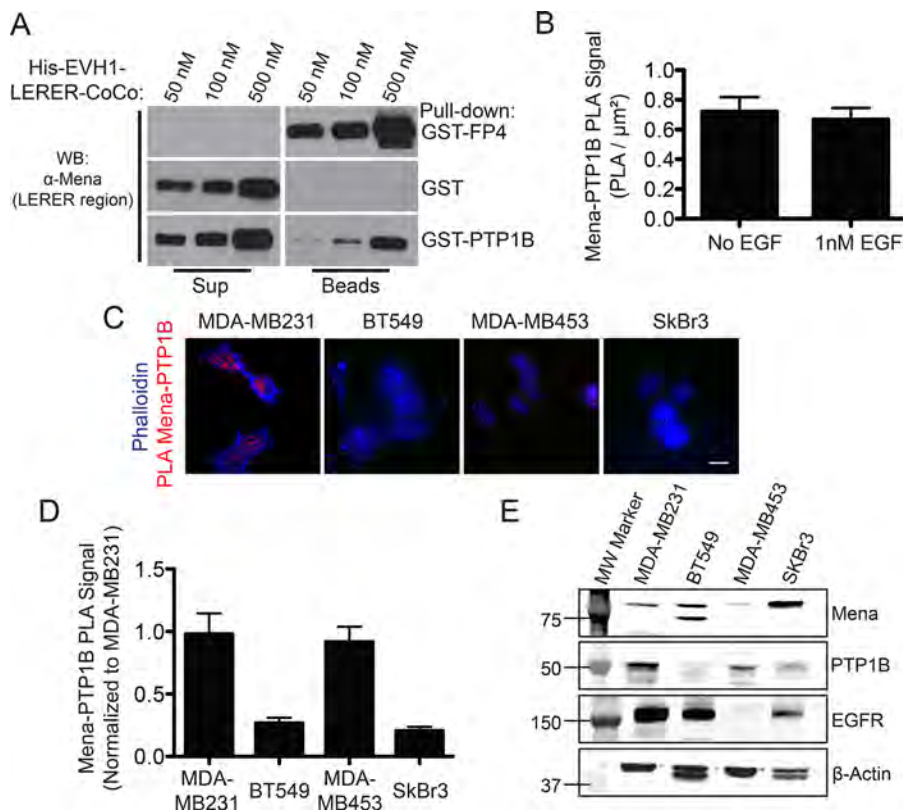


**FIGURE 4:** Mena interacts with PTP1B. (A) In vitro binding assay using immobilized GST-PTP1B and increasing concentrations of soluble His-Mini-Mena (containing Mena EVH1-LERER domains linked to the C-terminal coiled-coil; bottom lanes). Positive control with GST-FP4 (top lanes) and negative control with glutathione beads + GST alone (middle lanes) included to demonstrate assay specificity. Blots from representative experiment;  $n = 3$ . (B) Quantification of PLA for PTP1B and Mena in wild-type MDA-MB231  $\pm$  1 nM EGF for 60 s. Data shown as mean  $\pm$  SEM. Specificity of assay established using Mena<sup>-/-</sup> mouse embryonic fibroblasts, where background signal was negligible (data not shown). (C) Representative images for PTP1B-Mena PLA in four breast cancer cell lines: MDA-MB231, BT549, MDA-MB453, and SkBr3. (D) Mena-PTP1B PLA across four human breast cancer cell lines compared with signal measured in wild-type MDA-MB231 cells. Data shown as mean PLA/ $\mu\text{m}^2$  normalized to MDA-MB231  $\pm$  SEM (E) Western blot showing expression of Mena, PTP1B, and EGFR in four human breast cancer cell lines. See Supplemental Figure S4.

wild-type MTLn3 cells treated with the PTP1B inhibitor exhibited significantly greater PI(4,5)P<sub>2</sub> hydrolysis after EGF stimulation (Supplemental Figure S5C), similar to the increased PLC $\gamma$  activity exhibited by cells expressing Mena<sup>INV</sup> (Figure 3).

To identify other network participants that are dysregulated by Mena<sup>INV</sup> expression, we used liquid chromatography–tandem mass spectrometry (LC-MS/MS)–based phosphoproteomics to quantify tyrosine phosphorylation after incubation with or without 0.25 nM EGF. We detected 54 tyrosine phosphorylation sites across 41 proteins in at least biological duplicate (Supplemental Figure S6); phosphorylation across the 54 sites was significantly higher in cells expressing Mena<sup>INV</sup> versus control cells ( $p = 0.015$ ). Of the identified proteins, 12 are known PTP1B substrates; as a group, these exhibited significantly higher phosphorylation in Mena<sup>INV</sup>-expressing cells than in controls ( $p = 0.0078$ ); however, these 12 were not significantly more phosphorylated than the 54 phosphorylation sites overall ( $p = 0.06$ ).

#### A PTP1B-Mena-SHIP2-EGFR complex is dysregulated upon Mena<sup>INV</sup> expression

Because EGFR is a known PTP1B substrate (Haj et al., 2003; Mertins et al., 2008) and we identified complexes containing both Mena and

PTP1B in breast cancer cells, we examined whether Mena facilitates formation of EGFR-PTP1B complexes. In wild-type MDA-MB231 cells, complexes containing endogenous Mena-EGFR were detected by PLA (Figure 6A). EGF stimulation increased abundance of the PLA signal, indicating that EGFR activation induces formation of additional Mena-EGFR-containing complexes (Figure 6B). We then used PLA to quantify EGFR-PTP1B-containing complexes in GFP-, GFP-Mena-, and GFP-Mena<sup>INV</sup>-expressing cells before and after EGF treatment. EGF stimulation increased EGFR-PTP1B PLA in cells expressing GFP or GFP-Mena but had no effect on cells expressing Mena<sup>INV</sup> (Figure 6, C and D). Transient knockdown of PTP1B expression in MDA-MB231-GFP-Mena cells reduced the EGFR-PTP1B PLA signal, indicating that assay detected PTP1B/EGFR-containing complexes specifically (Supplemental Figure S7A). Therefore Mena<sup>INV</sup> expression blocks EGF-elicited recruitment of PTP1B to EGFR, providing a potential explanation for the increased receptor phosphorylation in cells expressing Mena<sup>INV</sup> (Figure 3).

All Mena isoforms are likely maintained as stable tetramers by their conserved C-terminal tetramerization domains (Gertler and Condeelis, 2011) and thus contain EVH1 domains at the N-terminal ends of each of the four subunits. Given their modular composition, the subunits of a Mena tetramer could potentially bind and link together up to four distinct EVH1 ligands. Therefore we asked whether another Mena EVH1-binding protein recruits Mena-PTP1B complexes to EGFR upon receptor activation. We identified SHIP2, a 5' inositol phosphatase that dephosphorylates phosphatidylinositol 3,4,5-trisphosphate to generate phosphatidylinositol 3,4-bisphosphate (PI(3,4)P<sub>2</sub>) in our mass spectrometry screen as one of the 41 proteins phosphorylated in EGF-stimulated MDA-MB231 cells (Supplemental Figure S6). On EGF stimulation, SHIP2 is recruited rapidly into complexes with activated EGFR (Pesesse et al., 2001). We inspected the SHIP2 sequence, found four canonical EVH1-binding motifs, and verified by coimmunoprecipitation (coIP) that endogenous SHIP2 associates with Mena (Figure 7A).

The foregoing observations led us to test the hypothesis that SHIP2 can recruit Mena-PTP1B complexes to activated EGFR by binding to one or more EVH1 domains in Mena tetramers. If SHIP2 links Mena-PTP1B complexes to activated EGFR, then SHIP2 depletion should abolish EGF-induced recruitment of PTP1B into complexes with EGFR. RNA interference–mediated SHIP2 depletion from wild-type MDA-MB231 cells (Supplemental Figure S7B) eliminated the EGF-induced increase in Mena-EGFR complexes, as indicated by PLA assays (Figure 7B). SHIP2 depletion in GFP- and GFP-Mena-expressing cells also eliminated the increase in EGFR-PTP1B complexes normally induced by stimulation with 0.25 nM EGF, reducing their abundance to a



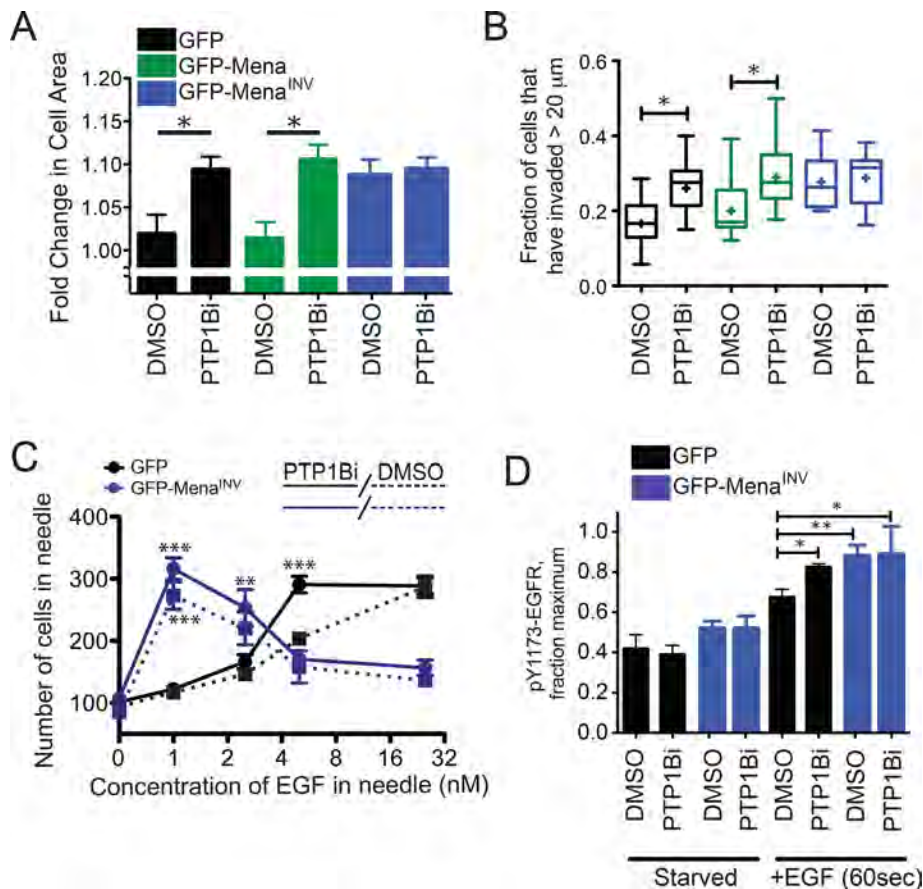


**FIGURE 5:** Inhibition of PTP1B mimics the effects of Mena<sup>INV</sup> expression. (A) Lamellipodial protrusion of MDA-MB231 cells 8 min poststimulation with 0.25 nM EGF after incubation with 0.1% DMSO or 10 μM PTP1B inhibitor for 60 min. Results are mean with 95% confidence intervals; 48 cells/condition. Asterisk indicates significant difference by ANOVA with Tukey multiple-comparison test (\**p* < 0.05). (B) 3D collagen invasion after 24 h in the presence of 0.25 nM EGF and 0.1% DMSO or 10 μM PTP1B inhibitor. Results are represented as box and whiskers at 5 and 95% percentiles; cross indicates mean value; five assays/condition. Asterisk indicates significant difference by nonparametric Kruskal–Wallis test and Dunn’s multiple-comparison test (\**p* < 0.05). (C) EGF dose-response of invasive cells collected from MTLn3 xenograft tumors expressing GFP (black solid and dotted lines) or GFP-Mena<sup>INV</sup> (blue solid or dotted lines). Needles contained EGF and 0.01% DMSO without (dotted lines) or with 10 μM PTP1B inhibitor (solid lines). Results are mean ± SEM and plotted on log<sub>2</sub> x-axis; more than three tumors for conditions with error bars; one tumor for conditions without error bars. Asterisks indicate significant difference by nonparametric Kruskal–Wallis test and Dunn’s multiple-comparison test (\*\**p* < 0.01 or \*\*\**p* < 0.001) at each concentration of EGF for conditions with more than three tumors. (D) EGFR phosphorylation at Y1173 (0.25 nM EGF, 3 min) after 60 min of preincubation with 0.1% DMSO or 10 μM PTP1B inhibitor after 4 h of serum starvation. Results are mean ± SEM; three experiments. Asterisks indicate significant difference by ANOVA with Student–Newman–Keuls multiple-comparison test (\**p* < 0.05, \*\**p* < 0.01). See also Supplemental Figure S5 and Supplemental Table S6.

level similar to that observed in GFP-Mena<sup>INV</sup> cells transfected with control small interfering RNA (siRNA; Figure 7, C and D). In addition to recruiting Mena-PTP1B complexes to activated EGFR, we wondered whether SHIP2 enzymatic activity might also contribute to the observed Mena<sup>INV</sup>-driven changes in breast cancer cell motility and invasion. We used the highly specific SHIP2 inhibitor AS1949490 (Suwa *et al.*, 2009) to determine whether its 5′ inositol phosphatase activity was required for Mena<sup>INV</sup>-enhanced membrane protrusion. SHIP2 inhibition attenuated protrusion at later time points in MDA-MB231-expressing Mena<sup>INV</sup> (Supplemental Figure S7D) and MTLn3 cells (Supplemental Figure S7C).

In sum, these data are consistent with a model in which activated EGFR rapidly recruits a SHIP2-Mena-PTP1B complex, which leads to receptor dephosphorylation by PTP1B. In cells that express Mena<sup>INV</sup>, however, SHIP2-dependent recruitment of PTP1B to EGFR is abolished, eliminating PTP1B-mediated dephosphorylation of EGFR (Figure 8). Thus we propose that Mena<sup>INV</sup> disrupts negative feedback to the EGFR and thereby increases signaling and, consequently, cellular responses elicited by low EGF concentrations.

## DISCUSSION

### Mena regulates signaling by specific RTKs

Mena and the other Ena/VASP proteins regulate motility and adhesion of numerous cell types (Pula and Krause, 2008); at a mechanistic level, their most extensively characterized functions influence actin polymerization and modulate the morphology and dynamics of membrane protrusions (Bear and Gertler, 2009). We found that Mena serves an additional, unanticipated, isoform-dependent role as a regulator of at least three RTKs known to drive invasion and metastasis in breast cancer (EGFR, IGFR and Met; Alexander and Friedl, 2012). Cellular responses to EGF and other growth factors are tightly regulated through control of receptor trafficking and activation state (Avraham and Yarden, 2011), with tyrosine phosphorylation of RTKs being regulated by a dynamic interplay between kinases and phosphatases (Kleiman *et al.*, 2011). Here we show that complexes containing Mena and PTP1B are recruited to activated EGFR in a SHIP2-dependent manner. Because PTP1B is known to regulate EGFR, IGFR, and Met signaling (Feldhammer *et al.*, 2013), our findings are consistent with a model in which ligand-induced, SHIP2-mediated recruitment of Mena- and PTP1B-containing complexes contributes to attenuation of signaling by these RTKs. Further, Mena<sup>INV</sup> disrupts EGF-elicited recruitment of PTP1B to EGFR, providing a basis for the enhanced signaling, motility and invasion

observed in response to stimulation with low EGF concentrations in cells expressing Mena<sup>INV</sup>.

Our PLA analysis indicated that complexes containing Mena and PTP1B present in unstimulated cells are recruited to the activated EGFR. We attempted to detect Mena and PTP1B in complex by colP without success, perhaps due to low affinity or stoichiometry of the complex. It is possible, however, that Mena associates directly with PTP1B, as the Mena EVH1 domain can bind purified PTP1B directly *in vitro* (Figure 4A). Future studies will address which region in Mena specifically regulates the interaction between these two proteins and whether the interaction is direct or requires additional components. Most of the PTP1B in cells is anchored to the outer

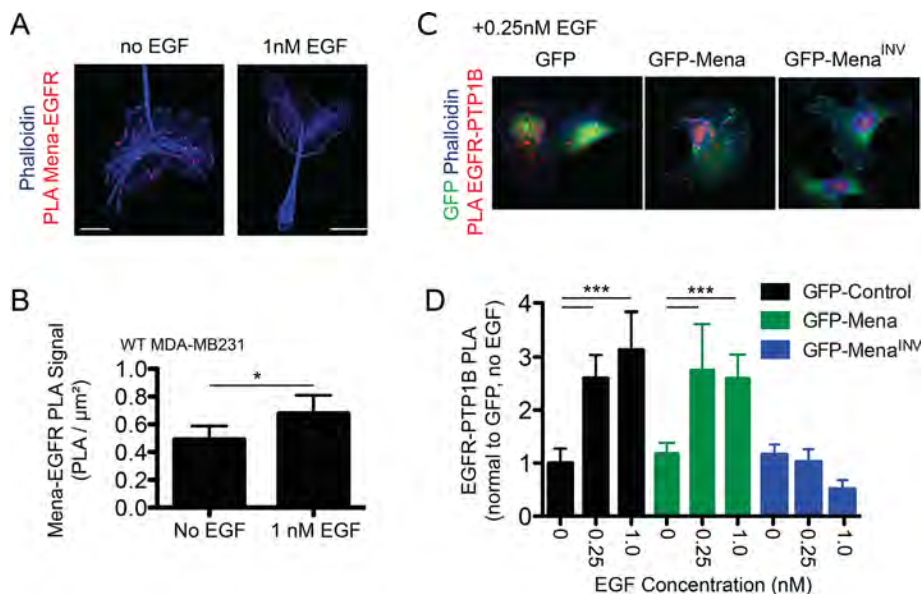


**FIGURE 6:** PTP1B recruitment to EGFR is abrogated in cells expressing Mena<sup>INV</sup>. (A) Representative images for Mena-EGFR PLA  $\pm$  EGF (1 nM, 60 s). Phalloidin shown in blue, and Mena-EGFR PLA shown in red. (B) Quantification of Mena-EGFR PLA in wild-type MDA-MB231 cells  $\pm$  EGF (1 nM, 60 s). Asterisk indicates significant difference by two-tailed t test (\* $p < 0.05$ ). (C) Representative images for EGFR-PTP1B PLA for MDA-MB231 cells expressing GFP, GFP-Mena, or GFP-Mena<sup>INV</sup> stimulated with 0.25 nM EGF for 60 s. GFP signal shown in green, phalloidin shown in blue, and EGFR-PTP1B PLA shown in red. (D) Quantification of EGFR-PTP1B PLA  $\pm$  0.25 nM EGF for 60 s. Data are mean with 95% confidence interval;  $>20$  cells/condition. Asterisks indicate significant difference by ANOVA with Tukey multiple-comparison test (\*\*\*) $p < 0.001$ .

membrane of the endoplasmic reticulum, where it can contact internalized transmembrane receptors (Eden *et al.*, 2010). However, in platelets (Frangioni *et al.*, 1993) and in MTLn3 rat adenocarcinoma cancer cells (Cortesio *et al.*, 2008), cleavage by calpain has been shown to release catalytically active PTP1B, which can then localize throughout the cytoplasm (Frangioni *et al.*, 1993; Feldhammer *et al.*, 2013). Therefore it is possible that calpain-dependent release of PTP1B into the cytoplasm could contribute to Mena-dependent association of PTP1B with RTKs in these cells. Despite the relatively small fraction present in the cytoplasm, PTP1B clearly functions at a variety of structures within the cytosol (Feldhammer *et al.*, 2013), including focal adhesions, filopodia on neuronal growth cones (Fuentes and Arregui, 2009), and invadopodia (Cortesio *et al.*, 2008), which are actin-driven protrusions that degrade the ECM during invasion. Of interest, these structures are also sites where Mena is localized (Philippart *et al.*, 2008; Pula and Krause, 2008).

In breast cancer cells, as little as 0.25 nM EGF induces rapid (within 60 s) recruitment of Mena-PTP1B complexes to EGFR, thereby dephosphorylating the receptor and attenuating its activity. Whereas PTP1B can regulate early endosome fusion and trafficking of Met and EGFR (Sangwan *et al.*, 2011), expression of Mena in MDA-MB231 cells was not associated with changes in EGFR surface abundance or distribution. The biochemical and biophysical effects of Mena on the EGF response occur within a time frame that is likely too brief to allow for receptor endocytosis and vesicle scission (Taylor *et al.*, 2011; Zheng *et al.*, 2013), although a novel mechanism for rapid endocytosis has recently been described (Boucrot *et al.*, 2014). Mena-dependent effects on EGFR signaling may occur while the receptor is still on the plasma membrane. Thus, in breast cancer cells, Mena, which enhances the actin polymerization underlying EGF-elicited lamellipodial protrusion (Philippart *et al.*, 2008), also directly participates in EGFR signal attenuation.

### SHIP2 mediates EGF-induced recruitment of Mena and PTP1B to EGFR

We also find that ligand-triggered recruitment of Mena-PTP1B complexes to EGFR requires SHIP2, an SH2 domain-containing inositol phosphatase with known scaffolding functions (Erneux *et al.*, 2011) that is rapidly recruited (via the adaptor protein SHC) to activated EGFR (Pesesse *et al.*, 2001). The kinetics of RTK-dependent recruitment of SHIP2 is very fast, and it occurs within 20 s of stimulation (Zheng *et al.*, 2013). Mena translocation to lamellipodia can also be observed within 20 s after EGF stimulation and depends on availability of F-actin barbed ends (Philippart *et al.*, 2008), which are generated by cofilin severing upon its PLC $\gamma$ -mediated release from the plasma membrane (Van Rhee *et al.*, 2007). The EGF-induced, EGFR-PTP1B-containing complexes form with kinetics similar to that of the Mena-dependent effects on both EGFR signaling and lamellipodial protrusion. Our data support a model in which individual Mena tetramers associate with both PTP1B and SHIP2 potentially through direct binding of their N-terminal EVH1 domains. This raises the interesting possibility that such complexes may also interact with F-actin barbed ends through the actin-binding motifs within the C-terminal EVH2 domains of Mena.

plexes may also interact with F-actin barbed ends through the actin-binding motifs within the C-terminal EVH2 domains of Mena.

Mena binds other EVH1 ligands that influence its subcellular localization and mediates interactions with signaling and scaffolding proteins (Pula and Krause, 2008; Bear and Gertler, 2009). Mena localization to the leading edge of lamellipodia and tips of filopodia depends, in part, on EVH1-mediated binding to lamellipodin (Lpd; Krause *et al.*, 2004). Recently Lpd was found in complexes with EGFR, and knockdown of Lpd or Mena disrupted scission of clathrin-coated pits, a late step in clathrin-mediated endocytosis (CME) of the receptor (Vehlow *et al.*, 2013). Lpd-EGFR associated constitutively in the HeLa cells used in that study, and, since CME of EGFR initiates only after EGF stimulation, the results of Vehlow *et al.* (2013) imply that growth factor stimulation induces Mena recruitment to the receptor. Our data are consistent with this model; however, we observed Mena recruitment to EGFR and effects on receptor signaling within 60s after stimulation, a time that precedes vesicle scission, the first step in CME affected by Mena depletion (Vehlow *et al.*, 2013). It is possible that the SHIP2-EGFR interaction helps to bring Mena into complex with Lpd or that Lpd in complex with EGFR increases Mena-PTP1B recruitment to the receptor at later times after EGF stimulation. Consistent with this possibility, we found that inhibition of SHIP2 5' inositol phosphatase activity, which produces PI(3,4)P<sub>2</sub>, affects EGF-stimulated protrusion. Of interest, Lpd contains one of the few PH domains specific for PI(3,4)P<sub>2</sub> (Krause *et al.*, 2004), and both SHIP2 and PI(3,4)P<sub>2</sub> regulate CME dynamics (Nakatsu *et al.*, 2010; Posor *et al.*, 2013). In sum, these data support a key role for Mena, via EVH1-mediated interactions, in the recruitment of important signaling proteins downstream of EGFR.



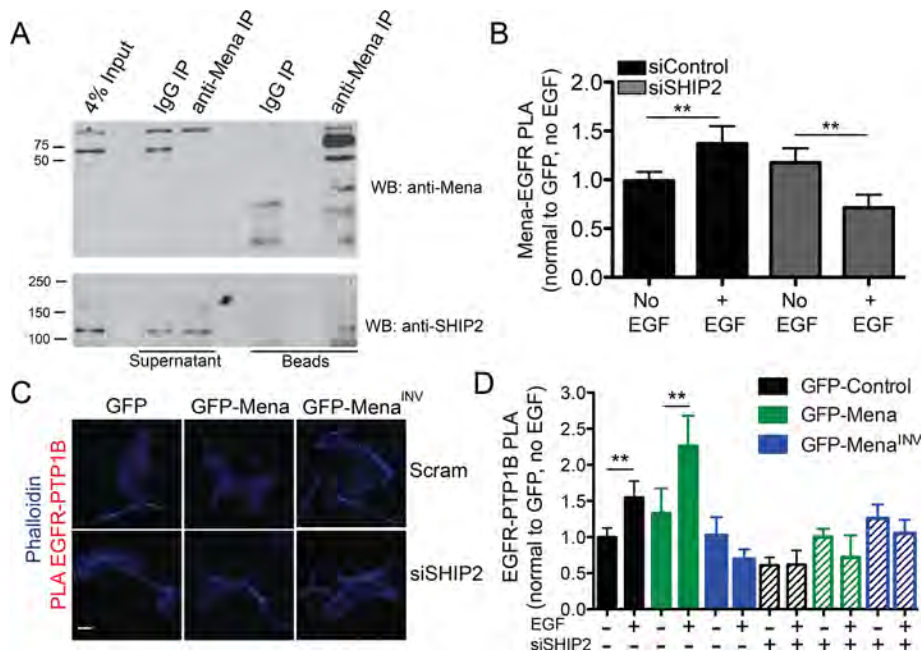


**FIGURE 7:** A SHIP2-Mena-PTP1B complex regulates EGFR-PTP1B interaction in MDA-MB231 cells. (A) Total Mena protein was immunoprecipitated from Rat2 fibroblast lysate and immunoblotted for SHIP2. (B) Quantification of Mena-EGFR PLA in wild-type MDA-MB231 cells starved or stimulated with 1 nM EGF for 60 s. Experiment performed 72 h posttransfection with 25 nM control (siControl) or SHIP2 (siSHIP2)-targeted SMARTPool siRNA. Results are shown as mean with 95% confidence intervals; >20 cells/condition. Asterisks indicate significant difference by ANOVA with Tukey multiple-comparison test (\*\* $p < 0.01$ ). (C) Representative images of EGFR-PTP1B PLA in MDA-MB231 cell lines 72 h posttransfection with siControl or siSHIP2. (D) EGFR-PTP1B PLA in MDA-MB231 cell lines 72 h posttransfection with siControl (indicated by “-” in siSHIP2 line) or siSHIP2. Cells stimulated  $\pm 0.25$  nM EGF for 60 s. Results are shown as mean with 95% confidence intervals; > 50 cells/condition. Asterisks indicate significant difference by nonparametric Kruskal-Wallis test and Dunn’s multiple-comparison test (\*\* $p < 0.05$ ). See also Supplemental Figure S7.

### Expression of Mena<sup>INV</sup> dysregulates phosphotyrosine signaling

Expression of Mena<sup>INV</sup> reduces PTP1B recruitment to the receptor and its dephosphorylation, thereby eliciting EGFR-dependent protrusion and motility-related responses at substantially reduced ligand concentration. Within tumors, spontaneous up-regulation of Mena<sup>INV</sup> expression likely enhances both paracrine signaling with macrophages and the autocrine loops that provide EGFR ligands to tumor cells, increasing prometastatic behaviors (Wyckoff et al., 2004; Patsialou et al., 2009; Zhou et al., 2014). Mena<sup>INV</sup> expression also increases tumor cell sensitivity to HGF and IGF-1 by 20- and 5-fold, respectively, suggesting that tumor cells expressing Mena<sup>INV</sup> in vivo may be sensitized to HGF and IGF-1 secreted by tumor-associated fibroblasts or other cells in the tumor microenvironment (Yee et al., 1989; Mueller et al., 2012). Selective inhibition of PTP1B by Mena<sup>INV</sup> likely affects a set of proteins that are normally dephosphorylated by PTP1B-containing Mena complexes. Mena<sup>INV</sup>, like Mena, localizes to filopodia, lamellipodia, and invadopodia, as well as to sites of cell matrix and cell:cell adhesion; Mena<sup>INV</sup>-mediated attenuation of PTP1B function (or localization) within these structures could have a large effect on tumor cell invasion and motility. Consistent with this idea, several PTP1B targets that localize to these structures and function in tumor cell migration and invasion were among the proteins detected in our mass spectrometry screen for Mena<sup>INV</sup>-induced dysregulated tyrosine phosphorylation. We also found that treatment

of breast cancer cells in vitro or in vivo with a targeted PTP1B inhibitor induced phenotypes that are strikingly similar to those caused by Mena<sup>INV</sup> expression.

The roles that PTP1B plays in cancer are complex and likely context dependent. Complete PTP1B deletion in the HER2/Neu model of murine mammary delays or prevents tumor formation (Bentires-Alj and Neel, 2007). However, mammary-specific ablation of PTP1B after tumor formation does not affect tumor maintenance or growth (Balavenkatraman et al., 2011). More work will be required to determine exactly how selective dysregulation of PTP1B by Mena<sup>INV</sup> contributes to tumor progression. The exact mechanism underlying Mena<sup>INV</sup>-mediated dysregulation of tyrosine phosphorylation remains to be determined. Given that the INV exon is located near the EVH1 domain of Mena, it is possible that inclusion of INV affects formation of complexes with PTP1B, SHIP2, or both, which in turn could affect recruitment of both proteins to RTKs. Because all Mena isoforms form stable tetramers (Gertler and Condeelis, 2011), it is possible that inclusion of INV could alter interactions with up to four distinct EVH1 ligands within a Mena<sup>INV</sup> tetramer. Future studies will address how inclusion of the sequence encoded by the INV exon regulates these interactions. Regardless of the outcome, our findings indicate that Mena and its isoforms act to modulate RTK signaling pathways in addition

to their known role in regulating actin dynamics.

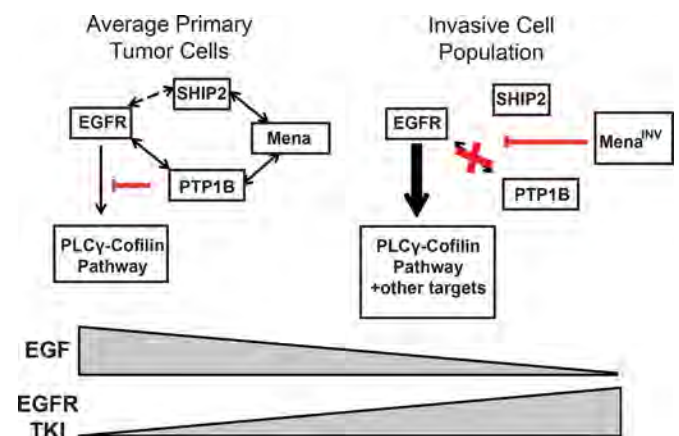


**FIGURE 8:** Model for Mena-dependent regulation of RTK signaling. In average primary tumor cells, activation of EGFR leads to rapid recruitment of a SHIP2-Mena-PTP1B complex, which leads to receptor dephosphorylation by PTP1B and sensitivity to TKIs. However, in the invasive tumor cell population, where levels of Mena<sup>INV</sup> are high, SHIP2-dependent recruitment of PTP1B to EGFR is abolished, eliminating PTP1B-mediated dephosphorylation of EGFR, causing sensitivity to EGF, as well as resistance to TKIs.

## MATERIALS AND METHODS

### Antibodies, growth factors, and inhibitors

Growth factors were purchased from Life Technologies, Carlsbad, CA (EGF), and PeproTech, Rocky Hill, NJ (HGF, NRG-1, and IGF). The compounds used were Met inhibitor SU11274 (Selleck Chemicals, Houston, TX), EGFR inhibitor erlotinib (LC Labs, Woburn, MA; PeproTech), PTP1B inhibitor (539741; Calbiochem, Billerica, MA), and SHIP2 inhibitor AS1949490 (Tocris, Minneapolis, MN). The following antibodies were used: EGFR (Cell Signaling Technology, Danvers, MA), pEGFR Y1173 (Cell Signaling Technology; Epitomics), vimentin (BD Transduction Laboratories, San Jose, CA), E-cadherin (Cell Signaling Technology), PTP1B (Millipore, Burlington, MA), SHIP2 (Cell Signaling Technology), and panMena (Lebrand *et al.*, 2004).

### Cell culture

All breast cancer cell lines were obtained from the American Type Culture Collection and cultured in DMEM with 10% heat-inactivated fetal bovine serum. Cell lines were engineered to stably express 10- to 15-fold-higher levels of Mena isoforms more than for wild-type cell lines. For siRNA-mediated knockdown experiments, 25 nM SHIP2- or PTP1B-targeted ON-TARGETplus SMARTpool siRNA (Dharmacon, GE Lifesciences, Lafayette, CO) was transfected in serum-free OptiMeM using Dharmafect4 with assays performed 72 h posttransfection. The ON-TARGETplus nontargeted control pool (25 nM) was used in those conditions labeled “scramble.”

### PTP1B and Mena-EVH1 in vitro binding assay

Constructs used for recombinant protein production were GST-PTP1B (Addgene, Cambridge, MA; plasmid #8602), GST, and GST-FP4 His-Mini-Mena (His-TEV-EVH1-LERER-6xGly-CoCo), which contains mouse Mena (Gertler *et al.*, 1996) residues 1–258 fused, via a 6xGly linker, to the C-terminal 31-residue coiled-coil from Mena. The coiled-coil, which mediates Mena tetramerization, was included to allow for the potential effects of avidity in the binding assay (Gupton *et al.*, 2012), and intervening sequences were omitted to enable recovery of soluble, purified protein. Detailed protocols for protein expression and purification are given in the Supplemental Experimental Procedures.

GST, GST-FP4, and GST-PTP1B (3  $\mu$ M) were immobilized on glutathione beads and blocked for 2 h at 4°C (20 mM 4-(2-hydroxyethyl)-1-piperazineethanesulfonic acid [HEPES], pH 7.6, 150 mM NaCl, 1% NP-40, 3% bovine serum albumin [BSA]). Beads were washed once and incubated with 50, 100, 500 nM His-Mini-Mena, rotating for 2 h at 4°C in binding buffer (20 mM HEPES, pH 7.6, 150 mM NaCl, 1% NP-40). Beads were washed three times in binding buffer while rotating at 4°C for 5 min. Proteins were eluted in 4 $\times$  SDS-PAGE sample buffer and assayed by Western blotting.

### EGFR internalization assays

Surface proteins were biotinylated using the method of Roberts *et al.* (2001; see the Supplemental Experimental Procedures). Cells were lysed in 75 mM HEPES (pH 7.5), 200 mM NaCl, 10% glycerol, 1.5% Triton-X 100, and 0.75% NP-40 with a protease Mini-Complete protease inhibitor tablet (Roche, Indianapolis, IN) on ice. To measure the surface level of EGFR, cells were lysed immediately after labeling with biotin. EGFR STAR enzyme-linked immunosorbent assay (ELISA; Millipore) was used to quantify total and biotinylated EGFR by modifying the protocol to replace the anti-rabbit immunoglobulin G (IgG)–horseradish peroxidase conjugate with anti-rabbit IR800 and streptavidin-IR680 (Li-Cor, Lincoln, NE) antibodies to facilitate dual detection of total and biotinylated EGFR using the Li-Cor Odyssey scanning system. Negative controls of

nonlabeled samples or surface-stripped samples (without the internalization step) were included for each experiment.

### Protrusion and 3D invasion assays

Protrusion assays were performed as described (Meyer *et al.*, 2012). Briefly, serum-starved cells plated on collagen- and Matrigel-coated dishes were imaged every 20 s for 10 min at 37°C (TE2000 microscope; Nikon) with a 20 $\times$  objective. Growth factor/inhibitor solutions were added after 80 s. Cell areas were traced immediately before stimulation and 9 min after stimulation using ImageJ (National Institutes of Health, Bethesda, MD). Data shown are from individual cells pooled from at least three separate experiments. The 3D invasion assay in Figure 6B was performed as described (Giampieri *et al.*, 2009). See the Supplemental Experimental Procedures.

### PI(4,5)P<sub>2</sub> hydrolysis assay

PI(4,5)P<sub>2</sub> hydrolysis was assayed as described (Van Rhee *et al.*, 2007). See the Supplemental Experimental Procedures.

### Cofilin:actin fluorescence resonance energy transfer

F-actin:cofilin binding was measured by fluorescence resonance energy transfer (FRET) efficiency using acceptor photobleaching as described (Van Rhee *et al.*, 2007). See the Supplemental Experimental Procedures.

### Immunoprecipitation and Western blotting

Standard procedures were used for protein electrophoresis, Western blotting, and IP. For IP, cells were lysed in 20 mM HEPES, pH 7.4, 200 mM NaCl, 2 mM MgCl<sub>2</sub>, 5% glycerol, 1% NP-40, and phosphatase inhibitors. See the Supplemental Experimental Procedures. For the Mena-SHIP2 IP, cells were harvested in chilled lysis buffer (20 mM HEPES, pH 7.4, 200 mM NaCl, 2 mM MgCl<sub>2</sub>, 5% glycerol) supplemented with Mini-Complete EDTA-free protease inhibitors (Roche) and a phosphatase inhibitor cocktail (PhosSTOP; Roche) at 4°C. Precleared lysate was incubated with 40  $\mu$ l of 50% slurry of Protein A Plus beads (Pierce, Grand Island, NY) and Mena antibody or IgG control for 3 h at 4°C. Beads were washed three times in lysis buffer, eluted in 2 $\times$  SDS sample buffer, and resolved by SDS-PAGE.

### Proximity ligation assay

Cells were prepared as for protrusion assay and stimulated with growth factor as indicated. Cells were fixed for 20 min in 4% paraformaldehyde in PHEM buffer (60 mM PIPES [piperazine-*N,N'*-bis(ethanesulfonic acid)], pH 7.0, 25 mM HEPES [4-(2-hydroxyethyl)-1-piperazineethanesulfonic acid], pH 7.0, 10 mM EGTA [ethylene glycol tetraacetic acid], pH 8.0, 2 mM MgCl<sub>2</sub>, 0.12 M sucrose), permeabilized with 0.2% Triton X-100, blocked with 10% BSA, and incubated with primary antibodies overnight at 4°C. PLA was then performed according to the manufacturer's protocol (Olink Biosciences, Uppsala, Sweden). The spots per cell were counted, and the number was normalized relative to cell area and/or GFP expression. Data are pooled from at least three different experiments.

### In vivo invasion assay

The in vivo invasion assay was performed in three mice per condition as described (Wyckoff *et al.*, 2000). Briefly, needles were held in place by a micromanipulator around a single mammary tumor of an anesthetized mouse. Needles contained a mixture of Matrigel, 0–25 nM EGF, buffer, and EDTA with either 0.01% dimethyl sulfoxide (DMSO), or 10  $\mu$ M PTP1B inhibitor. After 4 h of cell collection, the contents of the needles were extruded. Cells were stained with

4',6-diamidino-2-phenylindole and counted on an Olympus IX70 inverted microscope.

## Phosphotyrosine analysis via LC-MS/MS

Serum-starved MDA-MB231 cells expressing GFP or GFP-Mena<sup>INV</sup> were stimulated with 0, 0.25, 0.5, or 15.8 nM EGF for 1 min. Cells were immediately lysed in 8 M urea (Sigma-Aldrich, St. Louis, MO) and quantified using the BCA assay (Pierce). As previously described, quantitative LC-MS/MS analyses of tyrosine-phosphorylated peptides using iTRAQ 8plex and an Orbitrap Elite mass spectrometer (Thermo) were performed (Johnson *et al.*, 2012). In brief, proteins were reduced, alkylated, and digested with modified trypsin (Promega, Madison, WI). Peptides were desalted, lyophilized, and labeled with iTRAQ 8plex (AB Sciex, Framingham, MA). Tyrosine-phosphorylated peptides were enriched using IP and immobilized metal affinity chromatography. Mascot peptide identifications, phosphorylation-site assignments, and quantification were verified manually with the assistance of computer-aided manual validation software (Curran *et al.*, 2013). Supplemental Table S1 contains the sequences of identified phosphotyrosine peptides along with relative quantification and statistical analysis. See the Supplemental Experimental Procedures.

## ACKNOWLEDGMENTS

We thank Evanthia Roussos, Michele Balsamo, and Aaron Meyer for advice and John Lamar for advice and for gifts of tumor tissue. This work was supported by DOD Breast Cancer Research Program Grants W81XWH-10-1-0040 to S.K.H. and W81XWH-13-1-0031 to M.J.O., National Institutes of Health Grants U54-CA112967 to F.B.G., F.W., and D.A.L. and GM58801 to F.B.G., funds from the Ludwig Center at the Massachusetts Institute of Technology to F.B.G., Koch Institute National Cancer Institute Core Grant P30-CA14051, and CA150344 to J.C. and CA100324 for J.J. We thank the Flow Cytometry, Microscopy and Histology facilities in the Koch Institute Swanson Biotechnology Center for support and the Analytical Imaging Facility in the Biophotonics Center at the Albert Einstein College of Medicine.

## REFERENCES

Alexander S, Friedl P (2012). Cancer invasion and resistance: interconnected processes of disease progression and therapy failure. *Trends Mol Med* 18, 13–26.

Avraham R, Yarden Y (2011). Feedback regulation of EGFR signalling: decision making by early and delayed loops. *Nat Rev Mol Cell Biol* 12, 104–117.

Bailey M, Wyckoff J, Bouzazhah B, Hammerman R, Sylvestre V, Cammer M, Pestell R, Segall JE (2000). Epidermal growth factor receptor distribution during chemotactic responses. *Mol Biol Cell* 11, 3873–3883.

Balavenkatraman KK, Aceto N, Britschgi A, Mueller U, Bence KK, Neel BG, Bentes-Alj M (2011). Epithelial protein-tyrosine phosphatase 1B contributes to the induction of mammary tumors by HER2/Neu but is not essential for tumor maintenance. *Mol Cancer Res* 9, 1377–1384.

Ball LJ, Jarchau T, Oschkinat H, Walter U (2002). EVH1 domains: structure, function and interactions. *FEBS Lett* 513, 45–52.

Bear JE, Gertler FB (2009). Ena/VASP: towards resolving a pointed controversy at the barbed end. *J Cell Sci* 122, 1947–1953.

Bear JE, Haugh JM (2014). Directed migration of mesenchymal cells: where signaling and the cytoskeleton meet. *Curr Opin Cell Biol* 30C, 74–82.

Bentes-Alj M, Neel BG (2007). Protein-tyrosine phosphatase 1B is required for HER2/Neu-induced breast cancer. *Cancer Res* 67, 2420–2424.

Boucrot E, Ferreira APA, Almeida-Souza L, Debarb S, Vallis Y, Howard G, Bertot L, Sauvonnnet N, McMahon HT (2014). Endophilin marks and controls a clathrin-independent endocytic pathway. *Nature* 517, 460–465.

Breitsprecher D, Kiesewetter AK, Linkner J, Vinzenz M, Stradal TEB, Small JV, Curth U, Dickinson RB, Faix J (2011). Molecular mechanism of Ena/VASP-mediated actin-filament elongation. *EMBO J* 30, 456–467.

Cortesio CL, Chan KT, Perrin BJ, Burton NO, Zhang S, Zhang Z-Y, Huttenlocher A (2008). Calpain 2 and PTP1B function in a novel pathway with Src to regulate invadopodia dynamics and breast cancer cell invasion. *J Cell Biol* 180, 957–971.

Curran TG, Bryson BD, Reigelhaupt M, Johnson H, White FM (2013). Computer aided manual validation of mass spectrometry-based proteomic data. *Methods* 61, 219–226.

Eden ER, White IJ, Tsapara A, Futter CE (2010). Membrane contacts between endosomes and ER provide sites for PTP1B-epidermal growth factor receptor interaction. *Nat Cell Biol* 12, 267–272.

Erneux C, Edimo WE, Deneubourg L, Pirson I (2011). SHIP2 multiple functions: a balance between a negative control of PtdIns(3,4,5)P<sub>3</sub> level, a positive control of PtdIns(3,4)P<sub>2</sub> production, and intrinsic docking properties. *J Cell Biochem* 112, 2203–2209.

Feldhammer M, Uetani N, Miranda-Saavedra D, Tremblay ML (2013). PTP1B: a simple enzyme for a complex world. *Crit Rev Biochem Mol Biol* 48, 430–445.

Frangioni J V, Oda A, Smith M, Salzman EW, Neel BG (1993). Calpain-catalyzed cleavage and subcellular relocation of protein phosphotyrosine phosphatase 1B (PTP-1B) in human platelets. *EMBO J* 12, 4843–4856.

Friedl P, Alexander S (2011). Cancer invasion and the microenvironment: plasticity and reciprocity. *Cell* 147, 992–1009.

Fuentes F, Arregui CO (2009). Microtubule and cell contact dependency of ER-bound PTP1B localization in growth cones. *Mol Biol Cell* 20, 1878–1889.

Gertler F, Condeelis J (2011). Metastasis: tumor cells becoming MENAcing. *Trends Cell Biol* 21, 81–90.

Gertler FB, Niebuhr K, Reinhard M, Wehland J, Soriano P (1996). Mena, a relative of VASP and Drosophila Enabled, is implicated in the control of microfilament dynamics. *Cell* 87, 227–239.

Giampieri S, Manning C, Hooper S, Jones L, Hill CS, Sahai E (2009). Localized and reversible TGFβ signalling switches breast cancer cells from cohesive to single cell motility. *Nat Cell Biol* 11, 1287–1296.

Gupton SL, Riquelme D, Hughes-Alford SK, Tadros J, Rudina SS, Hynes RO, Lauffenburger DG, Gertler FB (2012). Mena binds α5 integrin directly and modulates α5β1 function. *J Cell Biol* 198, 657–676.

Gusenbauer S, Vlaicu P, Ullrich A (2013). HGF induces novel EGFR functions involved in resistance formation to tyrosine kinase inhibitors. *Oncogene* 32, 3846–3856.

Haj FG, Markova B, Klamann LD, Bohmer FD, Neel BG (2003). Regulation of receptor tyrosine kinase signaling by protein tyrosine phosphatase-1B. *J Biol Chem* 278, 739–744.

Hanahan D, Weinberg RA (2011). Hallmarks of cancer: the next generation. *Cell* 144, 646–674.

Hansen SD, Mullins RD (2010). VASP is a processive actin polymerase that requires monomeric actin for barbed end association. *J Cell Biol* 191, 571–584.

Johnson H, Del Rosario AM, Bryson BD, Schroeder MA, Sarkaria JN, White FM (2012). Molecular characterization of EGFR and EGFRvIII signaling networks in human glioblastoma tumor xenografts. *Mol Cell Proteomics* 11, 1724–1740.

Joyce JA, Pollard JW (2009). Microenvironmental regulation of metastasis. *Nat Rev Cancer* 9, 239–252.

Kleiman LB, Maiwald T, Conzelmann H, Lauffenburger DA, Sorger PK (2011). Rapid phospho-turnover by receptor tyrosine kinases impacts downstream signaling and drug binding. *Mol Cell* 43, 723–737.

Krause M, Leslie JD, Stewart M, Lafuente EM, Valderrama F, Jagannathan R, Strasser GA, Robinson DA, Liu H, Way M, *et al.* (2004). Lamellipodin, an Ena/VASP ligand, is implicated in the regulation of lamellipodial dynamics. *Dev Cell* 7, 571–583.

Lebrand C, Dent EW, Strasser GA, Lanier LM, Krause M, Svitkina TM, Borisy GG, Gertler FB (2004). Critical role of Ena/VASP proteins for filopodia formation in neurons and in function downstream of netrin-1. *Neuron* 42, 37–49.

Mertins P, Eberl HC, Renkawitz J, Olsen J V, Tremblay ML, Mann M, Ullrich A, Daub H (2008). Investigation of protein-tyrosine phosphatase 1B function by quantitative proteomics. *Mol Cell Proteomics* 7, 1763–1777.

Meyer AS, Hughes-Alford SK, Kay JE, Castillo A, Wells A, Gertler FB, Lauffenburger DA (2012). 2D protrusion but not motility predicts growth factor-induced cancer cell migration in 3D collagen. *J Cell Biol* 197, 721–729.

Mueller KL, Madden JM, Zoratti GL, Kuperwasser C, List K, Boerner JL (2012). Fibroblast-secreted hepatocyte growth factor mediates epidermal growth factor receptor tyrosine kinase inhibitor resistance in triple-negative breast cancers through paracrine activation of Met. *Breast Cancer Res* 14, R104.



- Nakatsu F, Perera RM, Lucast L, Zoncu R, Domin J, Gertler FB, Toomre D, De Camilli P (2010). The inositol 5-phosphatase SHIP2 regulates endocytic clathrin-coated pit dynamics. *J Cell Biol* 190, 307–315.
- Nürnberg A, Kitzing T, Grosse R (2011). Nucleating actin for invasion. *Nat Rev Cancer* 11, 177–187.
- Patsialou A, Wyckoff J, Wang Y, Goswami S, Stanley ER, Condeelis JS (2009). Invasion of human breast cancer cells in vivo requires both paracrine and autocrine loops involving the colony-stimulating factor-1 receptor. *Cancer Res* 69, 9498–9506.
- Pesesse X, Dewaste V, De Smedt F, Laffargue M, Giuriato S, Moreau C, Payrastré B, Erneux C (2001). The Src homology 2 domain containing inositol 5-phosphatase SHIP2 is recruited to the epidermal growth factor (EGF) receptor and dephosphorylates phosphatidylinositol 3,4,5-trisphosphate in EGF-stimulated COS-7 cells. *J Biol Chem* 276, 28348–28355.
- Petrie RJ, Yamada KM (2012). At the leading edge of three-dimensional cell migration. *J Cell Sci* 125, 5917–5926.
- Philippart U, Roussos ET, Oser M, Yamaguchi H, Kim H-D, Giampieri S, Wang Y, Goswami S, Wyckoff JB, Lauffenburger DA, et al. (2008). A Mena invasion isoform potentiates EGF-induced carcinoma cell invasion and metastasis. *Dev Cell* 15, 813–828.
- Pignatelli J, Goswami S, Jones JG, Rohan TE, Pieri E, Chen X, Adler E, Cox D, Maleki S, Bresnick A, et al. (2014). Invasive breast carcinoma cells from patients exhibit Mena<sup>INV</sup>- and macrophage-dependent transendothelial migration. *Sci Signal* 7, ra112.
- Posor Y, Eichhorn-Gruenig M, Puchkov D, Schöneberg J, Ullrich A, Lampe A, Müller R, Zerbakhsh S, Gulluni F, Hirsch E, et al. (2013). Spatiotemporal control of endocytosis by phosphatidylinositol-3,4-bisphosphate. *Nature* 499, 233–237.
- Pula G, Krause M (2008). Role of Ena/VASP proteins in homeostasis and disease. *Handb Exp Pharmacol* 2008, 39–65.
- Roberts M, Barry S, Woods A, van der Sluijs P, Norman J (2001). PDGF-regulated rab4-dependent recycling of alphavbeta3 integrin from early endosomes is necessary for cell adhesion and spreading. *Curr Biol* 11, 1392–1402.
- Robinson BD, Sica GL, Liu Y-F, Rohan TE, Gertler FB, Condeelis JS, Jones JG (2009). Tumor microenvironment of metastasis in human breast carcinoma: a potential prognostic marker linked to hematogenous dissemination. *Clin Cancer Res* 15, 2433–2441.
- Rohan TE, Xue X, Lin H-M, D'Alfonso TM, Ginter PS, Oktay MH, Robinson BD, Ginsberg M, Gertler FB, Glass AG, et al. (2014). Tumor microenvironment of metastasis and risk of distant metastasis of breast cancer. *J Natl Cancer Inst* 106, 1–11.
- Roussos ET, Balsamo M, Alford SK, Wyckoff JB, Gligorijevic B, Wang Y, Pozzuto M, Stobezki R, Goswami S, Segall JE, et al. (2011a). Mena invasive (Mena<sup>INV</sup>) promotes multicellular streaming motility and transendothelial migration in a mouse model of breast cancer. *J Cell Sci* 124, 2120–2131.
- Roussos ET, Condeelis JS, Patsialou A (2011b). Chemotaxis in cancer. *Nat Rev Cancer* 11, 573–587.
- Roussos ET, Goswami S, Balsamo M, Wang Y, Stobezki R, Adler E, Robinson BD, Jones JG, Gertler FB, Condeelis JS, et al. (2011c). Mena invasive (Mena<sup>INV</sup>) and Mena<sup>11a</sup> isoforms play distinct roles in breast cancer cell cohesion and association with TMEM. *Clin Exp Metastasis* 28, 515–527.
- Roussos ET, Wang Y, Wyckoff JB, Sellers RS, Wang W, Li J, Pollard JW, Gertler FB, Condeelis JS (2010). Mena deficiency delays tumor progression and decreases metastasis in polyoma middle-T transgenic mouse mammary tumors. *Breast Cancer Res* 12, R101.
- Sangwan V, Abella J, Lai A, Bertos N, Stuble M, Tremblay ML, Park M (2011). Protein-tyrosine phosphatase 1B modulates early endosome fusion and trafficking of Met and epidermal growth factor receptors. *J Biol Chem* 286, 45000–45013.
- Suda K, Murakami I, Katayama T, Tomizawa K, Osada H, Sekido Y, Maehara Y, Yatabe Y, Mitsudomi T (2010). Reciprocal and complementary role of MET amplification and EGFR T790M mutation in acquired resistance to kinase inhibitors in lung cancer. *Clin Cancer Res* 16, 5489–5498.
- Suwa A, Yamamoto T, Sawada A, Minoura K, Hosogai N, Tahara A, Kurama T, Shimokawa T, Aramori I (2009). Discovery and functional characterization of a novel small molecule inhibitor of the intracellular phosphatase, SHIP2. *Br J Pharmacol* 158, 879–887.
- Taylor MJ, Perrais D, Merrifield CJ (2011). A high precision survey of the molecular dynamics of mammalian clathrin-mediated endocytosis. *PLoS Biol* 9, e1000604.
- Van Rheenen J, Song X, van Roosmalen W, Cammer M, Chen X, Desmarais V, Yip S-CC, Backer JM, Eddy RJ, Condeelis JS (2007). EGF-induced PIP2 hydrolysis releases and activates cofilin locally in carcinoma cells. *J Cell Biol* 179, 1247–1259.
- Vehlow A, Soong D, Vizcay-Barrena G, Bodo C, Law A-L, Perera U, Krause M (2013). Endophilin, Lamellipodin, and Mena cooperate to regulate F-actin-dependent EGF-receptor endocytosis. *EMBO J* 32, 2722–2734.
- Wang W, Goswami S, Lapidus K, Wells AL, Wyckoff JB, Sahai E, Singer RH, Segall JE, Condeelis JS (2004). Identification and testing of a gene expression signature of invasive carcinoma cells within primary mammary tumors. *Cancer Res* 64, 8585–8594.
- Wyckoff J, Wang W, Lin EY, Wang Y, Pixley F, Stanley ER, Graf T, Pollard JW, Segall J, Condeelis J (2004). A paracrine loop between tumor cells and macrophages is required for tumor cell migration in mammary tumors. *Cancer Res* 64, 7022–7029.
- Wyckoff JB, Segall JE, Condeelis JS (2000). The collection of the motile population of cells from a living tumor. *Cancer Res* 60, 5401–5404.
- Yee D, Paik S, Lebovic GS, Marcus RR, Favoni RE, Cullen KJ, Lippman ME, Rosen N (1989). Analysis of insulin-like growth factor I gene expression in malignancy: evidence for a paracrine role in human breast cancer. *Mol Endocrinol* 3, 509–517.
- Zheng Y, Zhang C, Croucher DR, Soliman MA, St-Denis N, Pasculescu A, Taylor L, Tate SA, Hardy WR, Colwill K, et al. (2013). Temporal regulation of EGF signalling networks by the scaffold protein Shc1. *Nature* 499, 166–171.
- Zhou ZN, Sharma VP, Beaty BT, Roh-Johnson M, Peterson EA, Van Rooijen N, Kenny PA, Wiley HS, Condeelis JS, Segall JE (2014). Autocrine HBEGF expression promotes breast cancer intravasation, metastasis and macrophage-independent invasion in vivo. *Oncogene* 33, 3784–3793.

# Characterization of the expression of the pro-metastatic Mena<sup>INV</sup> isoform during breast tumor progression

Madeleine J. Oudin<sup>1</sup> · Shannon K. Hughes<sup>1,2</sup> · Nazanin Rohani<sup>1</sup> ·  
Mira N. Moufarrej<sup>2</sup> · Joan G. Jones<sup>5</sup> · John S. Condeelis<sup>3</sup> ·  
Douglas A. Lauffenburger<sup>1,2</sup> · Frank B. Gertler<sup>1,4</sup>

Received: 24 August 2015 / Accepted: 7 December 2015  
© Springer Science+Business Media Dordrecht 2015

**Abstract** Several functionally distinct isoforms of the actin regulatory Mena are produced by alternative splicing during tumor progression. Forced expression of the Mena<sup>INV</sup> isoform drives invasion, intravasation and metastasis. However, the abundance and distribution of endogenously expressed Mena<sup>INV</sup> within primary tumors during progression remain unknown, as most studies to date have only assessed relative mRNA levels from dissociated tumor samples. We have developed a Mena<sup>INV</sup> isoform-specific monoclonal antibody and used it to examine Mena<sup>INV</sup> expression patterns in mouse mammary and human breast tumors. Mena<sup>INV</sup> expression increases during tumor progression and to examine the relationship between Mena<sup>INV</sup> expression and markers for epithelial or mesenchymal status, stemness, stromal cell types and hypoxic regions. Further,

while Mena<sup>INV</sup> robustly expressed in vascularized areas of the tumor, it is not confined to cells adjacent to blood vessels. Altogether, these data demonstrate the specificity and utility of the anti-Mena<sup>INV</sup>-isoform specific antibody, and provide the first description of endogenous Mena<sup>INV</sup> protein expression in mouse and human tumors.

**Keywords** Breast cancer · Mena · Hypoxia · Stemness · Microenvironment · Metastasis

## Abbreviations

DCIS	Ductal carcinoma in situ
EGF	Epidermal growth factor
EMT	Epithelial to mesenchymal transition
FFPE	Formalin fixed paraffin embedded
GFP	Green fluorescent protein
IP	Immunoprecipitation
LN	Lymph node
SMA	Smooth muscle actin
TMEM	Tumor microenvironment of metastasis

Madeleine J. Oudin and Shannon K. Hughes have contributed equally to this work.

**Electronic supplementary material** The online version of this article (doi:[10.1007/s10585-015-9775-5](https://doi.org/10.1007/s10585-015-9775-5)) contains supplementary material, which is available to authorized users.

✉ Madeleine J. Oudin  
mjoudin@mit.edu

- <sup>1</sup> Koch Institute for Integrative Cancer Research, MIT, 76-317, 77 Massachusetts Ave, Cambridge, MA 02139, USA
- <sup>2</sup> Department of Biological Engineering, MIT, Cambridge, MA 02139, USA
- <sup>3</sup> Department of Anatomy and Structural Biology, Albert Einstein College of Medicine, Bronx, NY 10461, USA
- <sup>4</sup> Department of Biology, MIT, Cambridge, MA 02139, USA
- <sup>5</sup> Integrated Imaging Program, Albert Einstein College of Medicine, Bronx, NY 10461, USA

## Introduction

While metastasis remains the leading cause of death in cancer patients, the molecular mechanisms driving this process are incompletely understood. Changes within the primary tumor itself or in the microenvironment can lead to local invasion and ultimately metastasis. For example, during the epithelial to mesenchymal transition (EMT), cells can undergo changes in gene expression which endow carcinoma cells with aggressive, metastatic characteristics [1]. Increased matrix stiffening, collagen crosslinking and

integrin-dependent focal adhesion are also associated with breast tumorigenesis and can promote progression to an invasive and metastatic phenotype [2, 3]. Hypoxia, via stabilization of hypoxia-inducible factor (HIF1 $\alpha$ ), regulates the expression of multiple genes that can lead to changes in anaerobic metabolism, angiogenesis, invasion and survival [4]. Finally, the tumor stroma plays an important role in promoting metastasis as recruitment of macrophages or bone marrow derived cells to the primary tumor site can increase cell migration, invasion and intravasation [5].

Mena, a member of the Ena/VASP family, is a known regulator of actin polymerization and cell:matrix, and cell:adhesion that is upregulated in various human epithelial tumors, including breast, pancreas, lung, colon and cervix [6]. In the MMTV–PyMT genetic model of breast cancer, genetic ablation of Mena significantly reduces in vivo tumor cell motility, intravasation and metastasis without altering mammary tumor burden, growth or histologic progression to carcinoma [7]. Mena-expressing cells are components of tumor microenvironment of metastasis (TMEM), tripartite structures comprised of a Mena-expressing tumor cell, an endothelial cell and a macrophage all contacting each other. TMEMs are sites of intravasation in mouse mammary tumors [8], and TMEM density correlates with risk of distant metastasis in ER–/HER2+ breast cancer patients [9, 10].

During tumor progression, Mena is alternatively spliced to produce multiple isoforms that can affect tumor cell phenotypes in different ways [6]. Expression of Mena11a, an isoform of Mena that contains an additional 21 amino acids in the EVH2 domain of Mena, is highly expressed in primary tumor cells, but downregulated in invasive cells [11], and has been shown to decrease motility in vivo and dampen invasion responses to EGF [12]. In two patient cohorts, quantitative immunofluorescence of a biomarker Mena<sup>calc</sup> derived from the difference in expression levels of all Mena isoforms (“panMena”) and Mena11a showed that high Mena<sup>calc</sup> levels are associated with poor disease-specific survival [13, 14].

Conversely, inclusion of the 19-amino acid sequence encoded by the ‘INV’ exon (Fig. 1a) in Mena promotes invasion, intravasation and metastasis by sensitizing cells to EGF, subsequently allowing them to invade in response to low concentrations of growth factor [12, 15]. Notably, the lack of a sensitive isoform-specific antibody capable of detecting Mena<sup>INV</sup> in tumors has necessitated use of RT-PCR analysis of mRNA isolated from dissociated tumor tissues as a proxy for the protein. Using xenograft and spontaneous breast tumor models, we found that expression of Mena<sup>INV</sup> mRNA is comparatively high in invasive cells collected by EGF chemotaxis from the primary tumor [11]. Furthermore, in cells isolated from fine needle aspirates (FNA) of breast human tumors, Mena<sup>INV</sup> mRNA levels

were relatively higher in the subset of tumor cells that had traversed a human endothelial cell monolayer in in vitro intravasation assays [16]. Finally, in human breast cancer patients, relative levels Mena<sup>INV</sup> mRNA in FNA biopsies from freshly resected breast tumor samples were observed to correlate with the number of TMEM sites found histological sections from the matched tumor tissue [16, 17]. However, the abundance and distribution of Mena<sup>INV</sup> protein within primary tumors have not yet been determined. Given the relatively high expression of Mena<sup>INV</sup> in invasive tumor cell subpopulations, and the ability of Mena<sup>INV</sup> expression to enhance microenvironment-dependent metastatic phenotypes, reagents that allow for analysis of Mena<sup>INV</sup> protein levels and distribution within histological sections of patient tumors might be used to gain insight into the biology of tumor progression and, potentially, as a prognostic biomarker.

Using a newly generated isoform-specific antibody validated in three assays, we show that Mena<sup>INV</sup> protein expression increases during tumorigenesis and progression and is correlated with blood vessel density. Furthermore, we show that while Mena<sup>INV</sup> expression is inversely correlated with E-cadherin, it is not restricted to mesenchymal-like cells, is not detected in stromal cells, and does not correlate with increased proliferation, stemness, macrophage density, or hypoxia. These results provide insight into the spatiotemporal distribution of Mena<sup>INV</sup> within primary tumors, key information needed to develop models to describe its pro-metastatic effects, and provide the basis for evaluating Mena<sup>INV</sup> as potential biomarker for clinical use.

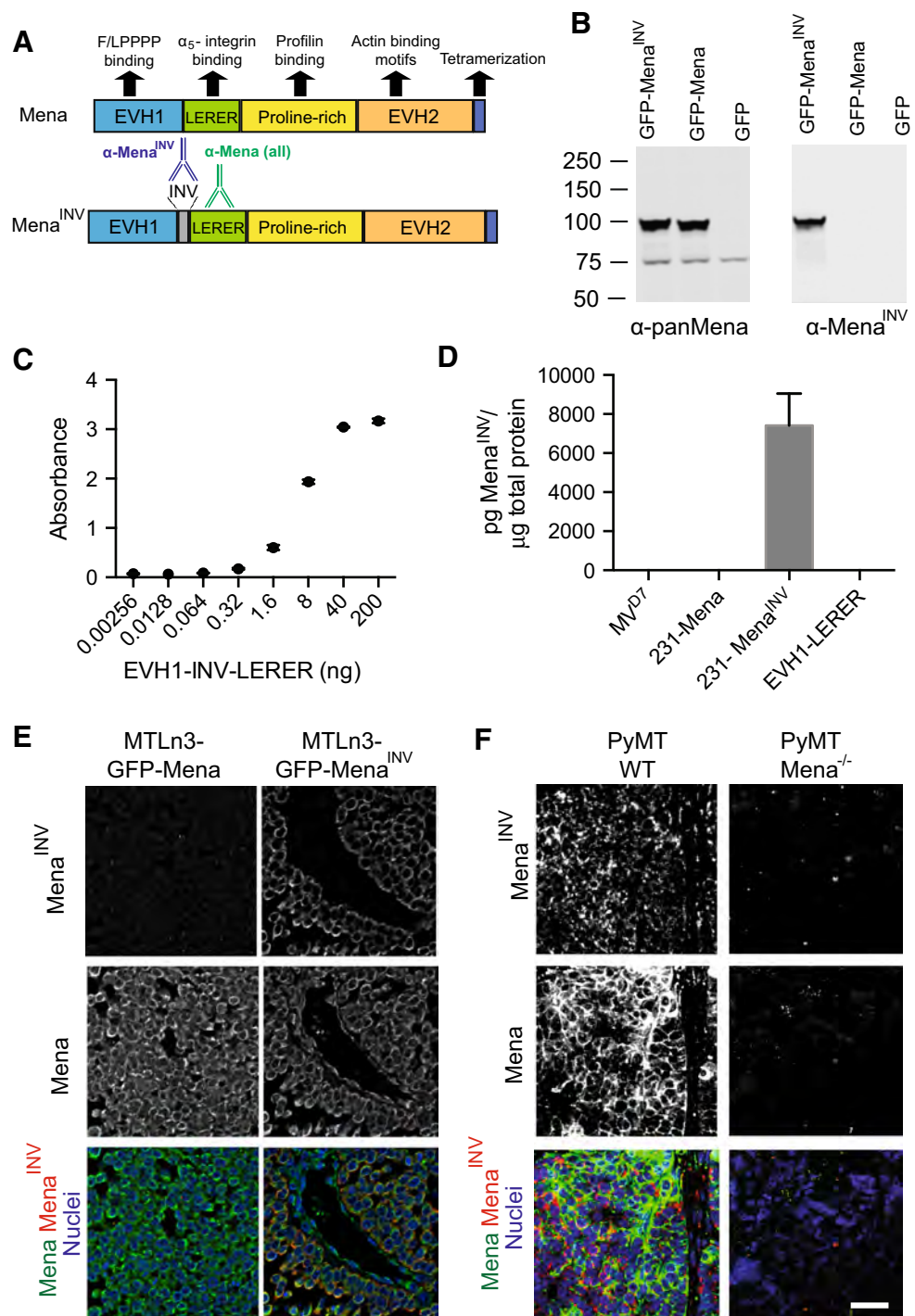
## Results

### Validation of the Mena<sup>INV</sup> antibody for use in western blot, ELISA and immunohistochemistry

To analyze Mena<sup>INV</sup> protein expression and distribution, we developed an isoform-specific monoclonal antibody that selectively recognizes the 19aa sequence (identical in human and mouse) encoded by the INV exon (“anti-INV”) [18] (Fig. 1a). Anti-INV recognized GFP-Mena<sup>INV</sup>—but not GFP-Mena or GFP alone—in western blots of lysates of MDA-MB231 cells that express the corresponding constructs. Anti-panMena, which recognizes all known Mena isoforms [19], detected ectopic GFP-Mena, GFP-Mena<sup>INV</sup> and endogenous Mena (Fig. 1b). We developed an ELISA assay to detect and to quantify Mena<sup>INV</sup> levels in protein lysates. We confirmed the specificity of the ELISA assay using two peptides expressing either EVH1-LERER or EVH1-INV-LERER. Increasing the concentration of the EVH1-INV-LERER peptide correlated with an increase in



**Fig. 1** Validation of the Mena<sup>INV</sup> antibody. **a** Schematic diagram of cancer-relevant alternatively spliced Mena isoforms and in-house antibodies utilized for detection. **b** Western blot of MDA-MB231 cells overexpressing GFP, GFP-Mena or GFP-Mena<sup>INV</sup>. Mena<sup>INV</sup> antibody only recognizes GFP-Mena<sup>INV</sup>, while the Mena antibody recognizes both isoforms. **c** Standard curve for Mena<sup>INV</sup> ELISA assay, plotting concentration of pure recombinant protein EVH1-INV-LERER versus absorbance. Protein concentrations were estimated by comparison to purified recombinant Mena<sup>INV</sup> mini-protein. **d** Mena<sup>INV</sup> protein concentration in MV<sup>D7</sup> fibroblasts, 231-Mena and 231-Mena<sup>INV</sup> cultured cells, and using EVH1-LERER as a negative control, quantified by sandwich ELISA using anti-panMena for capture and anti-Mena<sup>INV</sup> for detection. **e** Representative images of FFPE sections from Mtn3 tumors expressing GFP-Mena or GFP-Mena<sup>INV</sup>, stained with Mena (green), Mena<sup>INV</sup> (red) and DAPI (blue). Similarly, Mena<sup>INV</sup> antibody only recognizes GFP-Mena<sup>INV</sup>, while the Mena antibody recognizes both isoforms. **f** Staining for Mena and Mena<sup>INV</sup> on an FFPE section from a wild-type PyMT mouse or a PyMT mouse null for Mena. Scale bar is 30  $\mu$ m. (Color figure online)



signal as detected by the ELISA assay, while no signal was detected with the EVH1-LERER peptide (Fig. 1c). We then measured Mena<sup>INV</sup> expression in lysates collected from MV<sup>D7</sup> fibroblasts, which lack all three Ena/VASP proteins [20], MDA-MB-231 cells expressing ectopic GFP-Mena (“231-Mena”) or GFP-Mena<sup>INV</sup> (“231-Mena<sup>INV</sup>”). Using the ELISA assay, no signal above the assay detection limit for Mena<sup>INV</sup> was detected in MV<sup>D7</sup> fibroblasts, or

231-Mena cells; while a strong signal was detected in 231-Mena<sup>INV</sup> cells (Fig. 1d). Together, these data confirmed the specificity of the antibody and quantitative nature of the ELISA assay.

Given that we have shown that at the mRNA level, Mena<sup>INV</sup> expression is enriched in invasive cell populations of xenograft tumors, PyMT tumors [21], and in FNA biopsies of human breast tumors [16], we were interested in

visualizing the distribution of Mena<sup>INV</sup> protein within tumors. The Mena<sup>INV</sup> antibody was validated for use and specificity in staining of formalin-fixed paraffin embedded (FFPE) tumor sections by comparing anti-INV signals in xenografts of cells expressing GFP-Mena<sup>INV</sup> or GFP-Mena (Fig. 1e). As expected, strong signal for Mena<sup>INV</sup> was observed in GFP-Mena<sup>INV</sup> xenograft tissue sections, but absent in GFP-Mena tumor sections. Secondly, we examined mammary carcinomas arising from transgenic MMTV-PyMT expression and found that Mena<sup>INV</sup> was heterogeneously distributed in this model. Furthermore, as expected we did not detect specific Mena<sup>INV</sup> signal in tissue sections of tumors isolated from Mena knockout mice carrying the MMTV-PyMT transgene, used here as a negative control (Fig. 1f). These data confirm the specificity and utility of the antibody for use in immunodetection of Mena<sup>INV</sup> in FFPE tissue sections.

### **Mena<sup>INV</sup> expression in tumors is heterogeneous, but increases during progression in mouse and human samples**

Next, we examined Mena and Mena<sup>INV</sup> staining in normal mammary gland fat pad tissue and in advanced MMTV-PyMT tumors by immunofluorescence of FFPE sections (Fig. 2a, b). While Mena is widely expressed in ducts, we found low, heterogeneous staining for Mena<sup>INV</sup> in normal ductal structures within the mammary gland, with significantly stronger Mena<sup>INV</sup> staining intensity in tumor tissue (Fig. 2c). We then asked if Mena<sup>INV</sup> is expressed in cells within non-invasive tumor structures with intact basement membranes, marked by staining with Laminin, and found that Mena<sup>INV</sup> detectable in encapsulated pre-invasive tumor structures.

We then studied the relationship between Mena and Mena<sup>INV</sup> expression during tumor progression in the MMTV-PyMT model [22]. Overall, we observed heterogeneous Mena<sup>INV</sup> staining in subsets of Mena-expressing cells in MMTV-PyMT tumors (Fig. 2e). Specifically, there were significant increases in both Mena and Mena<sup>INV</sup> staining in both adenoma and carcinoma tumor regions relative to hyperplasia (Fig. 2f, g). Together, these data suggest that in the MMTV-PyMT model Mena and Mena<sup>INV</sup> expression increases during progression from hyperplasia to adenoma, with no further increases during progression to carcinoma.

Next, we examined Mena and Mena<sup>INV</sup> protein expression and localization in a small cohort of both metastatic and non-metastatic human breast tumors (tumor characteristics described in Fig S1). We found that while Mena is expressed at high levels in ductal structures in non-metastatic tumors (Fig. 3a–c) only low levels of Mena<sup>INV</sup>

were detected. As shown in the PyMT mouse model, we found robust levels of Mena<sup>INV</sup> in structures characterized as ductal carcinoma in situ (DCIS), which are known to contain an intact basement membrane (Fig. 3d–f), with both isoforms expressed in these tissues. Finally, relatively higher levels of Mena<sup>INV</sup> were observed in metastatic patients. Patients with metastatic disease showed increased percentage of cells expressing Mena<sup>INV</sup> (Fig. 3j), as well as increased levels of Mena<sup>INV</sup>, as detected by quantitative immunofluorescence (Fig. 3l). Levels of Mena were not significantly different between non-metastatic and metastatic cases (Fig. 3k). Overall, these data demonstrate that Mena<sup>INV</sup> expression increases during tumor progression in both mouse and human tumors.

### **Mena<sup>INV</sup> is not expressed in macrophages, endothelial cells or fibroblasts**

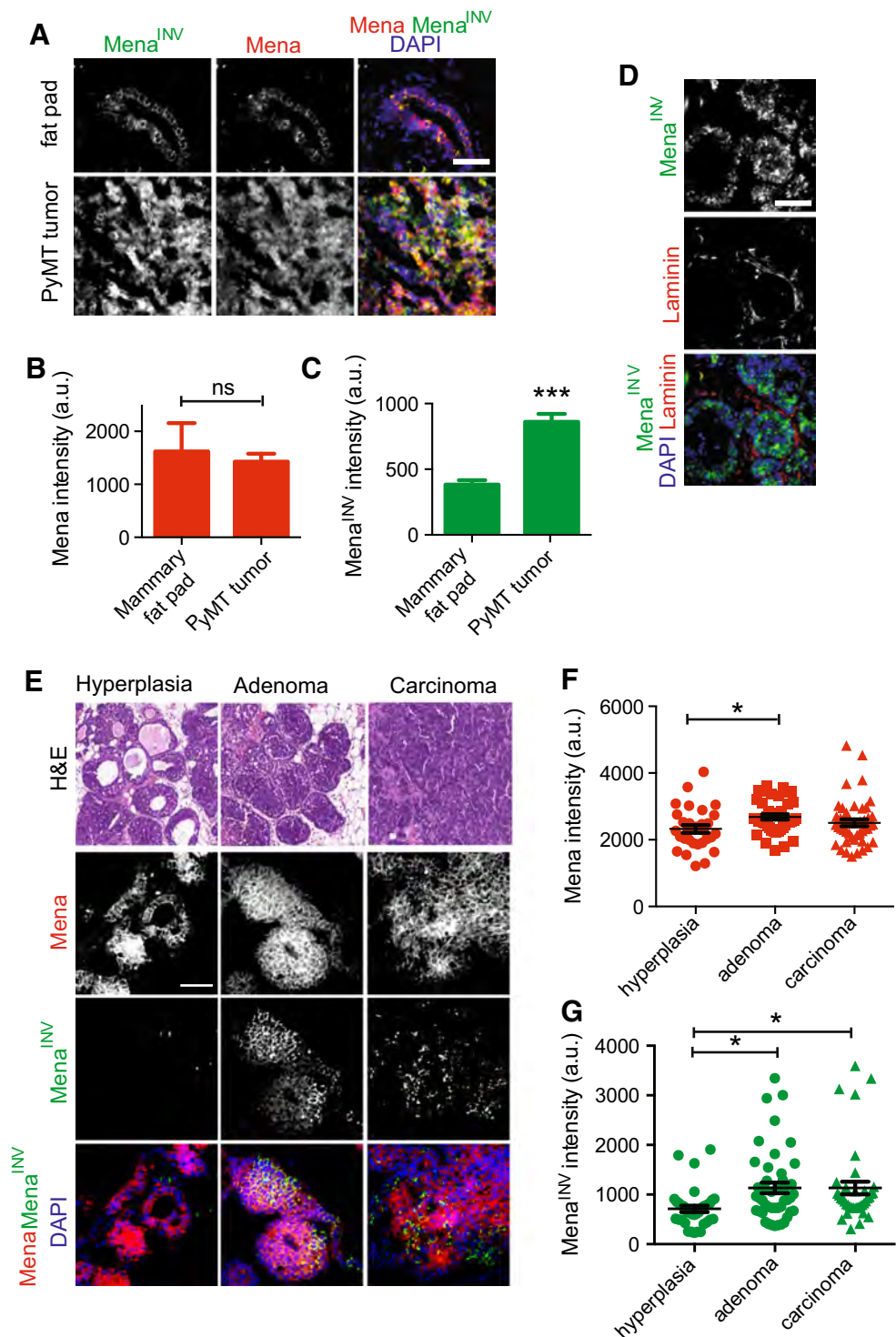
The tumor microenvironment is composed of a variety of tumor and stromal cells, which can also contribute to tumor progression [5]. We were interested in investigating whether Mena<sup>INV</sup> was expressed in endothelial cells, macrophages and fibroblasts within tumors. We used established markers to stain for all three subpopulations in PyMT tumors: Iba1 for macrophages (Fig. 4a);  $\alpha$ SMA (smooth muscle actin) for fibroblasts (Fig. 4b); CD31 for endothelial cells (Fig. 4c). We did not detect Mena<sup>INV</sup> signal in any of the cells expressing these markers and conclude that Mena<sup>INV</sup> is either absent or expressed at low levels in these stromal subtypes.

### **Mena<sup>INV</sup> expression is not restricted to cells that have undergone EMT**

To characterize the identity of the cells that express Mena<sup>INV</sup> in the tumor compartment, we compared the distribution of anti-INV staining to markers of tumor cell phenotype. First, we wondered if expression of Mena<sup>INV</sup> was associated with EMT, a process that has been associated with increased metastatic potential [23]. Antibodies to E-Cadherin and vimentin, markers for epithelial and mesenchymal phenotypes respectively, were used to examine levels of Mena<sup>INV</sup> varied throughout mouse and human tumors in relation to EMT. Line scans of the signal intensities showed regions that appeared to have relatively high Mena<sup>INV</sup> and low E-cadherin signals (Fig. 5a). Quantitative analysis throughout entire image fields revealed a significant, inverse correlation between relative levels of Mena<sup>INV</sup> and of E-cadherin (Fig. 5b, c): Mena<sup>INV</sup> was detected in 62 and 74 % of vimentin positive cells in human and mouse tumors, respectively (Fig. 5d), however,

**Fig. 2** Mena<sup>INV</sup> expression increases during tumor progression. **a** Representative images of FFPE sections from a normal mammary fat pad tissue from an adult mouse and an advanced MMTV-PYMT tumor stained for Mena, Mena<sup>INV</sup> and DAPI. Scale bar is 30  $\mu$ m. Quantification of Mena (**b**) and Mena<sup>INV</sup> (**c**) staining intensity in mammary fat pad versus advanced tumor.

**d** Representative images of FFPE sections from an MMTV-PYMT tumor stained for Mena<sup>INV</sup>, the basement member laminin and DAPI. Scale bar is 30  $\mu$ m. **e** Representative images of areas from MMTV-PyMT tumor sections depicting hyperplasia, adenoma and carcinoma tumor. H&E image depicts histology of area chosen for for Mena, Mena<sup>INV</sup> and DAPI staining. Scale bar is 100  $\mu$ m for H&E image, and 30  $\mu$ m for fluorescent images. Quantification of Mena (**f**) and Mena<sup>INV</sup> (**g**) staining intensity in different areas of PyMT tumors. Data pooled from four tumors, with at least four fields of view per sample. Each dot represents a field of view. Asterisk indicates significant difference by *t* test (\**p* < 0.05)



vimentin was detected in only 27 and 18 % of Mena<sup>INV</sup> - positive cells in human and mouse tumors, respectively. Together, these results indicate that while Mena<sup>INV</sup> protein distribution is inversely correlated with E-Cadherin, it is observed frequently in cells lacking vimentin, a canonical marker for passage through EMT.

#### Mena<sup>INV</sup> expression is not enriched with cells expressing proliferation and stem cell markers

More recently, EMT has been associated with the gain of stem cell characteristics, which endow cells with the ability to metastasize and colonize more efficiently [24]. We



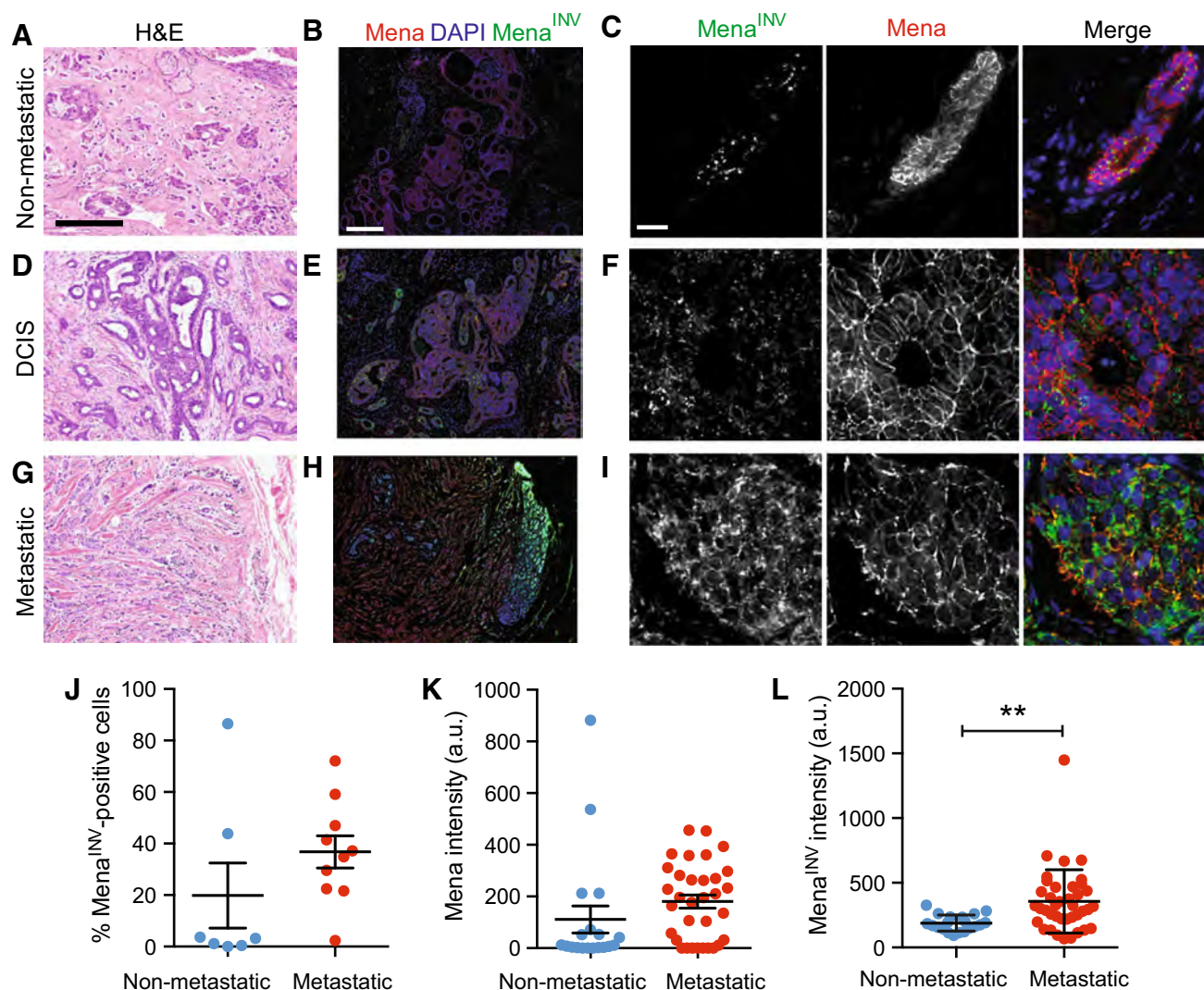


**Fig. 3** Mena<sup>INV</sup> expression patterns in human breast cancer. Representative images of human breast tumor FFPE sections with H&E staining (a, d, g), low (b, e, h) and high (c, f, i) magnification images of immunofluorescence staining for Mena (red) and Mena<sup>INV</sup> (green). Images are from a non-metastatic (a–c), DCIS (d–f) and metastatic tumor (g–i). Scale bar for a, d, g is 300  $\mu$ m, for b, e, h is 100 and 30  $\mu$ m for c, f, i. j Quantification of the percentage of total

cells (as counted by DAPI staining) expressing Mena<sup>INV</sup> within a 40X field. Quantification of Mena (k) and Mena<sup>INV</sup> (l) staining intensity in non-metastatic and metastatic human tumor samples. Data pooled for three metastatic and three non-metastatic samples, with at least three fields of view per sample. Each dot represents a field of view. Asterisk indicates significant difference by *t* test (\*\**p* < 0.01). (Color figure online)

investigated whether expression of Mena<sup>INV</sup> was associated with the proliferation or acquisition of stem cell characteristics. First, we examined the proliferation levels of Mena<sup>INV</sup>-positive cells, by staining for the proliferation marker Ki67 (Fig. 6a). In both mouse and human tumors, approximately 30 % of Mena<sup>INV</sup> cells were Ki67-positive. Conversely, approximately 50 % of Ki67-positive cells were Mena<sup>INV</sup>-positive (Fig. 6b, c). These data suggest that Mena<sup>INV</sup> expression is not restricted to highly proliferative cells. Secondly, we examined Mena<sup>INV</sup> expression relative to two known stem cell markers in mouse PyMT tumors, ALDH and CD133, whose expression has been associated

with stemness (Fig. 6d). Indeed, recent studies have shown that cells expressing high levels of CD133 showed higher invasive potential and drug resistance, while cells that were ALDH- and CD133-positive were highly tumorigenic [25–27]. As expected, we observed a positive correlation between CD133 and ALDH expression (Fig. 6e); however, no significant association between cells expressing Mena<sup>INV</sup> and those expressing canonical stem cell markers. Only 15 and 23 % of Mena<sup>INV</sup>-positive cells expressed CD133 or ALDH, respectively (Fig. 6f, h). Similarly, approximately 28 and 41 % of CD133- and ALDH-positive cells, respectively, expressed Mena<sup>INV</sup> in PyMT tumors

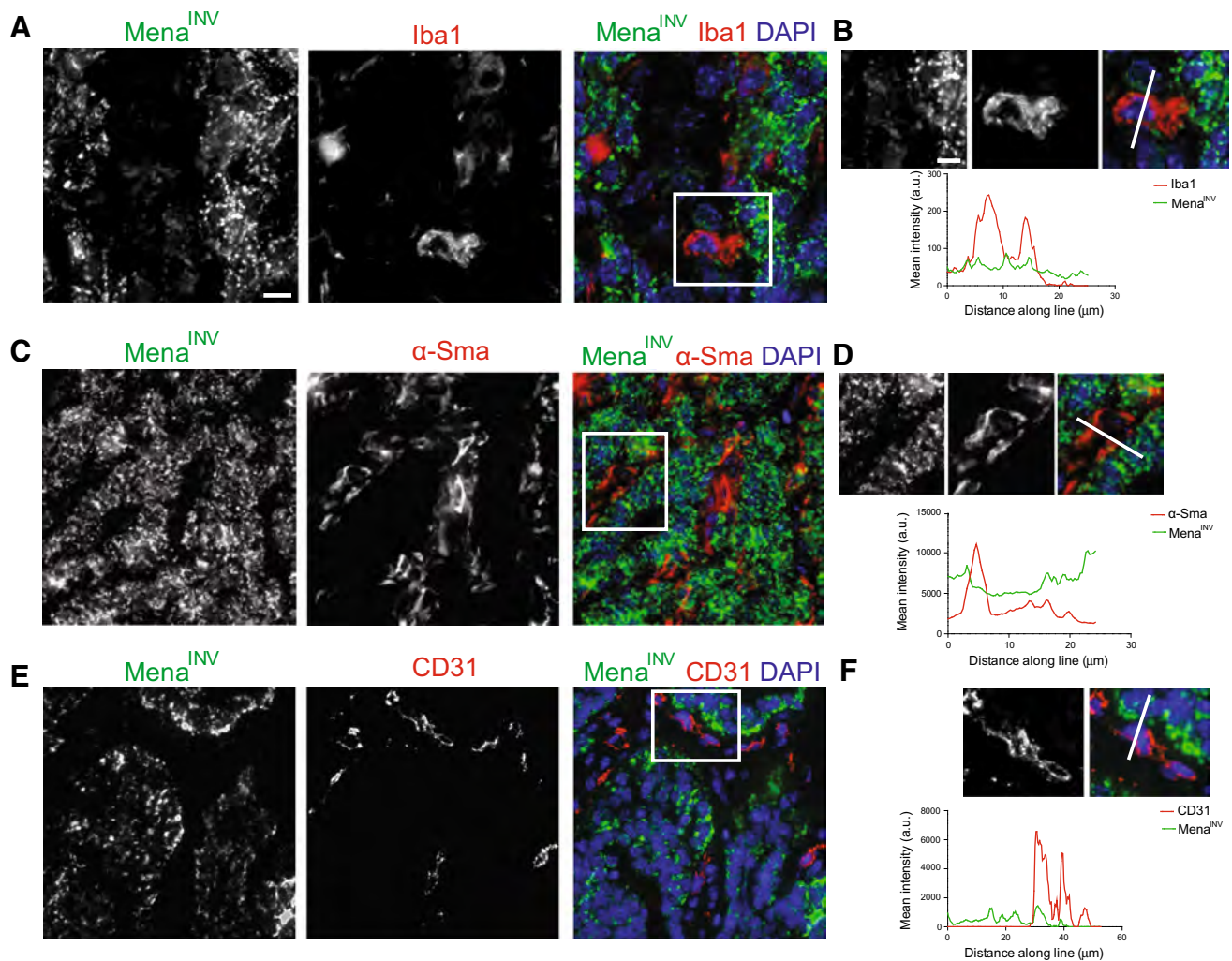


**Fig. 4** Mena<sup>INV</sup> expression is restricted to the tumor compartment. Representative images of staining for Mena<sup>INV</sup> and the macrophage marker Iba1 (a, b), the fibroblast marker αSMA (c, d) and the

endothelial cell marker CD31 (e, f). b–d Magnification of boxed area and signal intensity for both markers is quantified along the white line. Scale bar for a, c, e is 30 and 10 μm for b, d, f

(Fig. 6f, h). These data indicate that Mena<sup>INV</sup> is expressed in both stem and non-stem cell populations within advanced tumors. We compared Mena<sup>INV</sup> and CD133 or ALDH staining intensity in different regions of PyMT tumors and observed no significant correlation between Mena<sup>INV</sup> signal and the levels of these stem cell markers.

#### Mena<sup>INV</sup> expression is high in vascularized tumor areas

Dissemination of primary tumor cells occurs primarily through the vasculature and lymphatics. We examined patterns of Mena<sup>INV</sup> expression relative to blood vessels in mouse and human tumors. In both mouse and human

tumors, we found that Mena<sup>INV</sup> expression was not restricted to cells adjacent to blood vessels (Fig. 7a, b). However, there was a significant correlation between Mena<sup>INV</sup> expression levels and blood vessel density in both non-metastatic and metastatic human tumors (Fig. 7c). Together, these data confirm that while Mena<sup>INV</sup> expression is associated with higher blood vessel density, it is not restricted to expression in cells adjacent to the vasculature.

Blood vessel density can also affect oxygen levels within a tumor, which in turn, can drive metastatic phenotypes. Using hypoxyprobe to label hypoxic tumor areas [28], we quantified Mena<sup>INV</sup> staining intensity in PyMT–MMTV tumors relative to hypoxia (Fig. 7d, e) and determined that Mena<sup>INV</sup> expression was not restricted to hypoxic areas within the tumor.

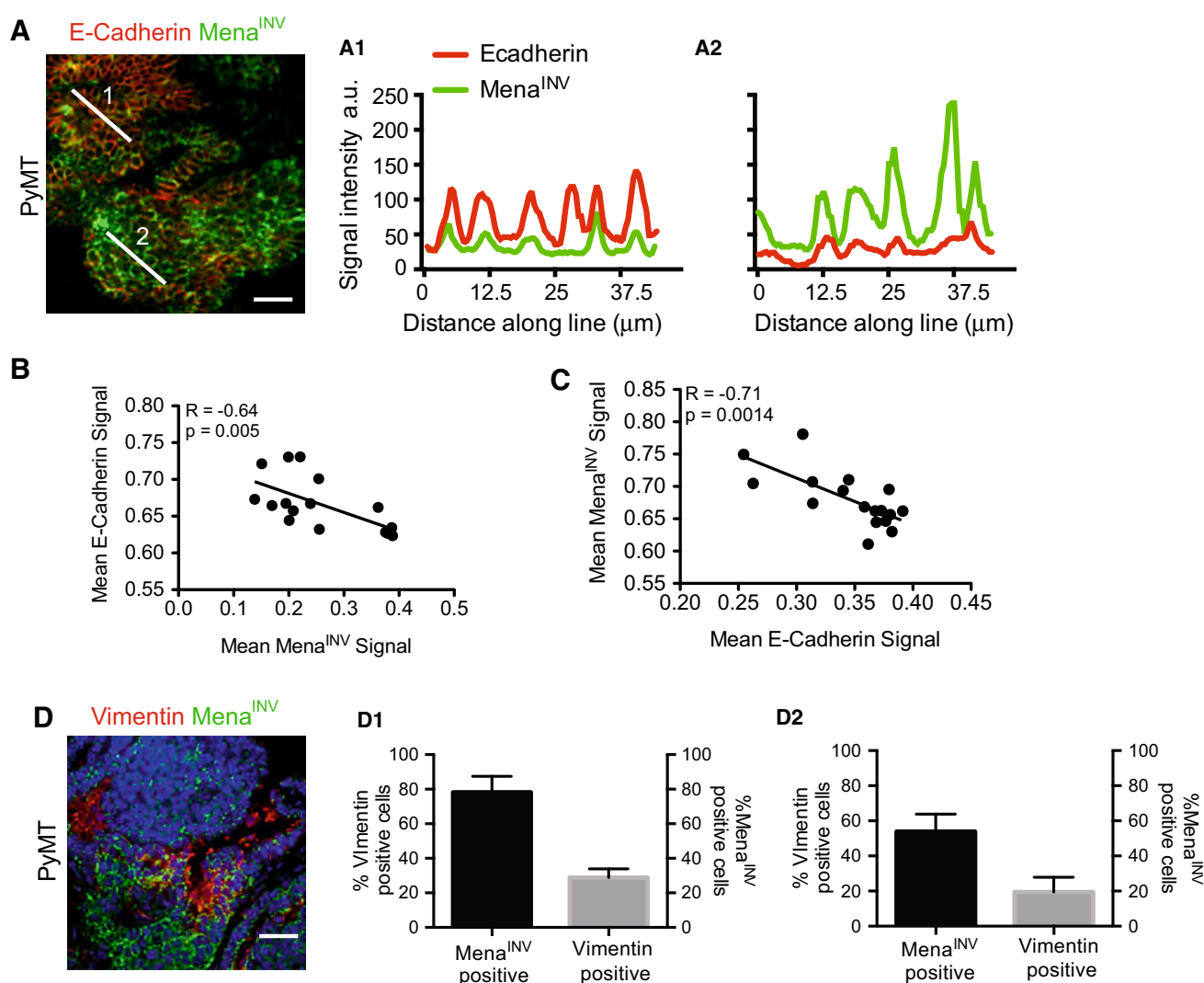


**Fig. 5** Mena<sup>INV</sup> expression and EMT markers. **a** MMV-PyMT tissue section stained for Mena<sup>INV</sup> (green) and the epithelial marker E-cadherin (red). **a1-2** Intensity of Mena<sup>INV</sup> and E-cadherin signal along two lines shown in **a**. **b** Mean fluorescence signal intensity plotted for Mena<sup>INV</sup> intensity >0.55 and E-cadherin intensity <0.5. **c** Mean fluorescence signal intensity plotted for E-cadherin intensity >0.55 and Mena<sup>INV</sup> intensity <0.5. Raw pixel values were normalized by the range of intensities in each image.  $n = 5$  mice, three image fields per tumor. **d** MMTV-PyMT tissue section stained for Mena<sup>INV</sup> (red) and vimentin (green). **d1** Black bar quantifies the

fraction of vimentin-positive cells that are also Mena<sup>INV</sup>-positive, grey bar quantifies the fraction of Mena<sup>INV</sup>-positive cells that are also vimentin-positive. Results are shown as mean  $\pm$  SEM = 2 mice, 5–7 image fields per tumor for **f, g**. Scale bar = 20  $\mu$ m for **f, g**. **d2** Black bar quantifies the fraction of vimentin+ cells that are also Mena<sup>INV</sup>+ in human sections, grey bar quantifies the fraction of Mena<sup>INV</sup>-positive cells that are also vimentin+. Results are shown as mean  $\pm$  SEM,  $n = 2$ , 5–7 image fields per tumor for **f, g**. (Color figure online)

## Discussion

The data presented here provide the first characterization of endogenous Mena<sup>INV</sup> protein expression in mouse breast cancer models and in human invasive ductal carcinomas. Our studies reveal that expression of Mena<sup>INV</sup> is heterogeneously distributed in tumors and that Mena<sup>INV</sup> expression can be detected in early tumors with increasing levels during early tumor progression. Our comparison of Mena<sup>INV</sup> staining to the distributions of well-established

markers provides insight into the nature of the tumor cells that express Mena<sup>INV</sup>.

We developed a Mena<sup>INV</sup> isoform-specific monoclonal antibody, and demonstrated its specificity and functionality in ELISA and Western blot assays, and for immunodetection of endogenously expressed protein in human and mouse sections of FFPE tumor tissue. Our analysis provides important information on the properties of cells that express Mena<sup>INV</sup>, allowing us to gain further insight into the potential mechanisms by which it drives metastasis. We



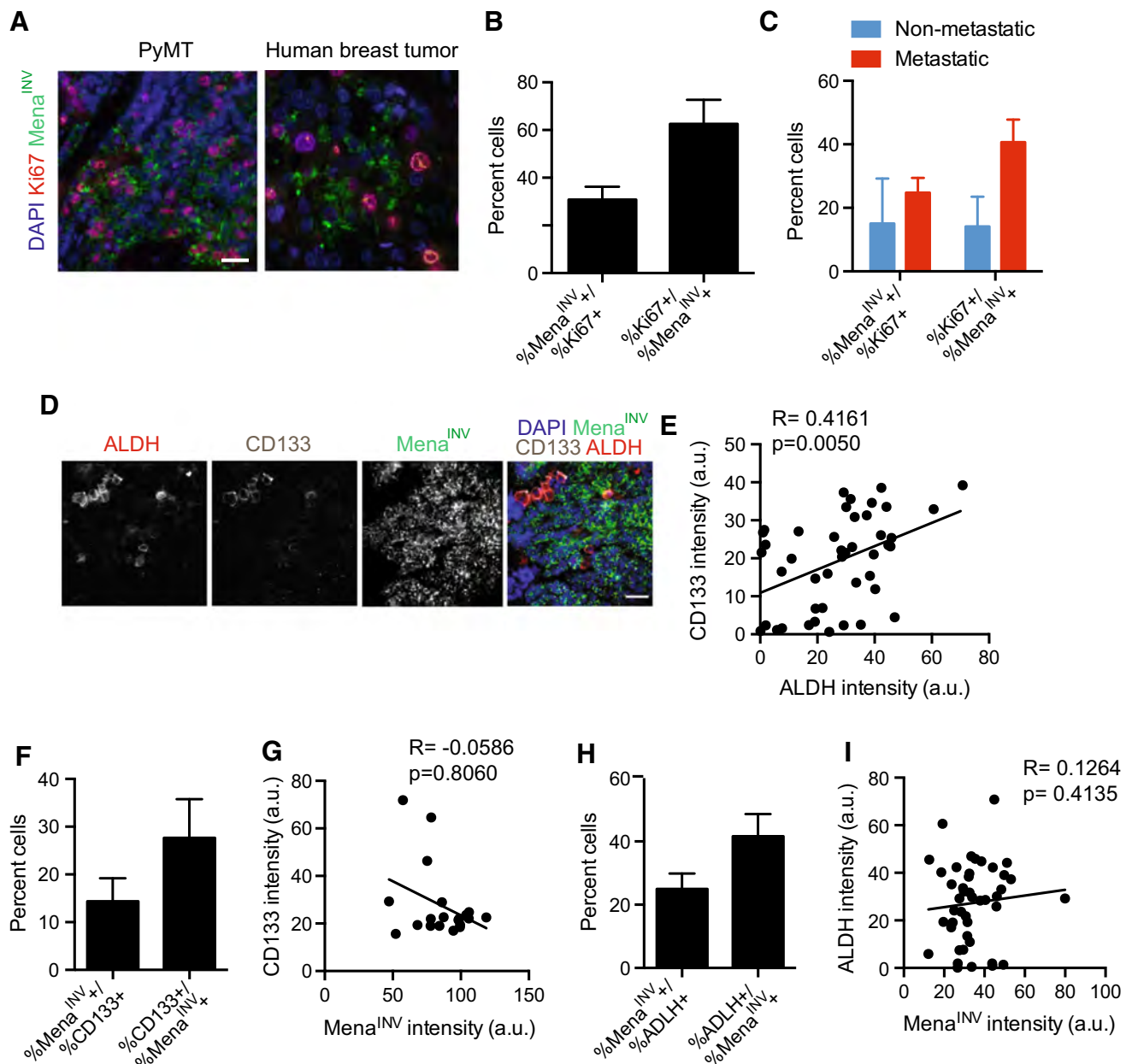


**Fig. 6** Mena<sup>INV</sup> expression is not restricted to cancer stem cells. **a** Representative images of PyMT tumors and human breast tumors stained for Mena<sup>INV</sup> (green) and Ki67 (red). Scale bar is 30  $\mu$ m. **b** Quantification of the fraction of Mena<sup>INV</sup>-positive cells that are also Ki67-positive and the fraction of Ki67-positive cells that are also Mena<sup>INV</sup>-positive in mouse PyMT tumors. Results are shown as mean  $\pm$  SEM, n = 2 mice, five image fields per mouse. **c** Quantification of the fraction of Mena<sup>INV</sup>-positive cells that are also Ki67-positive and the fraction of Ki67-positive cells that are also Mena<sup>INV</sup>-positive in human breast tumors from metastatic and non-metastatic patients. Results are shown as mean  $\pm$  SEM, n = 3 tumors, five image fields per tumor. **d** Representative images of PyMT tumors

stained for Mena<sup>INV</sup> (green) and the stem cell markers ALDH (red) and CD133 (blue). **e** Positive correlation between staining intensity for CD133 and ALDH in PyMT sections. **e** Quantification of the fraction of Mena<sup>INV</sup>-positive cells that are also CD133-positive and the fraction of CD133-positive cells that are also Mena<sup>INV</sup>-positive in mouse PyMT tumors. **f** Correlation between Mena<sup>INV</sup> and CD133 staining intensity in PyMT tumors. **g** Quantification of the fraction of Mena<sup>INV</sup>-positive cells that are also ALDH-positive and the fraction of ALDH-positive cells that are also Mena<sup>INV</sup>-positive in mouse PyMT tumors. **f** Correlation between Mena<sup>INV</sup> and ALDH staining intensity in PyMT tumors. Results are shown as mean  $\pm$  SEM, n = 4 tumors, 3–5 image fields per sample. (Color figure online)

show that Mena<sup>INV</sup> expression is not enriched in cells with increased proliferation as identified by Ki67, or stemness, as identified by cancer stem cell markers CD133 and

ALDH. Furthermore, we show that within the tumor microenvironment, Mena<sup>INV</sup> expression is absent from macrophages, endothelial cells and fibroblasts, suggesting

**Fig. 7** Mena<sup>INV</sup> expression is high in vascularized areas.

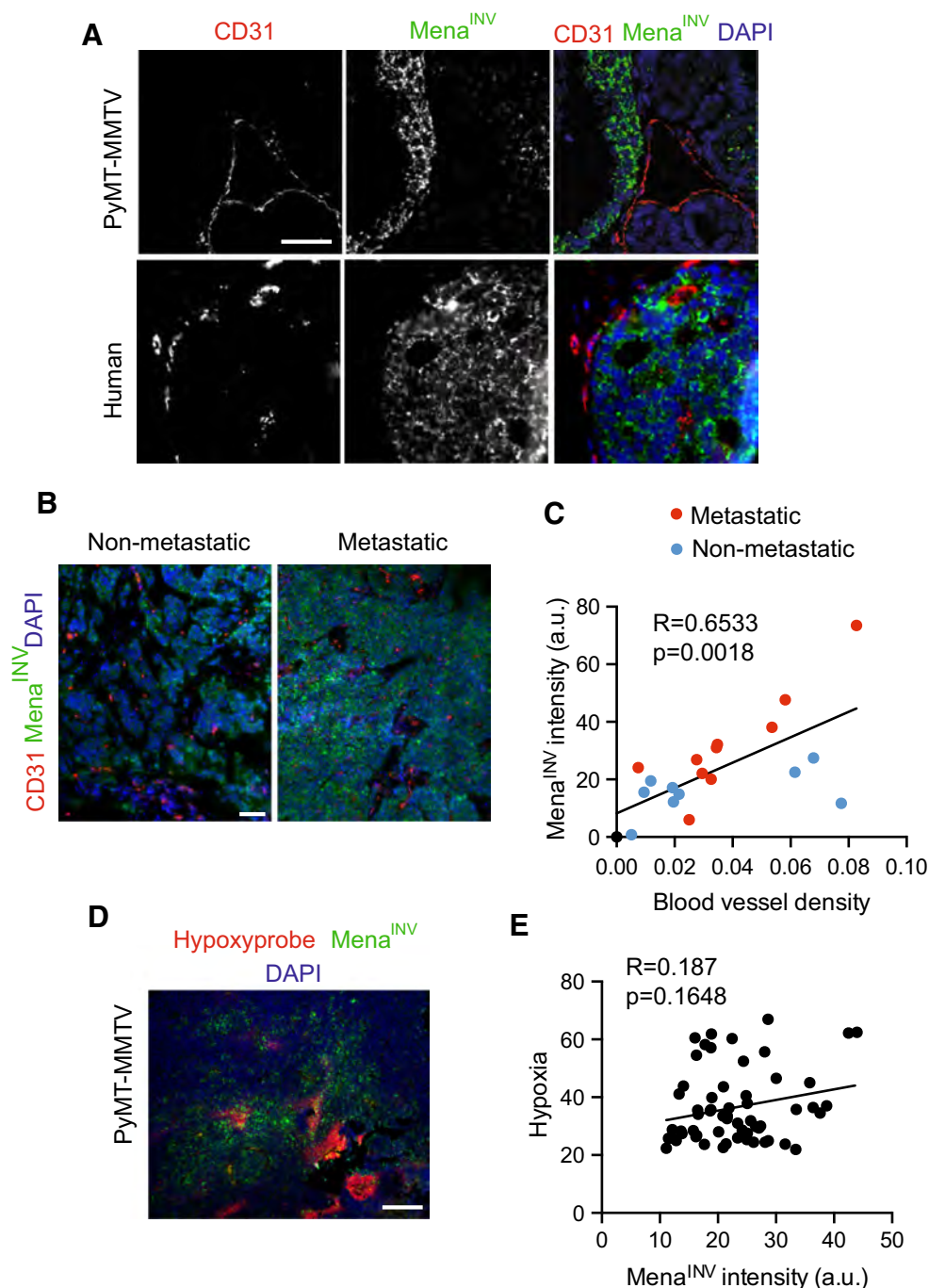
**a** MMTV-PyMT and human tissue section stained for Mena<sup>INV</sup> (green) and the endothelial marker CD31 (red). Scale bar is 30  $\mu$ m.

**b** Representative images of human breast tumors from a metastatic and non-metastatic tumor, showing staining for Mena<sup>INV</sup> (green) and the endothelial marker CD31 (red). Scale bar is 100  $\mu$ m.

**c** Correlation between blood vessel density and Mena<sup>INV</sup> staining intensity in human breast tumors. Data pooled for three metastatic and three non-metastatic samples, with 2–3 fields of view per sample. Each dot represents a field of view.

**e** Representative image from an MMTV-PyMT tumor stained for Mena<sup>INV</sup> and hypoxic areas, which were detected using the Hypoxyprobe. Scale bar is 100  $\mu$ m.

**f** Correlation between hypoxia (as measured by intensity of the Hypoxyprobe staining) and Mena<sup>INV</sup> staining intensity in PyMT-MMTV tumors. Data pooled from 2 tumors, with over 40 fields of view analyzed. Each dot represents a field of view. (Color figure online)



it is likely restricted to the tumor compartment. Finally, we show that while expression of Mena<sup>INV</sup> is high in areas of high blood vessel density, it is heterogeneous within the primary tumor and not confined to cells adjacent to blood vessels. In fact, Mena<sup>INV</sup> expression can also be detected in non- (or perhaps pre-) invasive tumor compartments with an intact basement membrane, suggesting that Mena<sup>INV</sup> is expressed early during breast cancer progression and in multiple locations. Together, these data suggest the role of

Mena<sup>INV</sup> in promoting invasion and metastasis is not restricted to a role only in perivascular tumor cells at sites of intravasation, like those found in TMEM. This finding is consistent with our previous work showing that Mena<sup>INV</sup> promotes matrix degradation, paracrine signaling with macrophages, discohesive tumor morphology and increased tumor cell motility [12, 15, 29]. As recent work demonstrates that the Mena-expressing tumor cell in TMEM is relatively stable [8], it will be interesting to



determine whether and how Mena<sup>INV</sup> may contribute to TMEM assembly and function.

We have yet to identify what aspects of the tumor microenvironment drive Mena<sup>INV</sup> expression or the identity of the splicing factor(s) responsible for INV inclusion. During tumor progression, EMT-associated transcription factors including Twist, Snail and Zeb1 drive a wide variety of alternative splicing that contribute to the mesenchymal phenotype and drive increased motility [30]. Here, we find that Mena<sup>INV</sup> expression in mouse and human tumors is not restricted to either epithelial or mesenchymal cells, suggesting that a full passage through EMT is not required for INV inclusion. A variety of other microenvironmental characteristics can facilitate tumor progression and could be responsible for promoting inclusion of INV. We initially hypothesized that increases in blood vessel density or changes in oxygen availability might drive INV inclusion. However, we found that Mena<sup>INV</sup> expression is not confined to hypoxic or highly vascularized areas within tumor, suggesting that these factors alone may not be sufficient to induce Mena<sup>INV</sup> expression.

Changes in extracellular matrix composition or mechanical stimuli and secretion of a variety of soluble factors from tumor-associated stroma or the immune system also play an important role during tumor progression. We hypothesize that stiffness changes in combination with stromal factors will inclusion of the INV exon. Future work, using in part the assays described in this manuscript, will focus on how these combined stimuli might drive Mena<sup>INV</sup> expression. Once the signals that trigger Mena<sup>INV</sup> protein accumulation are defined, it will be interesting to determine whether expression of other cancer relevant protein isoforms is regulated coordinately with Mena<sup>INV</sup>. Whether this substantial microenvironment-dependent increase in Mena<sup>INV</sup> protein arises predominately from changes in INV exon inclusion in its mRNA or involves additional levels of regulation is also under investigation.

The development of the isoform specific antibody will also help advance the development of Mena isoform assessment as prognostic markers in cancer. Efforts are currently underway to determine whether analysis of Mena<sup>INV</sup> protein levels, either alone or in combination with other prognostic metrics associated with Mena (e.g. Mena<sup>Calc</sup> [13] or TMEM [9]), provides clinically useful information. More recently, an additional Mena isoform, Mena $\Delta$ V6, has been identified in some mesenchymal-like tumor cell lines [31]. It will be interesting to compare the distributions of all Mena protein isoforms throughout tumor progression. Finally, we have shown that Mena<sup>INV</sup> expression sensitizes cells to several growth factors, whose signaling pathways are targets of clinical trials for

metastatic breast cancer [32]. Monitoring expression of Mena<sup>INV</sup> in tumors might help optimise drug treatment for specific patients, as well as provide a means to monitor for acquired resistance to tyrosine kinase inhibitors.

## Materials and methods

### Antibodies

The following antibodies were used for immunohistochemistry: CD31 (R&D Systems, AF806), Vimentin (BD, RV202), Ecadherin (CST, 24E10), panMena [19], Ki67 (CST #9037), CD133 (EBioscience, clone 13A4), ALDH (BD, Clone 44), Iba1 (Abcam ab15690),  $\alpha$ SMA (Sigma clone 1A4).

### Production of anti-INV monoclonal antibody

Rabbit monoclonal antibodies were generated by Epitomics, INC. Animals were immunized with a peptide containing the sequence encoded by the INV exon. Clones were screened for Mena<sup>INV</sup> specificity in Western blot assays and by immunostaining of FFPE tumor sections from wild type or Mena-null mice (Fig S1).

### Anti-INV ELISA

Mena<sup>INV</sup> protein levels in lysates were quantified by a custom sandwich ELISA. Anti-panMena antibody (1.8  $\mu$ g/mL) was coated overnight at 4 °C in 96-well Nunc Maxisorb plates (Sigma). After washing with PBS + 0.5 % Tween-20, assay plates were blocked at 25 °C with Licor Odyssey Blocking Buffer (Licor) and lysates were added overnight at 4 °C. Anti-Mena<sup>INV</sup> antibody (0.38  $\mu$ g/mL) was added for 2 h at 25 °C. Anti-rabbit horseradish peroxidase secondary antibody (1:4000) (Millipore) and TMB substrate (Sigma) were used for detection. Recombinant proteins that contained a 6XHIS-tagged Mena-EVH1-INV-LERER sequence or a control 6XHIS-tagged Mena-EVH1-LERER construct that lacks the 19 residue INV peptide sequence were utilized to create a standard curve via four-parameter logistic regression in MATLAB, or act as a negative control, respectively. Relative protein concentrations were normalized to total protein content in  $\mu$ g.

### Cell culture

All breast cancer cell lines were obtained from ATCC and cultured in DMEM + 10 % FBS (Hyclone). Cell lines were engineered to stably express 10–15 fold higher levels of Mena isoforms more than wild-type cell lines.

## Mouse models

All animal experiments were approved by the MIT Division of Comparative Medicine. PyMT–MMTV mice at 12 weeks of age were injected with 10 mg/kg Hypoxyprobe 1 h before sacrifice. To detect hypoxic areas, we used the Hypoxyprobe kit according to the manufacturer's protocol [28]. We injected 60 mg/kg of Piminidazole-HCl IP 1 h before sacrificing mice. Signal was then detected by immunostaining. Dissected tumors were dissociated using lysis buffer (see below) and mortar and pestle.

## Western blotting

MDAMB231 expressing different Mena isoforms were lysed in 25 mM Tris, 150 mM NaCl, 10 % glycerol, 1 % NP 40 and 0.5 M EDTA with a protease Mini-complete protease inhibitors (Roche) and a phosphatase inhibitor cocktail (PhosSTOP, Roche) at 4 °C. Protein lysates were separated by SDS-PAGE, transferred to a nitrocellulose membrane, blocked with Odyssey Blocking Buffer (LiCor), incubated in primary antibody overnight at 4 °C. Proteins were detected using Licor secondary antibodies.

## Immunostaining

Tumors from MMTV–PyMT mice were fixed in 10 % buffered formalin and embedded in paraffin. Sections from FFPE human breast cancer tumors were obtained from Dr. Joan Jones. Tissue sections (5 µm thick) were deparaffinized followed by antigen retrieval using Citra Plus solution (Biogenex). After treatment with 3 % H<sub>2</sub>O<sub>2</sub>, sections were blocked with serum and incubated with primary antibodies overnight at 4 °C. Fluorescently labeled secondary antibodies were added at 25 °C for 2 h. For detection of Mena<sup>INV</sup> in FFPE sections, the INV antibody was biotinylated, followed by amplification with streptavidin-horseradish peroxidase, tyramide-biotin amplification (Perkin Elmer), and detection with a fluorescently tagged streptavidin antibody. Serial Z series image stacks were collected using a DeltaVision microscope controlled by Softworx software (GE Health) with a 40 × 1.3 NA plan-apo objective and deconvolved using Softworx. Images were then analyzed using ImageJ.

## Image analysis

For Fig. 2, images within each panel were taken with the same settings and can be compared. However, panels a, d, e cannot be directly compared for intensity readings. Tumor area was delimited using DAPI staining, and intensity of signal was measured in each field of view using ImageJ. For Fig. 3, all images were acquired simultaneously and

intensity can be compared within the figure. For Figs. 3g, 5d, 6a–d, f, h, analysis of expression of markers was done on a per cell basis in multiple fields of view from multiple tissue samples. The number of positive cells for a specific marker was made relative to the total number of DAPI-positive cells in the field of view. For Fig. 5, custom written Matlab scripts were used for image analysis of ECadherin levels. For Fig. 7, blood vessel density was quantified using ImageJ, quantifying the area covered by blood vessels as marked by CD31 staining relative to the area of the field of view.

**Acknowledgments** This work was supported by Department of Defense Breast Cancer Research Program Grants W81XWH-10-1-0040 to SKH and W81XWH-13-1-0031 to MJO, NIH Grant U54-CA112967 to FBG and DAL and GM58801 to FBG, funds from the Ludwig Center at MIT to FBG and NR, the KI NCI Core Grant P30-CA14051, and CA150344 to JC and CA100324 for JJ. JJ, JC and FG are compensated members of the scientific advisory board of MetaStat. No funding was provided by MetaStat for this work. We thank the Histology facilities in the KI Swanson Biotechnology Center for support. We thank Evanthis Roussos for gifts of tumor tissue.

**Author contributions** MJO designed and performed experiments, data analysis and prepared the manuscript. SKH developed and validated the INV antibody, designed and performed experiments and completed data analysis. NR performed immunostaining experiments and image analysis. MNM developed Mena<sup>INV</sup> ELISA, performed experiments and completed data analysis. FBG and DAL guided overall experimental design. JJ and JC contributed human tissue sections and interpretation of them. All authors commented on the manuscript.

## References

1. Hanahan D, Weinberg RA (2011) Hallmarks of cancer: the next generation. *Cell* 144(5):646–674
2. Levental KR, Yu H, Kass L, Lakins JN, Egeblad M, Erler JT, Fong SFT, Csiszar K, Giaccia A, Weninger W, Yamauchi M, Gasser DL, Weaver VM (2009) Matrix crosslinking forces tumor progression by enhancing integrin signaling. *Cell* 139(5):891–906
3. Lu P, Weaver VM, Werb Z (2012) The extracellular matrix: a dynamic niche in cancer progression. *J Cell Biol* 196(4):395–406
4. Pouyssegur J, Dayan F, Mazure NM (2006) Hypoxia signalling in cancer and approaches to enforce tumour regression. *Nature* 441(7092):437–443
5. Joyce JA, Pollard JW (2009) Microenvironmental regulation of metastasis. *Nat Rev Cancer* 9(4):239–252
6. Gertler F, Condeelis J (2011) Metastasis: tumor cells becoming MENAcing. *Trends Cell Biol* 21(2):81–90
7. Roussos ET, Wang Y, Wyckoff JB, Sellers RS, Wang W, Li J, Pollard JW, Gertler FB, Condeelis JS (2010) Mena deficiency delays tumor progression and decreases metastasis in polyoma middle-T transgenic mouse mammary tumors. *Breast Cancer Res* 12(6):R101
8. Harney AS, Arwert EN, Entenberg D, Wang Y, Guo P, Qian B-Z, Oktay MH, Pollard JW, Jones JG, Condeelis JS (2015) Real-time imaging reveals local, transient vascular permeability, and tumor

- cell intravasation stimulated by TIE2hi macrophage-derived VEGFA. *Cancer Discov*
9. Robinson BD, Sica GL, Liu Y-F, Rohan TE, Gertler FB, Condeelis JS, Jones JG (2009) Tumor microenvironment of metastasis in human breast carcinoma: a potential prognostic marker linked to hematogenous dissemination. *Clin Cancer Res* 15(7):2433–2441
  10. Rohan TE, Xue X, Lin H-M, D'Alfonso TM, Ginter PS, Oktay MH, Robinson BD, Ginsberg M, Gertler FB, Glass AG, Sparano JA, Condeelis JS, Jones JG (2014) Tumor microenvironment of metastasis and risk of distant metastasis of breast cancer. *J Natl Cancer Inst* 106(8):1–11
  11. Goswami S, Philippar U, Sun D, Patsialou A, Avraham J, Wang W, Di Modugno F, Nistico P, Gertler FB, Condeelis JS (2009) Identification of invasion specific splice variants of the cytoskeletal protein Mena present in mammary tumor cells during invasion in vivo. *Clin Exp Metastasis* 26(2):153–159
  12. Roussos ET, Balsamo M, Alford SK, Wyckoff JB, Gligorijevic B, Wang Y, Pozzuto M, Stobezki R, Goswami S, Segall JE, Lauffenburger DA, Bresnick AR, Gertler FB, Condeelis JS (2011) Mena invasive (MenaINV) promotes multicellular streaming motility and transendothelial migration in a mouse model of breast cancer. *J Cell Sci* 124(Pt 13):2120–2131
  13. Agarwal S, Gertler FB, Balsamo M, Condeelis JS, Camp RL, Xue X, Lin J, Rohan TE, Rimm DL (2012) Quantitative assessment of invasive mena isoforms (Menacalc) as an independent prognostic marker in breast cancer. *Breast Cancer Res* 14(5):R124
  14. Forse CL, Agarwal S, Pinnaduwa D, Gertler F, Condeelis JS, Lin J, Xue X, Johung K, Mulligan AM, Rohan TE, Bull SB, Andrulis IL (2015) Menacalc, a quantitative method of metastasis assessment, as a prognostic marker for axillary node-negative breast cancer. *BMC Cancer* 15:483
  15. Philippar U, Roussos ET, Oser M, Yamaguchi H, Kim H-D, Giampieri S, Wang Y, Goswami S, Wyckoff JB, Lauffenburger DA, Sahai E, Condeelis JS, Gertler FB (2008) A mena invasion isoform potentiates EGF-induced carcinoma cell invasion and metastasis. *Dev Cell* 15(6):813–828
  16. Pignatelli J, Goswami S, Jones JG, Rohan TE, Pieri E, Chen X, Adler E, Cox D, Maleki S, Bresnick A, Gertler FB, Condeelis JS, Oktay MH (2014) Invasive breast carcinoma cells from patients exhibit MenaINV- and macrophage-dependent transendothelial migration. *Sci Signal* 7(353):ra112
  17. Roussos ET, Goswami S, Balsamo M, Wang Y, Stobezki R, Adler E, Robinson BD, Jones JG, Gertler FB, Condeelis JS, Oktay MH (2011) Mena invasive (Mena(INV)) and Mena11a isoforms play distinct roles in breast cancer cell cohesion and association with TMEM. *Clin Exp Metastasis* 28(6):515–527
  18. Gertler FB, Niebuhr K, Reinhard M, Wehland J, Soriano P (1996) Mena, a relative of VASP and Drosophila Enabled, is implicated in the control of microfilament dynamics. *Cell* 87(2):227–239
  19. Lebrand C, Dent EW, Strasser GA, Lanier LM, Krause M, Svitkina TM, Borisy GG, Gertler FB (2004) Critical role of Ena/VASP proteins for filopodia formation in neurons and in function downstream of netrin-1. *Neuron* 42:37–49
  20. Bear JE, Loureiro JJJ, Libova II, Fässler RR, Wehland JJ, Gertler FB (2000) Negative regulation of fibroblast motility by Ena/VASP proteins. *Cell* 101(7):717–728
  21. Goswami S, Philippar U, Sun D, Patsialou A, Avraham J, Wang W, Di Modugno F, Nistico P, Gertler FB, Condeelis JS (2009) Identification of invasion specific splice variants of the cytoskeletal protein Mena present in mammary tumor cells during invasion in vivo. *Clin Exp Metastasis* 26(2):153–159
  22. Lin EY, Jones JG, Li P, Zhu L, Whitney KD, Muller WJ, Pollard JW (2003) Progression to malignancy in the polyoma middle T oncoprotein mouse breast cancer model provides a reliable model for human diseases. *Am J Pathol* 163(5):2113–2126
  23. Valastyan S, Weinberg RA (2011) Tumor metastasis: molecular insights and evolving paradigms. *Cell* 147:275–292
  24. Chaffer CL, Marjanovic ND, Lee T, Bell G, Kleer CG, Reinhardt F, D'Alessio AC, Young RA, Weinberg RA (2013) Poised chromatin at the ZEB1 promoter enables breast cancer cell plasticity and enhances tumorigenicity. *Cell* 154(1):61–74
  25. Brugnoti F, Grassilli S, Piazzini M, Palomba M, Nika E, Bavelloni A, Capitani S, Bertagnolo V (2013) In triple negative breast tumor cells, PLC- $\beta$ 2 promotes the conversion of CD133high to CD133low phenotype and reduces the CD133-related invasiveness. *Mol Cancer* 12:165
  26. Chen Y-C, Chen Y-W, Hsu H-S, Tseng L-M, Huang P-I, Lu K-H, Chen D-T, Tai L-K, Yung M-C, Chang S-C, Ku H-H, Chiou S-H, Lo W-L (2009) Aldehyde dehydrogenase 1 is a putative marker for cancer stem cells in head and neck squamous cancer. *Biochem Biophys Res Commun* 385(3):307–313
  27. Ginestier C, Hur MH, Charafe-Jauffret E, Monville F, Dutcher J, Brown M, Jacquemier J, Viens P, Kleer CG, Liu S, Schott A, Hayes D, Birnbaum D, Wicha MS, Dontu G (2007) ALDH1 is a marker of normal and malignant human mammary stem cells and a predictor of poor clinical outcome. *Cell Stem Cell* 1(5):555–567
  28. Murphy PA, Kim TN, Lu G, Bollen AW, Schaffer CB, Wang RA (2012) Notch4 normalization reduces blood vessel size in arteriovenous malformations. *Sci Transl Med* 4(117):117ra8
  29. Roussos ET, Goswami S, Balsamo M, Wang Y, Stobezki R, Adler E, Robinson BD, Jones JG, Gertler FB, Condeelis JS, Oktay MH (2011) Mena invasive (Mena(INV)) and Mena11a isoforms play distinct roles in breast cancer cell cohesion and association with TMEM. *Clin Exp Metastasis* 28(6):515–527
  30. Shapiro IM, Cheng AW, Flytzanis NC, Balsamo M, Condeelis JS, Oktay MH, Burge CB, Gertler FB (2011) An EMT-driven alternative splicing program occurs in human breast cancer and modulates cellular phenotype. *PLoS Genet* 7(8):e1002218
  31. Di Modugno F, Iapicca P, Boudreau A, Mottotese M, Terrenato I, Perracchio L, Carstens RP, Santoni A, Bissell MJ, Nistico P (2012) Splicing program of human MENA produces a previously undescribed isoform associated with invasive, mesenchymal-like breast tumors. *Proc Natl Acad Sci USA* 109(47):19280–19285
  32. Zardavas D, Baselga J, Piccart M (2013) Emerging targeted agents in metastatic breast cancer. *Nat Rev Clin Oncol* 10(4):191–210

**Tumor cell-driven extracellular matrix remodeling drives haptotaxis  
during metastatic progression**

Madeleine J. Oudin<sup>1</sup>, Oliver Jonas<sup>1</sup>, Tatsiana Kosciuk<sup>1</sup>, Liliane C. Broye<sup>1</sup>, Bruna C. Guido<sup>1</sup>, Jeff Wyckoff<sup>1</sup>, Daisy Riquelme<sup>1</sup>, John M. Lamar<sup>1</sup>, Sreeja B. Asokan<sup>3</sup>, Charlie Whittaker<sup>1</sup>, Duanduan Ma<sup>1</sup>, Robert Langer<sup>1</sup>, Michael J. Cima<sup>1</sup>, Kari B. Wisinski<sup>7</sup>, Richard O. Hynes<sup>1,5,6</sup>, Douglas A. Lauffenburger<sup>1,2</sup>, Patricia J. Keely<sup>4</sup>, James E. Bear<sup>3,6</sup>, Frank B. Gertler<sup>\*1,5</sup>

<sup>1</sup> David H. Koch Institute for Integrative Cancer Research, MIT, Cambridge, MA, USA

<sup>2</sup> Department of Biological Engineering, MIT, Cambridge, MA, USA

<sup>3</sup> Lineberger Comprehensive Cancer Center, UNC Chapel Hill, Chapel Hill, NC, USA

<sup>4</sup> Department of Cell and Regenerative Biology, University of Wisconsin Madison, Madison, WI, USA

<sup>5</sup> Department of Biology, MIT, Cambridge, MA, USA

<sup>6</sup> Howard Hughes Medical Institute

<sup>7</sup> Department of Medicine, University of Wisconsin Carbone Cancer Center, Madison, WI, USA

**Running Title:** Haptotaxis and metastasis

**Keywords:** breast cancer, cell adhesion and extracellular matrix, cell motility and migration, imaging of tumor progression and metastasis, metastasis/metastasis genes/metastasis models, tumor markers and detection of metastasis, haptotaxis, Mena, Ena/VASP

**Abbreviations list:**

CI confidence interval, ECM extracellular matrix, EGF epidermal growth factor, GFP green fluorescent protein, FAK focal adhesion kinase, FX focal complexes, FMI forward migration index, FN fibronectin, IP immunoprecipitation, HR hazard ratio, LN laminin, MMP matrix metalloproteinase, RTK receptor tyrosine kinase, SHG second harmonic generation, TCGA The Cancer Genome Atlas, TMA tissue microarray, VN vitronectin.

**Financial support:**

This work was supported by a DoD Breast Cancer Research Program post-doctoral fellowship to W81XWH-12-1-0031 to MJO, funds from the Ludwig Center at MIT to FBG and ROH, NIH grant U54-CA112967 to FBG, ROH and DAL, HHMI funding to ROH, NIH grants R01 CA142833, R01 CA114462 and U01 CA143069 to PJK, a Science without borders/CNPq fellowship to BCG, the Koch Institute Frontier Award from the Kathy and Kurt Marble Research Fund to FBG, MJC and RL, funds from the Prostate Cancer Foundation to OJ and RL and the Koch Institute NCI core grant P30-CA14051.

\*Corresponding author:

Frank B. Gertler

Koch Institute for Integrative Cancer Research

MIT 76-361a

77 Massachusetts Ave

Cambridge, MA 02139

617-253-5511

fgertler@mit.edu

Conflict of interest: FBG is on the advisory board for MetaStat. MetaStat did not provide any direct funding for this work.



## **Abstract**

Fibronectin (FN) is a major component of the tumor microenvironment, but its role in promoting metastasis is incompletely understood. Here we show that FN gradients elicit directional movement of breast cancer cells, *in vitro* and *in vivo*. Haptotaxis on FN gradients requires direct interaction between  $\alpha 5 \beta 1$  integrin and Mena, an actin regulator, and involves increases in focal complex signaling and tumor-cell-mediated extracellular matrix (ECM) remodeling. Compared to Mena, higher levels of the pro-metastatic Mena<sup>INV</sup> isoform associate with  $\alpha 5$ , which enables 3D haptotaxis of tumor cells towards the high FN concentrations typically present in perivascular space and in the periphery of breast tumor tissue. Mena<sup>INV</sup> and FN levels were correlated in two breast cancer cohorts, and high levels of Mena<sup>INV</sup> were significantly associated with increased tumor recurrence as well as decreased patient survival. Our results identify a novel tumor-cell-intrinsic mechanism that promotes metastasis through ECM remodeling and ECM guided directional migration.

## **Statement of significance**

Here, we provide new insight into how tumor cell: ECM interactions generate signals and structures that promote directed tumor cell migration, a critical component of metastasis. Our results identify a tumor-cell-intrinsic mechanism driven by the actin regulatory protein Mena, that promotes ECM remodeling and haptotaxis along FN gradients.

## Introduction

The tissue microenvironment is composed of stromal cells and extracellular matrix (ECM) and is known to contribute to tumor progression(1). This compartment is rich in substrate-bound and soluble cues, and provides both the structure and signals that promote tumor cell proliferation, survival and invasion(2). The most abundant ECM proteins in mouse metastatic breast tumors are fibronectin (FN) and collagens(3). In breast cancer patients, collagen organization has high prognostic value(4,5) and increased FN correlates with disease progression and mortality(6,7). The context and mechanisms by which tumor cells sense and respond to changes in ECM abundance and architecture during invasion and metastasis, however, remain poorly understood.

Cancer cells can respond to a variety of cues in order to locally invade and metastasize. Growth factor-mediated chemotaxis is known to be important for local invasion and metastasis(8). Far less is known about haptotaxis, a process in which cell migration is guided by gradients of surface-bound molecules such as ECM. This is particularly relevant to cancer, where the amount of FN within tumors can vary greatly, with high concentrations of FN typically found near blood vessels, tumor periphery and in metastatic sites(9,10). While FN can activate intracellular signaling pathways via integrins(11), the predominant class of surface adhesion receptors, cells can also remodel the ECM, for example, by driving integrin-mediated assembly of soluble FN into fibrils(12). FN is also known to play an important role in collagen fibrillogenesis(13). Bi-directional communication between cells and ECM cues regulates cell behavior as well as the composition and structure of the surrounding ECM.

Mena, a member of the Ena/VASP family of actin filament elongation factors, is upregulated in various cancers and undergoes alternative splicing during breast cancer progression(14). Mena binds to the C-terminal end of the cytoplasmic tail of the integrin

$\alpha 5$  via an LERER repeat domain absent from other Ena/VASP proteins(15). In fibroblasts, Mena regulates both outside-in and inside-out signaling at focal complexes via its interaction with  $\alpha 5$  (15). Mena<sup>INV</sup>, an alternatively spliced isoform containing a 19-amino acid inclusion (encoded by the “INV” exon), is expressed in aggressive tumor cell subpopulations(16). Mena<sup>INV</sup> expression promotes metastasis by increasing sensitivity to EGF(17) and the efficiency of matrix degradation, invasion and intravasation (18). Together, these findings led us to hypothesize that the ECM may also play an important role in Mena/Mena<sup>INV</sup>-driven metastasis. Using pre-clinical models and analysis of patient samples, we describe a previously unappreciated mechanism of metastasis, where upregulation of Mena and its invasive isoform endows tumor cells with the ability to migrate up FN gradients and fashion their own pathway towards the bloodstream.

## Results

### **Mena drives haptotaxis of tumor cells on FN gradients via its interactions with $\alpha 5 \beta 1$ and F-actin**

Based on the recent finding that Mena interacts with the cytoplasmic tail of one of the main FN receptors  $\alpha 5$ , we hypothesized that Mena may be involved in directional migration responses to gradients of FN. Using a recently developed microfluidic device, we studied cells migrating on FN gradients by time-lapse imaging, and quantified their forward migration index (FMI) to assess haptotaxis (Fig1A) (19,20). First, MV<sup>D7</sup> fibroblasts, which lack all three Ena/VASP proteins (Mena, VASP and EVL(21)) migrated actively in the device, however, they failed to haptotax on the FN gradient. Interestingly, Mena-, but not VASP-, EVL- expressing MV<sup>D7</sup> cells exhibited a robust haptotactic response and migrated up the FN gradient (Fig1B), even though expression of each of the three Ena/VASP proteins had previously reported, similar effects on cell speed (21) (FigS1A).

We next examined Mena-dependent effects on haptotaxis of breast cancer cells. In serum-free conditions, MDAMB231 cells become enriched on the FN coated undersides of porous filters in transwell assays(22), however, we found that this cell type failed to exhibit directional movement on FN gradients (Fig1C). MDAMB231 cell lines stably expressing GFP-tagged Mena or control-GFP construct at levels similar to those seen in invading cells *in vivo* were generated (referred to as 231-Control or Mena) (23)(FigS1B,C). Ectopic expression of Mena enabled significant haptotactic responses on 2D gradients of FN, but not of on 2D laminin (LN) or vitronectin (VN) gradients (Fig1C), without affecting cell speed (FigS1D). Varying the concentration of either VN or LN affected the speed of MDAMB231 and 231-Mena cells, but failed to elicit significant haptotactic responses at any concentration tested (FigS1D-G).

In 3D collagen gels with FN gradients, Mena expression also induced a strong haptotactic response (Fig1D), independently of velocity (FigS1E). While the exact concentration of FN in tumors is unknown, FN is expressed by tumor and stromal cells, and accumulates in the perivascular area via leakage from the bloodstream, where FN levels as high as 400 $\mu$ g/ml have been observed(24). Due to the heterogeneous levels of FN found in tumors, we studied haptotaxis 3D collagen gels in response to gradients generated from different source concentrations of FN. In high levels of FN (up to 500 $\mu$ g/ml), 231-GFP and 231-Mena cells were unable to migrate up the FN gradient and instead migrated away from the FN source, indicating that the pro-haptotactic effect of Mena on FN gradients is concentration-dependent.

The role of integrins in FN haptotaxis, in particular the two major FN-binding integrins,  $\alpha$ 5 $\beta$ 1 and  $\alpha$ v $\beta$ 3 integrins, remains poorly understood. Inhibition of  $\alpha$ 5 $\beta$ 1 by the function blocking antibody P1D6, but not of  $\alpha$ v $\beta$ 3 by Cilengitide (25), blocked haptotaxis of 231-Mena cells (FMI values decreased by over 90%; Fig1E), indicating that Mena-driven FN haptotaxis requires  $\alpha$ 5 $\beta$ 1 signaling specifically. We tested whether Mena's ability to bind  $\alpha$ 5 via its LERER domain was required for Mena to support haptotaxis (Fig1F). MDAMB231 cell lines stably expressing GFP-tagged Mena in which the LERER domain was deleted to abrogate the interaction between Mena and  $\alpha$ 5 (231-Mena $\Delta$ LERER)(15) showed no apparent defects in protein localization (as judged by the GFP-tag), cell morphology, cell area or proliferation on plastic at steady state (FigS1B,C,F,G). 231-Mena $\Delta$ LERER cells failed to haptotax in 3D to FN (FMIs reduced by over 90%; Fig1G), however, their migration velocity was similar to cells expressing intact Mena (Fig1H). Similar results were obtained in MV<sup>D7</sup> fibroblasts on a 2D FN gradient (FigS1H,I). Previously, we found that, while the LERER domain was required for fibroblast spreading on FN, the F-actin binding site in Mena was



dispensable(15)(Fig1F). Therefore, we investigated the role of the F-actin binding (FAB) site of Mena in FN-driven haptotaxis. 231-Mena $\Delta$ FAB cells failed to haptotax in a FN gradient in a 3D collagen gel (Fig1G), while also displaying slight reductions in cell velocity (Fig1H). Overall, these data demonstrate that sensing changes in FN concentrations depends on  $\alpha 5\beta 1$  function, as well as the ability of Mena to bind  $\alpha 5$  and to F-actin.

### **Mena<sup>INV</sup> drives haptotaxis in high FN concentrations *in vitro* and *in vivo***

We next investigated the role of the Mena<sup>INV</sup> isoform in driving haptotaxis. Cultured cells show little to no detectable Mena<sup>INV</sup> compared to spontaneous or xenograft mammary tumors(26). MDAMB231 and SUM159 cell lines stably expressing GFP-tagged Mena<sup>INV</sup> or Mena<sup>INV</sup> $\Delta$ LERER constructs at levels similar to those generated for Mena (referred to as 231- or 159-Mena<sup>INV</sup> or Mena<sup>INV</sup> $\Delta$ LERER) were made (FigS1B,C). Surprisingly, unlike Mena, Mena<sup>INV</sup> enabled tumor cell haptotaxis through gradients of high FN concentrations, even up to 500  $\mu$ g/ml (Fig2A), effects that were independent of velocity (FigS2A,B). In contrast, varied concentration gradients of either VN or LN failed to elicit significant haptotactic responses by 231-Mena<sup>INV</sup> cells, suggesting this response was specific to FN (FigS2D,E). Inhibition of  $\alpha 5\beta 1$ , but not of  $\alpha \nu \beta 3$  blocked haptotaxis of 231-Mena<sup>INV</sup> cells (Fig2B,S2C). Mena<sup>INV</sup> also binds the cytoplasmic tail of  $\alpha 5$  directly via its LERER domain; we found that 231-Mena<sup>INV</sup> $\Delta$ LERER and 231-Mena<sup>INV</sup> $\Delta$ FAB cells also failed to haptotax in 3D to FN (Fig2B). These findings were confirmed in 2D and 3D collagen gels using SUM-159 cells expressing the different GFP-tagged Mena isoforms (FigS2F-I). Overall, these data suggest that expression of Mena<sup>INV</sup> enables cells to haptotax at higher FN concentrations than Mena.

While upregulation of FN in aggressive tumors is thought to promote invasion and metastasis, whether FN gradients play a role in guiding tumor cell migration *in vivo* has not been established. Xenograft tumors were generated in the mammary fat pad of immunocompromised mice using MDAMB231 and SUM159 cells. We assayed the ability of cells from the primary tumor to invade actively into microneedles loaded with collagen and increasing concentrations of FN(27). 231-Control tumor cells were not attracted to FN *in vivo* (Fig2C), while 231-Mena tumor cells exhibited a biphasic response with robust invasion by 231-Mena cells at intermediate FN concentrations, but little to no invasion into needles with either low or high FN concentrations (Fig2C). Interestingly, 231-Mena<sup>INV</sup> cells were still attracted into the needles containing the high concentrations of FN (Fig2C). While Mena can promote invasion *in vivo* in response to intermediate FN gradients, Mena<sup>INV</sup> allows tumor cells to migrate through substantially higher (2-fold greater) FN concentrations.

To visualize FN-driven haptotactic responses inside tumors, we used a microscale implantable device that allows for *in vivo* release of molecules in gradients(28). Devices filled with Rhodamine-labeled FN were implanted near the edges of MDAMB231 or SUM159 orthotopic tumors to generate high concentration FN gradients (Fig2D). Using intravital imaging, cell motility and FMI were quantified in response to gradients of FN or to fluorescently labeled dextran similar of size to FN as a control (FigS2J). Expression of Mena<sup>INV</sup>, but not Mena, in human MDAMB231 and SUM159 cells significantly increased the number of cells moving in the xenograft tumors an effect dependent on the interaction with  $\alpha 5\beta 1$  (FigS2L,M). In tumors implanted with FN-loaded devices, 231-Mena<sup>INV</sup>, but not 231-Control or 231-Mena cells moved towards the FN gradient (Fig2E, representative images with cell tracks FigS2K and supplementary videos 1&2). In contrast, 231-Mena $\Delta$ LERER and Mena<sup>INV</sup> $\Delta$ LERER cells

did not. Similarly, cells in 159-Mena<sup>INV</sup> tumors migrated towards the FN, an effect that was absent in 159-Control or 159-Mena<sup>INV</sup>ΔLERER tumor cells (Fig2F). Altogether, using the needle collection assay and intravital imaging, we show for the first time that haptotaxis towards FN occurring *in vivo* is driven by Mena<sup>INV</sup> and its interaction with α5.

### **Mena isoform expression correlates with FN and integrin α5 expression levels as well as outcome in human breast cancer patients**

Previous work demonstrated that forced expression of Mena<sup>INV</sup> drives metastasis in xenograft tumor models(17) and that Mena<sup>INV</sup> mRNA levels, as detected by qPCR are relatively higher in cells that intravasate efficiently and in patients with high numbers of TMEM (a structure containing a tumor cell, macrophage and endothelial cell associated with the likelihood of metastasis in ER<sup>+</sup>/Her2<sup>-</sup> breast cancer patients) (29). However, the relationship between Mena<sup>INV</sup> mRNA or protein levels and patient outcome in human breast cancer patients has not been investigated. First, we analyzed the 1060 breast cancer patients in the TCGA cohort with RNAseq and clinical data available (30). Since the INV exon was not annotated when the RNAseq data were first analyzed, we accessed the raw sequence data and mapped reads in each sample to all Mena exons. Separating patients into quartiles according to Mena expression failed to reveal any significant correlations between Mena levels (judged by levels of constitutively-included exons) and overall survival in the entire TCGA breast cancer cohort (Fig S3A) or in the subset of patients with >10yr follow-up (Fig 3A). However, patients with high levels (top 1/4) of Mena<sup>INV</sup> mRNA (as assessed by the abundance of INV exon sequence reads) exhibited significantly reduced survival compared to patients in each of the three lower quartiles of Mena<sup>INV</sup> expression (Figs 3B, S3B). Similar results were found in the node-negative patient subgroup (FigS3E). Furthermore, both Cox and logistic regression

demonstrated that Mena<sup>INV</sup> was a substantially stronger predictor of poor outcome in patients with 10-year follow up than Mena alone (Figs 3C,D, S3C,D); models combining Mena<sup>INV</sup> and Mena expression levels failed to increase the predictive power beyond that of Mena<sup>INV</sup>. We next studied how Mena<sup>INV</sup> levels correlated with FN and  $\alpha 5$  expression in this dataset. Overall Mena and Mena<sup>INV</sup> expression were both significantly correlated with FN, and to a lesser degree  $\alpha 5$  (FigS3F). In particular, in patients with >10yr follow-up, we observed a highly significant correlation between Mena, Mena<sup>INV</sup> and FN or  $\alpha 5$  in patients that succumbed to their disease, that was absent in surviving patients (FigS3G,H).

Using a newly developed antibody specific for Mena<sup>INV</sup>(26), we then investigated the relationship between endogenous Mena<sup>INV</sup>,  $\alpha 5$  and FN protein using immunostaining in the MMTV-PyMT spontaneous mouse model of breast cancer(31) and in a previously characterized tissue microarray (TMA) of 300 patients(32). Both Mena and Mena<sup>INV</sup> are expressed in PyMT tumors (Fig3E) and can be detected in cells that also express  $\alpha 5\beta 1$  (Fig3F). Mena<sup>INV</sup> expression and distribution significantly correlated with that of FN in this model (Fig3G,H). We also found a significant correlation between FN and Mena<sup>INV</sup> levels in the TMA (Fig3I,J). Similarly, in patients represented by the TMA, higher Mena<sup>INV</sup> levels were significantly correlated with poor outcome (FigS3I). In addition, patients with recurrent disease, either local or at a distant site, had significantly higher levels of Mena<sup>INV</sup> (Fig3K). Logistic regression analysis indicated that Mena<sup>INV</sup> expression Mena<sup>INV</sup> was a significant predictor of recurrence (Coefficient of 0.377,  $p = 0.0186$ ). An average 4.6-fold increase in Mena<sup>INV</sup> expression correlated with a 2-fold increase in the number of patients with recurrence (FigS3J,K). Further increases in Mena<sup>INV</sup> expression did not correlate with further increases in recurrence, suggesting that even small increases in Mena<sup>INV</sup> protein expression can affect recurrence. While mRNA levels of either Mena<sup>INV</sup>

or FN alone did not correlate with time to disease recurrence, patients with high levels of *both* Mena<sup>INV</sup> and FN showed a statistically significant decrease in time to recurrence (Fig3L). Together, these data provide the first evidence that Mena<sup>INV</sup> RNA and protein levels correlate with tumor recurrence and survival and support a link between endogenous Mena<sup>INV</sup>,  $\alpha 5$  and FN expression in breast cancer patients.

To evaluate the role of Mena/Mena<sup>INV</sup>-driven haptotaxis in metastasis, we quantified the number of spontaneous metastases in the lungs of mice with MDAMB231 and SUM159 xenografts. Mice were sacrificed when primary tumor size reached 1cm in diameter. Interestingly, the initial growth rate of 231- and 159-Mena<sup>INV</sup> $\Delta$ LERER tumors was slower than that of tumors generated from the other cell lines (FigS4A,B). While there were only minor changes in proliferation levels as detected using the marker Ki67, 231-Mena<sup>INV</sup> $\Delta$ LERER tumors had a 6-fold increase in levels of the apoptotic marker cleaved caspase-3 (FigS4D,E). This delay in tumor growth and increase in cell death could be rescued by co-injecting 231-Mena<sup>INV</sup> $\Delta$ LERER cells with wild-type MDAMB231 cells expressing mCherry or by letting them grow for 12 weeks instead of 8 to reach 1cm in diameter (FigS4D,E). Expression of Mena<sup>INV</sup> significantly increased the metastatic index in the lungs 5-fold in both human cell lines at 8 weeks, compared to control 231s (Fig3M-O). Deletion of the LERER region in both Mena and Mena<sup>INV</sup> significantly decreased the lung metastatic index (Fig3N,O). Similar results were found in the poorly metastatic SUM159 cell line (Fig S4E). Similarly, depletion of all Mena isoforms in MDAMB231 cells using shRNA also delayed tumor growth, as well as decreasing tumor cell motility and metastasis (FigS4G-M). These data support a model whereby Mena/Mena<sup>INV</sup>-driven  $\alpha 5$ -dependent haptotaxis plays a key role in promoting tumor metastasis.



### **Haptotaxis on FN gradients is dependent on signaling at focal complexes (FXs)**

We next investigated the mechanism by which Mena isoforms drive haptotaxis at low and high FN concentrations. One way FN can support cell migration is by activating integrin-mediated intracellular signaling pathways at FXs that promote cell motility(11). When plated on 2D collagen and FN, both 231-Mena and 231-Mena<sup>INV</sup> cells showed increases in cell area and in the number of  $\alpha 5$ -positive adhesions relative to control cells, or to cells plated on collagen only, an effect dependent on  $\alpha 5$  activity as well as the  $\alpha 5$ -binding LERER domain (Fig4A-E). While 231-Mena<sup>INV</sup> cells showed a 30% increase in both total and surface levels of  $\alpha 5$ , the steady state levels of  $\alpha v$ ,  $\beta 1$  and other integrins examined were unchanged (FigS5A-G). Furthermore, plating cells on FN also increased the levels of  $\alpha 5$  within Mena-positive adhesions (indicated by the GFP tag), with 231-Mena<sup>INV</sup> cells showing increased  $\alpha 5$  levels relative 231-Mena cells (Fig4B,F). The FN-driven recruitment of  $\alpha 5$  to Mena-positive adhesions was dependent on  $\alpha 5$  activity as well as the LERER domain for both isoforms (Fig4F,G). 231-Mena<sup>INV</sup> $\Delta$ LERER cells also had reduced number of Mena-positive adhesions (FigS5I).

Phosphorylation of several proteins at focal adhesions downstream of integrin activation, particularly focal adhesion kinase (FAK), is important for motility and tumorigenesis (11,33). Pharmacological inhibition of FAK inhibited Mena and Mena<sup>INV</sup>-driven haptotaxis on low FN gradients (Fig4H). Immunofluorescence of haptotaxing cells revealed that both 231-Mena and Mena<sup>INV</sup> cells show increased number of pFAK397-positive adhesions (Fig4I,J). In 231-Mena<sup>INV</sup> $\Delta$ LERER or 231-Mena<sup>INV</sup> $\Delta$ FAB cells, the number of pFAK397-positive adhesions in the cells was significantly lower than in 231-Mena<sup>INV</sup> cells (Fig4K). When cells were plated on high FN gradients, only 231-Mena<sup>INV</sup> cells haptotaxed (Fig S5J) and accordingly, these cells had a significant increase in the number of pFAK397-positive adhesions relative to 231-Mena or control cells (Fig4L).

These data suggest that outside-in activation of integrins and Mena-dependent FX signaling by FN is important for haptotaxis of tumor cells.

The differences between focal complex composition, signaling and haptotaxis arising from expression of Mena<sup>INV</sup> vs. Mena prompted us to ask whether we could detect any relevant biochemical differences between the isoforms. Previously we demonstrated that Mena could be detected in complex with  $\alpha 5$  by co-immunoprecipitation (IP)(15). We performed  $\alpha 5$  IPs to compare the amounts of Mena and Mena<sup>INV</sup> in complex with  $\alpha 5$ , and reproducibly detected an average 2.2 fold greater level of Mena<sup>INV</sup> compared to Mena by western blot of anti- $\alpha 5$  IPs (Fig4M,N). Thus inclusion of INV in Mena leads to significantly increased association with  $\alpha 5\beta 1$ .

### **Mena<sup>INV</sup>-driven ECM remodeling is required for 3D haptotaxis**

FN could also support haptotaxis through its role in providing structural support for cells, particularly in 3D and in the presence of collagen. FN fibrillogenesis exposes cryptic binding sites in FN normally hidden in the globular form(12) and fibrillar FN can bind collagen and regulate its deposition and organization(13). 231-Mena and Mena<sup>INV</sup> cells had increased number of protrusions in low FN gradients, while in high FN gradients, only 231-Mena<sup>INV</sup> cells showed this phenotype (Fig S6A). Similarly, 231-Mena<sup>INV</sup> cells were more elongated than Mena or Control cells in the presence of a FN gradient *in vivo*, an effect dependent on the interaction with  $\alpha 5$  (FigS6B,C). We also found that 231-Mena<sup>INV</sup> exhibited increased accumulation (20%) of FN (Fig5A,B) and collagen (Fig5A,C) at both low and high FN concentrations after 24 hrs, while neither 231-Mena nor 231-Control cells exhibited any significant accumulation of the two ECM proteins. FN-triggered outside-in signaling was insufficient to support Mena<sup>INV</sup>-dependent haptotaxis in 3D gels, as 231-Mena<sup>INV</sup> cells failed to haptotax on a gradient of FN7-11, a

fragment of FN that activates signaling via RGD-binding integrins, but cannot form fibrils (12) (Fig5D). Inhibition of fibrillogenesis by addition of a 70kD FN fragment that contains the cryptic FN- and collagen binding sites in FN (34) blocked Mena<sup>INV</sup>-driven 3D haptotaxis (Fig5E). Therefore, the formation of FN fibrils is important for FN to evoke directional motility of tumor cells in 3D. Addition of the 70kD FN fragment to spreading 231-Mena<sup>INV</sup> cells decreased the number of  $\alpha$ 5-positive adhesions as well as  $\alpha$ 5 recruitment to Mena<sup>INV</sup>-positive adhesions (FigS6D-G), suggesting that fibrillar FN may enhance assembly of  $\alpha$ 5 $\beta$ 1-containing adhesions.

In 231-Mena<sup>INV</sup> cells, inhibition of  $\alpha$ 5 $\beta$ 1 decreased accumulation of both FN and collagen, while inhibition of  $\alpha$ v $\beta$ 3 had little or no effect. 231- Mena<sup>INV</sup> $\Delta$ LERER and 231-Mena<sup>INV</sup> $\Delta$ FAB cells had decreased FN and collagen (Fig5F,G) accumulation around the cells. Inhibition of protease activity with the broad-spectrum matrix metalloproteinase (MMP) inhibitor BB94 had no effect on ECM reorganization, but inhibition of acto-myosin contractility by the ROCK inhibitor Y-27632 did decrease collagen and FN accumulation around the cells (FigS6H,I). These results indicate that Mena<sup>INV</sup>-driven  $\alpha$ 5-dependent FN and collagen accumulation by the tumor cells themselves is important for haptotaxis.

### **Mena<sup>INV</sup> expression drives collagen reorganization in tumors**

Given the role of Mena<sup>INV</sup> in driving ECM reorganization *in vitro*, the importance of FN for collagen fibrillogenesis(13), and recent published work showing that collagen organization can correlate with disease outcome(5), we next examined whether the changes in ECM accumulation observed short-term *in vitro* translated into significant changes in the structure and abundance of collagen *in vivo*. Using Second Harmonic Generation (SHG), we examined the structure and abundance of collagen in multiple tumors to investigate whether Mena and Mena<sup>INV</sup> were associated with changes in

collagen abundance and organization *in vivo*. We examined the thickness of the collagen capsule surrounding the tumors. Intravital imaging of tumors revealed that deletion of the LERER in both 231-Mena and Mena<sup>INV</sup> tumors lead to significantly thicker, collagen capsules (FigS6J). Similarly, knockdown of Mena in 231 cells also led to an increase in collagen thickness (FigS6K). Histological analysis of tumor sections showed that tumors in MMTV-PyMT mice null for Mena, known to have significantly lower levels of metastasis(35), showed significantly increased collagen levels, compared to wild-type mice (Fig6A,B). Endogenous Mena<sup>INV</sup> levels in wild-type PyMT tumors were correlated with lower levels of collagen (Fig6C,D). In patients with high Mena<sup>INV</sup> expression, there was significantly lower collagen signal than in patients with low Mena<sup>INV</sup> expression (Fig6E,F). Together, these data suggest that highly invasive tumors arising from, or correlating with Mena<sup>INV</sup> expression were associated with thinner collagen capsules, while the poorly metastatic tumors arising from Mena deficient cells were associated with thicker collagen capsules.

While the amount of collagen deposition surrounding tumor an important factor in local invasion, changes in collagen shape and orientation have also been linked with invasiveness. A lower density of collagen organized into straight fibers oriented perpendicularly to the edge of the tumor has been associated with poor outcome in a breast cancer cohort (5). Representative images of the collagen at the edge of the MDAMB231 and SUM159 xenograft tumors show 231-Control and 231-Mena tumors had dense, curly collagen fibers, organized in all directions relative to the tumor edge (Fig6G,H, FigS6L). However, 231-Mena<sup>INV</sup> tumors displayed a significantly increased frequency of fibers orientated perpendicular to the tumor edge (Fig6G,H). 231-Mena $\Delta$ LERER and 231-Mena<sup>INV</sup> $\Delta$ LERER tumors had collagen fibers parallel to the tumor edge (FigS6L,M). Indeed, these tumors contained abundant collagen fibers with

very small angles relative to the tumor edge. Both phenotypes were also observed in tumors generated with SUM159 cells (Fig6G, S6N,O). Together, these results indicate that the initial Mena<sup>INV</sup>-dependent changes in ECM accumulation observed in our short-term *in vitro* assays can translate *in vivo* (over much longer time scales associated with tumor progression) into significant reductions in overall accumulation of encapsulating collagen accompanied by increased abundance of linear fibers oriented perpendicularly to the tumor margin.



## Discussion

Our results lead us to propose a novel mechanism by which tumor cells sense, respond to, and reorganize the ECM to support metastasis (summarized in Fig 7). Integrin-dependent outside-in signaling at FXs, as well as inside-out ECM remodeling are necessary for directional migration towards FN. FN and  $\alpha 5$  expression are upregulated in breast cancer tumors and high levels of tumor FN and  $\alpha 5$  have been associated with poor outcome(7), though not, by themselves, in the datasets we analyzed. Given the heterogeneous levels of FN within both the primary tumor and metastatic niche, disseminating cells must be able to migrate effectively through areas of different FN concentrations, as well as to move from areas of low FN to areas of high FN and vice versa. In addition to simply being permissive for migration, we show that FN acts as a directional cue *in vivo*. Expression of Mena drives haptotaxis at low FN concentrations, while expression of Mena<sup>INV</sup> allows cells to migrate at high concentrations of FN similar to those present around blood vessels in tumors(9). Abrogation of the interaction between Mena/Mena<sup>INV</sup> and  $\alpha 5\beta 1$  abolished haptotaxis *in vitro*, while also significantly decreasing metastasis in two mouse xenograft breast cancer models. Together, these findings support the idea that FN can act as a potent guidance and motility cue for tumor cells during metastatic progression.

At a mechanistic level, inclusion of the INV sequence increases the association of Mena with  $\alpha 5$  by 2.2 fold. We propose that increased association of Mena<sup>INV</sup> vs. Mena with  $\alpha 5$  likely underlies the isoform-specific differences in  $\alpha 5\beta 1$ -mediated effects on haptotaxis and focal complexes. The INV sequence is inserted between the amino terminal EVH1 domain in Mena, which mediates interactions with several other molecules associated with integrin function, and the LERER domain, which binds directly

to  $\alpha 5$ (15,36). It will be of great interest to determine exactly how the INV sequence modifies interactions with  $\alpha 5$ .

The ECM can also deliver signals to other types of receptors by providing binding sites for their ligands (37). While it is well established that proteoglycans directly bind growth factors, allowing the ECM to act as a reservoir for invasive signals (38), emerging evidence suggests that ECM proteins contain domains that may allow them to activate receptor tyrosine kinases directly. FN-mediated activation of  $\alpha 5\beta 1$  can, for example, lead to HGF-independent activation of Met to promote invasion in ovarian cancer cells (39). In addition, expression of mutant p53 protein, which is mutated in 50% of cancers (40), can drive invasion through enhanced RCP-dependent co-recycling of  $\alpha 5\beta 1$  with several receptor tyrosine kinases (RTKs), including EGFR and Met (25,41). Given that Mena<sup>INV</sup> expression sensitizes cells to EGF, enabling them to invade and migrate in response to low EGF concentrations (17,18,42), it will be interesting to investigate the potential role of crosstalk with RTK signaling in Mena<sup>INV</sup>-driven haptotaxis.

The importance of tumor-cell-driven FN fibrillogenesis and ECM remodeling in Mena<sup>INV</sup>-driven haptotaxis is surprising. FN polymerization is required for deposition of collagen I(34) and antibody binding to the collagen-binding site on FN inhibits collagen fibrillogenesis(43). Here, we show for the first time that tumor-cell-mediated FN fibrillogenesis is required for haptotaxis, a process driven by expression of Mena<sup>INV</sup>. We also show the first evidence for tumor-cell-driven collagen reorganization in vivo, also driven by Mena<sup>INV</sup> and its interaction with  $\alpha 5\beta 1$ . Together, these data suggest that tumor cells can pave their own way to blood vessels. While the mechanism by which FN and integrins drive collagen fibrillogenesis remains incompletely understood, our results indicate that Mena<sup>INV</sup> provides a link between integrin activation and the cytoskeleton to drive ECM organization by tumor cells. The Mena<sup>INV</sup>-driven reduction in collagen

encapsulation and increase in linear fibrils radiating from the tumor periphery, in turn, further enhance metastatic phenotypes. Overall, our findings highlight the potential importance of bi-directional integrin-mediated signaling in the tumor cell compartment in addition to the previously characterized contributions from stromal cells(4) in the regulation of ECM structure.

Our data also support a role for the relationship between Mena<sup>INV</sup>,  $\alpha 5$  and FN in human breast cancer. Using an isoform-specific antibody and bioinformatic analysis of available TCGA data, we found that high expression levels of Mena<sup>INV</sup> and FN are associated with increased recurrence and poor outcome in two human breast cancer cohorts. Future studies on larger patient cohorts will be needed to help determine the utility of Mena<sup>INV</sup> as a diagnostic and prognostic marker, and whether it provides additional information when used in conjunction with other tumor markers. Altogether, our findings reinforce the importance of Mena<sup>INV</sup> in human breast cancer, and suggest that targeting the chemotactic and haptotactic pathways by which Mena<sup>INV</sup> promotes invasion could be useful therapeutically for metastatic breast cancer.

## **Materials and methods**

### **Antibody reagents, growth factors and inhibitors**

Antibodies:  $\alpha 5$  (for IF: BD Biosciences, #555651, for IP: Millipore, AB1928 and for WB: Santa Cruz Biotechnology, sc-166681),  $\alpha v$  (BD Biosciences, 611012),  $\alpha 6$  (Abcam, ab10566),  $\alpha 2$  (Abcam, ab133557),  $\beta 1$  (BD Biosciences, 610467), FAK (BD Biosciences, 610087), pFAK Y397 (Invitrogen, 44-625G), Cleaved Caspase 3 (CST, 9661), Ki67 (CST, 9027), FN (BD Biosciences), p53 (CST, clone 1C12), RCP (Sigma). See (26) for description of Mena<sup>INV</sup> rabbit monoclonal antibody. Animals were immunized with a peptide containing the sequence encoded by the INV exon. Clones were screened for Mena<sup>INV</sup> specificity in Western blot assays and by immunostaining of FFPE tumor sections from wild type or Mena-null mice (FigS3) (26). Cilengitide (Selleck Chemicals), P1D6  $\alpha 5$  blocking antibody (DSHB), FAKi (Santa Cruz), 70kD fragment and its control peptide for blockade of fibrillogenesis (gift from Dr. Sottile, University of Rochester), FN 7-11, purified from a plasmid from ROH).

### **Cell culture**

MDAMB231 cells were purchased directly from ATCC in June 2012, where cell lines are authenticated by short tandem repeat profiling. These cells not re-authenticated by our lab, and were cultured in DMEM with 10% FBS (Hyclone). SUM159 cells were obtained from Joan Brugge's lab at Harvard Medical School (January 2011) and were not re-authenticated in our lab. SUM159 cells were cultured according to the ATCC protocols. MV<sup>D7</sup> fibroblasts cells were isolated from mice in our lab in October 1999 and cultured as previously described(15). These cell lines were authenticated in our lab and deletion of Mena was verified at the mRNA and protein level. Retroviral packaging, infection, and FACS were performed as previously described (15). Cell lines were engineered to

express Mena isoforms stably at 10-15-fold higher levels than parental lines. MV<sup>D7</sup> fibroblasts were isolated were maintained at 32°C, 5% CO<sub>2</sub> in DME supplemented with l-Glutamine, penicillin and streptomycin, 15% fetal bovine serum, and 50U/ml interferon (I-4777; Sigma) (15). Stable Knockdown cell lines were generated using mir30-based shRNA sequence 'CAGAAGACAATCGCCCTTTAA' for Mena expressing an mCherry tag.

### **Immunohistochemistry**

Fixation, processing and staining of tissue sections from tumors was carried out as previously described (18). Tumors dissected from NOD/SCID mice were fixed in 10% buffered formalin and embedded in paraffin. Tissue sections (5µm thick) were deparaffinized followed by antigen retrieval using Citra Plus solution (Biogenex). After endogenous peroxidase inactivation, sections were incubated with primary antibodies overnight at 4°C and fluorescently labeled secondary antibodies at room temperature for 2 hrs. Sections were stained using the following antibodies: anti-Mena (1:500), anti-Ki67 (BD Biosciences), cleaved Caspase-3 (BD Biosciences). Fluorochromes on secondary antibodies included AlexaFluor 594, AlexaFluor488 and AlexaFluor 647 (Jackson ImmunoResearch). Sections were mounted in Fluoromount mounting media and imaged at room temperature. Z series of images were taken on an Applied precision DeltaVision microscope using Softworx acquisition, an Olympus 40x 1.3 NA plan apo objective and a Photometrics CoolSNAP HQ camera. Images were deconvolved using Deltavision Softworx software and objective specific point spread function. At least 4 images were captured for each tumor, with at least 3 tumors per tumor group.

### **TMA**



Details of the patient cohort and associated data used to generate the TMA are published (32). The TMA was stained by immunofluorescence and imaged with a Vectra automated slide scanner and a 20X objective. The field of view with this objective covers 90% of the core spot. Each patient had three cores on the TMA. All were imaged, but some had to be removed due to lack of tissue or folded tissue. Fluorescence intensity in the tumor compartment was analyzed using Inform software. Mena<sup>INV</sup> and FN intensity metrics are in arbitrary units.

### **Haptotaxis assays**

Microfluidic devices were prepared as described (19). For haptotaxis on a 2D matrix, after bonding PDMS devices to Mattek dishes, the chamber was coated with 0.1mg/ml Collagen I for 1hr at 37°C and then 250µg/ml fluorescently-labeled FN was flowed through the source channel for 1hr. Cells were then plated in the device in full serum media and left to attach for 1hr before imaging. For haptotaxis in a 3D matrix, cells were resuspended in 1mg/ml collagen I (BD Biosciences) with 10X DMEM and 1N NaOH and 3nM EGF in full serum media, plated in the cell culture chamber, and left to settle for 8hrs at 37°C. Fluorescently-labeled FN was then flowed through the source channel for 1hr before imaging. For all haptotaxis experiments, the FN concentration represents the concentration at the top of the gradient. Unless mentioned, FN concentration at the top of the gradient is 125µg/ml. Cells were imaged overnight in the haptotaxis device, with images being acquired every 10min for 16hr in an environmentally controlled microscope (TE2000, Nikon) with a 20X objective and a Photometrics Coolsnap HQ camera. Individual cells were manually tracked using ImageJ software Manual Tracking plug-in. The tracks obtained were analyzed using the Chemotaxis Tool ImageJ plugin (from Ibidi). This analysis tool was used to extract the FMI (Fig 1A) along with the velocity of

migration and the persistence of migration using the D/T ratio (net path length/total path length) (20,44).

### **Tumor formation and metastasis assay**

All animal experiments were approved by the MIT Division of Comparative Medicine. For xenograft experiments, MDAMB231 or SUM159 cells (2 million per mouse in PBS and 20% collagen I) expressing different Mena isoforms were injected into the 4<sup>th</sup> right mammary fat pad of six week-old female NOD-SCID mice (Taconic). Tumor size was measured weekly with calipers. 8 or 12 weeks post-surgery, once tumors had reached 1cm in diameter, mice were used for intravital imaging, and then sacrificed and their tumors and lungs were fixed in 4% formalin overnight. Metastatic index was calculated by counting the number of metastases in each lobe relative to the weight of the tumor. Each tumor group contained 4-6 mice. PyMT-MMTV mice were obtained from Jackson, mice were left to growth for 15-20 weeks, when they had developed tumors of about 1.5 cm in diameter. Histological analysis of H&Es from these tumors confirmed these tumors were advanced carcinoma.

### ***In vivo* invasion assay**

The *in vivo* invasion assay was performed in at least 4 mice per condition as previously described (45). Briefly, needles were held in place by a micromanipulator around a single mammary tumor of an anesthetized mouse. Needles contained a mixture of 0.5mg/ml Collagen I, EDTA with L-15 media or increasing amounts with FN. After four hours, the contents of the needles were extruded. Cells were stained with DAPI and counted.

### **Intravital Imaging and *in vivo* haptotaxis**

Intravital multiphoton imaging was performed as described previously (23) using a 25x 1.05NA water immersion objective with correction lens. For *in vivo* haptotaxis, a microscale device filled with multiple reservoirs(28) with powdered rhodamine-FN or dextran was prepared. After exposing the tumor, the device was implanted into the tumor edge. Hour-long time-lapse movies were analyzed for frequency of motility and tracking, and to measure and quantify cell characteristics in 3D and over time using NIH ImageJ. Cells that were either protruding or moving were counted as motile. For each movie, the FMI was calculated, with the angle for each track made relative to the direction of FN gradient for each frame. Data is pooled from 2-4 mice per tumor group, with 4-10 fields imaged per mouse, with a total of at least 70 cells per tumor type tracked. Collagen signal was visualized by second harmonic generation and images were analyzed using CT-Fire software (46) to calculate collagen fiber orientation, width and length. Data were pooled from 2-4 mice per tumor group, with 4-10 fields imaged per mouse.

### **Western Blot/Immunoprecipitation**

For the  $\alpha 5$  immunoprecipitation, 231-Mena and 231-Mena<sup>INV</sup> were lysed with CSK buffer (10 mM PIPES – pH 6.8, 50 mM NaCl, 150 mM sucrose, 3 mM MgCl<sub>2</sub>, 1 mM MnCl<sub>2</sub>, 0.5% Triton X-10, protease and phosphatase inhibitors) and passed through a 23-gauge needle. Lysates were precleared with protein A beads for 1.5 h, incubated with the integrin  $\alpha 5$  antibody (1928; Millipore) for 2.5 h at 4°C, and then captured with 3% BSA-blocked protein A beads for 2 h. Beads were washed three times in CSK lysis buffer, and proteins were eluted in 2x sample buffer. Standard procedures were used for protein electrophoresis, western blotting, and immunoprecipitation. MDAMB231 expressing different Mena isoforms were lysed in 25mM Tris, 150mM NaCl, 10% glycerol, 1% NP

40 and 0.5M EDTA with a protease Mini-complete protease inhibitors (Roche) and a phosphatase inhibitor cocktail (PhosSTOP, Roche) at 4°C. Protein lysates were separated by SDS-PAGE, transferred to a nitrocellulose membrane, blocked with Odyssey Blocking Buffer (LiCor), incubated in primary antibody overnight at 4°C. Proteins were detected using Licor secondary antibodies. Protein level intensity was measured with Image J and data were pooled from at least 3 different experiments.

### **FACs**

MDAMB231 cells expressing the different isoforms were trypsinized, resuspended in media, and then incubated with a primary antibody in PBS and 5% media for 30mins on ice. Next, the cells were incubated with a species appropriate Alexa647-tagged secondary antibody and then resuspended in PBS with 10µg/ml propidium iodide. Samples were then analyzed on a FACS-Calibur machine (BD Biosciences). Data is pooled from at least 3 separate experiments, with 10 000 cells analyzed per experiment.

### **Immunofluorescence**

Cells were plated in a haptotaxis device on a 125 µg/ml 2D FN gradient for 3 hr or on collagen-coated glass-bottomed dishes (MatTek) in serum-free media for 30 min at 37°C. Cells were then fixed for 20 min in 4% paraformaldehyde in PHEM buffer, then permeabilized with 0.2% TritonX-100, blocked with 10% BSA and incubated with primary antibodies overnight at 37°C. Z series of images were taken on an Applied Precision DeltaVision microscope using Softworx acquisition, an Olympus 40x 1.3 NA plan apo objective and a Photometrics CoolSNAP HQ camera. Images were deconvolved using Deltavision Softworx software and objective specific point spread function. Images were analyzed with ImageJ. Images are pooled from at least 3 independent experiments, at

least 10 cells per experiment.

### **Mena<sup>INV</sup> TCGA data retrieval**

RNAseq data in fastq format were obtained from TCGA. For each sample, ENAH (Mena)-derived reads were extracted from the full dataset by aligning to a target database that contained collection of all possible ENAH isoforms using BWA version 0.7.10. Properly paired ENAH reads were then extracted with Samtools version 0.1.19. ENAH isoforms were then quantified by aligning to hg19 using tophat2 version 2.0.12 guided with an edited GTF file derived from the USCS known genes annotation that contained all ENAH variants of interest. Bedtools version 2.20.1 and a custom python script were then used to count reads that overlap with each ENAH exon. The resulting counts per exon were then normalized for RNA loading by calculating a counts per million reads per Kb of mRNA using a sum of exon-level counts in the publicly available and preprocessed TCGA data as the total aligned counts denominator.

### **Survival/recurrence data analysis**

The relationship between Mena/Mena<sup>INV</sup> expression levels (from mRNA TCGA or protein TMA) and survival (time to death) or metastasis (time to recurrence) was assessed by Log rank Mantel-Cox test. In each samples, patients were binned into quartiles according Mena or Mena<sup>INV</sup> expression (Q1 being the highest level of expression and Q4 being the lowest). The hazard ratio for each quartile (with 95% confidence interval values) was calculated. The p value generated by this log rank test evaluates whether the difference in the curves is significantly different. We also performed the Log rank test for trend to further assess the differences between the curves representing patients with varying levels of Mena isoform expression.



The hazard effects of Mena<sup>INV</sup> and Mena upon the time to death were investigated by Cox regression using R 2.15.3 basing on TCGA BRCA data. In order to make comparison across variables, we first standardized Mena and Mena<sup>INV</sup> RPKM values to mean zero and standard deviation one. Cox regressions were then carried out basing on the standardized Mena<sup>INV</sup> values or the standardized Mena RPKM values as the only independent variable to predict the effects upon the time of death of the BRCA patients in TCGA study. The association between Mena<sup>INV</sup>/Mena expression level and survival status of TCGA BRCA subjects was evaluated by logistic regression using R 2.15.3. In order to compare coefficients across tests, we first standardized INV and Mena values to be mean zero and standard deviation one. Logistic regressions were conducted by choosing survival status as dependent variable (1 as death, and 0 as alive). The only independent variable fitted in the model was INV, or Mena respectively. P values and coefficients corresponding to the independent variables were used to judge the significance of the association as well as the strength of the association.

**Author contributions:**

MJO designed and performed experiments, data analysis and prepared the manuscript. FBG guided overall experimental design, performed TCGA data analysis and helped prepare the manuscript. OJ developed the microscale device and helped design *in vivo* haptotaxis experiments, TK and LCB performed haptotaxis assays, immunofluorescence, western blots, BCG performed the Mena- $\alpha$ 5 IP experiments, JW assisted with intravital imaging and intravital imaging, DR developed and validated the shMena constructs, JML helped with animal experiments, SBA helped with *in vitro* haptotaxis assays. CW and DM performed TCGA data retrieval and analysis. KBW generated the TMA. RL, MJC, JEB, DAL, PK, ROH and FBG were involved in the study design and data interpretation. All authors discussed the results and commented on the manuscript.

**Acknowledgements:**

We thank the Microscopy, Flow Cytometry and Histology facilities in the KI Swanson Biotechnology Center for support. We thank MetaStat for use of a Vectra scanner and software. We thank Jenny Tadros for help with cell line generation, Shannon Hughes for the cloning of Mena shRNA constructs, and Jane Sottile (Rochester) for the 70kD FN fragment.

## References

1. Joyce JA, Pollard JW. Microenvironmental regulation of metastasis. *Nat Rev Cancer*. 2009;9:239–52.
2. Pickup MW, Mouw JK, Weaver VM. The extracellular matrix modulates the hallmarks of cancer. *EMBO Rep*. EMBO Press; 2014;15:1243–53.
3. Naba A, Clauser KR, Lamar JM, Carr SA, Hynes RO. Extracellular matrix signatures of human mammary carcinoma identify novel metastasis promoters. *Elife*. 2014; 3:e01308.
4. Conklin MW, Keely PJ. Why the stroma matters in breast cancer: insights into breast cancer patient outcomes through the examination of stromal biomarkers. *Cell Adh Migr*; 2012;6:249–60.
5. Conklin MW, Eickhoff JC, Riching KM, Pehlke CA, Eliceiri KW, Provenzano PP, et al. Aligned collagen is a prognostic signature for survival in human breast carcinoma. *Am J Pathol*; 2011;178:1221–32.
6. Ioachim E, Charchanti A, Briasoulis E, Karavasili V, Tsanou H, Arvanitis DL, et al. Immunohistochemical expression of extracellular matrix components tenascin, fibronectin, collagen type IV and laminin in breast cancer: Their prognostic value and role in tumour invasion and progression. *Eur J Cancer*. 2002;38:2362–70.
7. Bae YK, Kim A, Kim MK, Choi JE, Kang SH, Lee SJ. Fibronectin expression in carcinoma cells correlates with tumor aggressiveness and poor clinical outcome in patients with invasive breast cancer. *Hum Pathol*. 2013;44:2028–37.
8. Roussos ET, Condeelis JS, Patsialou A. Chemotaxis in cancer. *Nat Rev Cancer*; 2011;11:573–87.
9. Astrof S, Crowley D, George EL, Fukuda T, Sekiguchi K, Hanahan D, et al. Direct test of potential roles of EIIIA and EIIIB alternatively spliced segments of fibronectin in physiological and tumor angiogenesis. *Mol Cell Biol*. 2004;24:8662–70.
10. Levental KR, Yu H, Kass L, Lakins JN, Egeblad M, Erler JT, et al. Matrix Crosslinking Forces Tumor Progression by Enhancing Integrin Signaling. *Cell*. 2009;139:891–906.
11. Huttenlocher A, Horwitz AR. Integrins in cell migration. *Cold Spring Harb Perspect Biol*. 2011;3:1–16.
12. Schwarzbauer JE, DeSimone DW. Fibronectins, their fibrillogenesis, and in vivo functions. *Cold Spring Harb. Perspect. Biol*. 2011; 3:1–19.
13. Kadler KE, Hill A, Canty-Laird EG. Collagen fibrillogenesis: fibronectin, integrins, and minor collagens as organizers and nucleators. *Curr. Opin. Cell Biol*. 2008; 20: 495–501.
14. Gertler F, Condeelis J. Metastasis: tumor cells becoming MENAcing. *Trends Cell Biol*. 2011;21:81–90.
15. Gupton SL, Riquelme D, Hughes-Alford SK, Tadros J, Rudina SS, Hynes RO, et al. Mena binds  $\alpha 5$  integrin directly and modulates  $\alpha 5 \beta 1$  function. *J Cell Biol*; 2012;198:657–76.
16. Goswami S, Philippar U, Sun D, Patsialou A, Avraham J, Wang W, et al. Identification of invasion specific splice variants of the cytoskeletal protein Mena

- present in mammary tumor cells during invasion in vivo. *Clin Exp Metastasis*; 2009;26:153–9.
17. Philippar U, Roussos ET, Oser M, Yamaguchi H, Kim H-D, Giampieri S, et al. A Mena Invasion Isoform Potentiates EGF-Induced Carcinoma Cell Invasion and Metastasis. *Dev Cell*; 2008;15:813–28.
  18. Roussos ET, Balsamo M, Alford SK, Wyckoff JB, Gligorijevic B, Wang Y, et al. Mena invasive (MenaINV) promotes multicellular streaming motility and transendothelial migration in a mouse model of breast cancer. *J Cell Sci*; 2011;124:2120–31.
  19. Wu C, Asokan SB, Berginski ME, Haynes EM, Sharpless NE, Griffith JD, et al. Arp2/3 is critical for lamellipodia and response to extracellular matrix cues but is dispensable for chemotaxis. *Cell*. 2012;148:973–87.
  20. Asokan SB, Johnson HE, Rahman A, King SJ, Rotty JD, Lebedeva IP, et al. Mesenchymal Chemotaxis Requires Selective Inactivation of Myosin II at the Leading Edge via a Noncanonical PLC $\gamma$ /PKC $\alpha$  Pathway. *Dev Cell*; 2014;31:747–60.
  21. Bear JE, Loureiro JJ, Libova II, Fässler RR, Wehland JJ, Gertler FBFB. Negative regulation of fibroblast motility by Ena/VASP proteins. *Cell*; 2000;101:717–28.
  22. Leyme A, Marivin A, Perez-Gutierrez L, Nguyen LT, Garcia-Marcos M. Integrins activate trimeric G proteins via the nonreceptor protein GIV/Girdin. *J Cell Biol*. 2015;210:1165–84.
  23. Wang W, Goswami S, Lapidus K, Wells AL, Wyckoff JB, Sahai E, et al. Identification and testing of a gene expression signature of invasive carcinoma cells within primary mammary tumors. *Cancer Res*. 2004;64:8585–94.
  24. Hynes RO, Yamada KM. Fibronectins: Multifunctional modular glycoproteins. *J. Cell Biol*. 1982;95:369–77.
  25. Muller PAJ, Caswell PT, Doyle B, Iwanicki MP, Tan EH, Karim S, et al. Mutant p53 Drives Invasion by Promoting Integrin Recycling. *Cell*. 2009;139:1327–41.
  26. Oudin MJ, Hughes SK, Rohani N, Moufarrej MN, Jones JG, Condeelis JS, et al. Characterization of the expression of the pro-metastatic Mena(INV) isoform during breast tumor progression. *Clin Exp Metastasis*. 2015, Dec 17, Epub ahead of print
  27. Wyckoff JB, Segall JE, Condeelis JS. The collection of the motile population of cells from a living tumor. *Cancer Res*; 2000;60:5401-4.
  28. Jonas O, Landry HM, Fuller JE, Santini JT, Baselga J, Tepper RI, et al. An implantable microdevice to perform high-throughput in vivo drug sensitivity testing in tumors. *Sci Transl Med*. 2015;7:284ra57.
  29. Pignatelli J, Goswami S, Jones JG, Rohan TE, Pieri E, Chen X, et al. Invasive breast carcinoma cells from patients exhibit MenaINV- and macrophage-dependent transendothelial migration. *Sci Signal*. 2014;7:ra112.
  30. Cancer Genome Atlas Network. Comprehensive molecular portraits of human breast tumours. *Nature*; 2012;490:61–70.
  31. Lin EY, Jones JG, Li P, Zhu L, Whitney KD, Muller WJ, et al. Progression to malignancy in the polyoma middle T oncoprotein mouse breast cancer model provides a reliable model for human diseases. *Am J Pathol*; 2003;163:2113–26.

32. Wang L, Zhao Z, Meyer M, Saha S, Yu M, Guo A, et al. CARM1 methylates chromatin remodeling factor BAF155 to enhance tumor progression and metastasis. *Cancer Cell*. 2014;25:21–36.
33. Hynes RO. Integrins: Bidirectional, allosteric signaling machines. *Cell*. 2002; 110: 673–87.
34. Sottile J, Hocking DC. Fibronectin polymerization regulates the composition and stability of extracellular matrix fibrils and cell-matrix adhesions. *Mol Biol Cell*. 2002;13:3546–59.
35. Roussos ET, Wang Y, Wyckoff JB, Sellers RS, Wang W, Li J, et al. Mena deficiency delays tumor progression and decreases metastasis in polyoma middle-T transgenic mouse mammary tumors. *Breast Cancer Res*; 2010;12:R101.
36. Gertler F, Condeelis J. Metastasis: tumor cells becoming MENAcing. *Trends Cell Biol*. 2011;21:81–90.
37. Hynes RO. The extracellular matrix: not just pretty fibrils. *Science*; 2009;326:1216–9.
38. Iyer AK V, Tran KT, Griffith L, Wells A. Cell surface restriction of EGFR by a tenascin cytotactin-encoded EGF-like repeat is preferential for motility-related signaling. *J Cell Physiol*. 2008;214:504–12.
39. Mitra AK, Sawada K, Tiwari P, Mui K, Gwin K, Lengyel E. Ligand-independent activation of c-Met by fibronectin and  $\alpha(5)\beta(1)$ -integrin regulates ovarian cancer invasion and metastasis. *Oncogene*. 2011;30:1566–76.
40. Vogelstein B, Lane D, Levine AJ. Surfing the p53 network. *Nature*. 2000; 408:307–10.
41. Muller PAJ, Trinidad AG, Timpson P, Morton JP, Zanivan S, van den Berghe PVE, et al. Mutant p53 enhances MET trafficking and signalling to drive cell scattering and invasion. *Oncogene*. 2013; 32:1252-65.
42. Hughes SK, Oudin MJ, Tadros J, Neil J, Del Rosario A, Joughin BA, et al. PTP1B-dependent regulation of receptor tyrosine kinase signaling by the actin-binding protein Mena. *Mol Biol Cell*. 2015; 26:3867-78.
43. McDonald JA, Kelley DG, Broekelmann TJ. Role of fibronectin in collagen deposition: Fab' to the gelatin-binding domain of fibronectin inhibits both fibronectin and collagen organization in fibroblast extracellular matrix. *J Cell Biol*. 1982;92:485–92.
44. Chan KT, Asokan SB, King SJ, Bo T, Dubose ES, Liu W, et al. LKB1 loss in melanoma disrupts directional migration toward extracellular matrix cues. *J Cell Biol*. 2014;207:299–315.
45. Wyckoff J. A Paracrine Loop between Tumor Cells and Macrophages Is Required for Tumor Cell Migration in Mammary Tumors. *Cancer Res*. 2004;64:7022–9.
46. Bredfeldt JS, Liu Y, Pehlke C a, Conklin MW, Szulczewski JM, Inman DR, et al. Computational segmentation of collagen fibers from second-harmonic generation images of breast cancer. *J Biomed Opt*. 2014;19:16007.

## Figure legends

**Figure 1: Mena-driven haptotaxis *in vitro* on FN gradients in 2D and 3D is dependent upon its direct interaction with  $\alpha 5$  integrin and F-actin.** A) Schematic diagram of a microfluidic device used for 2D or 3D haptotaxis, representative image of a FN gradient in a collagen gel, and a diagram describing the FMI used to quantify haptotaxis. B) Expression of Mena, but not VASP or EVL, in MV<sup>D7</sup> fibroblasts drives haptotaxis on a 2D FN gradient (125 $\mu$ g/ml at top of gradient), as measured by the FMI. C) 231-Mena cells haptotax when plated on a 2D FN gradient (125 $\mu$ g/ml at top of gradient), but not on a LN or VN gradient, as measured by the FMI. D) MDAMB231 cells 231-Mena cells plated in a 3D collagen gel and subjected to increasing concentrations of FN at the top of the gradient. E) Inhibition of  $\alpha 5\beta 1$  with P1D6 (0.5 $\mu$ g/ml) blocked Mena-driven haptotaxis in 3D collagen gels, as measured by FMI, while inhibition of  $\alpha \nu \beta 3$  with Cilengitide (1 $\mu$ M) had no effect. F) Diagram of structure of Mena and its domains, including the LERER domain and the F-Actin binding domain (FAB). Deletion of the LERER domain abrogates the interaction of Mena/Mena<sup>INV</sup> with  $\alpha 5$ . G) 231-Mena $\Delta$ LERER and Mena $\Delta$ FAB cells did not haptotax in 3D collagen gels and this effect was independent of an effect on velocity ( $\mu$ m/min) (H). For each experiment, n=3 experiments, at least 80 cells tracked per condition. Results show mean  $\pm$  SEM, significance by one way ANOVA, \*p<0.5, \*\*p<0.01, \*\*\*p<0.005. See FigS1.

**Figure 2: Mena<sup>INV</sup>-drives haptotaxis at high FN concentrations *in vivo* and *in vitro***

A) 231-Mena<sup>INV</sup> cells plated in a 3D collagen gel and subjected to increasing concentrations of FN at the top of the gradient B) Inhibition of  $\alpha 5$  with P1D6 (0.5 $\mu$ g/ml) blocked Mena<sup>INV</sup>-driven 3D haptotaxis, as measured by FMI, while inhibition of  $\alpha \nu \beta 3$  with Cilengitide had no effect. 231-Mena<sup>INV</sup> $\Delta$ LERER or 231-Mena<sup>INV</sup> $\Delta$ FAB did not haptotax in



3D. (n=3 experiments,  $\geq 150$  cells tracked per condition). C) *In vivo* invasion assay into needles inserted in tumors generated in NOD/SCID mice with MDAMB231 cells expressing Control-GFP, Mena or Mena<sup>INV</sup>. Needles contained 0.5mg/ml collagen and increasing amounts of FN (n=4 mice per condition). Results show mean  $\pm$  SEM. Stars above columns represent significance relative to collagen only by one-way ANOVA. D) Representative image of a FN gradient (Rhodamine-labeled FN, shown in red) on collagen fibers (shown in white) generated using a microscale implantable device implanted into the tumor (tumor cells labeled with GFP shown in green) and visualized by intravital imaging. Scale bar is 100 $\mu$ m. FMI of E) MDAMB231 and F) SUM159 tumor cells expressing different Mena isoforms in the absence of a device, or in the presence of a device releasing fluorescently labeled FN or similarly sized Dextran (data pooled  $\geq 8$  movies from  $\geq 2$  mice per condition). Results show mean  $\pm$  SEM, significance by one way ANOVA, \*p<0.5, \*\*p<0.01, \*\*\*p<0.005. See FigS2.

**Figure 3: Mena<sup>INV</sup> is associated with poor outcome in human tumors and requires its interaction with  $\alpha 5$  integrin for metastasis**

Kaplan-Meier curves for survival of breast cancer patients binned by quartiles of Mena (A) or Mena<sup>INV</sup> (B) mRNA levels, as indicated (Q1 had the highest expression, Q4 the lowest). Data are from 128 breast cancer cases with >10 years of follow up BRCA TCGA dataset (data from entire 1060 patient cohort in Figs S3A-D). Significance calculated by log-rank Mantel-Cox test, hazard ratio calculated by logrank test,  $p_{Trend}$  calculated by log-rank test for Trend (see methods). C) COX regression carried out to assess the relationship between Mena or Mena<sup>INV</sup> and time to death in breast cancer patients (patients with 10-year follow-up). D) Logistic regression carried out to assess the relationship between Mena or Mena<sup>INV</sup> and survival in breast cancer patients (patients with 10-year follow-up). E) Representative images of PyMT-MMTV tumors stained for

Mena (red) and Mena<sup>INV</sup> (green) Scale bar = 20μm. F) Representative images of PyMT-MMTV stained for Mena<sup>INV</sup> (green) and integrin α5 (red) Same scale as E. G) Representative image from a wild-type PyMT tumor FN (red), Mena<sup>INV</sup> (green) and nuclei (DAPI staining) Scale bar = 100μm. H) Correlation between Mena<sup>INV</sup> and collagen FN intensity. Data from over 50 fields from 4 PyMT mice, each dot represents an individual field. I) Representative image of tumor spot from a tissue microarray with high levels of Mena<sup>INV</sup> (green) and FN (red). J) Correlation between FN and Mena<sup>INV</sup> staining in the entire patient cohort. K) Mena<sup>INV</sup> expression in 300 breast cancer patients comparing patients with or without recurrence, data shows mean +/- SEM. L) Table showing the median recurrence-free time in months and corresponding p-value in patients with high vs. low Mena<sup>INV</sup>, high vs., low FN or high vs. low Mena<sup>INV</sup>+FN. Significance calculated by log-rank Mantel-Cox test. M) Representative fluorescence images of GFP-positive metastasis in lungs of mice with 231-Control, Mena or Mena<sup>INV</sup> tumors. Scale bar = 50μm. N) H&E images of FFPE sections cut from the lungs of mice bearing MDAMB231 tumors expressing different Mena isoforms. Scale bar is 100μm. O) Lung metastatic index of NOD-SCID mice bearing tumors grown from MDAMB231 cells expressing different GFP-tagged Mena isoforms and measuring at least 1 cm in diameter (n≥4 mice per cell line). Data show mean ± SEM, significance by one way ANOVA, \*p<0.5, \*\*p<0.01, \*\*\*p<0.005. See FigS3 and S4.

**Figure 4: Mena<sup>INV</sup> drives haptotaxis via increased FX signaling** A) Representative images of 231-Control, Mena and Mena<sup>INV</sup> cells plated on FN and collagen, stained with antibodies to α5, and GFP (to visualize tagged GFP-Mena or GFP- Mena<sup>INV</sup>) and with phalloidin to visualize F-actin. Scale bar = 5μm. B) Magnification of inset shown in (A). Scale bar = 1μm. C) Quantification of cell area (in μm<sup>2</sup>) of MDAMB231 cells expressing different isoforms when plated on collagen (0.1mg/ml) + FN (50μg/ml). D) Number of α5-

positive adhesions relative to cell area for 231-Mena and 231-Mena<sup>INV</sup> cells for cells plated on collagen only, collagen (0.1mg/ml) + FN (50µg/ml), and in the presence of P1D6, α5-function blocking antibody. E) Number of α5-positive adhesions relative to cell area for cells plated on collagen + FN. F) Intensity of α5 signal in Mena-positive adhesions (as counted by GFP positivity) for 231-Mena and 231-Mena<sup>INV</sup> cells plated on collagen only, collagen (0.1mg/ml) + FN (50µg/ml), and in the presence of P1D6, α5-function blocking antibody. G) Intensity of α5 signal in Mena-positive adhesions (as counted by GFP positivity) in cells plated on a low 2D 125 µg/ml FN gradient. H) Inhibition of FAK (0.5µM) decreased Mena<sup>INV</sup>-driven 2D haptotaxis on a low 2D 125 µg/ml FN gradient. Data from ≥3 experiments, with ≥80 cells tracked per condition. I) Representative images of 231-Control, Mena and Mena<sup>INV</sup>, 231-MenaΔLERER and MenaΔFAB cells plated on a low 2D 125 µg/ml FN gradient, stained with pFAK397 (red) and Phalloidin to visualize F-actin (blue). Scale bar = 5µm. J) Quantification of pFAK Y397-positive adhesions in 231-Control, Mena or Mena<sup>INV</sup>, while plated on a 2D low 125 µg/ml FN gradient K) 231-Mena<sup>INV</sup>ΔLERER or 231-Mena<sup>INV</sup>ΔFAB cells had decreased number of pFAK Y397-positive adhesions on a 2D low 125 µg/ml FN gradient. L) Quantification of pFAK Y397-positive adhesions in 231-Control, Mena or Mena<sup>INV</sup>, while plated on a 2D high 500 µg/ml FN gradient Data pooled from 3 experiments, with at least 30 cells analyzed per condition. M) Representative image of a WB for α5-immunoprecipitation from 231-Mena and 231-Mena<sup>INV</sup> lysates, probed for Mena, α5 and Tubulin. N) Quantification of fold increase in Mena pulled down in α5-IP, n=4. For all staining experiments, data pooled from at least 3 experiments, with at least 10 cells analyzed per experiments. Results show mean ± SEM, significance by one way ANOVA, \*p<0.5, \*\*p<0.01, \*\*\*p<0.005. Stars above data set represent significance relative to control. See FigS5.

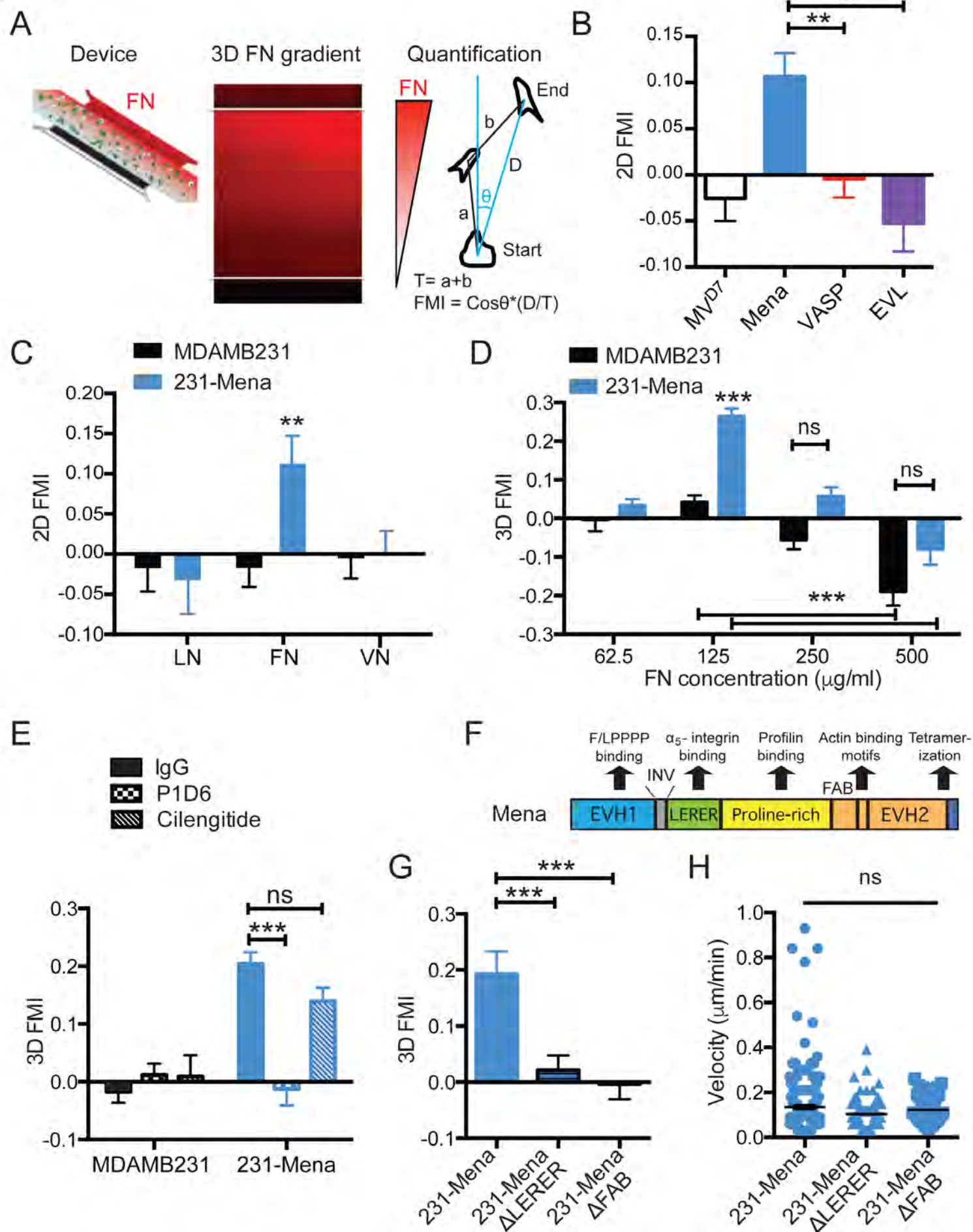
**Figure 5: Mena<sup>INV</sup>-dependent directional motility requires ECM reorganization *in vitro*** A) Representative images of MDAMB231 cells (outlined in white) and 231-Mena<sup>INV</sup> cells (green) in a 3D 125µg/ml FN gradient (red) in a collagen gel (blue) in merged image; middle and right panels show grayscale images of FN and Collagen alone, respectively. Scale bar is 25µm. 231-Mena<sup>INV</sup> showed increased accumulation and reorganization of B) FN and C) Collagen, in both low 125µg/ml and high 500µg/ml 3D FN gradients. D) A gradient of recombinant 7-11 domains of FN failed to induce 3D haptotaxis of 231-Mena<sup>INV</sup> cells, as measured by the FMI E) Inhibition of FN fibrillogenesis by inclusion of a 70kD fragment ablated Mena<sup>INV</sup>-dependent haptotaxis in 3D FN gradients (n=3 experiments, ≥80 cells tracked per condition). Deletion of the FAB and LERER regions in Mena<sup>INV</sup>, and inhibition of α5β1 with P1D6, but not Cilengitide, reduced collagen (F) and collagen (G) accumulation at low FN concentrations. Data from ≥3 experiments, with ≥30 cells analyzed per condition. Results show mean ± SEM, significance by one way ANOVA, \*p<0.5, \*\*p<0.01, \*\*\*p<0.005. See FigS6.

**Figure 6: Mena<sup>INV</sup> drives collagen reorganization in tumors.** A) Representative image from a wild type and Mena<sup>-/-</sup> PyMT tumor showing collagen as imaged by SHG (gray) and nuclei (DAPI staining). Scale bar = 100µm. B) Quantification of collagen signal as measured by SHG signal in wild type and Mena<sup>-/-</sup> PyMT tumors. Data from over 30 fields from 4 mice for wild-type mice and 2 mice for Mena<sup>-/-</sup>, each dot represents an individual field. C) Representative image from a wild-type PyMT tumor showing collagen as imaged by SHG (gray) and Mena<sup>INV</sup> (green). Scale bar = 100µm. D) Correlation between Mena<sup>INV</sup> and collagen intensity. Data from over 50 fields from 4 mice, each dot represents an individual field. E) Representative images showing collagen by SHG from a breast cancer patient samples with high or low Mena<sup>INV</sup>. F) Collagen intensity in 30 patients with high or low Mena<sup>INV</sup> expression. G) Representative images of collagen

organization (gray) of 231-Control, Mena and Mena<sup>INV</sup> xenograft tumors taken by intravital imaging. Scale bar is 100µm. H) Representative diagram of angle used to measure the orientation of individual collagen fibers relative to the edge of the tumors. Plotted distributions of collagen fiber orientation relative to tumors edge comparing Control, Mena and Mena<sup>INV</sup> expressing H1) MDAMB231 and H2) SUM159 cells. Data pooled from ≥15 images from ≥4 mice per condition. Results show mean ± SEM, significance by t-test, \*p<0.5, \*\*p<0.01, \*\*\*p<0.005. See Fig S6

**Figure 7: Summary diagram:** FN levels are high around blood vessels and at invasive edges in tumors. Expression of Mena in tumor cells allows cells to haptotax on low gradients of FN, via its weak association with α5 and increased FX signaling. Expression of Mena<sup>INV</sup> allows cells to haptotax on both low and high FN gradients via increased association with α5, leading to increased FX number and FAK signaling at FXs, as well as through ECM reorganization.

# Figure 1





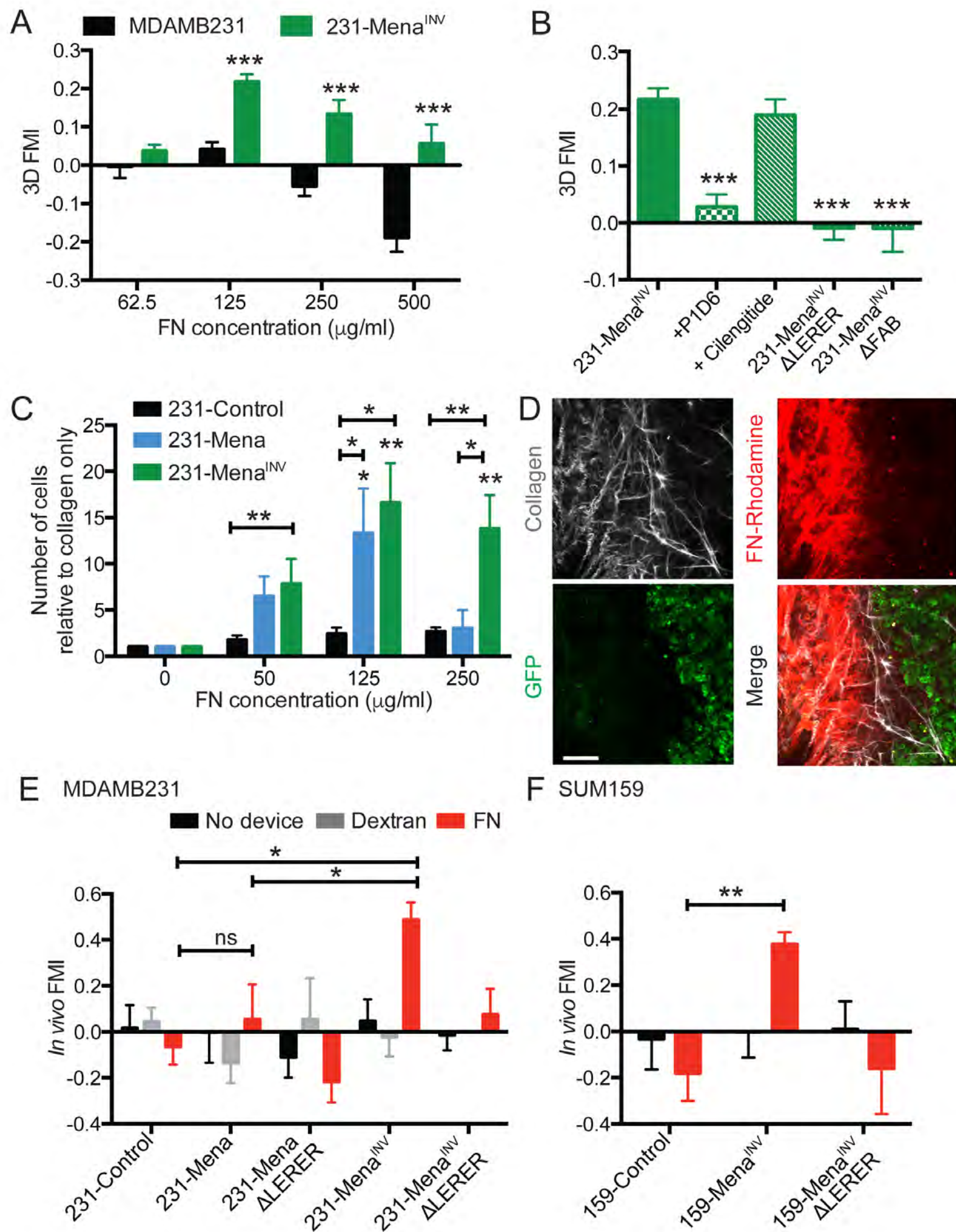
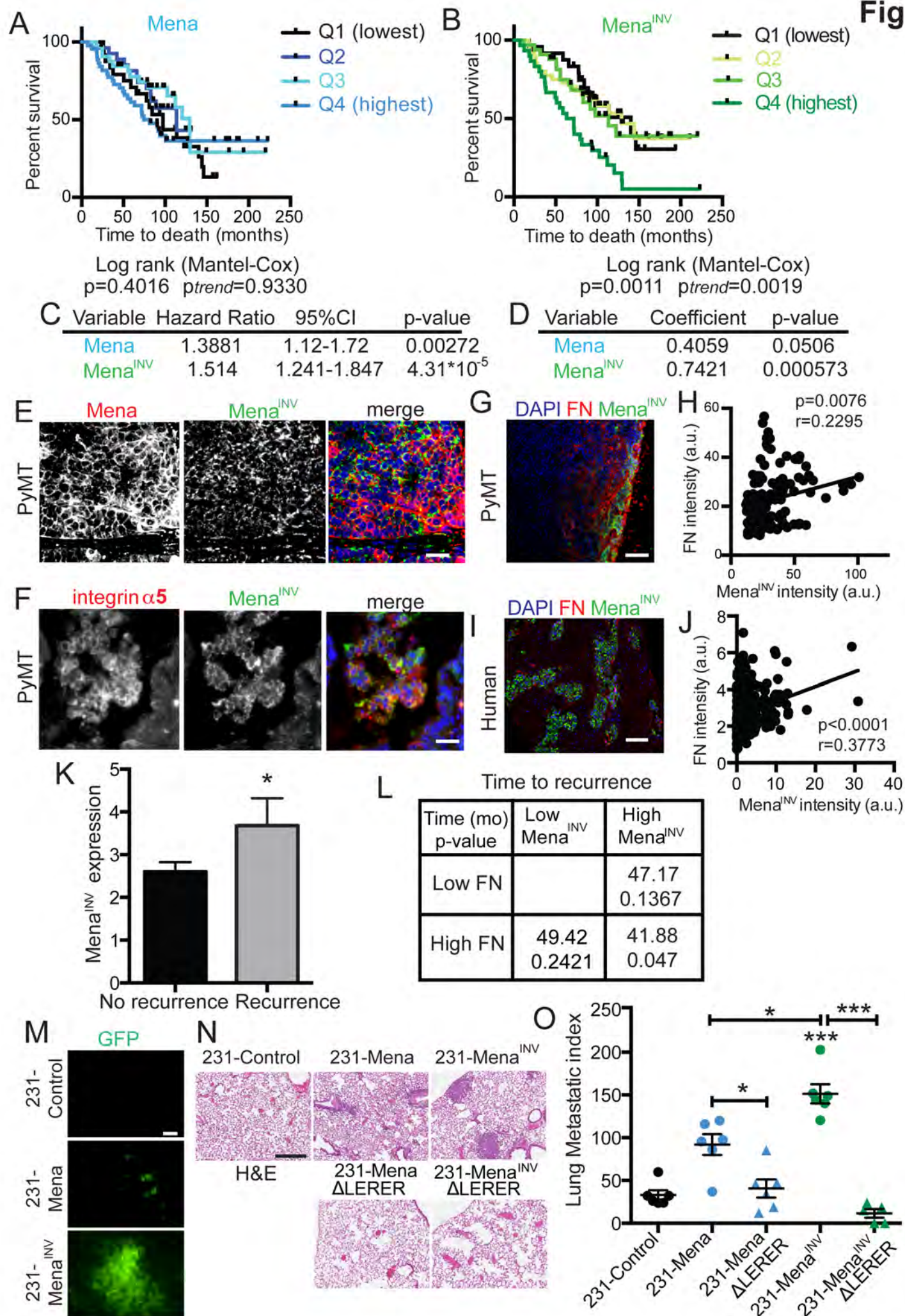
**Figure 2**

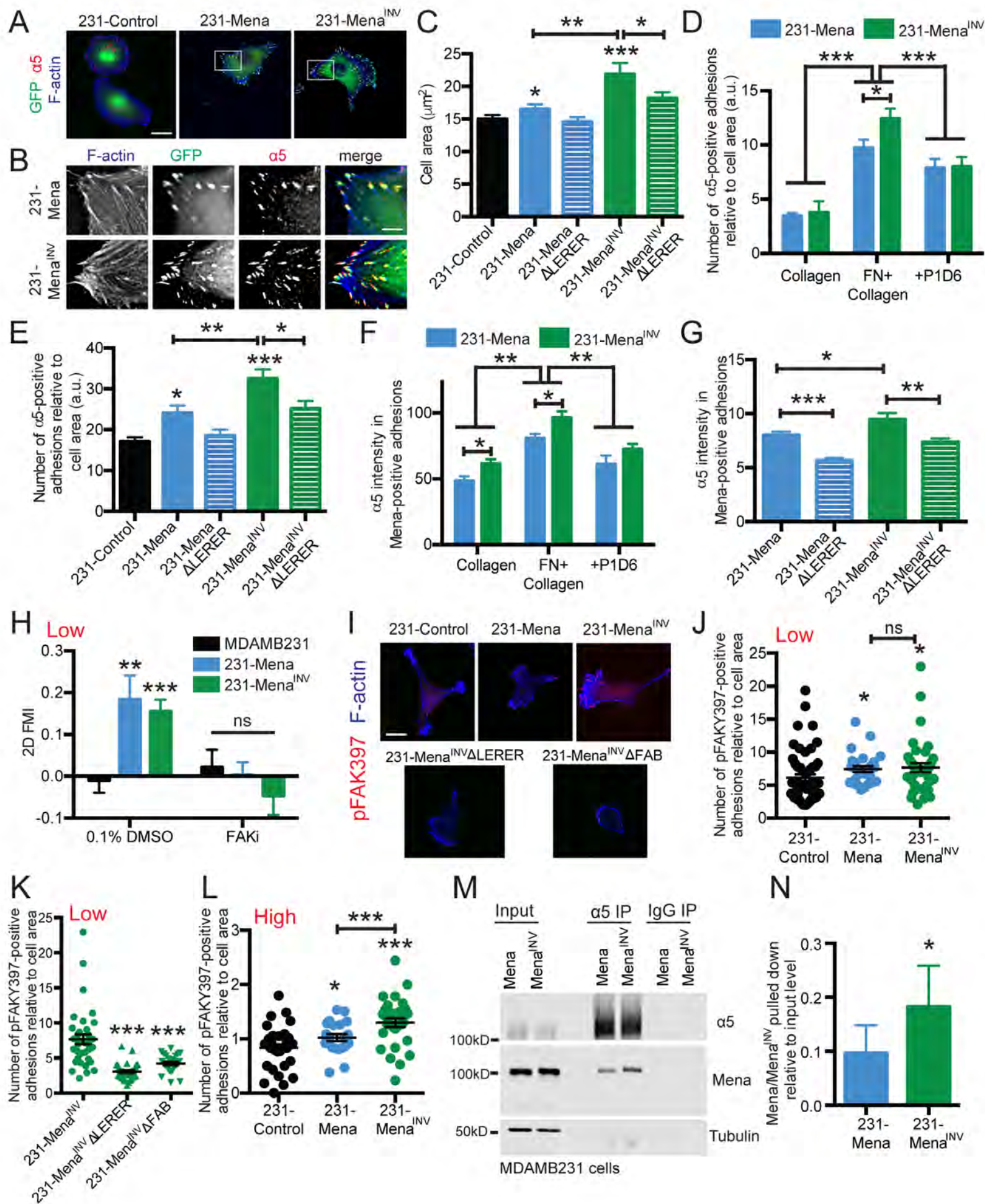


Figure 3





# Figure 4



# Figure 5

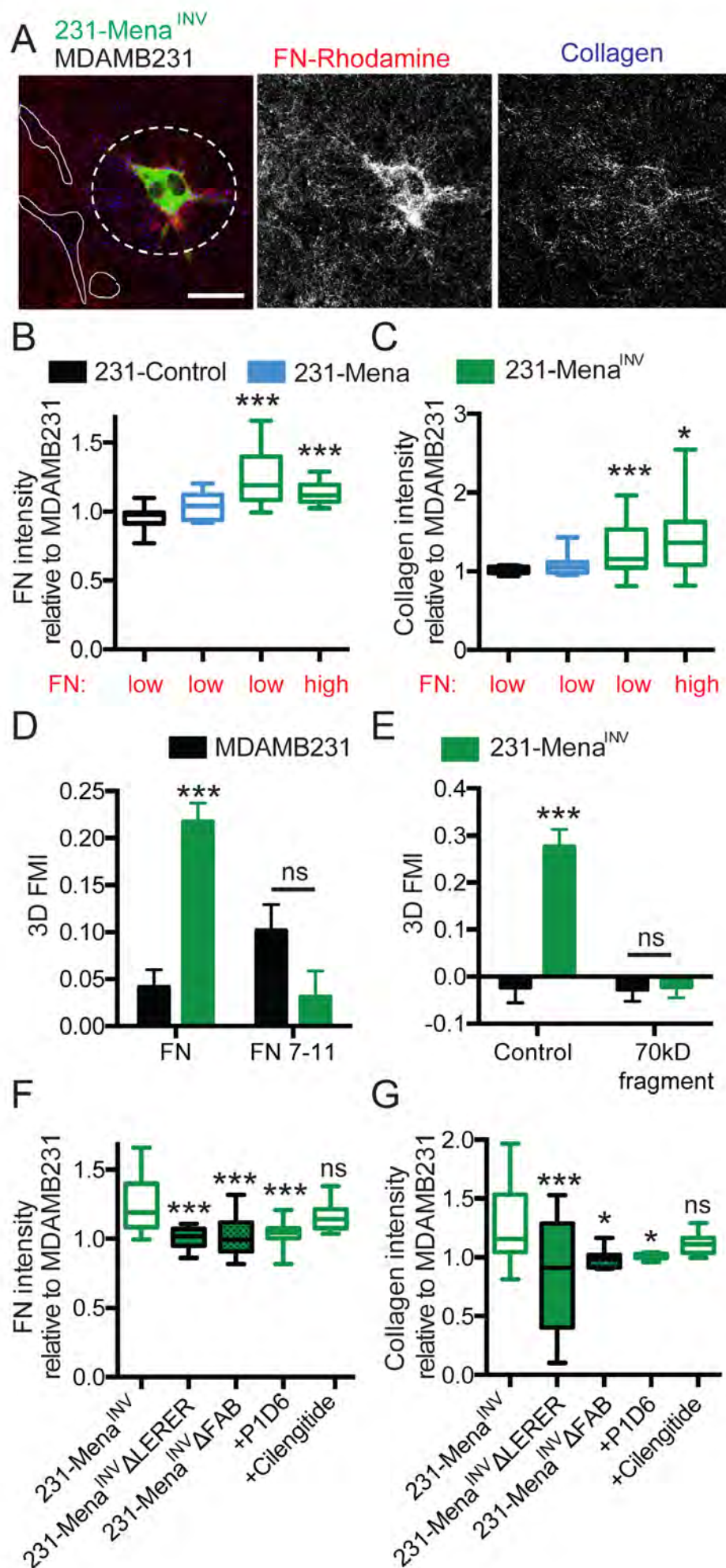
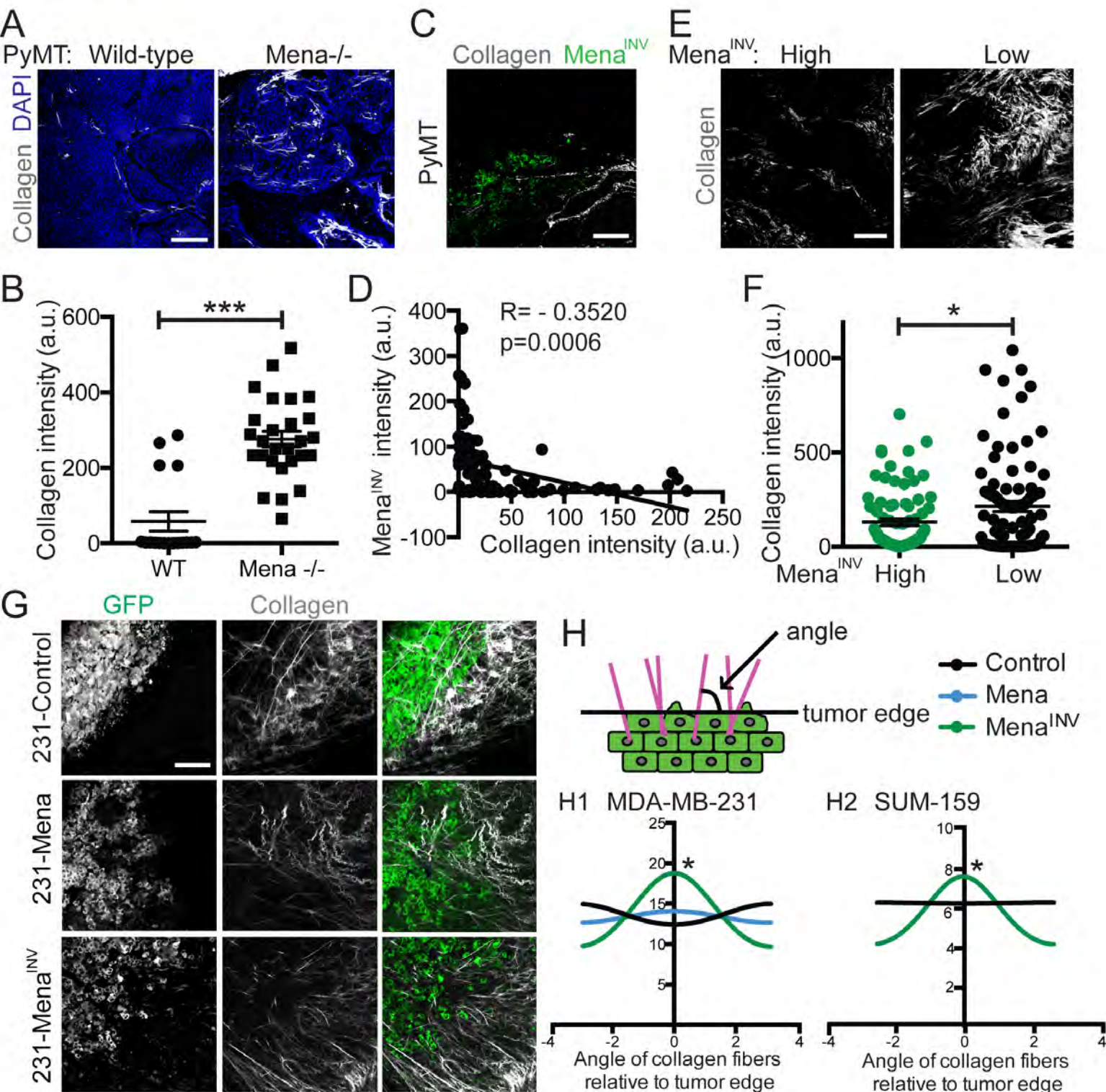
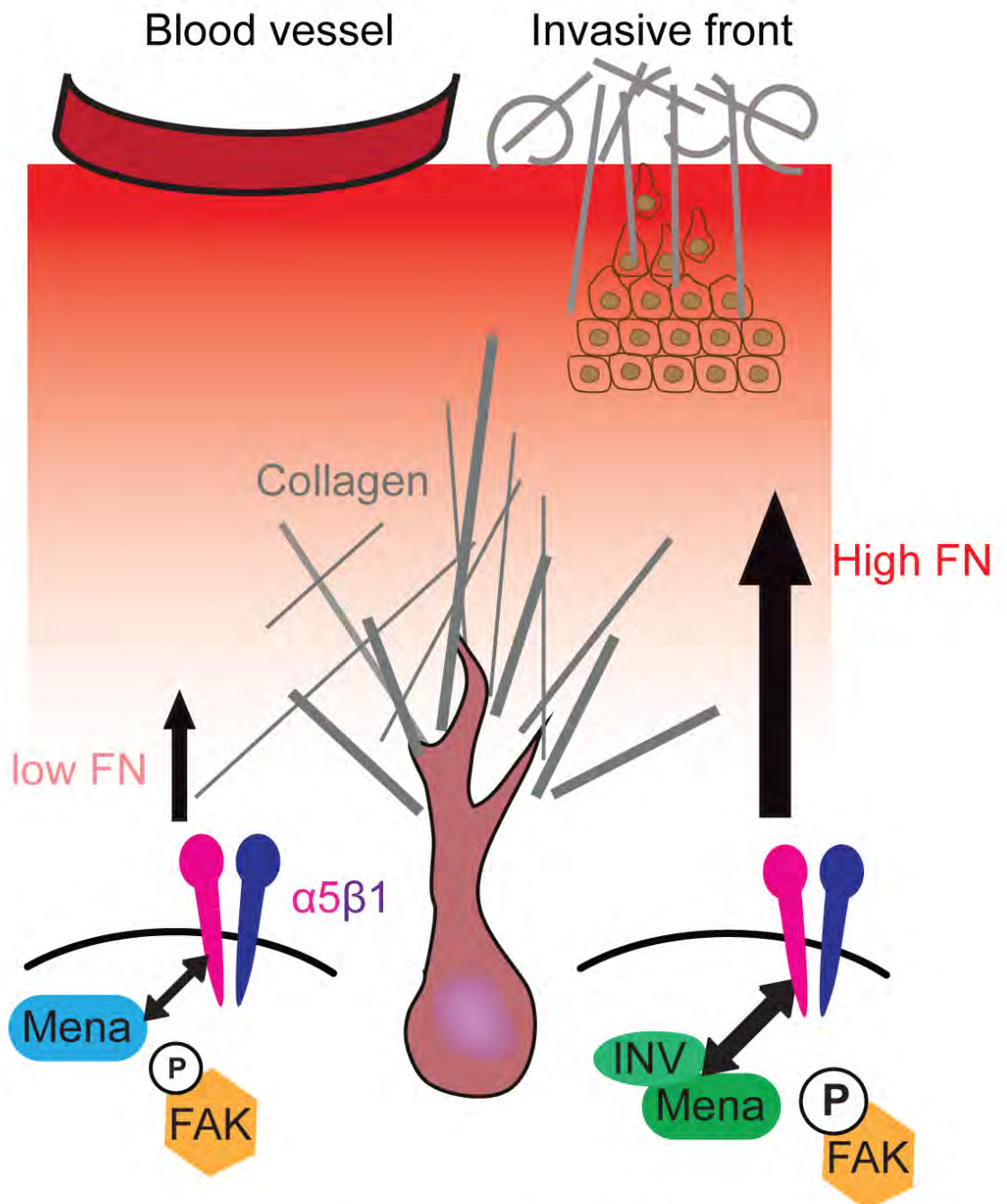




Figure 6



# Figure 7



Haptotaxis at **low** FN via:

- weak Mena- $\alpha5$  interaction
- Mena- $\alpha5$  FX signaling

**Low metastatic potential**

Haptotaxis at **high** FN via:

- stronger Mena- $\alpha5$  interaction
- increased FX number and signaling
- Collagen + FN reorganization

**High metastatic potential**



# **Reduced Proteolytic Shedding of Receptor Tyrosine Kinases is a Post-Translational Mechanism of Kinase Inhibitor Resistance**

Miles A. Miller<sup>1,6\*</sup>, Madeleine J. Oudin<sup>2\*</sup>, Ryan J. Sullivan<sup>3</sup>, Stephanie J. Wang<sup>1</sup>, Aaron S. Meyer<sup>1,2</sup>, Hyungsoon Im<sup>6</sup>, Dennie T. Frederick<sup>4</sup>, Jenny Tadros<sup>2</sup>, Linda G. Griffith<sup>1</sup>, Hakho Lee<sup>6</sup>, Ralph Weissleder<sup>6</sup>, Keith T. Flaherty<sup>3</sup>, Frank B. Gertler<sup>2,5</sup>, Douglas A. Lauffenburger<sup>1,2,5\*\*</sup>

<sup>1</sup>Department of Biological Engineering, Massachusetts Institute of Technology, Cambridge, MA 02139, USA

<sup>2</sup>David H. Koch Institute for Integrative Cancer Research, Massachusetts Institute of Technology, Cambridge, MA 02139, USA

<sup>3</sup>Division of Medical Oncology, Massachusetts General Hospital Cancer Center, Harvard Medical School, Boston, MA, 02114 USA

<sup>4</sup>Division of Surgical Oncology, Massachusetts General Hospital, Boston, MA, 02114 USA

<sup>5</sup>Department of Biology, Massachusetts Institute of Technology, Cambridge, MA 02139, USA

<sup>6</sup>Center for Systems Biology, Massachusetts General Hospital, Harvard Medical School, Boston, MA 02114 USA

\*Contributed equally to this work.

\*\*Corresponding author.

Email: lauffen@mit.edu

Phone: (617) 252-1629

Fax: (617) 258-0204

Address: 77 Massachusetts Ave., Cambridge, MA 02139

RUNNING TITLE: Drug resistance via reduced RTK shedding

KEYWORDS: mitogen activated protein kinase (MAPK), tissue inhibitor of metalloproteinase (TIMP), a disintegrin and metalloproteinase (ADAM), *Kras* mutation

DISCLOSURE OF POTENTIAL CONFLICTS OF INTEREST: No potential conflicts of interest were disclosed.

GRANT SUPPORT: This work was supported by NIH grants U54-CA112967 and R01-CA096504 to D.A.L., and DoD award W81XWH-13-1-0031 to M.J.O.

#### ABSTRACT:

Kinase inhibitor resistance often involves upregulation of poorly understood “bypass” signaling pathways. Here, we show that extracellular proteomic adaptation is one path to bypass signaling and drug resistance. Proteolytic shedding of surface receptors, which can provide negative feedback on signaling activity, is blocked by kinase inhibitor treatment and enhances bypass signaling. In particular, MEK inhibition broadly decreases shedding of multiple receptor tyrosine kinases (RTKs) including HER4, MET, and most prominently AXL, an ADAM10 and ADAM17 substrate, thus increasing surface RTK levels and mitogenic signaling. Progression-free survival of melanoma patients treated with clinical BRAF/MEK inhibitors inversely correlates with RTK shedding reduction following treatment, as measured non-invasively in blood plasma. Disrupting protease inhibition by neutralizing TIMP1 improves MAPK inhibitor efficacy, and combined MAPK/AXL inhibition synergistically reduces tumor growth and metastasis in xenograft models. Altogether, extracellular proteomic rewiring through reduced RTK shedding represents a surprising mechanism for bypass signaling in cancer drug resistance.

#### STATEMENT OF SIGNIFICANCE:

Genetic, epigenetic, and gene expression alterations often fail to explain adaptive drug resistance in cancer. This work presents a novel post-translational mechanism of such resistance: kinase inhibitors, particularly targeting MAPK signaling, increase tumor cell surface receptor levels due to widely reduced proteolysis, allowing tumor signaling to circumvent intended drug action.

## INTRODUCTION:

Mere overexpression of a drug's target often fails to predict efficacy, in part due to "bypass" signaling whereby inhibition of one signaling pathway leads to compensatory signaling through alternative routes. Previous work has largely focused on how intracellular processes such as gene expression changes and mutations contribute to bypass signaling, heterogeneous drug responses, and drug resistance. For example, targeting mitogen-activated-protein-kinase (MAPK) signaling through MEK or B-RAF inhibition leads to increased transcription of multiple receptor tyrosine kinases (RTKs), which then provide alternative pro-growth and pro-survival signals that circumvent the intended inhibitor effects (1-3). However, genetic and gene expression changes account for only a fraction of observed bypass signaling (4, 5). For instance, only half of melanoma patients receiving B-RAF inhibitor therapy exhibit mutations in known B-RAF resistance genes upon emergence of drug resistance; a large fraction of drug resistance arises without defined genetic or epigenetic explanation; and the functional consequences of common genetic or translational alterations often still depend on the activity of signaling through RAS-CRAF and other pathways (6). Importantly, these observations carry substantial implications in the clinic, where many strategies for designing and monitoring an individual's therapeutic course rely largely on genetic or transcriptional information.

This work investigates several cancer types where bypass signaling is evident (1, 2, 7, 8), and focuses primarily on malignant melanoma and triple-negative breast cancer (TNBC), a subtype of breast cancer with poor prognosis, no approved targeted therapies, and which is classified by low expression of estrogen receptor, progesterone receptor, and HER2 (9). MEK inhibition (MEKi) represents one promising therapeutic strategy, as MAPK signaling is dysregulated in many cancers, including TNBC and melanoma (9, 10), and clinical trials have

recently been completed or are ongoing in several cancers including TNBC (9). As a treatment strategy, MAPK inhibition (MAPKi) has been most successful in melanoma, with three such inhibitors gaining FDA approval since 2011. However, resistance to MAPKi develops in most patients within a year (11). More generally, MAPKi carries broad importance given many other relevant drug targets including various RTKs are upstream of the MAPK pathway and indirectly affect its activity.

Relative to tumor gene expression changes, little attention has been paid to how the tumor-derived extracellular proteome changes in response to targeted kinase inhibitors, and how such changes impact bypass signaling and drug efficacy. Of central importance, the ‘A Disintegrin and Metalloproteinases’ (ADAMs) ADAM10 and ADAM17 are widely known as the principal “shedases” of the cell surface responsible for shedding ectodomains of hundreds of transmembrane substrates, including many growth factors, cytokines, adhesion molecules, and metalloproteinases involved in the processes described above. ADAM10 is required for activation of the Notch signaling pathway, while ADAM17 is needed for TNF $\alpha$  cleavage, and both *ADAM10*<sup>-/-</sup> and *ADAM17*<sup>-/-</sup> mice are not viable (12). *ADAM10* and *ADAM17* are particularly overexpressed in many cancers including breast cancer and melanoma (13, 14), with activities governed by frequently dysregulated MAPK signaling (10, 15). Furthermore, ADAM10 and ADAM17 have been considered promising drug targets for their part in shedding EGF-family growth factor ligands from the surface of cancer cells, a process that mediates ErbB-family receptor mitogenic signaling in an autocrine manner (13, 16, 17). Unfortunately, metalloproteinase inhibitors, including a second-generation inhibitor with specificity towards ADAM10 and ADAM17 (INCB7839, Incyte), have failed in clinical trials despite promising initial results (18). These failures can largely be attributed to a poor understanding of how the

broad activity of ADAMs, and metalloproteinases in general, integrate to influence overall tumor behavior (19).

Here, we identify differential extracellular proteolytic shedding as a major post-translational mechanism of bypass signaling that complements other pathways of drug resistance. Proteolytic shedding of surface receptors, which can provide negative feedback on signaling network activity, is dramatically reduced upon inhibition of kinase pathways such as the MAPK pathway. Decreased RTK proteolysis consequently leads to surface RTK accumulation and increased signaling through other pathways that support mitogenesis. Thus, we hypothesized that RTK proteolysis could (a) be non-invasively monitored in patients; (b) enable early detection of drug resistance in the clinic; and (c) guide the design of combination therapies that forestall disease progression. Indeed, we found that circulating RTKs were detectable at elevated levels in a subset of patients, and that shed RTK levels accurately predicted clinical MAPKi response better than mere RTK gene expression. We tested two strategies to enhance MAPKi efficacy: (1) modulating ADAM10 through neutralizing its cognate inhibitor “tissue inhibitor of metalloproteinases 1” (TIMP1), and (2) inhibiting the RTK AXL, a key protease substrate that we observed to be upregulated following MAPKi. In several orthotopic animal models, combination therapies exhibited synergistic effects on tumor growth, metastasis, and survival. Altogether, our findings demonstrate that extracellular proteomic rewiring through reduced proteolytic receptor shedding represents a significant and targetable mechanism for bypass signaling in acquired cancer drug resistance.

## RESULTS

### ***MAPKi causes a global reduction in circulating RTKs***

RTK signaling mediates drug resistance (1, 7, 20), and the release of RTK ectodomains from the cell surface has become an increasingly appreciated regulator of signaling activity in contexts of cancer metastasis (21), antibody therapies (22), and in other invasive diseases (15). However, little is known regarding how extracellular RTK levels change in response to targeted kinase inhibitor treatment, and how such changes influence drug efficacy in cancer. To study these effects, we first measured how MEKi impacts the supernatant accumulation of seven key RTKs that have been implicated in drug resistance: the four ErbB-family receptors (epidermal growth factor receptor EGFR, HER2, HER3, and HER4); insulin-like growth factor receptor 1 (IGF1R); hepatocyte growth factor receptor (HGFR/MET); and the TAM-family RTK member, AXL. Using two MEK inhibitors U0126 and PD325901 (Fig 1A, Fig. S1A validates reduction in pErk), we examined a panel of 12 cell lines from several cancer types where bypass signaling has been implicated, including malignant melanoma (MM), TNBC, non-small cell lung cancer (NSCLC), and glioblastoma multiforme (GBM). We surprisingly found that only decreased (rather than increased) supernatant RTK accumulation was consistently and significantly observed across the panel of measurements (Fig. 1A-B). Most prominently, supernatant AXL and MET decreased by roughly 50% in nearly every cell line. We confirmed by ultra-centrifugation that AXL and MET were unassociated with supernatant microvesicles (Fig. S1B). Supernatant accumulation of both RTKs could be blocked by broad-spectrum metalloproteinase inhibition (MPi) using batimastat (BB94), suggesting their accumulation resulted from proteolytic release off the cell surface (Fig. S1C). EGFR, which is not a suspected



metalloproteinase substrate, behaved in stark contrast to MET and AXL: in the supernatant, EGFR i) did not consistently decrease in response to MEKi (Fig. 1A-B) ii) was substantially associated with microvesicles (Fig. S1B), and iii) did not decrease in response to MPi (Fig. S1C). Thus, we find that MEKi treatment induces significant changes in supernatant RTK levels, which contains a combination of free proteolytically shed soluble receptor (as with AXL and MET), and surface receptor on microvesicles (as with EGFR), with the significant effects of MEKi dominated by the former (Fig. 1A-B).

We next examined if reduced accumulation of extracellular RTK ectodomain was detectable in mice undergoing MAPKi therapy. We used two different xenograft tumor models: subcutaneous *BRAF*-mutant melanoma using LOX-IMVI cells, and orthotopic TNBC using the *BRAF/KRAS* mutant LM2 cells. With human-specific solution-phase immunoassays, we measured plasma levels of tumor-derived receptors in tumor-bearing mice following drug treatment. Indeed, MAPKi using combined MEKi (trametinib) and BRAFi (vemurafenib) treatment in the melanoma model decreased circulating levels of tumor-derived AXL and MET (Fig. 1C). Similarly, MEKi significantly reduced levels of the circulating AXL and MET in mice with mammary fat pad tumors (Fig. 1D).

To test whether this RTK ectodomain accumulation may be relevant to clinical pathology, we measured circulating levels of AXL, MET, HER2, and HER4 ectodomains in stage I and stage IV breast cancer patients along with healthy controls, and observed that AXL contributes to an overall pattern of increased RTKs in patients (Fig. S1D-F). The combined level of these four RTKs in a given serum sample increased significantly in breast cancer patients who have not been exposed to the inhibitors shown here, compared to healthy controls (Fig. S1D). In other words, roughly 50% of stage I (10/20) and stage IV (9/19) patient samples exhibited a

“quadruple-positive” phenotype with increased levels of all four RTKs in circulation, compared to 5% (1/20) of healthy controls (Fig. S1E). Among “quadruple-positive” samples, circulating RTK levels in stage IV patients were 40% higher than levels from stage I patients (Fig. S1E;  $p=0.03$ , two-tailed t-test). The statistical significance of an elevated serum RTK signature was dependent upon inclusion of AXL measurements (Fig. S1F), indicating it as the most vital among the four. These data confirm that stage I and especially advanced metastatic stage IV diseases are associated with changes in RTK shedding that are detectable circulating in human patients.

***Circulating RTK levels but not their mere tumor expression predict MAPKi resistance in melanoma patients***

We next investigated whether reduced RTK ectodomain levels were observable in patients undergoing MAPKi therapy and if markers of RTK accumulation correlated with clinical outcomes. Plasma, rather than serum which was used in the breast cancer cohort, was collected from melanoma patients undergoing treatment with a combination of trametinib (MEKi) and dabrafenib (BRAFi), both before and while on treatment. As a surrogate marker of RTK shedding, we measured soluble levels of six RTKs known to be sheddase substrates: MET, HER2, HER4, and the three TAM receptors (AXL, MERTK, and TYRO3) using solution-phase antibody arrays (Fig. 1E, Fig. S1G). With this blood-based test, we found that patients showing high levels of circulating RTKs before MAPKi treatment exhibited rapid disease progression (Fig. 1F). Motivated by the hypothesis that reduced RTK shedding may lead to MAPKi resistance, we next examined (a) if circulating RTK levels changed with MAPKi treatment, and (b) if changes correlated with disease progression. We found that 5/11 patients, principally those

with high initial circulating RTK levels, showed decreased circulating RTK levels upon initiation of MAPKi treatment (Fig. 1G), and that disease rapidly progressed in these patients (Fig. 1H). In fact, these circulating RTK changes were highly predictive of progression-free survival (PFS;  $p=0.005$ ;  $n=11$ ; two-tailed log-rank test) (Fig. 1H). In contrast, initial tumor response as measured by Response Evaluation Criteria for Solid Tumors (RECIST) failed to reliably predict PFS in a statistically significant manner ( $p=0.08$ ;  $n=11$ ; two-tailed log-rank test), as observed in other cancers (23), thus demonstrating the comparative superiority of circulating RTKs as predictive markers of disease progression.

We next examined whether mere RTK expression in the tumor, rather than levels of circulating RTKs, could similarly predict PFS in patients. In the same cohort used to assess circulating RTKs, total tumor AXL measured by immunohistochemistry of its intracellular C-terminus failed to correlate with PFS (Fig. S1H). Furthermore, in an independent dataset of 21 melanoma patients undergoing BRAFi therapy, RNA expression of the six RTKs measured here did not substantially predict PFS (Fig. S1I). Up-regulation of RTK RNA expression, measured by comparing matched gene expression before and after BRAFi therapy began, only mildly trended towards worse PFS but the difference was not significant (Fig. S1J;  $p=0.055$ , two-tailed log-rank test). These results, combined with the aforementioned TNBC and melanoma xenograft studies, show that circulating RTK levels (a) can be non-invasively, quantitatively, and longitudinally monitored in patients undergoing MAPKi treatment, (b) provide an early indication of MAPKi efficacy, (c) are more predictive of MAPKi efficacy than mere expression in the tumor, and (d) may consequently have utility as a patient selection criterion.

***MEKi increases total and phosphorylated AXL on the cell surface***

We next investigated the relationship between AXL levels in circulation and within the tumors of melanoma patients. We used samples from patients with similar initial tumor responses by RECIST (Fig. S2A), yet very different plasma RTK patterns and times of disease progression (Fig 2A). To simultaneously measure total tumor AXL and its ectodomain release from the tumor, we compared immunostaining by antibodies targeting either the AXL intracellular C-terminus (corresponding to total tumor AXL) or the N-terminus ectodomain (the latter was also used to detect circulating AXL in plasma). In one patient exhibiting relatively long PFS (patient #9), low plasma AXL levels (Fig. 2A, top row) corresponded to low tumor AXL levels pre-treatment (Fig. 2B, top row). A sustained increase in AXL and other RTKs was detected in plasma (Fig. 2A, top row) with MAPKi treatment initiation, and indeed C-terminus AXL expression was detected at higher levels in a subset of the tumor cells analyzed on treatment (Fig. 2B; S2B). In contrast, another patient showing rapid disease progression (patient #4) exhibited high pre-treatment AXL levels both in plasma and in the pre-treatment tumor (Fig. 2A-B, bottom row), but tumor AXL appeared to be shed at high levels: although AXL C-terminus was high in this tumor, ectodomain staining was low by comparison. Even though plasma AXL levels declined with MAPKi therapy in this patient (Fig. 2B, bottom row), AXL C-terminus staining remained high in the on-treatment tumor biopsy and tumor AXL ectodomain increased substantially (Fig. 2C). This evidence suggests that MAPKi-induced decrease in plasma RTK does not reflect decreased AXL expression in the tumor, but rather decreased release of the AXL ectodomain from the tumor.

Circulating tumor-derived extracellular vesicles (EVs) including exosomes can also be detected in patients, and surface proteins on such vesicles often correlate with membrane protein levels on the tumor (Fig. 2D) (24). We examined if changes in EV RTK levels could also explain

the post-treatment decrease in circulating RTKs seen for patient #4. Using the recently developed nPLEX (nanoplasmonic exosome) assay to sensitively detect surface RTK ectodomains on EVs (24), we found that these EVs did not explain the overall circulating RTK decrease (Fig. 2E; Fig. S2C). In fact, EV AXL and MET ectodomain levels increased with MAPKi in patient #4, which is consistent with the observed tumor histology (Fig. 2C) and likely reflects intact RTK ectodomain on the tumor cell surfaces. In sum, these data demonstrate the divergence between the levels of circulating, soluble RTKs and RTK levels on cancer cell membranes following MAPKi in patients: decreased circulating RTK levels do not simply reflect decreased expression in the tumor.

We next sought to understand how MEKi affects AXL surface levels and signaling activity in cultured melanoma (LOX-IMVI) and TNBC (MDA-MB231) cells. Consistent with the clinical melanoma findings, we observed that although MEKi reduced total supernatant RTK for both cell lines (Fig. 1A), these changes did not correlate with exosomal RTK levels within that same supernatant (Fig. 2F-G). MEKi did not impact exosome production or size in MDA-MB231 (Fig. S2D), and previously discussed control experiments revealed that the majority of supernatant MET and AXL from MDA-MB231 and LOX-IMVI cell culture was not exosome-anchored (Fig. S1B). We next examined how MEKi influenced protein levels on the cell surface and lysate. Changes in both surface and phosphorylated AXL were detectable by 3h post-treatment and further increased by 24h (Fig. S2E). However, MEKi did not similarly increase RNA levels of AXL (Fig. S2F-G), suggesting that surface AXL changes are not simply due to transcriptional regulation.

For a dose-response analysis of MEKi-induced AXL effects, we treated LOX-IMVI (Fig. 2H-I) and MDA-MB231 (Fig. 2J-K) cells with increasing concentrations of the MEK inhibitors

PD325901 and U0126; measured p-ERK1/2 as a readout of proximal MEKi efficacy; monitored cell survival; measured supernatant RTK ectodomain levels; and assessed levels of full-length intact AXL in cell lysates using antibodies targeted to either the ectodomain (N-terminus) or the intracellular domain (C-terminus) (also Fig. S2H-I). Reduction of supernatant RTK correlated with p-Erk1/2 decrease and anti-correlated with lysate levels of full-length AXL, which increased. Particularly with U0126 treatment, coordinated changes in p-Erk1/2, supernatant RTK, and lysate AXL all were observable at lower MEKi concentrations that did not substantially impact cell growth, therefore suggesting the RTK changes are not directly caused by cell death and/or apoptosis processes.

To parallel the clinical and *in vitro* observations, we next tested whether MEKi similarly increased tumor AXL in a TNBC xenograft model. In association with our data that circulating RTK levels decreased substantially with MEKi (Fig. 1D), we observed that MEKi concomitantly increased AXL in the primary tumor, particularly at tumor edges (Fig. 2L-M). Overall, MEKi-induced reduction in extracellular soluble RTKs corresponds with a contrasting accumulation on the membranes of cells and exosomes, with corresponding increases in AXL phosphorylation.

***AXL mediates MEKi resistance, and co-treatment with AXLi synergistically reduces tumor growth, metastasis, and extends survival in mice.***

We next asked how increased RTK surface accumulation following MEKi relates to overall drug response. Across 11 cancer cell lines, we observed a significant correlation between MEKi resistance and surface changes in MET and AXL: cells showing RTK accumulation following MEKi were insensitive to MEKi as measured by proliferation across a dose-response (Fig. 3A-B). From these data, we hypothesized that MEKi-induced AXL upregulation would



also correlate with synergistic response to combined MEKi/AXLi treatment. To test this, we quantified MEKi/AXLi synergistic response using a model of bliss independence across 10 cell lines and correlated the results to changes in surface AXL (Fig. S3A-C). Consistent with our model, cell lines displaying synergistic responses to combined AXLi/MEKi treatment also showed corresponding upregulation of surface AXL following MEKi, in comparison to cell lines displaying non-synergistic responses (Fig. 3C, Fig. S3C). Notably, cell lines displaying synergistic response were also enriched for RAS mutation, which is possibly related to a decreased reliance on signaling through proteolytically shed EGF-ligands for MAPK activity, and which is clinically relevant due to the frequent assessment of RAS mutation in patient tumors (Fig. 3C; Fig. S3D). Indeed, RAS-mutant MDA-MB231 cells, among others, were resistant to treatment with an anti-EGFR antibody that blocks ligand binding (mAb225, non-humanized cetuximab; Fig. S3E), and *Kras* mutation is a contra-indication for cetuximab therapy in the colorectal cancer setting due to lack of efficacy in those patients (25).

We next tested the synergistic efficacy of dual MEKi/AXLi treatment in two mouse xenograft models, using cancer cell lines that showed increased surface AXL following MEKi. First, we employed orthotopic TNBC xenografts using the highly lung-metastatic derivative of MDA-MB231, LM2. Combined MEKi/AXLi treatment reduced both tumor growth (Fig. 3D) and metastasis (Fig. 3E) more than either treatment alone, with significant super-additive synergistic effects in tumor growth reduction ( $p=0.015$ ; two-way ANOVA interaction term;  $n \geq 7$ ). In melanoma LOX-IMVI xenografts, we hypothesized that MEKi+BRAF<sup>i</sup> (trametinib+vemurafenib) combined with the AXL inhibitor R428 (AXLi) might extend progression free survival (PFS) by compensating for drug resistance arising via AXL-mediated bypass signaling. Using an *in vitro* proliferation/cytotoxicity assay, AXLi combined with either

MEKi or BRAFi showed synergistic effects in LOX-IMVI (Fig. S3F). In the LOX-IMVI xenograft, addition of AXLi to the BRAFi/MEKi treatment regimen led to an enhanced initial tumor response (Fig. 3F), delayed tumor recurrence after the initial treatment course ended (Fig. 3G), and extended median overall survival by roughly 50% more than MAPKi treatment alone (Fig. 3H). In contrast, AXLi treatment by itself had no significant impact on overall survival, thus demonstrating that the interaction between MAPKi and AXLi is synergistic (Fig. 3H). Overall, these results provide evidence that AXL mediates bypass signaling in response to BRAFi/MEKi treatment, contributes to drug resistance, and is therapeutically targetable using combination treatment regimens.

***MEKi-induced AXL and MET upregulation is consistent with decreased proteolytic receptor shedding***

We next investigated the mechanism by which AXL and MET accumulate on the cell surface following MEKi, while simultaneously decreasing levels in the supernatant and in circulation. We first took a proteomic approach to look for global patterns in how the tumor-derived extracellular proteome changes in response to targeted kinase inhibitor treatment, using antibody microarrays to screen 1000 proteins for differential supernatant accumulation following MEKi in the TNBC MDA-MB231 cell line. Gene set enrichment analysis (26) of the ~200 proteins exhibiting significantly altered levels in the supernatant indicated that MEKi reduced transmembrane receptor ectodomain abundance (Fig. 4A) while increasing secreted (not proteolytically shed) cytokine levels (Fig. S4A). Among proteins that were depleted with MEKi from the supernatant, the top-ranked “transmembrane receptor activity” gene-set (Fig. 4A) comprised various known sheddase substrates including amyloid precursor protein (APP) (27)

and low-density lipoprotein receptor (LDLR) (28). These results combined with the significantly decreased supernatant accumulation of RTKs including known sheddase substrates MET and HER4 (Fig. 1A-B) collectively implicate reduced proteolytic activity as a potentially key effect of MEKi.

We next compared the supernatant effects of MEKi with broad-spectrum metalloproteinase inhibition (MPi) using batimastat (BB94), and found similar patterns of widely decreased sheddase substrates amphiregulin (AREG), heparin-binding epidermal growth factor (HBEGF), tumor necrosis factor receptor 1 (TNFR1), and AXL following inhibitor treatment (Fig. 4B). AREG, HBEGF, and TNFR1 have been largely associated with ADAM17 cleavage (13, 17) but all may also be shed by ADAM10 depending on the context (15, 29-32). Reduced sheddase substrate accumulation was not an exclusive effect of direct MEKi: among 19 clinical and pre-clinical inhibitors targeting diverse signaling pathways and RTKs, roughly 80% (15/19) inhibited substrate accumulation to some degree. Nonetheless, MEKi exhibited some of the strongest effects (Fig. 4B). p38, PI3K, and c-JUN N-terminal kinase (JNK) inhibitors also significantly reduced sheddase-substrate accumulation, consistent with previous reports describing their effects on ADAM activity (15, 33). In contrast to supernatant decreases, surface levels of sheddase-substrates AXL and TNFR1 correspondingly increased in response to several other inhibitors, but most significantly with MPi and MEKi (Fig. S4B). Kinetics of surface and phosphorylated AXL following MPi (Fig. S4C) closely resembled MEKi changes (Fig. S2D), with observable increases by 3h post-treatment and continued accumulation by 24h. To further compare the effects of MEKi and MPi, we profiled gene expression changes using RNA microarrays following either of the two treatments. Results show substantial overlap in the transcriptional responses arising from MEKi and MPi, suggesting a shared mechanism of action

(Fig. 4C; Fig. S4D). However, gene set enrichment analysis indicated MEKi, but not MPi, induced growth arrest (Fig. S4E); in fact, MPi did not elicit any significant gene-set enrichment. Overall, these results show that reduced metalloproteinase activity is a surprisingly prominent effect of MEKi. Furthermore, these data implicate MAPK signaling as one of the key pathways broadly regulating supernatant sheddase-substrate accumulation, with effects similar to those seen when proteolytic shedding is directly inhibited.

We next compared the effects of MPi and MEKi on RTK changes in levels in cell lysate, cell surface, and in exosomes. Focusing on RTKs and key sheddase substrates identified in the Ab-microarray, we first analyzed changes in surface levels of proteins (Fig. 4D). In two TNBC cell lines (MDA-MB231 and MDA-MB157), we measured a panel of 18 sheddase-substrates on the cell surface in response MPi and MEKi, and found significant correlation between changes with MEKi compared to MPi (Pearson's correlation = 0.56;  $p=0.0003$ , two-tailed t-test). Results show AXL as one of the most significantly upregulated membrane proteins (Fig. 4D). Across a panel of 12 cell lines, we observed a modest yet statistically significant correlation between changes in surface AXL and MET in response to either MEKi or MPi, such that cells are more likely to exhibit increased surface AXL or MET following MEKi if they also showed increased levels following MPi (Fig. S4F). Gene expression helps explains why some sheddase-substrates actually decrease on the cell surface following MPi; for example, HBEGF and AREG expression decrease following BB94 treatment, and their levels correspondingly decrease on the cell surface (Fig. S4G). In contrast, AXL expression does not significantly change with either MPi or MEKi, and in LOX-IMVI (Fig. 4E) and MDA-MB231 cells (Fig. 4F) treatment with both MPi and MEKi significantly increase levels of full-length intact lysate AXL (see Fig. S4H-I for confirming pErk reduction). Similarly, we found increased intact AXL levels in CD63+

exosomes isolated from supernatant of the same cells (Fig. 4G). To confirm the hypothesis that this is due to changes in AXL proteolysis, we measured levels of ectodomain AXL receptor fragment in the supernatant of treated cells. Indeed, MPi and MEKi both decreased the accumulation of an AXL ectodomain fragment in the supernatant (Fig. 4H), and full-length intact AXL protein was not detectable to any similar degree compared to the ectodomain fragment in the supernatant (Fig. 4H). No substantial increases in cell death, apoptosis, or autophagy were observed with BB94 or PD325901 at the concentrations tested, suggesting these processes are not involved in the AXL phenotype described above (Fig. S4J). Taken together, these data provide further evidence that MEKi effects on RTK processing are highly consistent with reduced proteolysis by metalloproteinases.

To more broadly assess the impact of direct MPi on RTK signaling, we next examined MPi-induced changes in total, phosphorylated, and supernatant RTK levels across a panel of 19 diverse cell lines. MPi widely decreased AXL, MET, HER2, and HER4 in the supernatant, and increased total and phospho-RTK levels in many cases, most significantly and consistently for AXL and MET (Fig. 4I; Fig. S4K-L). Overall, these data show that proteolytic RTK shedding substantially impacts RTK levels and signaling in many cells, especially for AXL.

***MPi and MEKi cause AXL-dependent bypass JNK/cJUN signaling.***

We next tested how AXL accumulation after MEKi or MPi leads to corresponding changes in downstream signaling events. At the RTK level, MEKi and MPi increase co-immunoprecipitation of AXL with MET and HER2, which has been associated with RTK co-localization, signaling cross-talk, and AXL transactivation (Fig. S5A) (34). Downstream of receptor signaling, we found that although MEKi reduced pErk, it increased phosphorylation in

other signaling pathways (Fig. S1A). Previous reports have implicated signaling of JNK and its substrate cJUN in MAPKi resistance (35), and here we found p-cJUN consistently increased with MEKi treatment more than 5 other canonical signaling pathways averaged across 8 cell lines; p-Akt was also consistently elevated (Fig. S1A). In response to MPi, JNK and cJUN phosphorylation were among the strongest correlates with fluctuating surface AXL and p-AXL levels compared to 21 other signaling measurements across 13 cell lines (Fig. S5B-C), suggesting that accumulation of cell surface AXL following MPi leads to increased AXL phosphorylation and downstream signaling through the JNK/cJUN pathway. To test whether the observed JNK/cJUN signaling in fact depends on AXL activity, we monitored p-JNK following MPi or MEKi in the presence or absence of various AXL perturbations. After 2h MPi treatment, compensatory increase in phosphorylation occurs more in p-JNK than 4 other key phosphoproteins, and this increase can be blocked by co-treatment with AXLi using R428 (Fig. S5D). After 3h treatment with either MPi or MEKi, we found that compensatory increase in p-JNK can be eliminated by siRNA targeting either AXL, or to a lesser extent, MET (Fig. 5A; siRNA validation Fig. S5E). By 24h post-treatment, compensatory increases in p-cJUN and p-Akt are likewise blocked by co-treatment with AXLi using R428 (Fig. 5B-C). Compensatory JNK signaling in response to MAPKi leads to a synergistic response to dual JNK and MAPK inhibition (35), and our data suggest that sheddase activity is a key feedback component driving this synergistic interaction. To test this model, we measured the degree of drug synergy as a response to combination MAPKi and JNKi treatment, in the presence or absence of MPi, and found that the degree of synergy between JNKi and MAPKi is strongly reduced in the absence of metalloproteinase activity (Fig. S5F-G).

***MPi drives AXL-dependent cell proliferation and blocks response synergy to dual MEKi and AXLi.***

We next evaluated the direct effect of MPi on cell proliferation. MPi using BB94 caused a dose-dependent increase in cell growth in the absence of AXLi; however, in the presence of AXLi using R428, MPi actually caused a dose-dependent decrease in cell growth (Fig. 5D). Furthermore, MPi increased the mitotic index of two TNBC cell lines, and this increase was also blocked by R428 (Fig. 5E). Next, we directly tested the role of proteolytic activity in mediating MEKi/AXLi synergy. We treated cells with combinations of MEKi and AXLi in the presence or absence of MPi (using BB94), and then fit the resulting cell growth measurements to a computational model of Loewe synergy, as done above with MAPKi and JNKi. This model fits the response data to a parameter  $\alpha$  that quantifies the degree to which drugs act in a synergistic, super-additive manner where the effect of both drugs combined is greater than what would be expected if the effects were independent and additive (simulated in Fig. 5F). This analysis revealed that synergistic interactions between MEKi and AXLi were substantially reduced in the absence of metalloproteinase activity (Fig. 5G-H), suggesting that proteolytic activity significantly contributes to AXL-dependent MEKi resistance.

***ADAM10 and ADAM17 proteolytically shed AXL to downregulate mitogenic signaling activity.***

We next investigated which sheddases cleave AXL directly, focusing on ADAM17 as a principal sheddase and ADAM10 because AXL and MET shedding are closely correlated throughout our data, and MET is a previously-known ADAM10 substrate (15, 21, 36). ADAM17 and ADAM10 knockdown using pooled small interfering RNA (siRNA; validation, Fig. S6A)



decreased supernatant AXL accumulation (Fig. 6A) and enhanced its levels on the cell surface in both MDA-MB231 (Fig. 6B) and MDA-MB157 cell lines (Fig. S6B). Combined ADAM10 and ADAM17 knockdown yielded even greater effects, underscoring a role for both (Fig. 6A-B). Stable short hairpin RNA (shRNA) knockdown of either ADAM10 or ADAM17 also caused AXL accumulation on the surface of LOX-IMVI melanoma cells (Fig. S6C-D) and decreased supernatant AXL accumulation (Fig. S6E). ADAM10 inhibition with the ADAM10-selective inhibitor GI-254023X caused a dose-dependent decrease in supernatant AXL ectodomain (Fig. 6C). Similarly, treatment with the specific ADAM10 inhibitor proA10 (37) reduced supernatant AXL (Fig. 6D).

We examined the ability of recombinant ADAM10 to cleave purified AXL protein, and show by western blot that ADAM10 cleaves recombinant AXL (Fig. 6E-F) in a dose-dependent manner into ectodomain fragments of roughly the same size (~85kDa) as found in cell supernatant (Fig. 4H). As a control, we confirmed these cleavage products were reduced in the presence of MPi (Fig. 6G). We also confirmed the ability of ADAM17 to cleave both recombinant AXL (Fig. 6G) and full-length AXL that had been immunopurified from cell lysate (Fig. S6F-G).

Specific ADAM10 inhibition also affected cell proliferation in an AXL-dependent manner. Treatment with either GI-254023X or ADAM10 siRNA knockdown had minimal impact on cell growth in the absence of AXLi (Fig. 6H), and stable ADAM10 knockdown using shRNA had minimal impact on the growth of LOX-IMVI xenograft tumors (Fig. S6H). However, when AXL signaling was inhibited by R428, ADAM10 inhibition was effective in reducing cell growth (Fig. 6H). Similar trends were observed with ADAM17 siRNA knockdown (Fig. 6H). These combined results are consistent with BB94 effects on proliferation (Fig. 5D-E)

and demonstrate AXL upregulation as significantly counteracting the anti-proliferative capacity of metalloproteinase inhibitors.

***MEKi dynamically enhances cell surface TIMP1 association with ADAM10, thus reducing ADAM10 activity and causing drug resistance.***

We next investigated the mechanism through which MAPKi decreases AXL shedding. MEKi significantly reduced ADAM10 and ADAM17 catalytic activities in a live-cell assay (38) (Fig. 7A), without affecting their cell surface levels (Fig. S7A), suggesting direct regulation of the protease activities themselves. As further evidence of direct protease regulation, ADAM17 phosphorylation at a site previously associated with activity (33) decreased with MEKi (Fig. S7B-C). The regulated binding of ADAMs with Tissue Inhibitor of Metalloproteinases (TIMPs) including TIMP1 and TIMP3 has been implicated as a mechanism for governing protease activity, and we next tested the role of TIMPs on AXL shedding. SiRNA knockdown of TIMP1 but not TIMP3 mitigated MEKi-induced AXL accumulation on the surface (Fig. 7B; knockdown validation, Fig. S7D). In a melanoma xenograft model, we tested the *in vivo* effect of TIMP1 on AXL shedding by using a TIMP1 neutralizing antibody (T1-NAB) that binds TIMP1 and competitively prevents it from associating with proteases. Co-treatment with T1-NAB blocked tumor AXL accumulation after MAPKi treatment (Fig. 7C). Given that knockdown of TIMP3, which preferentially inhibits ADAM17, had no effect on AXL shedding, and because TIMP1 preferentially inhibits ADAM10, our data suggest a more prominent role for TIMP1 and ADAM10 regulating MEKi-driven AXL shedding.

We found that MEKi continually enhanced the binding of TIMP1 to the cell surface from 30 min (Fig. 7D) to 24h (Fig. S7E). In contrast, TIMP1 supernatant levels actually declined after

MEKi (Fig. S7F), indicating enhanced TIMP1 surface levels do not simply reflect enhanced TIMP1 secretion. We thus hypothesized that MEKi induced a rapid change on the cell surface that enhanced TIMP1 binding. To test this, we first treated cells for 5 min with MEKi, rinsed, and incubated cells on ice with a fixed amount of fluorescently-tagged recombinant TIMP1 (rTIMP1-fluor). MEKi enhanced rTIMP1-fluor binding to the cell surface by nearly 50% (Fig. 7E), supporting the idea that MEKi treatment leads to increased accumulation of TIMP1 on the cell surface.

We next evaluated the role of ADAM10 in regulating MEKi-driven TIMP1 cell surface accumulation. Using siRNA, we found that TIMP1 accumulation on the cell surface was dependent upon ADAM10 expression (Fig. S7G; knockdown validation S6A). To directly observe interaction between TIMP1 and ADAM10, we over-expressed transgenic HA-tagged ADAM10 by 2-fold (Fig. S7H), treated cells for 5 min with MEKi, rinsed, and again incubated cells on ice with a fixed amount of rTIMP1-fluor. Proteins associating with ADAM10 were co-immunopurified (co-IP) using EGS crosslinking and anti-HA agarose resin. To sensitively detect rTIMP1-fluor co-IP, bulk immunoprecipitate was analyzed by fluorometry and found to exhibit detectable rTIMP1 fluorescence only after MEKi (Fig. 7F), further suggesting that MEKi induces ADAM10-driven cell surface TIMP1 accumulation.

We then investigated how MEKi dynamically influences interactions between ADAM10 and TIMP1. ADAM10 and ADAM17 dimerization has been associated with direct activity regulation (39, 40), and we hypothesized that MEKi elicited increased ADAM10 dimerization and association with TIMP1. Previously, immunoblots of EGS-crosslinked lysate have shown ADAM10 forms a dimerization band at roughly 120kDa (39), and here we found that this band increases with MEKi and co-immunostains for TIMP1 (Fig. 7G-H), indicating TIMP1-ADAM10

interaction. Thus, MEKi broadly reduces proteolytic shedding by enhanced TIMP1 association with ADAM10, negatively regulating its activity.

We next examined the role of TIMP1 in influencing the therapeutic response to MAPKi. We co-treated cells with T1-NAB and either MEKi or BRAFi. While T1-NAB had no detectable effect on cell growth in the absence of MAPKi, it enhanced MAPKi sensitivity by up to 50% (Fig. 7I; Fig. S7I). For more clinical relevance, we next examined the effect of T1-NAB co-treatment in a melanoma xenograft model undergoing a combined MEKi/BRAFi inhibitor regimen similar to those used in the clinic. T1-NAB treatment alone did not significantly reduce tumor growth (Fig. 7J;  $p=0.56$ , two-way ANOVA independent effect term, total  $n=46$ ). In contrast, T1-NAB significantly enhanced the ability of MEKi/BRAFi to reduce tumor size by an additional 70% (Fig. 7J; note log-scale). Furthermore, T1-NAB extended the time to tumor recurrence after MEKi/BRAFi treatment had ended (Fig. 7K). Recurrent outgrown tumors from this study did not exhibit altered AXL levels (Fig. S7J), which is in contrast to tumors analyzed while on drug treatment (Fig. 7C), and suggests that effects on AXL shedding largely reverted during the roughly 3 weeks after treatment ended. Nevertheless, these results provide evidence that reduced proteolytic AXL shedding via TIMP1 association leads to blunted MAPKi efficacy.

## DISCUSSION

We have elucidated a new targetable mechanism of bypass cancer cell signaling with implications for the design and monitoring of cancer therapies (Fig. 7L). Inhibition of multiple signaling pathways, particularly ERK signaling through MEK1/2, reduces proteolytic RTK shedding and leads to enhanced mitogenic signaling through bypass kinase pathways including JNK. Numerous examples of increased RTK signaling activity have been observed following

targeted kinase inhibitor treatment, often with little mechanistic explanation outside of transcriptional upregulation (1, 4, 5, 41). MEK and PI3K kinase inhibition have been shown to enhance the signaling of sheddase substrates including HER2 (3, 5) and AXL (1, 42), and we show here that inhibition of MEK, BRAF, and to some extent PI3K, p38, and JNK (as in Fig. 4B) reduce RTK shedding. The direct inhibition of RTKs also gives rise to bypass signaling. For example, enhanced AXL signaling mediates resistance to the EGFR/HER2 inhibitor lapatinib, even in the absence of AXL transcriptional upregulation (4). Although transcriptional and chromosomal reprogramming affect bypass signaling (2), these processes often fail to fully explain signaling network dynamics following drug treatment; this is especially true for AXL, which often exhibits little transcriptional upregulation despite sharply enhanced activity (1, 4). Here, we offer reduced proteolytic RTK shedding as a likely explanatory mechanism.

The promiscuous nature of metalloproteinases has made it difficult to anticipate the overall effects of perturbing their activities, especially in response to kinase inhibition (17, 19). Ectodomain shedding can be regulated through substrate-specific pathways (43), and in this work we find that substrate-specific regulation, for example through differential substrate accumulation on the cell-surface, can only be explained partially by transcriptional regulation (Fig. S4G). Nonetheless, substantial evidence suggests that MEKi inhibits ADAM catalytic activities themselves (Fig. 7), and we highlight an unappreciated role for TIMP1 association in this context. Consequently, MEKi essentially leads to a global reduction of ectodomain shedding across a wide range of substrates (Fig. 1; Fig. 4A). Sheddase substrates, such as EGF-ligands, have been studied for their role in autocrine growth factor signaling and have motivated protease inhibitor development (particularly targeting ADAM10 and ADAM17) for clinical use

(44). This work suggests that past metalloproteinase inhibitor clinical trials may have failed partly due to unanticipated compensatory signaling feedback from unshed RTKs.

In general, we find that AXL and MET shedding downregulate signaling activity by limiting the accumulation of full-length, signaling-competent RTK on the cell surface. Ligand-dependent receptor activation is an important signaling feature, particularly in the context of receptor shedding (15), and is relevant for future studies. Nonetheless, AXL and the other RTKs studied here exhibit significant ligand-independent activity (34, 41), which amplifies as they accumulate on the cell surface following protease downregulation. Clinically, AXL upregulation often occurs without apparent dysregulation of its ligand Gas6, and roughly half of observed AXL bypass signaling acts independently of Gas6 in drug-resistant cell lines (41). Receptor shedding also results in the generation of inhibitory “decoy” receptors that both compete for binding of free extracellular ligand and block cell-surface dimerization between signaling-competent receptors; decoy functions have been therapeutically exploited for multiple receptors, including MET (45) and AXL (46). Here we show that kinase inhibition simultaneously increases full-length RTK on the cell surface while decreasing decoy receptor levels in the extracellular supernatant or in circulation.

Diminished RTK shedding likely complements other bypass signaling mechanisms. Many RTKs reported as transcriptionally upregulated in response to kinase inhibition are themselves sheddase substrates, including PDGFR $\beta$  (1, 8), VEGFR2 (1), and CD44 (47). In the context of MAPKi, AXL repeatedly surfaces in genome-wide screens as a top candidate for rescuing drug sensitivity upon transgenic overexpression (48). Reduced RTK shedding has the potential to amplify the effects of transcriptional upregulation by increasing the fraction of total RTK that remains intact on the cell surface. Within the tumor microenvironment, stromal-

derived growth factors, cytokines, and extracellular matrix contribute to drug resistance (20, 49-52). Here we find that receptors impacted by reduced RTK shedding are also implicated in tumor-stroma ligand interactions, with a prominent example being MET activation by stromal-derived hepatocyte growth factor (HGF) (51). Of note, extracellular HGF and Gas6 release occurs through secretion rather than metalloproteinase shedding. Consequently, reduced RTK shedding has the capacity to amplify pro-survival and pro-metastatic tumor-stroma interactions, and previous work has demonstrated RTK shedding as a modifier of ligand-dependent receptor activation (15).

The ability to assess RTK shedding in cancer patients using relevant biomarkers is essential for efficient clinical translation. A substantial proportion of molecular cancer diagnostics focuses on gene expression and/or genetic mutation analysis of tumors, is dependent on the presence of an accessible tumor, and is limited by factors such as tumor heterogeneity and post-translational regulation. We present RTK proteolysis as a mechanistic explanation for the discordance between gene expression and signaling activity, and provide evidence that receptor shedding can be non-invasively monitored in clinical samples following drug treatment. Although promising, the small cohort of patient samples examined here should be expanded to a study of both larger cohorts and a broader panel of sheddase substrates such as adhesion receptors, cytokines, and cytokine receptors. Importantly, RTK proteolysis may also reflect drug toxicity in addition to drug efficacy, and multiple physiological factors may influence altered circulating RTK levels. For instance, foretinib has been observed to cause elevated circulating MET in patients (53), which may be explained by its common liver toxicity (high AST/ALT) and the corresponding association of hepatotoxicity with elevated MET shedding (54). Changes may also be related to altered gene expression and known vascular effects of foretinib including



hypertension. Nonetheless, the value of a biomarker that can predict resistance and shed light on a next potential line of therapy cannot be underestimated. Ultimately, circulating RTKs hold the potential to stand alone and to complement other diagnostic biomarkers in guiding targeted combination therapies, monitoring drug response, and non-invasively detecting the emergence of drug resistance.

## METHODS

Unless otherwise stated, reported replicates are from unique biological samples, statistical tests used the two-sided Student's t-test for significance, and mean values are reported with error bars denoting standard error of the mean. With some explicitly stated exceptions, experiments used 10 $\mu$ M BB94, 3 $\mu$ M R428, 3 $\mu$ M PD325901, 5 $\mu$ M U0126, 10 $\mu$ M AZD6244, 15 $\mu$ M MP470, and 4 $\mu$ M pro-ADAM10. Please see Supplemental Experimental Procedures for further information regarding materials, experimental details, and computational analysis methods.

**Cell Lines:** The following cell lines were purchased directly from commercial or governmental repositories and immediately used for experiments in this manuscript: MDA-MB231 (ATCC, Jun. 2012); LOX-IMVI (NCI-DCTD repository, Mar. 2014); SUM149 and SUM102 (Asterand Biorepository, Nov. 2011); HCC827 (ATCC, Jan. 2012); BT549 (ATCC, Apr. 2010); BT20 (ATCC, Jan. 2012). Additional cell lines were procured from Massachusetts Institute of Technology (MIT), Harvard Medical School (HMS), and University of Michigan collaborating lab banks: MA2 and A375 cell lines (Richard Hynes, MIT, Jan. 2013); BT474, Hs578T, HCC38, MDAMB436, MDAMB468 (Mike Yaffe, MIT, Apr. 2011); A172 (Leona Samson, MIT, Jan. 2013); U87 (Dane Wittrup, MIT, May 2011); A549 (Linda Griffith, MIT, May 2011); SUM159 (Joan Brugge, HMS, Jan. 2011); LM2 (55) (Richard Hynes, MIT, Jan. 2013); SUM1315 (Stephen Ethier, Univ. Michigan, Dec. 2009). Cell lines were routinely tested for mycoplasma (Lonza MycoAlert) within 3 months of use and were not authenticated. All cell culture was performed according to the manufacturer's guidelines.

**Melanoma Patient Samples:** Patients with metastatic melanoma containing BRAF<sup>V600E</sup> mutation (confirmed by genotyping) were enrolled on clinical trials for treatment with a BRAF inhibitor or combined BRAF + MEK inhibitor (dabrafenib 150mg b.i.d., trametinib 2mg q.d.) at

Massachusetts General Hospital and were consented for blood and tissue acquisition per IRB-approved protocol, conducted in accordance with the Declaration of Helsinki. All patients (or legal representatives) gave written informed consent before enrollment. Blood was collected and tumor biopsies were performed pre-treatment (day 0), 10-14 days on treatment, and/or at time of progression if applicable. Multiple on treatment blood samples were collected over the course of therapy as available. Plasma was isolated immediately from blood samples using BD Vacutainer CPT tube with Sodium Citrate (BD 362761). Formalin-fixed tissue from each tissue biopsy was analyzed to confirm that viable tumor was present via hematoxylin and eosin (H&E) staining. Clinical response was assessed by RECIST (See supplemental experimental procedures).

**In vivo tumor growth and metastasis assays:** All animal experiments and husbandry were approved by the MIT Division of Comparative Medicine in accord with guidelines of the MIT-IACUC. For orthotopic mammary transplant assays, 6-week-old female NOD/SCID-gamma mice (JAX) were anesthetized by i.p. injection of 125–250 mg/kg body weight of Avertin (reconstituted in PBS), followed by i.p. injection of 100  $\mu$ L of 12  $\mu$ g/mL buprenorphine for analgesia. A small incision was made on the right flank, and 250,000 MDA-MB231-LM2 cells in 25  $\mu$ L of HBSS were injected into the right #4 fat pad using a 25- $\mu$ L Hamilton syringe. Mice received three additional i.p. injections of 100  $\mu$ L of 12  $\mu$ g/mL buprenorphine at 12h intervals following the surgery. Initial sample size was chosen based on previously published experiments with MDA-MB231-LM2 xenograft models (55), as well as previously published data with the MEK and AXL drugs of interest (56, 57). 20 days post-surgery, when tumor size was palpable, mice were ranked by tumor-size and semi-randomly divided into four groups of equal distribution in tumor size. Groups received one of four different drug treatments once daily for 21 days by oral gavage: vehicle (10% DMSO + 0.5% methylcellulose + 0.2% tween-80 in

water), Axl inhibitor R428 at 30 mg/kg, PD0325901 at 1 mg/kg or a combination of both R428 at 30 mg/kg and PD0325901 at 1 mg/kg. Animals were sacrificed at the predetermined time of 21 days following initiation of drug treatment.

For the xenograft melanoma experiment, 7 week old female athymic nude mice (Taconic) were injected with  $1 \times 10^6$  LOX-IMVI cells in 1:1 Matrigel:HBSS subcutaneously in each flank (58). 7 days post-cell injection, tumors were measured by calipers and mice were ranked by tumor size and semi-randomly divided into 6 groups of equal distribution in tumor size, with 10 mice per group. Groups received one of four different drug treatments once daily for 14 days by oral gavage: vehicle (10% DMSO + 0.5% methylcellulose + 0.2% tween-80 in water), Axl inhibitor R428 at 30 mg/kg, PD0325901 at 1 mg/kg and Vemurafinib at 10mg/kg or a combination of R428 at 30 mg/kg, PD0325901 at 1 mg/kg and Vemurafinib at 10mg/kg. To study the role TIMP1 in resistance to MAPKi, mice were treated with a TIMP1 neutralizing AB (AbD Serotec / Biorad) at 32 mg/kg IP (59) daily for 3 days prior to starting drug treatment and then every second day during drug treatment. Mice were sacrificed when overall tumor burden reached more than 3cm in diameter. Tumor size measurements, tissue processing, staining of tumors and exclusion criteria can be found in supplemental experimental procedures.

**Accession Numbers:** RNA microarray expression data can be found in the GEO repository under accession number GSE77868.

#### ACKNOWLEDGEMENTS

We acknowledge support from the MIT Koch Institute Swanson Biotechnology Center and MIT BioMicroCenter core facilities. The authors express appreciation to Mike Hemann, Kevin Janes, and Katherine Yang for very helpful comments.

## REFERENCES

1. Duncan JS, Whittle MC, Nakamura K, Abell AN, Midland AA, Zawistowski JS et al. Dynamic reprogramming of the kinome in response to targeted MEK inhibition in triple-negative breast cancer. *Cell*. 2012;149:307-21.
2. Nazarian R, Shi H, Wang Q, Kong X, Koya RC, Lee H et al. Melanomas acquire resistance to B-RAF(V600E) inhibition by RTK or N-RAS upregulation. *Nature*. 2010;468:973-7.
3. Turke AB, Song Y, Costa C, Cook R, Arteaga CL, Asara JM et al. MEK inhibition leads to PI3K/AKT activation by relieving a negative feedback on ERBB receptors. *Cancer Res*. 2012;72:3228-37.
4. Liu L, Greger J, Shi H, Liu Y, Greshock J, Annan R et al. Novel mechanism of lapatinib resistance in HER2-positive breast tumor cells: activation of AXL. *Cancer Res*. 2009;69:6871-8.
5. Serra V, Scaltriti M, Prudkin L, Eichhorn PJ, Ibrahim YH, Chandarlapaty S et al. PI3K inhibition results in enhanced HER signaling and acquired ERK dependency in HER2-overexpressing breast cancer. *Oncogene*. 2011;30:2547-57.
6. Van Allen EM, Wagle N, Sucker A, Treacy DJ, Johannessen CM, Goetz EM et al. The genetic landscape of clinical resistance to RAF inhibition in metastatic melanoma. *Cancer Discov*. 2014;4:94-109.
7. Turke AB, Zejnullahu K, Wu YL, Song Y, Dias-Santagata D, Lifshits E et al. Preexistence and clonal selection of MET amplification in EGFR mutant NSCLC. *Cancer Cell*. 2010;17:77-88.
8. Akhavan D, Pourzia AL, Nourian AA, Williams KJ, Nathanson D, Babic I et al. De-

- repression of PDGFR $\beta$  transcription promotes acquired resistance to EGFR tyrosine kinase inhibitors in glioblastoma patients. *Cancer Discov.* 2013;3:534-47.
9. Zardavas D, Baselga J, Piccart M. Emerging targeted agents in metastatic breast cancer. *Nat Rev Clin Oncol.* 2013;10:191-210.
  10. Bartholomeusz C, Gonzalez-Angulo AM, Liu P, Hayashi N, Lluch A, Ferrer-Lozano J et al. High ERK protein expression levels correlate with shorter survival in triple-negative breast cancer patients. *Oncologist.* 2012;17:766-74.
  11. Sullivan RJ, Flaherty KT. Resistance to BRAF-targeted therapy in melanoma. *Eur J Cancer.* 2013;49:1297-304.
  12. Edwards DR, Handsley MM, Pennington CJ. The ADAM metalloproteinases. *Mol Aspects Med.* 2008;29:258-89.
  13. McGowan PM, Mullooly M, Caiazza F, Sukor S, Madden SF, Maguire AA et al. ADAM-17: a novel therapeutic target for triple negative breast cancer. *Ann Oncol.* 2013;24:362-9.
  14. Lee SB, Schramme A, Doberstein K, Dummer R, Abdel-Bakky MS, Keller S et al. ADAM10 is upregulated in melanoma metastasis compared with primary melanoma. *J Invest Dermatol.* 2010;130:763-73.
  15. Miller MA, Meyer AS, Beste MT, Lasisi Z, Reddy S, Jeng KW et al. ADAM-10 and -17 regulate endometriotic cell migration via concerted ligand and receptor shedding feedback on kinase signaling. *Proc Natl Acad Sci U S A.* 2013;110:E2074-83.
  16. Witters L, Scherle P, Friedman S, Fridman J, Caulder E, Newton R et al. Synergistic inhibition with a dual epidermal growth factor receptor/HER-2/neu tyrosine kinase inhibitor and a disintegrin and metalloprotease inhibitor. *Cancer Res.* 2008;68:7083-9.
  17. Gooz M. ADAM-17: the enzyme that does it all. *Crit Rev Biochem Mol Biol.* 2010;45:146-

69.

18. Newton RC, Bradley EC, Levy RS, Doval D, Bondarle S, Sahoo TP et al. Clinical benefit of INCB7839, a potent and selective ADAM inhibitor, in combination with trastuzumab in patients with metastatic HER2+ breast cancer. *J Clin Oncol.* 2010;28:abstr 3025.
19. Kessenbrock K, Plaks V, Werb Z. Matrix metalloproteinases: regulators of the tumor microenvironment. *Cell.* 2010;141:52-67.
20. Wilson TR, Fridlyand J, Yan Y, Penuel E, Burton L, Chan E et al. Widespread potential for growth-factor-driven resistance to anticancer kinase inhibitors. *Nature.* 2012;487:505-9.
21. Schelter F, Grandl M, Seubert B, Schaten S, Hauser S, Gerg M et al. Tumor cell-derived Timp-1 is necessary for maintaining metastasis-promoting Met-signaling via inhibition of Adam-10. *Clin Exp Metastasis.* 2011;28:793-802.
22. Feldinger K, Generali D, Kramer-Marek G, Gijzen M, Ng TB, Wong JH et al. ADAM10 mediates trastuzumab resistance and is correlated with survival in HER2 positive breast cancer. *Oncotarget.* 2014;5:6633-46.
23. Takahashi R, Hirata H, Tachibana I, Shimosegawa E, Inoue A, Nagatomo I et al. Early [18F]fluorodeoxyglucose positron emission tomography at two days of gefitinib treatment predicts clinical outcome in patients with adenocarcinoma of the lung. *Clin Cancer Res.* 2012;18:220-8.
24. Im H, Shao H, Park YI, Peterson VM, Castro CM, Weissleder R et al. Label-free detection and molecular profiling of exosomes with a nano-plasmonic sensor. *Nat Biotechnol.* 2014;32:490-5.
25. Karapetis CS, Khambata-Ford S, Jonker DJ, O'Callaghan CJ, Tu D, Tebbutt NC et al. K-ras mutations and benefit from cetuximab in advanced colorectal cancer. *N Engl J Med.*



2008;359:1757-65.

26. Subramanian A, Tamayo P, Mootha VK, Mukherjee S, Ebert BL, Gillette MA et al. Gene set enrichment analysis: a knowledge-based approach for interpreting genome-wide expression profiles. *Proc Natl Acad Sci U S A*. 2005;102:15545-50.
27. Asai M, Hattori C, Szabó B, Sasagawa N, Maruyama K, Tanuma S et al. Putative function of ADAM9, ADAM10, and ADAM17 as APP alpha-secretase. *Biochem Biophys Res Commun*. 2003;301:231-5.
28. Guo L, Eisenman JR, Mahimkar RM, Peschon JJ, Paxton RJ, Black RA et al. A proteomic approach for the identification of cell-surface proteins shed by metalloproteases. *Mol Cell Proteomics*. 2002;1:30-6.
29. Yang WS, Yu H, Kim JJ, Lee MJ, Park SK. Vitamin D-induced ectodomain shedding of TNF receptor 1 as a nongenomic action: D3 vs D2 derivatives. *J Steroid Biochem Mol Biol*. 2016;155:18-25.
30. Lemjabbar H, Basbaum C. Platelet-activating factor receptor and ADAM10 mediate responses to *Staphylococcus aureus* in epithelial cells. *Nat Med*. 2002;8:41-6.
31. Yan Y, Shirakabe K, Werb Z. The metalloprotease Kuzbanian (ADAM10) mediates the transactivation of EGF receptor by G protein-coupled receptors. *J Cell Biol*. 2002;158:221-6.
32. Kasina S, Scherle PA, Hall CL, Macoska JA. ADAM-mediated amphiregulin shedding and EGFR transactivation. *Cell Prolif*. 2009;42:799-812.
33. Xu P, Derynck R. Direct activation of TACE-mediated ectodomain shedding by p38 MAP kinase regulates EGF receptor-dependent cell proliferation. *Mol Cell*. 2010;37:551-66.
34. Meyer AS, Miller MA, Gertler FB, Lauffenburger DA. The receptor AXL diversifies

- EGFR signaling and limits the response to EGFR-targeted inhibitors in triple-negative breast cancer cells. *Sci Signal*. 2013;6:ra66.
35. Fallahi-Sichani M, Moerke NJ, Niepel M, Zhang T, Gray NS, Sorger PK. Systematic analysis of BRAF(V600E) melanomas reveals a role for JNK/c-Jun pathway in adaptive resistance to drug-induced apoptosis. *Mol Syst Biol*. 2015;11:797.
  36. Schelter F, Kobuch J, Moss ML, Becherer JD, Comoglio PM, Boccaccio C et al. A disintegrin and metalloproteinase-10 (ADAM-10) mediates DN30 antibody-induced shedding of the met surface receptor. *J Biol Chem*. 2010;285:26335-40.
  37. Moss ML, Bomar M, Liu Q, Sage H, Dempsey P, Lenhart PM et al. The ADAM10 prodomain is a specific inhibitor of ADAM10 proteolytic activity and inhibits cellular shedding events. *J Biol Chem*. 2007;282:35712-21.
  38. Miller MA, Barkal L, Jeng K, Herrlich A, Moss M, Griffith LG et al. Proteolytic Activity Matrix Analysis (PrAMA) for simultaneous determination of multiple protease activities. *Integr Biol (Camb)*. 2011;3:422-38.
  39. Xu P, Liu J, Sakaki-Yumoto M, Derynck R. TACE activation by MAPK-mediated regulation of cell surface dimerization and TIMP3 association. *Sci Signal*. 2012;5:ra34.
  40. Deng W, Cho S, Su PC, Berger BW, Li R. Membrane-enabled dimerization of the intrinsically disordered cytoplasmic domain of ADAM10. *Proc Natl Acad Sci U S A*. 2014;111:15987-92.
  41. Zhang Z, Lee JC, Lin L, Olivas V, Au V, LaFramboise T et al. Activation of the AXL kinase causes resistance to EGFR-targeted therapy in lung cancer. *Nat Genet*. 2012;44:852-60.
  42. Byers LA, Diao L, Wang J, Saintigny P, Girard L, Peyton M et al. An epithelial-

- mesenchymal transition gene signature predicts resistance to EGFR and PI3K inhibitors and identifies Axl as a therapeutic target for overcoming EGFR inhibitor resistance. *Clin Cancer Res.* 2013;19:279-90.
43. Dang M, Armbruster N, Miller MA, Cermenio E, Hartmann M, Bell GW et al. Regulated ADAM17-dependent EGF family ligand release by substrate-selecting signaling pathways. *Proc Natl Acad Sci U S A.* 2013;110:9776-81.
  44. Duffy MJ, Mullooly M, O'Donovan N, Sukor S, Crown J, Pierce A et al. The ADAMs family of proteases: new biomarkers and therapeutic targets for cancer. *Clin Proteomics.* 2011;8:9.
  45. Michieli P, Mazzone M, Basilico C, Cavassa S, Sottile A, Naldini L et al. Targeting the tumor and its microenvironment by a dual-function decoy Met receptor. *Cancer Cell.* 2004;6:61-73.
  46. Kariolis MS, Miao YR, Jones DS, Kapur S, Mathews II, Giaccia AJ et al. An engineered Axl 'decoy receptor' effectively silences the Gas6-Axl signaling axis. *Nat Chem Biol.* 2014;10:977-83.
  47. To K, Fotovati A, Reipas KM, Law JH, Hu K, Wang J et al. Y-box binding protein-1 induces the expression of CD44 and CD49f leading to enhanced self-renewal, mammosphere growth, and drug resistance. *Cancer Res.* 2010;70:2840-51.
  48. Johannessen CM, Johnson LA, Piccioni F, Townes A, Frederick DT, Donahue MK et al. A melanocyte lineage program confers resistance to MAP kinase pathway inhibition. *Nature.* 2013;504:138-42.
  49. Gilbert LA, Hemann MT. DNA damage-mediated induction of a chemoresistant niche. *Cell.* 2010;143:355-66.

50. Muranen T, Selfors LM, Worster DT, Iwanicki MP, Song L, Morales FC et al. Inhibition of PI3K/mTOR leads to adaptive resistance in matrix-attached cancer cells. *Cancer Cell*. 2012;21:227-39.
51. Straussman R, Morikawa T, Shee K, Barzily-Rokni M, Qian ZR, Du J et al. Tumour micro-environment elicits innate resistance to RAF inhibitors through HGF secretion. *Nature*. 2012;487:500-4.
52. Obenauf AC, Zou Y, Ji AL, Vanharanta S, Shu W, Shi H et al. Therapy-induced tumour secretomes promote resistance and tumour progression. *Nature*. 2015;520:368-72.
53. Shah MA, Wainberg ZA, Catenacci DV, Hochster HS, Ford J, Kunz P et al. Phase II study evaluating 2 dosing schedules of oral foretinib (GSK1363089), cMET/VEGFR2 inhibitor, in patients with metastatic gastric cancer. *PLoS One*. 2013;8:e54014.
54. Chalupský K, Kanchev I, Žbodáková O, Buryová H, Jiroušková M, Kořínek V et al. ADAM10/17-dependent release of soluble c-Met correlates with hepatocellular damage. *Folia Biol (Praha)*. 2013;59:76-86.
55. Minn AJ, Gupta GP, Siegel PM, Bos PD, Shu W, Giri DD et al. Genes that mediate breast cancer metastasis to lung. *Nature*. 2005;436:518-24.
56. Hoeflich KP, O'Brien C, Boyd Z, Cavet G, Guerrero S, Jung K et al. In vivo antitumor activity of MEK and phosphatidylinositol 3-kinase inhibitors in basal-like breast cancer models. *Clin Cancer Res*. 2009;15:4649-64.
57. Holland SJ, Pan A, Franci C, Hu Y, Chang B, Li W et al. R428, a selective small molecule inhibitor of Axl kinase, blocks tumor spread and prolongs survival in models of metastatic breast cancer. *Cancer Res*. 2010;70:1544-54.
58. Yang Y, Wang Y, Zeng X, Ma XJ, Zhao Y, Qiao J et al. Self-control of HGF regulation on

human trophoblast cell invasion via enhancing c-Met receptor shedding by ADAM10 and ADAM17. *J Clin Endocrinol Metab.* 2012;97:E1390-401.

59. Stilley JA, Birt JA, Nagel SC, Sutovsky M, Sutovsky P, Sharpe-Timms KL. Neutralizing TIMP1 restores fecundity in a rat model of endometriosis and treating control rats with TIMP1 causes anomalies in ovarian function and embryo development. *Biol Reprod.* 2010;83:185-94.

#### AUTHOR CONTRIBUTIONS

M.A.M. helped design, perform, and analyze all experiments besides live animal work and clinical sample collection. M.J.O. measured melanoma patient samples; designed, performed, and analyzed the mouse xenograft experiments; performed *in vitro* cell cytotoxicity assays; and performed western blots. R.J.S., D.T.F, and K.T.F. designed and collected the melanoma patient samples, and performed immunohistochemistry. A.S.M. and S.J.W. performed phospho-signaling experiments, western blots, and soluble RTK measurements. J.T. helped with the mouse xenograft experiments. H.I., H.L., and R.W. helped design and perform exosome experiments. L.G.G. and F.B.G. were involved in the study design, data interpretation, and manuscript writing. M.A.M., M.J.O., and D.A.L. designed the study, analyzed the data, and wrote the paper. All authors discussed the results and commented on the manuscript.

## FIGURE LEGENDS

**Figure 1: MEKi broadly reduces extracellular release of protein ectodomains and correlates with drug resistance in melanoma patients.** **A)** MEKi with U0126 and PD325901 reduces supernatant accumulation of soluble RTKs (measured by ELISA) in multiple cancer cell lines ( $n \geq 2$ ). **B)** Change in supernatant RTKs after treatment with MEKi, averaged across all cell lines shown in A (pooled two-tailed t-test;  $n=22$ ). **C-D)** Circulating plasma levels of soluble AXL and MET decrease after (C) MAPKi treatment (10 mg/kg vemurafenib + 1 mg/kg trametinib) in LOX-IMVI melanoma xenografts ( $p=0.004$ ,  $n=4$ , pooled two-tailed t-test), or (D) MEKi treatment (1 mg/kg PD325901) in orthotopic LM2 breast cancer xenografts ( $p=0.0036$ ,  $n \geq 4$ , pooled two-tailed t-test). **E)** Plasma from melanoma patients was assayed for soluble RTK levels before and on treatment with dual BRAFi/MEKi therapy; heatmap shows the average of 6 RTK levels (Fig. S1G for full dataset). **F)** Kaplan-Meier analysis based on average pre-treatment RTK levels (see E;  $p=0.005$ ; two-tailed log-rank test; total  $n=11$ ). **G)** Circulating RTK levels decrease in melanoma patients with short progression free survival (PFS) after MAPKi treatment (median  $\pm$  IQR of RTK levels, averaged as in E). **H)** Kaplan-Meier analysis based on the change in RTK levels with MAPKi therapy initiation ( $p=0.005$ ; two-tailed log-rank test; total  $n=11$ ).

**Figure 2: Decreased circulating AXL correlates with increased AXL surface levels in the tumor after MEKi.** **A)** Longitudinal plasma RTK levels monitored in melanoma patients showing similar initial response to MAPKi (Fig. S2A) but dramatically different PFS. **B)** Immunofluorescence of AXL cytoplasmic domain (C-term) and ectodomain (N-term) from tumor biopsies from patients in A. **C)** Schematic of AXL measurements and quantification of

data from *B*. **D**) Multivesicular bodies (MVB) generate exosomes containing membrane proteins resembling those on the cell surface. **E**) Levels of MET, AXL, and the exosome marker CD63 on EVs isolated from plasma from patient #4 pre-treatment and after disease progression (nPLEX; \* $p=0.008$ ,  $n=8$ , two-tailed t-test). **F**) Levels of full-length AXL on exosomes isolated from LOX-IMVI cells in culture (western blot;  $n=3$ ). **G**) Levels of MET, AXL, and the exosome marker CD63 on exosomes isolated from MDA-MB231 cells +/- MEKi treatment (nPLEX; \* $p=0.01$ ,  $n\geq 2$ , two-tailed t-test). **H**) LOX-IMVI lysate western blot, probed with Abs for AXL ectodomain (N-term) and cytoplasmic (C-term) epitopes. **I**) Quantification of cell count, pERK1/2, and RTK levels in LOX-IMVI cells ( $n\geq 3$ ). **J**) MDA-MB231 lysate western blot, probed with Abs for AXL ectodomain (N-term) and cytoplasmic (C-term) epitopes. **K**) Quantification of cell count, pERK1/2, and RTK levels in MDA-MB231 ( $n\geq 3$ ). **L**) Representative immunofluorescence of LM2 primary TNBC tumors 21 days after PD325901 treatment, showing upregulation of AXL ectodomain near the tumor edge. Scale bar = 100 $\mu\text{m}$ . **M**) Mean (thick line) +/- SEM (shaded area) for staining intensity for MET and AXL measured within a 140  $\mu\text{m}$  sliding window from the tumor edge (\* $p=0.013$ ;  $n\geq 3$  tumors per group).

**Figure 3: Combination MEKi and AXLi synergistically reduce tumor growth and metastasis in mouse models of melanoma and TNBC.** **A**) Cell counts and surface AXL and MET changes (measured by live-cell immunostaining;  $n=3$ ) after 24h treatment with MEKi in 11 different cell lines. **B**) Correlation between cell count and surface RTK expression after MEKi treatment, ranked by order across cell lines in A ( $\rho$  = Spearman correlation, p-value from exact permutation test). **C**) U0126 and PD325901 increase surface AXL (measured by live-cell

immunostaining) more in cell lines showing synergistic inhibition of proliferation from dual AXLi/MEKi ( $p=0.01$ , two-tailed t-test). Dots represent data from 10 cell lines and two drug combinations (see Fig. S3). Treatments in *KRAS* or *HRAS* mutant cell lines are shown in red, and are significantly enriched among the synergistic responses ( $p=0.02$ , Fisher's exact test). **D**) Dual AXLi/MEKi reduces tumor growth more than either treatment individually (1 mg/kg PD325901; 30 mg/kg R428), in LM2 TNBC xenografts (\*two-tailed t-test,  $n\geq 7$ ). **E**) Dual AXLi/MEKi reduces metastasis after 21 days of treatment, corresponding to *D* (\*two-tailed t-test,  $n\geq 7$ ). **F-H**) AXLi (30 mg/kg R428) co-treatment synergistically increases efficacy of BRAFi/MEKi (1 mg/kg PD0325901 with 10 mg/kg vemurafinib) in LOX-IMVI xenografts by enhancing initial tumor shrinkage (F;  $p=0.031$ , two-tailed t-test), delaying tumor recurrence (G;  $p=0.002$ , two-tailed t-test), and extending survival (H;  $p=0.03$ , two-tailed log-rank test);  $n\geq 8$  animals per group for all. Note AXLi alone fails to significantly affect tumor growth and animal survival.

**Figure 4: MEKi-induced RTK changes are consistent with decreased proteolytic receptor shedding.** **A**) Top bar graph: Differentially detected supernatant proteins from MDA-MB231 treated with MEKi (PD325901) for 24h, measured by Ab-microarray ( $n=4$ ). Middle: Enrichment score (ES) trace for top-ranked gene-set of proteins depleted with MEKi; vertical bars below trace indicate location of proteins in the top-ranked gene-set. **B**) Diverse kinase inhibitors (labeled as drug target followed by drug name) affect supernatant concentrations in MDA-MB231 ( $n\geq 2$ ; ELISA), after normalizing to cell count. **C**) Venn diagram of differentially expressed genes (DEGs) from RNA microarray analysis of MDA-MB231 treated with PD325901 or BB94 for 24h ( $q=\text{FDR-corrected } p\text{-value}$ ;  $n\geq 2$ ). **D**) Surface level changes of



shedase substrates following MPi or MEKi in two TNBC cell lines (live-cell immunostaining; n=3). **E-F**) Intact lysate AXL from LOX-IMVI (*E*) and MDA-MB231 cells (*F*), as detected using Abs probing N-term or C-term epitopes (n=4). **G**) Full-length exosomal AXL and exosome markers CD63 and HSP70, isolated MDA-MB231 supernatant (n=6). **H**) The immunoprecipitated shed AXL fragment from supernatant of MDA-MB231 cells decreases in abundance with BB94 or PD320951 treatment (n=3). For *E-H*, \*p<0.05, two-tailed t-test. **I**) Supernatant, lysate total and phospho-RTK levels following MPi; each dot represents one of 19 cell lines tested (see Fig. S4K-L).

**Figure 5: MPi increases proliferation in an AXL-dependent manner and blocks**

**MEKi/AXLi synergy.** **A**) AXL and MET siRNAs reduce compensatory p-JNK signaling, measured following 3h drug treatment and 48h siRNA treatment in MDA-MB231 (\*p=0.014, pooled t-test, n=2 reps / cond; siRNA validation, Fig. S5E). **B-C**) Representative western blots (**B**) and quantification (**C**) show enhanced p-Akt and p-cJUN following 24h treatment with either MPi or MEKi, which is blocked in the presence of AXLi (\*p<0.05, two-tailed t-test, n≥3). **D**) MPi using BB94 enhances proliferation in the absence of R428, but decreases proliferation when R428 is present (p=0.02; n≥4, two-tailed t-test). **E**) BB94 increases mitotic index, measured by FACS cell cycle analysis, which is blocked by AXLi using R428 (bars denote p<0.05; n≥4 total reps; pooled two-tailed t-test). **F**) Computed simulations to illustrate how increasing the Loewe synergy term  $\alpha$  theoretically affects cell survival (shown by heatmaps) in response to varying combinations of AXLi and MEKi co-treatment. **G**) Cells were treated with varying combinations of MEKi and AXLi for 72h, in the presence or absence of BB94, after which cell count was measured (shown as numbers and heatmap as a fraction of the max cell count for each

plate). **H)** Data from combination drug treatments (*G*) were fit to a model of Loewe synergy, yielding the synergy interaction term  $\alpha$ , which significantly decreased with MPi (\**p*<0.05, two-tailed jackknife test, *n*=20 measurements over *n*=2 reps).

**Figure 6: ADAM10 and ADAM17 regulate cell surface AXL and alter cell growth in an AXL-dependent manner. A-B)** ADAM-targeted siRNAs (validation: Fig. S6A) reduce supernatant AXL (*A*; ELISA measurement) and increase surface AXL (*B*; live-cell immunostaining) compared to non-targeted siRNA (\**p*<0.05; *n*≥2) in MDA-MB231. **C)** The specific ADAM10 inhibitor GI-254023X decreases supernatant AXL from MDA-MB231 (\**p*<0.05; *n*=3). **D)** The specific ADAM10 inhibitor proA10 reduces supernatant AXL compared to the vehicle control, measured by ELISA using MDA-MB231 (\**p*<0.05; *n*≥2). **E-F)** Recombinant ADAM10 cleaves recombinant AXL in a dose-response fashion, shown by AXL immunoblot (*E*) and corresponding quantification (*F*; \**p*<0.05; two-tailed t-test; *n*=2). **G)** Recombinant ADAM10 and ADAM17 cleave recombinant AXL, and cleavage is blocked by MPi using BB94 (*n*=2). **H)** In MDA-MB231 cells, ADAM10 inhibition or knockdown by siRNA only decreases proliferation in the presence of AXLi using R428. ADAM17 siRNA only induces proliferation in the absence of AXLi. SiRNA results were measured 24h after AXLi, 72h after transfection, and GI-254023X results were measured after 72h treatment (\**p*<0.05; *n*≥4; two-tailed t-test).

**Figure 7: MEKi reduces sheddase activity via increased TIMP1 association, and TIMP1 neutralization enhances MAPKi efficacy. A)** MEKi reduces ADAM10 and ADAM17 catalytic activities in MDA-MB231, directly measured using the live-cell PrAMA assay (\**p*<0.05; *n*=4).

**B)** Live-cell immunostaining shows knockdown of TIMP1 but not TIMP3 reduces surface AXL in MDA-MB231, 24h after PD325901 treatment and 72h after transfection (\* $p < 0.05$ ;  $n = 3$ ; knockdown validation: Fig. S7D). **C)** Co-treatment with a TIMP1 neutralization antibody (T1-NAB) blocks tumor AXL accumulation following BRAFi/MEKi treatment in the LOX-IMVI melanoma xenograft model, shown by immunofluorescence quantification (\* $p = 0.02$ ;  $n \geq 2$ ). **D)** Live-cell immunostaining shows MEKi increases surface TIMP1 in MDA-MB231. **E)** Flow cytometry shows 5 min MEKi treatment increases rTIMP1-fluor binding to the cell surface (\* $p < 0.05$ ;  $n = 4$ ). **F)** Significant co-IP of ADAM10-HA and rTIMP-fluor is only detected in bulk anti-HA IP lysate from cells transfected with ADAM10-HA and treated with U0126 (\* $p < 0.05$ ;  $n = 3$ ; pooled two-tailed t-test). **G-H)** The 120kDa ADAM10 dimerization band (39) and co-IP with rTIMP1 increases with 5 min MEKi (\* $p < 0.05$ ;  $n > 3$ ). **I)** 24h pre-treatment with a TIMP1 neutralization antibody (T1-NAB) followed by co-treatment with PD325901 (MEKi) or vemurafenib (BRAFi) lead to enhanced reduction in cell count at 72h, normalized to the effect-size of BRAFi or MEKi alone (\* $p = 0.03$ , pooled two-tailed t-test,  $n = 18$  total reps). **J-K)** T1-NAB co-treatment synergistically increases BRAFi/MEKi efficacy in the LOX-IMVI xenograft model by enhancing initial tumor shrinkage (*J*;  $p = 0.014$ , two-way ANOVA interaction term, total  $n = 46$ ) and delaying tumor recurrence (*K*;  $p = 0.04$ , two-tailed t-test,  $n \geq 8$  per group). **L)** Overview schematic of RTK shedding as a mechanism of MAPKi resistance.

**Figure 1**

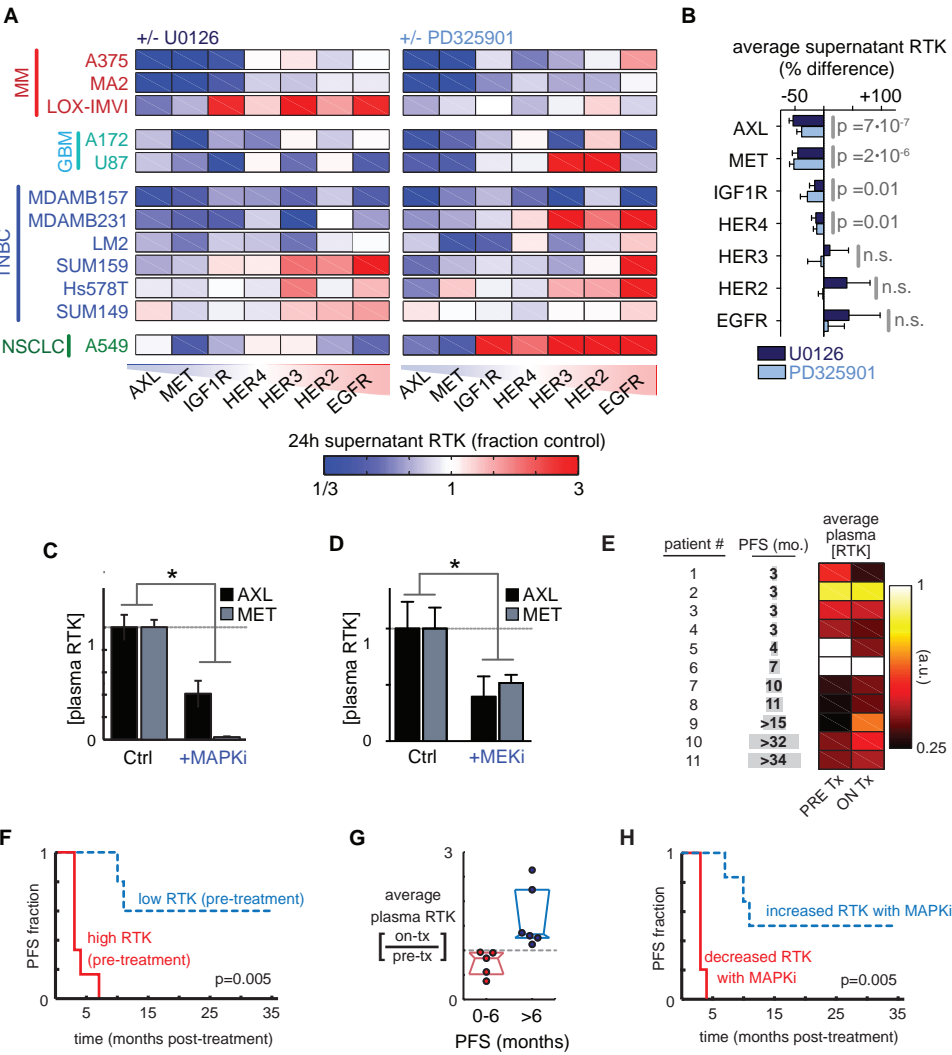
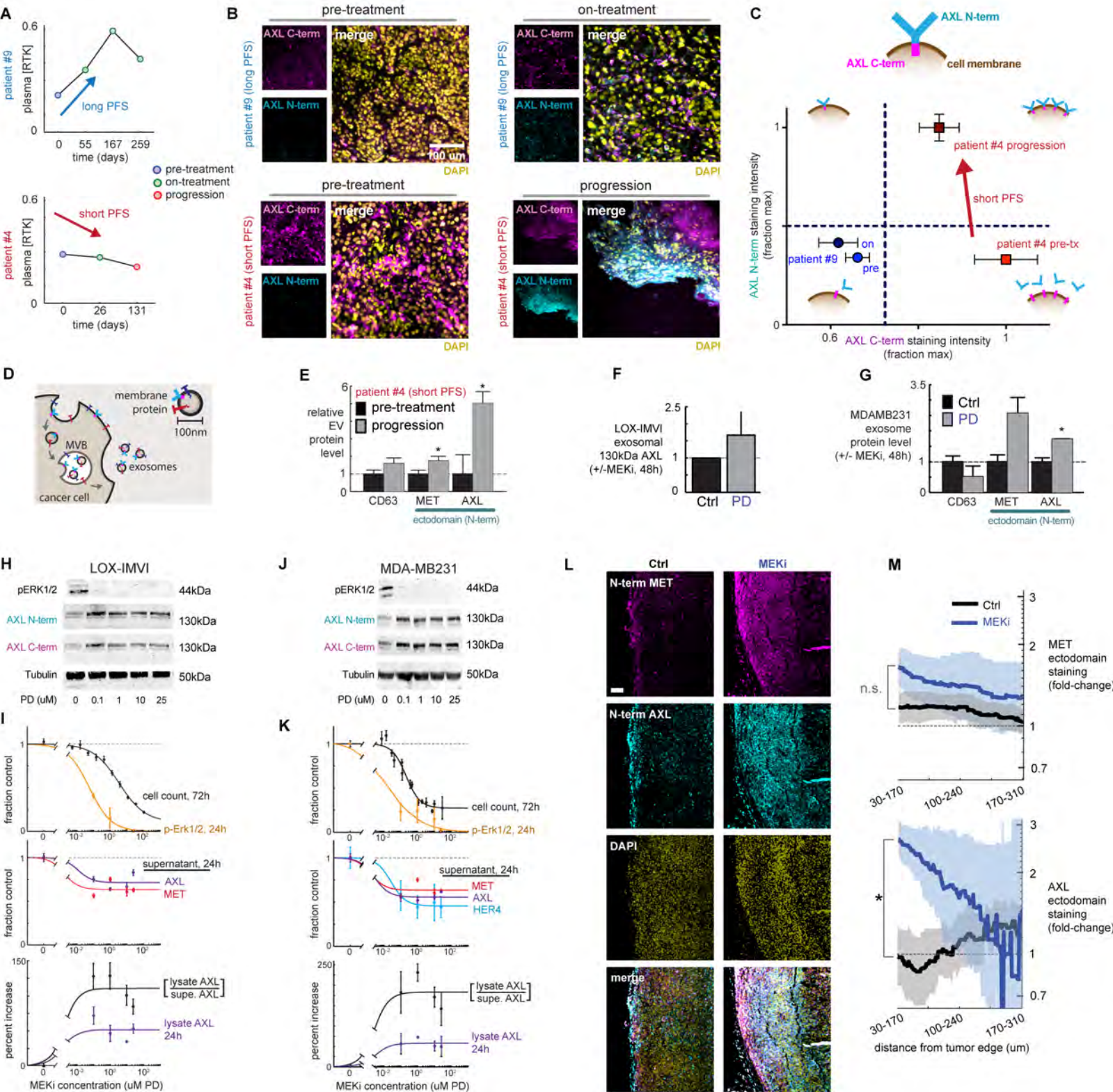
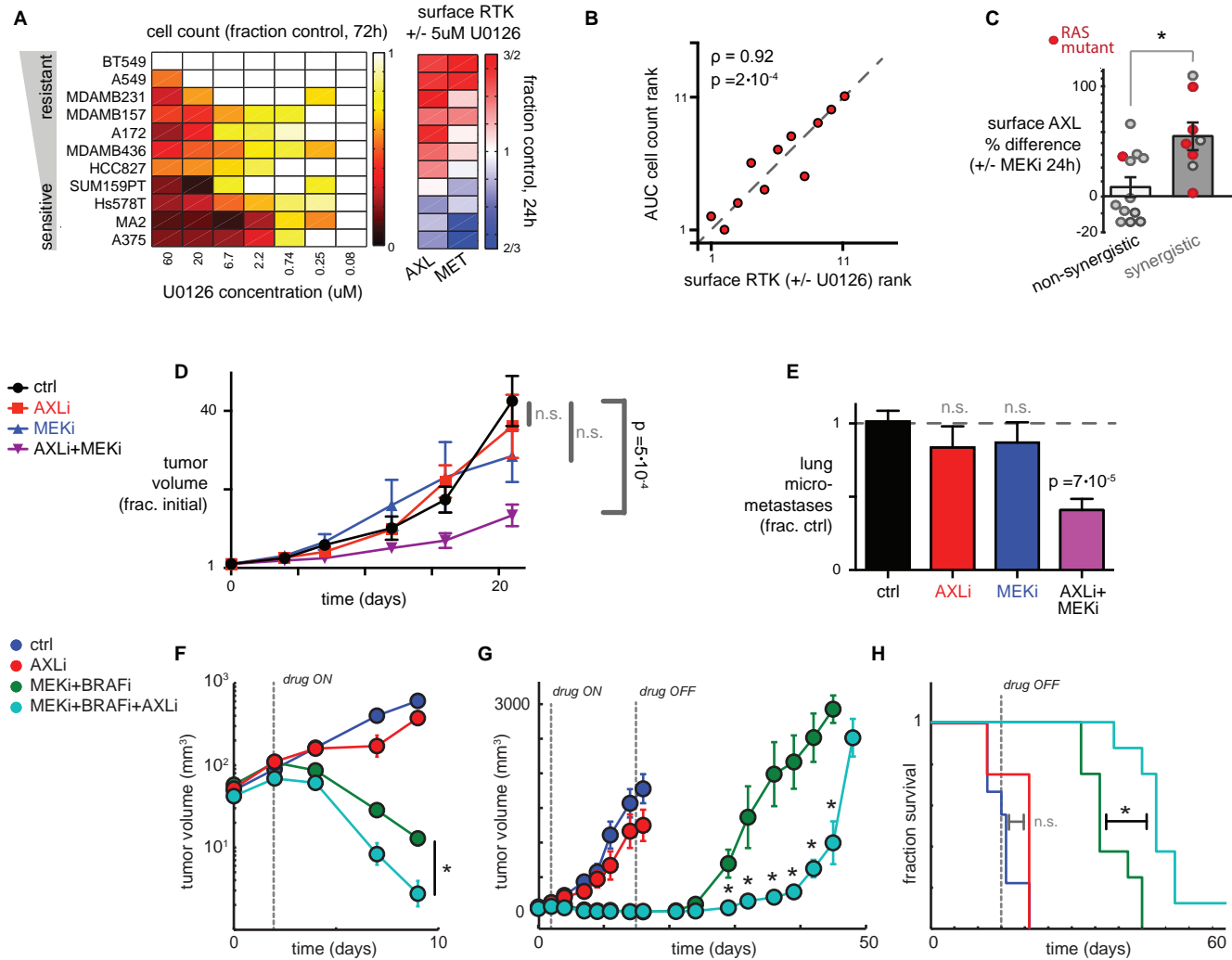
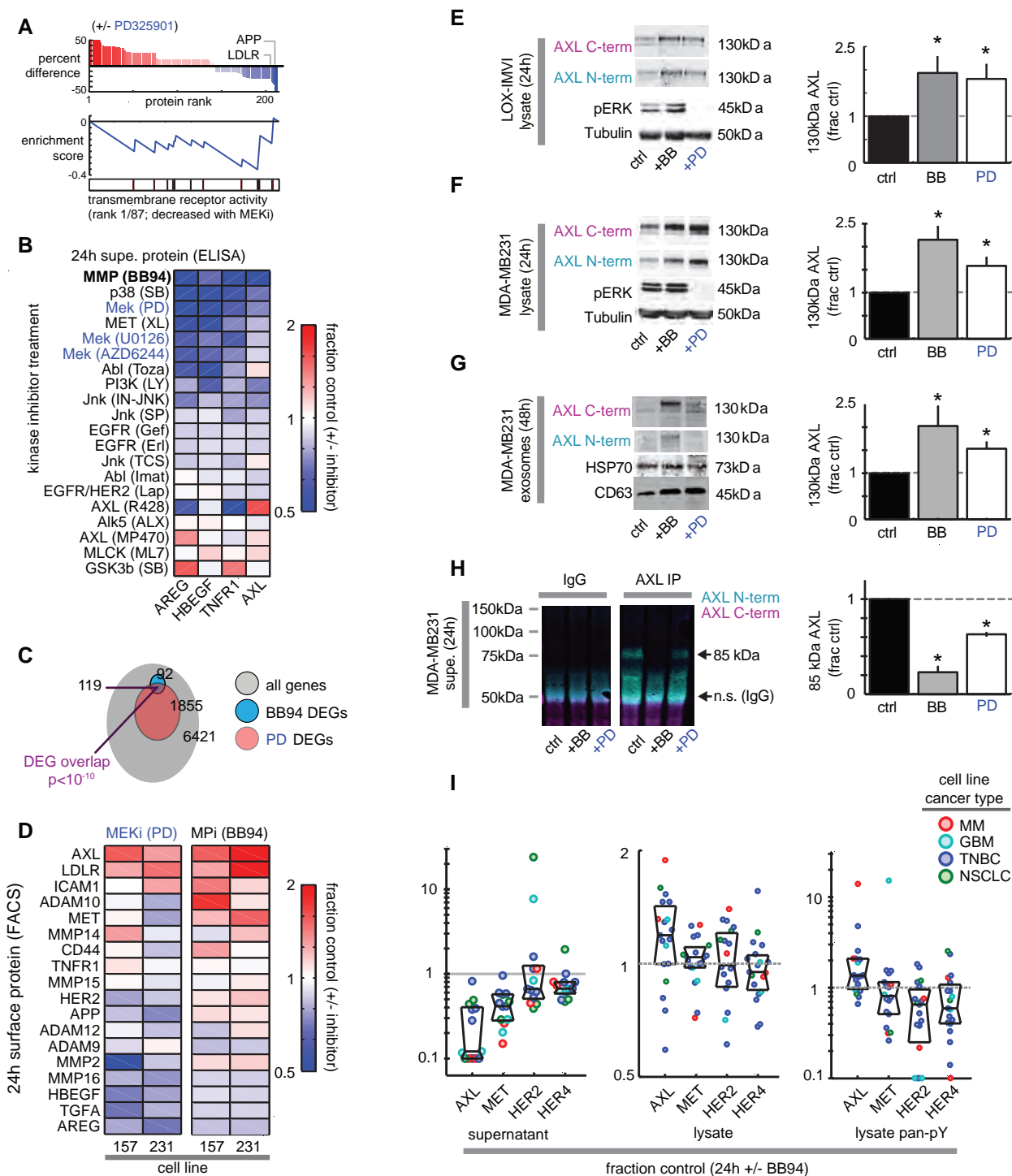


Figure 2

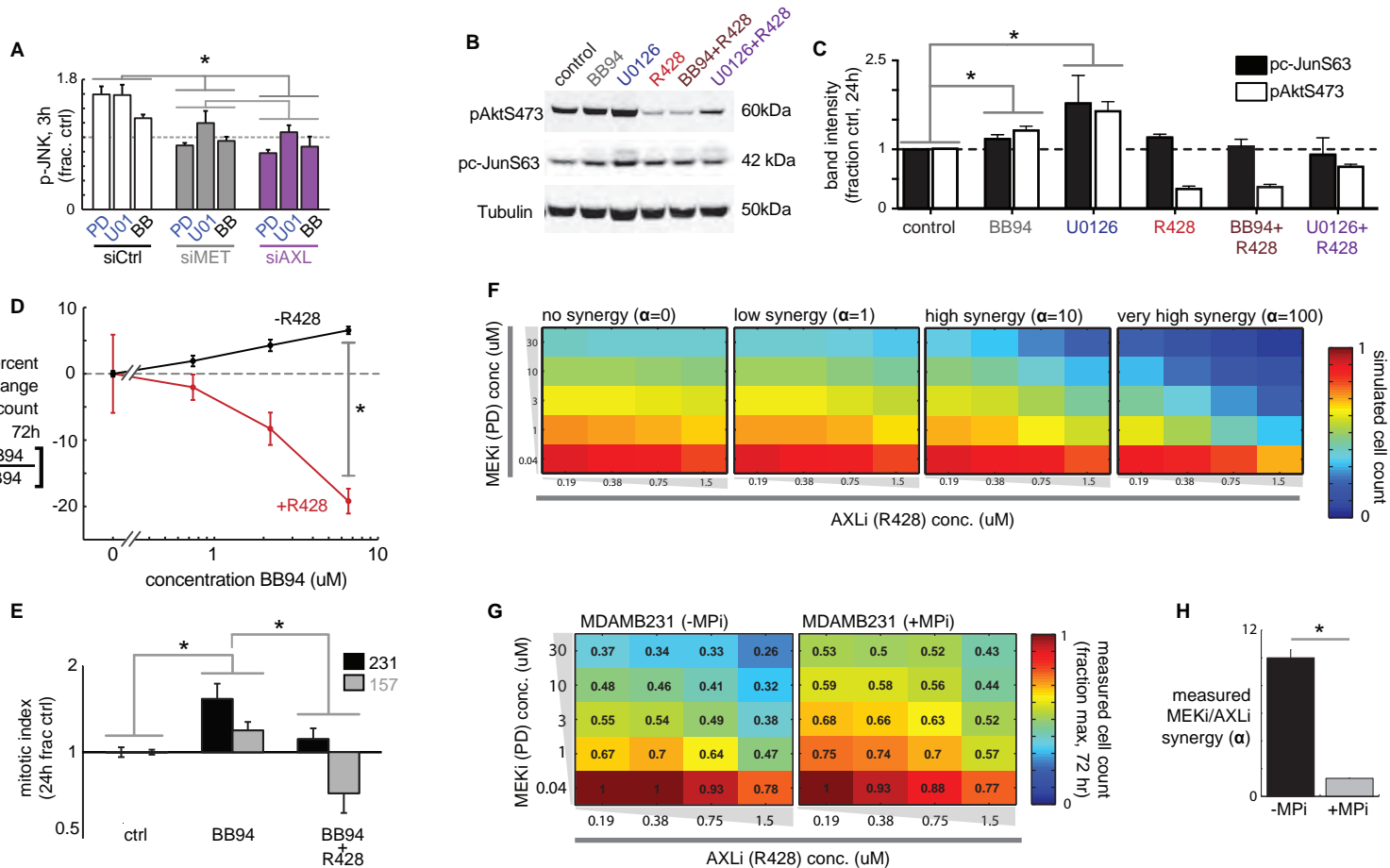


**Figure 3**

**Figure 4**





**Figure 5**



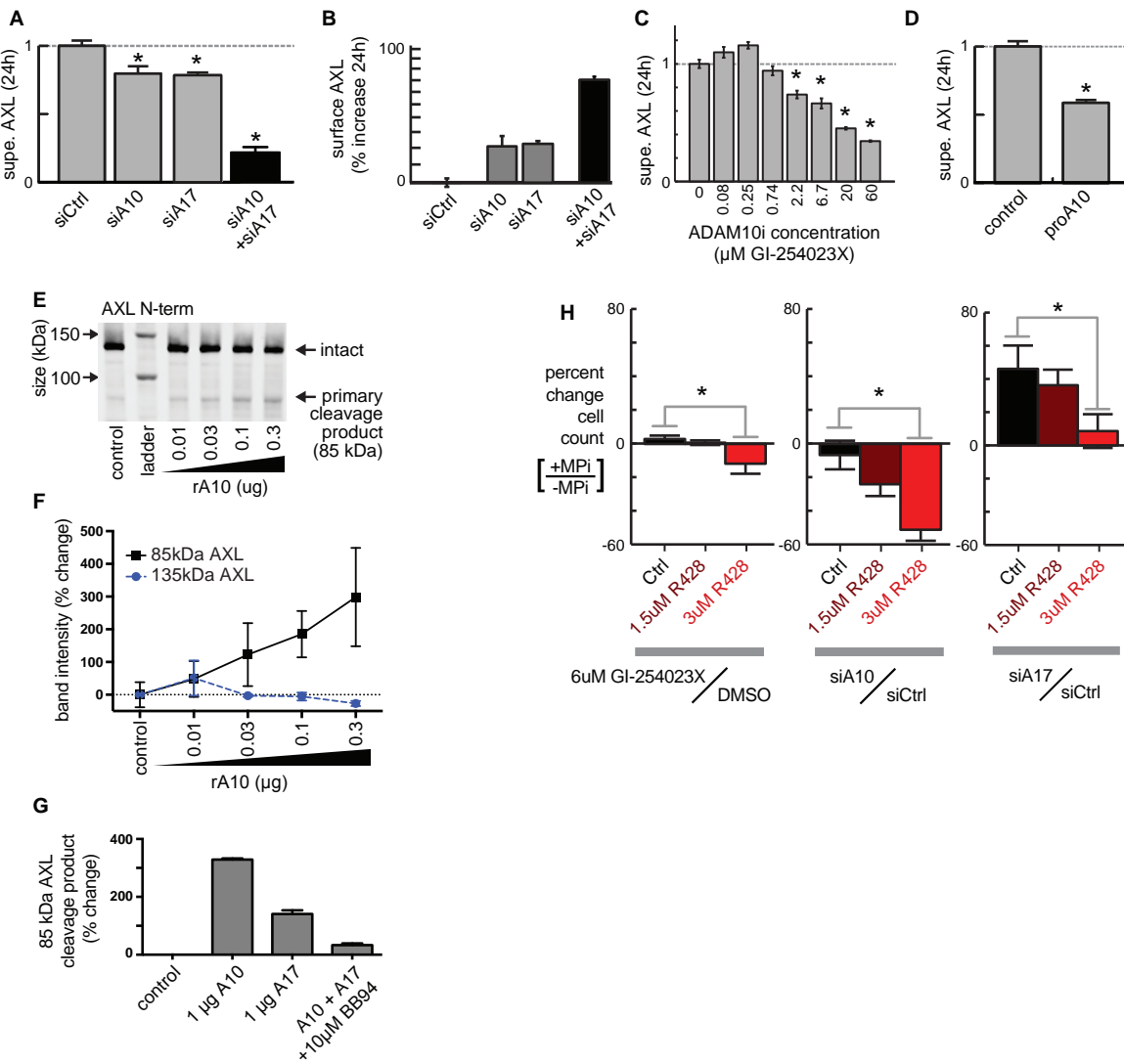
**Figure 6**

Figure 7

